THE OPTIMISATION OF THE PROPERTIES OF HIGH-STRENGTH SPRING STEELS FOR RAILWAY APPLICATION.

Velaphi Jeffrey Matjeke

A thesis submitted to the Faculty of Engineering and the Built Environment, University of Witwatersrand, Johannesburg, in fulfilment of the requirements for the degree of Doctor of Philosophy

Johannesburg, 2020

Abstract

Bogie springs are critical safety components because they are responsible for the safe operation of railway vehicles. They are also responsible for providing railway vehicles with smooth rides and stability by acting as shock absorbers, bearing load, and controlling motion. However, frequent maintenance interventions owing to premature spring failure result in derailments, logistical disruptions, and financial loss. The aim of this study is to provide a solution to premature spring failure and material scarcity in South Africa. To address these problems, a system thinking approach was used, in which existing failures were studied from the perspective of spring design and material. Additionally, the study investigated spring design using finite element analysis and developed tolerances to avoid operational defects and failures. The study also investigated the fundamental causes of premature spring failure on a newly designed spring that was supposed to fit on a recently purchased locomotive. The causes of the premature spring failures were found to be design related and were linked to an inadequate heat treatment process. The pitch angle contributed to spring coil contact, resulting in notches that accelerated fatigue crack initiation and fatigue failure, while quench cracks formed as a result of deteriorating quenching oil. Therefore, the pitch angle had to be carefully considered to avoid coil contact during loading and unloading of the springs, and the quenching oil had to be monitored to ensure that it did not lose its cooling capabilities over time. The material used for the springs was the Society of Automotive Engineers 5160 spring steel, which the original equipment manufacturer recommended. But because the local steel mill was unable to generate enough orders to keep the production line going, the availability of the recommended material became a concern. Additionally, the government enacted a local content legislation to encourage the localisation of skills and technology, which are not easily available in the country, and steel was deemed a local commodity by the Department of Trade, Industry, and Competition. As a result, alternative materials that can be used as a replacement had to be found. This presented the opportunity to research alternative spring steel grades and optimise heat treatment processes to manufacture bogie springs that are suitable for the existing design and configuration. A unique heat treatment was deployed by considering various quenching oils with different cooling rates that affect the steel grades differently. Quenching oils were also chosen based on the compositions of the different steel grades to avoid quench cracking, as well as quenching oils with the ability to produce desirable mechanical properties and microstructures. The exact critical transformation temperatures and oxidation rates along with

the optimum soaking time and tempering temperature were also determined and measured for each steel grade.

Publications

1. VJ Matjeke, G Mukwevho, JW Van Der Merwe, Effects of putrefied quenching oil on the transformation behaviour of railway spring steel. 2018 IOP Conf. Ser. Mater. Sci. Eng. doi:10.1088/1757-899X/430/1/012043.
2. VJ Matjeke, G Mukwevho, AM Maleka, JW Van Der Merwe, Effects of heat treatment on strength and ductility of 52CrMoV4 spring steel. 2018 IOP Conf. Ser. Mater. Sci. Eng. doi:10.1088/1757-899X/430/1/012044.
3. VJ Matjeke, JW Van Der Merwe, MJ Phasha, G Mukwevho, Thermal characteristics of spring steels used in railway bogies. 2019 SN applied nature journal. https://doi.org/10.1007/s42452-019-1546-5.
4. VJ Matjeke, JW Van Der Merwe, Determination of critical transformation temperatures for purposes of spring steel heat treatment optimisation process. *Multidisciplinary digital publishing institute; Metals.*

Declaration

I declare that this dissertation is my own unaided work and has not been submitted before for any degree or examination at any other university. This dissertation is being submitted for the degree of Doctor of Philosophy in Engineering at the University of the Witwatersrand, Johannesburg.

Matjeke VJ

23 October 2021

Date

Acknowledgements

I would like to express my greatest gratitude to my supervisor, Ass. Prof. JW van der Merwe, for his continuous support and encouragement; as well as to my inspirational manager at Transnet, Mr Moopanar, for his continuous support and understanding throughout my studies. I would also like to express my sincere gratitude to Ms G Mukwevho and colleagues for their support. I am most grateful to my family, without whom this would have been impossible to achieve. I am also very thankful to my colleagues and friends. To God be all the glory.

Dedication

I dedicate this work particularly to my mother, Meriam Matjeke; to my brothers, Dumisane Lincoln Matjeke and Lucky Mekateko Matjeke; and to my children, Lethabo Shadung, Lwandile Mulweri Matjeke, and Vululami Kabongwe Matjeke. Finally, I would like to thank my life partner, Senzeni Khanyema for the support and love provided throughout my studies.

Table of Contents

List of Figures

List of Tables

List of Abbreviations

AHSS Advanced high-strength steel
ASTM American Society for Testing and Materials
BCC Body-centred cubic
BCT Body-centred tetragonal
CCT Continuous cooling transformation
DSC Differential scanning calorimetry
FCC Face-centred cubic
FEA Finite element analysis
FEM Finite element model
HSLA High-strength low-alloy
RPM Revolutions per minute
RQ Research question
SAE Society of Automotive Engineers
SCC Stress corrosion cracking
SEM Scanning electron microscope
SSRT Slow strain rate test
TMT Thermo-mechanical treatment
TTT Time-temperature transformation
UTS Ultimate tensile strength
XRD X-ray diffraction
YS Yield strength

List of Symbols

C_E Fatigue strength coefficient

D Mean diameter of coil [m]

d Nominal diameter of wire [m]

e Engineering strain

Fe_3C Iron carbide

F Spring force [N]

G Shear modulus of elasticity [Pa]

K_E Endurance factor

K_{S1} Initial stress factor

K_{S2} Maximum stress factor

K_U Ultimate strength factor

k Stress correction factor

K Strength coefficient

L_0 Free length of spring [m]

n Number of active spring coils; life cycles

n_t Total number of spring coils

n Strain hardening exponent

p Pitch [m]

R Spring rate [N/m]

R_m Minimum value of tensile strength [MPa]

s Spring deflection [m]

S Engineering stress

w Spring index

Y Fatigue exponent

α Ferrite

γ Austinite

σ_T True stress

ε_T True strain

λ Pitch angle [rad]

τ Uncorrected torsional shear stress [Pa]

τ_k Corrected torsional shear stress [Pa]

$\tau_{k,shear}$ Corrected shear stress [Pa]; max principal shear value of stress [Pa]

Chapter 1

1.1 INTRODUCTION

Rail transportation is the most cost-effective method of freight transportation around the globe due to its large carrying capacity and speed (Izadi, Nabipour, and Titidezh, 2020). However, the premature failure of the springs used on railway vehicles results in catastrophic derailments of rolling stock, unnecessary delays, and an increase in operational costs, which negatively impact the economy (Ling *et al*., 2017). This study investigated the factors that resulted in a series of premature spring failures on railway bogies in South Africa.

A bogie is a framework of axles and wheels fitted underneath a railway vehicle and is classified as either a two-axle or three-axle bogie, which are most commonly used in modern locomotives. A locomotive configured with two-axle bogies is referred to as a BO-BO locomotive and consists of two bogies with two independently powered axles and four wheels per bogie, as shown in Figure 1.1. A locomotive configured with three-axle bogies is referred to as a CO-CO locomotive and consists of two bogies with three independently powered axles and six wheels per bogie (Naveen *et al*., 2014).

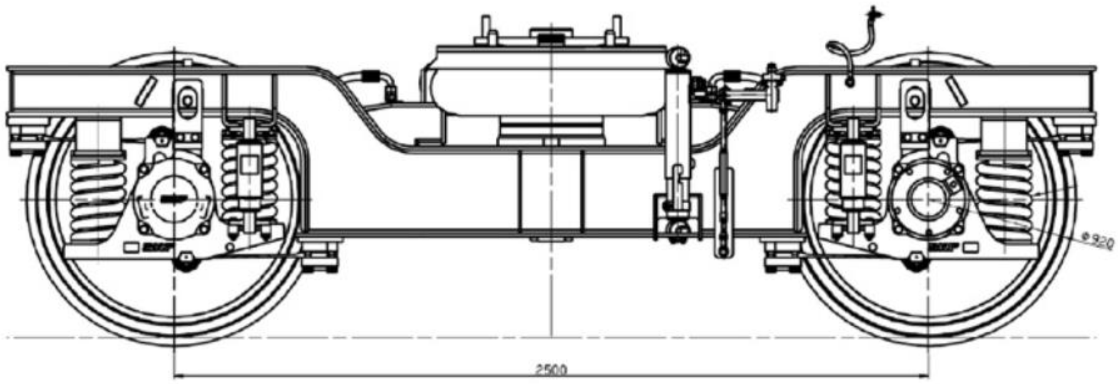

Figure 1.1 Side view of a two-axle bogie used on a BO-BO locomotive (Sayyaadi and Shokouhi, 2009).

Each axle is assembled with four sets of dual springs, with two sets sandwiching the axle at each wheel. A dual spring consists of an inner and an outer spring. The spring shown in Figure 1.2 is classified as a dual helical compression spring (Liu, Liu, and Liu, 2010).

Figure 1.2 A brand new dual helical compression spring used on a 22E locomotive.

Springs are elastic objects that are designed to obtain properties that allow for compression when a load is applied and to return to their original shape when the load is released (Fragoudakis, Karditsas, and Savaidis, 2014; Loganathan, 2019, Kobelev, 2020. The functionality of railway vehicles is dependent on the capability of the springs to absorb, store, and release elastic energy (de Crescenzo and Salvini, 2019). Various railway vehicles such as locomotives, railroad cars, and wagons use different kinds of compression springs due to their constant deformation rate when external loads are applied (Mishra and Aggarwal, 2020).

Compression springs, also known as helical compression springs or coil springs, were first developed in the 18th century. They are made of high tensile strength steel rods formed into a helical coil contour followed by a robust heat treatment process (Abidin *et al*., 2013). The function of a compression spring is to provide resistance to a force that causes two components to move towards each other, as well as to provide rolling stock with comfort and dynamic stability by absorbing shock and vibrations during movement (Baek *et al*., 2013). Helical compression springs are specifically used to suspend the payload and unsprung mass of the rolling stock.

It is critical that locomotives and bogies are equipped with springs capable of supporting them. Locomotive weight and bogie design are therefore taken into consideration when designing helical compression bogie springs, i.e. some bogies require dual helical compression springs, while others require multiple springs stacked in sequence. However, complexities arise from the fact that these springs are manufactured using different designs in terms of rod diameter, coil diameter, free length, and solid length, etc., as well as different materials.

1.1.1 Background

Organisation A is the name given to a South African freight rail operator who entered into a joint venture collaboration with an international original equipment manufacturer (OEM) to locally design, manufacture, and assemble a new locomotive. Organisation A depended on the OEM as it did not have any experience in building locomotives. Neither of these companies can be named as they are both involved in litigation. The spring manufacturing for the new locomotive was carried out by Plant A, which is a manufacturing subsidiary of Organisation A and wished to remain anonymous. The newly designed bogie springs manufactured in Plant A revealed manufacturing defects, which were predominately observed on the new locomotive.

The locomotive is electric-powered and carries a maximum load of 22 tons per axle. On average, the springs on a legacy locomotive have a lifespan of over 25 years, depending on their usage. The bogie springs manufactured for the new locomotive failed prematurely while in service and only survived a maximum of 120 km over a period of a months. Following a series of failures, the manufacturing process was altered, and nine sets of springs were subjected to fatigue testing with a target of 2×10^6 cycles. All nine sets of springs failed to successfully complete the test.

It is worth mentioning that time maintenance is practiced in South Africa as opposed to condition-based maintenance in other areas of the world. The best way to extend the lifespan of bogie springs is to preserve them from corrosion, which will ensure a long fatigue life. It is also important to generate the necessary measurements and criteria for reliable testing (Loganathan, 2019). Additionally, the reason for the failure of the original springs must be determined so that the material characteristics and spring design can be addressed.

1.1.2 Problem statement

Currently, the original bogie springs are manufactured from locally produced Society of Automotive Engineers (SAE) 5160 spring steel (Baek *et al*., 2013). However, the spring shop is not buying enough quantities of spring steel to sustain the continuous production of this steel grade. Therefore, the local steel producer has been encouraging the spring shop to develop springs from alternative materials to manage the risk of current material scarcity. The equivalent material used for the springs is currently manufactured abroad but the South African government passed a localisation legislation for parastatals to favour local manufacturers, in effect, preventing them from buying designated steels from outside the country.

Under the Preferential Procurement Policy Framework Act (PPPFA), 2000 (Act No. 5 of 2000); the National Industrial Participation Programme; and the Competitive Supplier Development Programme; South Africa has leveraged public procurement by designating products and sectors for local content (Crompton *et al.*, 2017). Local content designations for locomotives were added to the PPPFA section 9.1 designations in July 2012. As a result, the local supply of springs and other locomotive components had to be developed from a commercial and technical perspective. This research considered developing springs from locally produced spring steel. However, because SAE 5160 spring steel is no longer popular for bogie springs and the market in general, alternative materials, along with the appropriate heat treatment process, must be found.

1.1.3 Scope

Due to higher train speed and freight tonnages, the accuracy and reliability requirements of bogie springs have significantly increased in recent years. It is therefore necessary to develop bogie springs with improved properties and longer service life. Hence, this study was conducted to refine the mechanical properties of spring steel and the manufacturing process of bogie springs. This will be done by re-evaluating spring design, focusing on material composition, and optimising the heat treatment process, as well as investigating the influence of quenching media on the mechanical properties of spring steel.

Additionally, improved properties and prolonged service life of bogie springs will be achieved by optimising the heat treatment process based on material-specific characteristics. The materials investigated in this study are high silicon spring steel, high-strength low-alloy

(HSLA) spring steel, and high-strength spring steel alloyed with molybdenum and vanadium. The dimensions of the spring steel rods considered are 25 mm in diameter. The critical transformation parameters for the alternative steel grades and the atmospheric reaction on the steel surfaces during heat treatment are currently unavailable in the literature. The attainment and addition of this information will further enhance the lifespan of bogie springs and the body of knowledge with the literature.

Priority was given to improving the strength of spring steel, while preserving ductility, toughness, and fatigue properties. This can be done by developing alloy elements and optimising the heat treatment process (Podgornik *et al.*, 2015). The ultimate tensile strength (UTS) of the spring steel also had to be increased without compromising ductility or microstructural aspects to improve the fatigue life of the springs. Manufacturing processes such as alloying and hardening had to be modified to cater for the current requirements of extended spring lifespan (Fedin and Borts, 2009). Furthermore, alternative quenching media was investigated to reduce the possibilities of manufacturing-related defects such as quench cracks and stress corrosion cracking.

A detailed investigation of the manufacturing process of bogie springs is included in the study and largely covers the heat treatment process, which involves high-temperature coiling, normalising, re-austenitisation, quenching, and tempering (Rakhshtadt, 1991). The heat treatment process is intended to induce sufficient mechanical properties of spring steel that will ensure a predictably long service life for the springs (Liu *et al.*, 2010). The optimisation thereof will also increase the fatigue properties and overall performance of the bogie springs. This research, therefore, focuses on tailor-making and optimising the heat treatment process for the alternative spring steel grades by remodelling the combination of the coiling, quenching, and tempering temperatures. The heat treatment process was undertaken within a laboratory environment.

The study further explores the characteristics of helical compression bogie springs and compiles the information to accurately calculate and design them. Additionally, the effect of geometrical spring design on fatigue life is investigated. The study also includes failure analysis case studies, finite element analysis (FEA), as well as mathematical and numerical illustrations. Failure analysis can be used as a tool to determine the structural integrity of a spring and to ensure future improvement in spring design and material quality. FEA was used to re-evaluate the structural assessment of the newly-designed bogie springs to determine structural integrity, as well as to redesign the geometric and structural aspects of the springs.

1.1.4 Aims

The primary aim of this research is to develop and manufacture full-scale helical compression bogie springs from alternative local spring steel grades that are more resistant to defects for an optimum combination of performance and resistance. The secondary aim of this study is to improve the fatigue life of the bogie springs through heat treatment. To certify the springs, a fatigue test of 2×10^6 cycles was performed. The study further aims to gather data to fill the current research gap in the body of knowledge relevant to this field. In summary, this study aims to produce affordable bogie springs with excellent mechanical properties and quality, using a local material that is widely available.

1.1.5 Objectives

The objectives of this research are to:

- Select alternative local materials that are less prone to manufacturing flaws, such as quench cracks and consequently, produce superior spring properties.
- Improve material properties by optimising the soaking time and tempering temperature.
- Evaluate the effect of the pitch angle on the fatigue strength of the bogie springs.
- Evaluate the effect of the cooling rates of the deteriorated quenching oil on the transformation behaviour of the original material (SEA 5160 spring steel)
- Determine the exact critical transformation temperatures and decarburisation and oxidation rates of the three selected spring steel grades.
- Determine the thermomechanical properties of the three selected spring steel grades.

1.1.6 Research questions

The sudden development of microcracking in bogie springs during the manufacturing process has resulted in lifespan reduction of springs manufactured from SAE 5160 spring steel. The improvements in the lifespan will reduce the lifecycle cost of rolling stock. Therefore, the research questions are outlined as:

- Can the alternative material be optimised to provide the mechanical properties required for an optimum combination of strength, performance, and resistance of the springs?

- Can the spring performance and lifespan be improved by optimising the heat treatment process?
- Can the deterioration of quenching media cause the quench cracking observed in the original spring that failed?
- How can this study contribute to filling the existing knowledge gap regarding specific steel grade properties for the manufacturing of durable bogie springs?

1.1.7 Hypotheses

To improve the performance and lifespan of bogie springs, the following hypotheses are made:

- H01: The strength of spring steel can be increased by optimising the heat treatment process through the quenching media selection, tempering temperatures, and soaking times.
- H02: Selecting the quenching media for the specific spring steel grade based on the critical transformation temperatures can achieve the desired microstructure and mechanical properties without causing quench cracks.
- H03: The exact thermal characteristics such as the critical transformation temperatures, tempering temperatures, soaking times, and oxidation and decarburisation rates of each steel grade influence the attainable strength and fatigue life of the spring.

1.1.8 Research framework

To be able to address the research questions, a research framework was put in place:

- Chapter 1 gives a brief introduction and review of bogie springs and their application.
- Chapter 2 covers the literature review of the manufacturing process of bogie springs. This theoretical background consists of different fields such as the metallography of high-strength spring steel and the structural design, manufacturing, and heat treatment processes of bogie springs. Various scientific articles, books, and dissertations were studied to create a theoretical foundation for this research.
- Chapter 3 includes the methodology and experimental procedures. The heat treatment process, dilatometric testing, smart quench testing, differential scanning calorimetry (DSC) analysis, and characterisation techniques are also outlined.
- Chapter 4 focuses on a case study of prominent failure mechanisms of bogie springs, which was done by investigating the entire manufacturing process. The chapter also considers the design of dual springs and the effect of the pitch angle on the fatigue life

of the springs. The design assessment was done using mathematical demonstrations and FEA. This chapter also includes the experimental results, which are presented in a theme format.

- Chapter 5 presents the discussion of the results.
- Chapter 6 covers the overall conclusions based on the experimental results.

Chapter 2 : Literature

2.1 LITERATURE REVIEW

The safe operation of railway vehicles has been a priority and concern for engineers worldwide (Eom, Kang, and Lee, 2013). In the last century, efforts have been made to manufacture high-performance defect-free springs with increased lifespan and load capacity. In order to do so, a more in-depth knowledge of the material selection and production of bogie springs is needed. Therefore, the literature review focuses on the uses, materials, design, and manufacturing of bogie springs, as well as the in-service performance of railway vehicles.

Additionally, the literature review pays close attention to historical spring failures, the crystal structures and mechanical properties of spring steel, as well as the chemical composition of spring steel during microstructure transformation. The effect of heat treatment conditions are also scrutinised and the roles of austenitisation and tempering temperature in improving material properties are inspected and discussed, as well as the role of quenching media in relation to the material. The quenching media cooling rates and decarburisation and oxidation rates of each steel grade are also explored. Furthermore, the effect of silicon on the properties of alternative high-silicon spring steel are investigated, along with the role of molybdenum and vanadium. The literature review also emphasises evaluation and testing methods.

2.1.1 Premature spring failure

Bogie springs are mechanically coiled steel rods that store and release energy (Abidin *et al.,* 2013) and are critical safety components of the structural system of railway vehicles (Ji-Lin and Kai-Hong, 2013). They are responsible for the safe operation of railway vehicles and are essential for keeping railway fleets on track, as well as for ensuring smooth rides by absorbing shock and vibrations during movement of the vehicles (Baek *et al.*, 2013). However, bogie springs can result in catastrophic failures if they malfunction. The premature failure of bogie springs has been a nightmare for engineers and scientists since the beginning of railway transportation and has been investigated by many researchers (Mukhopadhyay *et al.*, 1997; Das *et al.,* 2007a; Zhu *et al.,* 2014b). Prawoto *et al.* (2008) stated that springs fail due to metallurgical factors related to heat treatment, while Das *et al.* (2007b) argued that it is rare for springs to fail due to faulty design.

Furthermore, Kumbhalkar, Yenarkar, and Grover (2011) found that the main cause of failure was due to the lack of lateral dumping on the curves. Additionally, the structural integrity of springs is often neglected during the failure investigation as it is assumed that metallurgical and manufacturing factors are the main source of failure (Dakhore and Bissa, 2013). Therefore, the purpose of this study is to investigate the primary causes of spring failures that are not properly covered and to evaluate the manufacturing process of springs. The springs that were involved in the failure investigation were manufactured from high stiffness SAE J404 grade 5160 spring steel. The quenched and tempered SAE J404 grade 5160 spring steel exhibited high UTS, high-yield strength, and a high endurance limit (BS EN 10089, 2002).

Although most spring failures are a result of manufacturing-related flaws, there are several mechanisms that also cause failure, most of which occur due to multifaceted stress distribution. These failure mechanisms range from design, raw material defects, manufacturing defects, and loading conditions, i.e. insufficient load-carrying capacity (Pyttel *et al.,* 2014; Vukelic and Brcic, 2016). Generally, springs are designed to withstand cyclic loading during their lifetime. However, spring failure usually progresses with fatigue cracking due to cyclic loading and unloading (Daudpoto *et al.,* 2021).

There are also external factors that determine lifespan such as corrosion and mechanical damages (Artaraz and Sánchez Beitia, 1991). Therefore, it is important to increase the fatigue endurance of bogie springs to improve their lifespan and reduce logistical disruptions. This can be done by optimising the heat treatment process and improving the mechanical properties of bogie springs. The service records of the bogie springs in South Africa indicate that they generally last for a period of 25 years, operating in similar conditions as those of the failed springs. Some of the failure mechanisms observed in South Africa over the years are undesirable microstructures, hydrogen embrittlement, temper embrittlement, and quench cracking caused by inadequate heat treatment (Mukwevho, 2016).

Other problems that occur in bogie springs are caused by corrosion, low fatigue life, and stiffness. Inclusions and surface roughness of the spring steel are also important stress-raisers (Vukelic and Brcic, 2016). Additionally, stress corrosion cracking (SCC) has been causing significant service disruptions across the world as it leads to sudden failure of the springs (Spisák and Szávai, 2019). SCC is a term used to describe in-service-related failures of material due to crack propagation caused by corrosive environments and external and residual stresses

(Nasirpouri, Alizadeh, and Hosseingholizadeh, 2011). SCC occurs when susceptible materials continuously experience mechanical load and electrochemical corrosion due to the environment (Khalifeh, 2019).

The rate of SCC is influenced by the composition, microstructure, and strength of alloys (Koch, 2001) and is predominant in low-carbon steels (Prakash, Hara, and Malik, 1999). The exact nature of this phenomenon has not been thoroughly explored in high-strength spring steels. Material selection can be considered to decrease SCC development. Therefore, this study investigates material-specific susceptibility of the three spring steel grades. SCC as a function of load and time is shown in Figure 2.1.

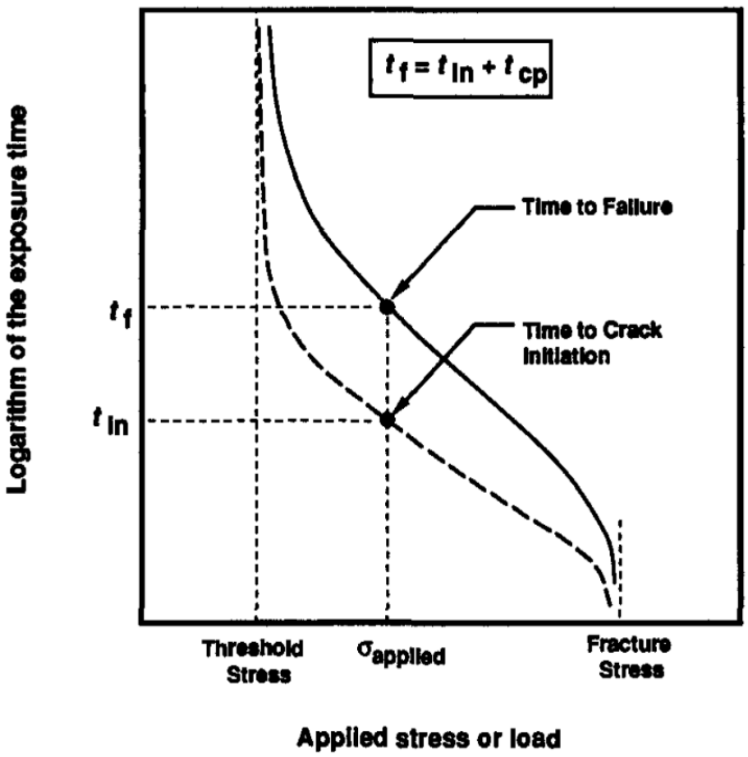

Figure 2.1 Typical time to failure as a function of load (Parkins, 1992).

2.1.2 Prolonging spring lifespan

Recent global economic growth has led to increased railway freight demands and consequently, increased railway traffic (Rashid Khan *et al.,* 2018). A solution to reducing railway traffic is to increase the speed and payload of railway vehicles (Naveen *et al.,* 2014). Therefore, the reliability of heavy-duty springs must be improved to safely operate heavy haul trains. Helical compression springs are commonly used as heavy-duty springs on railway bogies (Matjeke *et al.*, 2018).

Due to the inaccessibility of the springs, there is no way of detecting premature failure, which can result in catastrophic calamities and derailments (Joshi *et al.,* 2015). For this reason, it is important that bogie springs are designed for an infinite lifespan, along with increased capacity and improved productivity. Strength, therefore, becomes significantly important (Ahn *et al.,* 2020). A study by Pang *et al.,* (2013) showed the relationship between the fatigue strength and UTS of steel, as illustrated in Figure 2.2. The figure shows that fatigue strength generally increases when UTS increases.

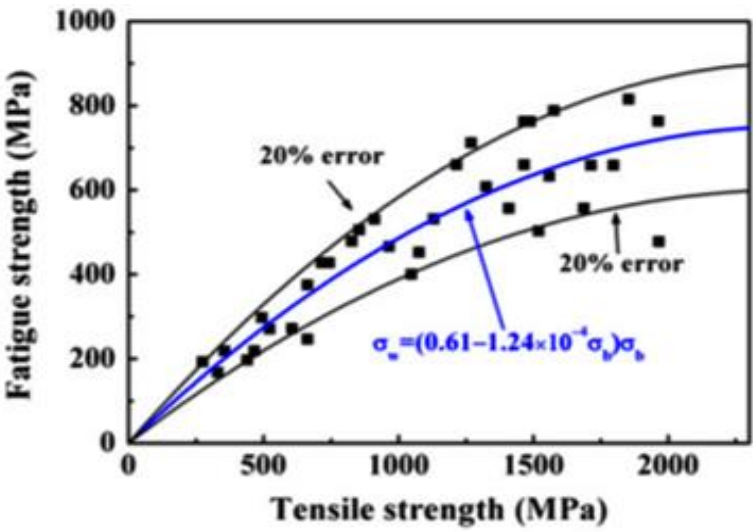

Figure 2.2 The relationship between the tensile strength and fatigue strength of steel (Pang *et al.*, 2013).

Heavy-duty helical compression springs experience a combination of tension, compression, and torsion in-service. They also endure in-service stresses, i.e. cyclic stress, axial stress, and torsional stress, which directly affect their lifespan. The stresses are shown in Equations 2.1 to 2.4, where $S_{e\,1000}$ and S_{e10^6} multiplied by the UTS are the estimated fatigue limits at a thousand and million cycles, respectively. The fatigue limit, or endurance limit, of steel is largely dependent on the UTS (Ibrahim Al-Zuhairi *et al.*, 2020). A schematic of a SN-Curve is plotted in Figure 2.3, using Equations 2.1 and 2.2.

$$S_{e\,1000} = 0.9\,S_{UTS} \qquad 2.1$$

$$S_{e10^6} = 0.5\,S_{UTS} \qquad 2.2$$

$$S_{e\,1000} = 0.72\, S_{UTS} \tag{2.3}$$

$$S_{e10^6} = 0.29\, S_{UTS} \tag{2.4}$$

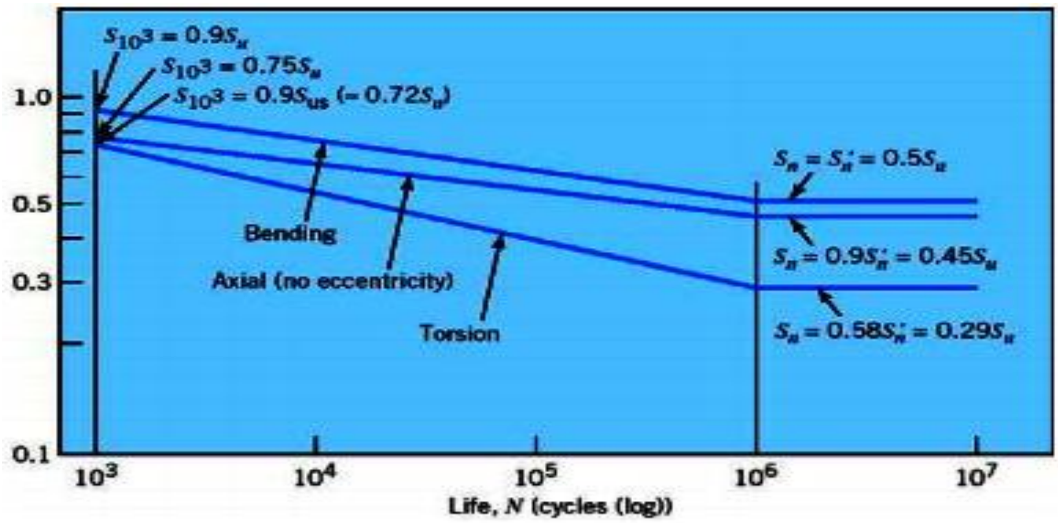

Figure 2.3 SN-curve for wrought steel (Juvinall, 1967).

Prolonged lifespan and improved performance are functions of strength and ductility (Matjeke *et al.*, 2018). Increasing the strength of the steel is simple, however, it is difficult to obtain a combination of both high strength and ductility, as the increase in the former generally results in a decrease of the latter (Li *et al.*, 2016). Alloying elements can be used to improvise for both, but the cost of alloyed steel is high (Podgornik *et al.*, 2015). Therefore, the material selection and manufacturing process must be optimised in such a way that the steel will exhibit excellent strength and ductility with minimal alloying elements. An exact understanding of material behaviour and the heat treatment process is required for the manufacturing of heavy-duty springs, as both directly influence lifespan (Fragoudakis, Savaidis, and Michailidis, 2017).

Heat treatment affects the strength and fatigue limit of springs (Kubit *et al.*, 2016) and alters the strength and microstructure of material. Additionally, the behaviour of each steel grade can deteriorate the mechanical properties of springs (Manuel and Cerda, 2017). 55Cr3, 54SiCr6, and 52CrMoV4 were selected as spring steel according to the BS EN 10089:2002 standard and were used in this study. The BS EN 10089:2002 standard relies on hardness and strength in the determination of suitable materials for springs (BS EN 10089, 2002). The three materials are classified as alloy steels; however, the compositions vary significantly.

The charging fees of the raw materials are worth noting: 55Cr3 and 52CrMoV4 cost 922 US dollars per ton and 54SiCr6 costs 953 US dollars per ton. The main cost driver for 54SiCr6 is the amount of silicon and vanadium present. The strength and hardenability of 52CrMoV4 steel is improved by the additions of chromium, molybdenum, and vanadium. Chromium and vanadium form carbides that improve the hardness of the material during tempering, while molybdenum forms fine carbide precipitates that increase the strain hardening effect (Vinet and Zhedanov, 2010). Molybdenum also provides solution strengthening in steel during the heat treatment (Kostryzhev *et al.*, 2018).

Vanadium improves the hardness and strength of HSLA steel by the formation of vanadium carbides and grain refinement (Kannan, 2011), while silicon improves the hardenability of steel by shifting the continuous cooling transformation (CCT) curve to the right (Frazier, Boulger, and Lorig, 1956). Silicon is often added as a deoxidiser and retards carbide formation to form cementite (Ardehali Barani *et al.*, 2006). However, although silicon-rich spring steels are popular in the railway industry, they often suffer from decarburisation (Shi, Yao, and Hui, 2008). To meet the objective of increased spring lifespan and performance, a good balance between strength and ductility are focused on in this study.

Salihu (2016) presented a range of mechanical properties of advanced high-strength steels (AHSS) shown in Figure 2.4. According to the categorisation illustrated in the figure, the current spring steel properties fall within the second-generation category. The objective of this study is to achieve strength and ductility equivalent to or exceeding the third-generation category.

This study aimed to attain high strength and good ductility by subjecting the material to a robust heat treatment process and quench media. The investigation specifically focused on the heat treatment process, quenching oil analysis, mechanical properties, and microstructure of the steels. The study further investigated whether conventional automotive spring steels can achieve and exceed the mechanical properties attained by AHSS. The majority of automotive springs are made from medium-carbon high-strength steels.

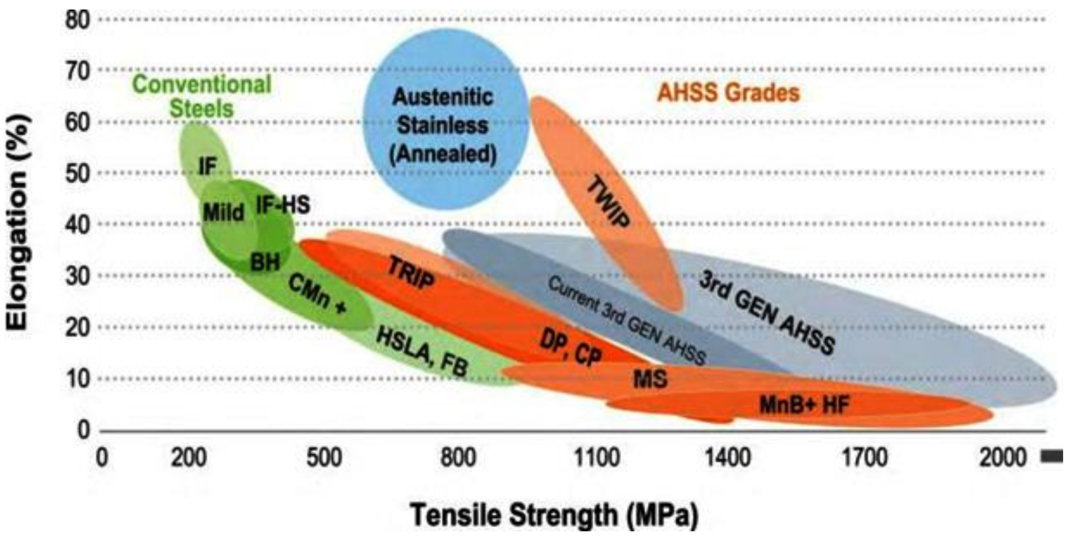

Figure 2.4 Global AHSS (Salihu, 2016).

2.1.3 Spring material

2.1.3.1 Steel and steel composition

Steel is the most widely used form of metal due to its extensive application (Totten, 2006). Steel commonly refers to the various alloys of iron, which differ by processing methods and elemental concentrations (Cain, 1984). The advantage of steel in comparison to other metals is its ductility, high strength, low cost, versatility, and ability to be recycled although it has relatively high density. Generally, steel is defined by the amount of carbon it contains (Cahn and Haasen, 1996). Therefore, different types of steel exist, two of which are alloy steel and carbon steel.

Carbon steel can be classified into plain-carbon steel, medium-carbon steel, and high-carbon steel (Totten, 2006). The optimisation of the mechanical properties of spring steel is dependent on the steel composition. Figure 2.5 shows the different spring classifications. It also highlights the spring steel composition investigated in this study, which is classified as medium-carbon steel. Spring steel has an average carbon percentage of 0.55%.

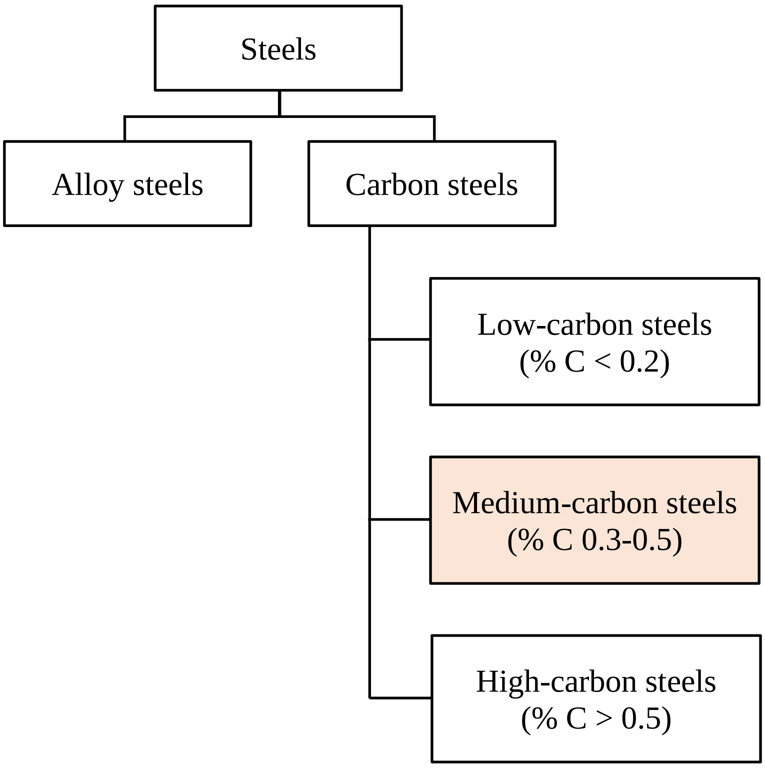

Figure 2.5 Steel types and classifications (Totten, 2006).

Before discussing the alloying elements of steel, continuous CCT and time-temperature transformation (TTT) must be discussed. Various steels behave differently during manufacturing and heat treatment processes. For example, rapid cooling to low temperatures leads to significant changes in the steel's mechanical properties and microstructures (Khovova *et al.*, 2010), which can have one or more phases, i.e. austenite, cementite, and ferrite (Smallman and Bishop, 1999). The reason for this is that the microstructural instability of the steel alloys with an austenite phase (FCC matrix) (Barbacki and Mikołajski, 1998).

CCT and TTT diagrams are effective in accurately predicting the mechanical properties and microstructures of various steel grades. Each steel grade has its own CCT curve (Zia-Ebrahimi and Krauss, 1984), which is largely influenced by the chemical composition of the alloying elements (Lingamanaik and Chen, 2014; Ravi Kumar *et al.*, 2000). Failure to adhere to the CCT diagrams of various steel grades may result in deficient microstructures and cracking due to inadequate heat treatment. Figure 2.6 shows the transformation range and CCT curves of SAE 5160 spring steel.

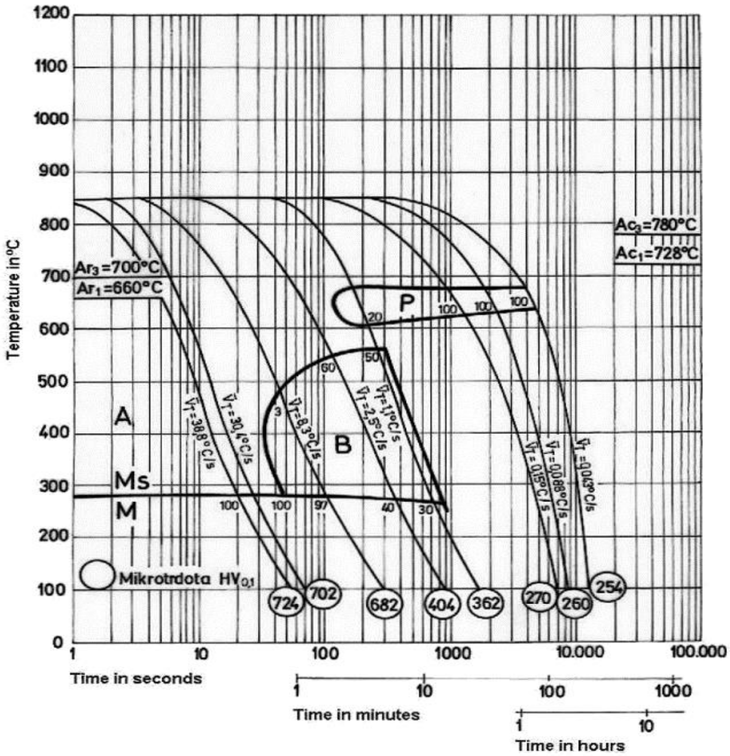

Figure 2.6 The CCT curve of SAE 5160 spring steel (Steel data, 2020).

The combination of various alloying elements can increase the hardenability and toughness of steel, as well as diminish the chances of grain growth. The most important alloying element in spring steel production is carbon (Totten, 2006), which ranges from approximately 0.008% to 2.0%, as shown in Figure 2.7.

The increase in carbon improves the hardenability and strength of steel but also increases the possibility of cracking during processing, while reducing weldability (Porter and Easterling, 1992). Hardenability is largely dependent on the solubility of the carbon atoms within the austenitic range (Manna, 2012). The steels that are considered for experimentation in this research have a carbon percentage ranging from 0.5% to 0.6%. These types of steels are regarded as adaptable high-carbon spring steels (Totten, 2006). As mentioned, the three spring steel grades focused on in this study are HSLA steel, high silicon steel, and high-strength steel alloyed with molybdenum and vanadium.

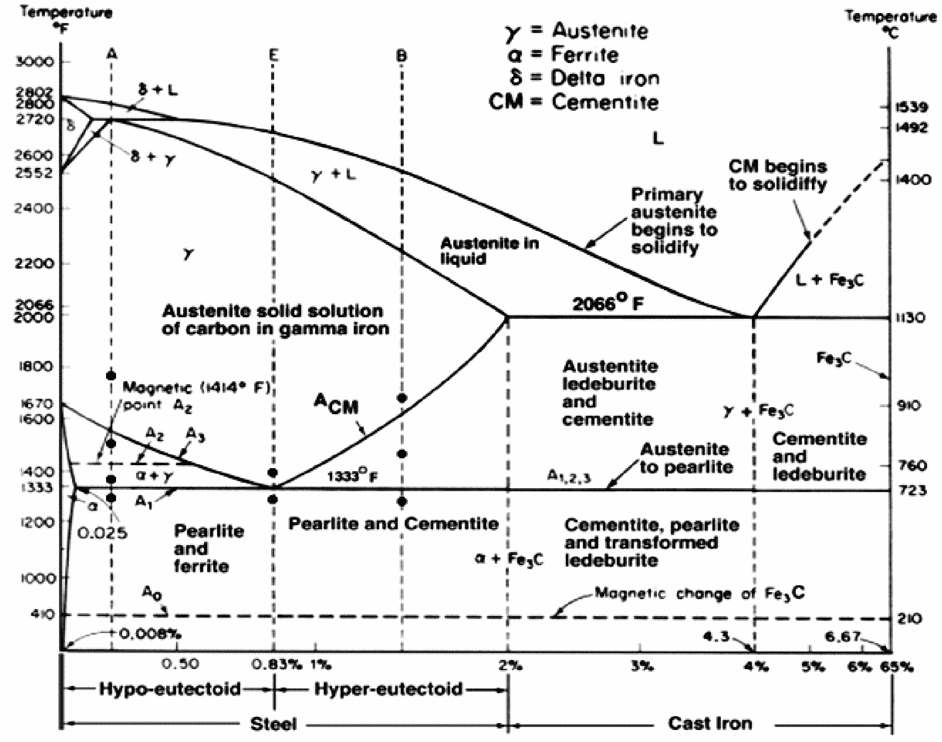

Figure 2.7 Fe-Fe3C phase diagram (Pandit, 2011).

Although carbon is the most important element in spring steel, other alloying elements are deliberately added to improve the mechanical properties and characteristics of the steel. Some of these elements include chromium, manganese, and silicon . Liu *et al.* (2012) also confirmed that enhanced properties in steel may be achieved by alloying with carbide-forming elements such as chromium, molybdenum, tungsten, and vanadium. These elements encourage the formation of stable martensite, as well as influence the martensite start (Ms) temperature and solubility equilibrium temperature of the phases (Reed-Hill, 1973). In this case, the spring steel is hardened simultaneously by the martensitic transformation, followed by tempering, and therefore retains both elongation and strength.

Chromium is the most common alloying element of all the selected alloys and improves resistance to corrosion, as well as the hardness and strength of steel. Chromium is also a carbide former, which may reduce the ductility of steel (Avner, 1998). Manganese is beneficial to the surface quality of all carbon ranges (Totten, 2006) and counteracts brittleness from sulphur and temper embrittlement; improves abrasion resistance, age hardening, hardenability, and hot and creep strength; and lastly, raises the grain coarsening temperature of austenite. Manganese tends to lower the eutectoid temperature, while chromium, molybdenum, and silicon are inclined to raise it. This is illustrated in Figure 2.8 by Porter and Easterling, (1992).

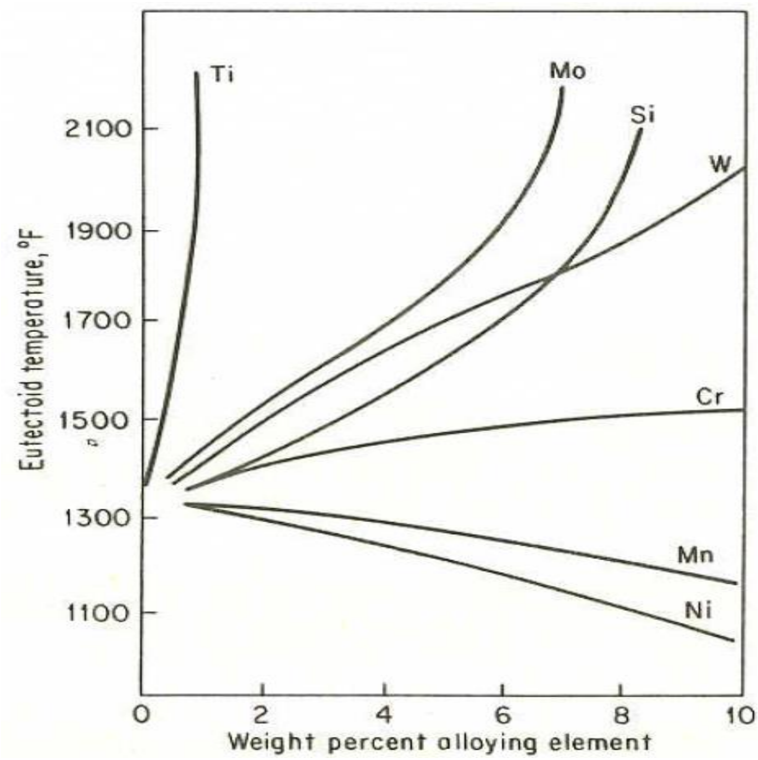

Figure 2.8 The effect of alloying elements on eutectoid temperature (Avner, 1998).

Silicon typically improves the oxidation resistance (Chatterjee, 2006). It also improves hardenability and remains so even after tempering, as well as offers good tensile test properties and toughness when added in appropriate proportions (Glebov *et al.,* 2010). Silicon dissolves into ferrite and is a ferrite stabiliser and further suppresses cementite precipitates from austenite.

It is worth noting that silicon is not an austenite former (Varshney *et al.,* 2017) as steels with low-silicon content are likely to also be low in retained austenite fraction. Silicon shifts the TTT curve of steel to the right without changing the shape (Walentek, 2007). The increase in silicon and molybdenum decreases the Ms temperature, as shown in Figure 2.9.

Molybdenum is a carbide former. The addition of Molybdenum on tempered steel provides secondary hardening and retards austenite to form ferrite and pearlite, thus, allowing bainite to form more readily (Leach, 2013). This was further documented by Lee *et al*. (2002) and is shown in Figure 2.10.

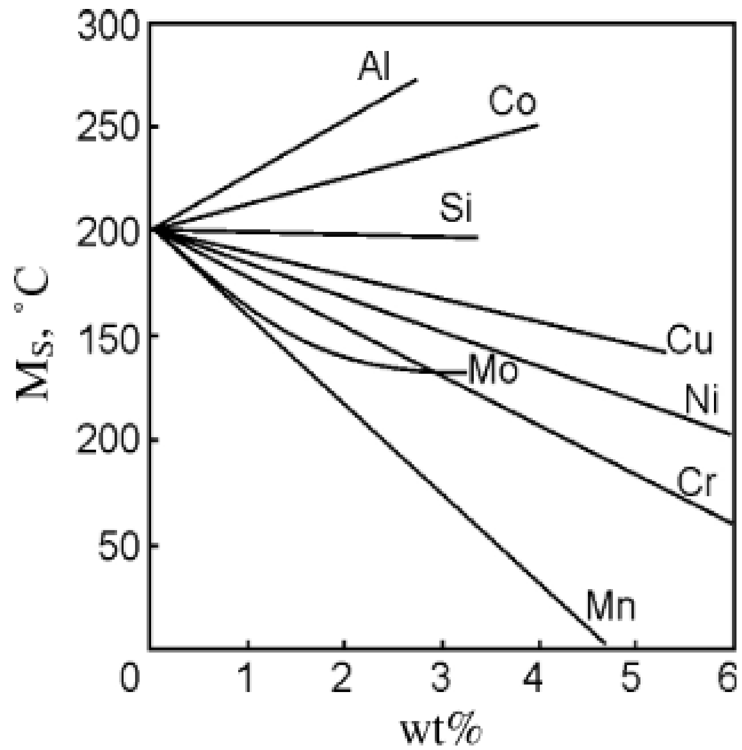

Figure 2.9 The influence of alloying elements on the Ms temperature of steel (Kobasko, Aronov, and Powell, 2009).

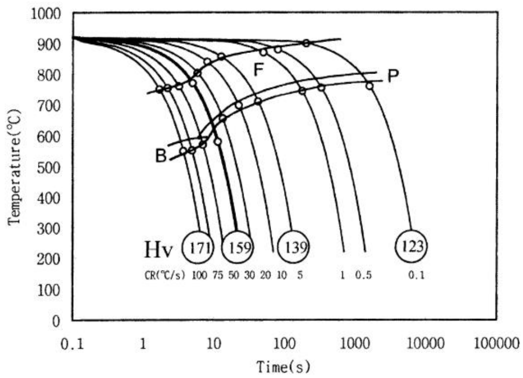

(a)

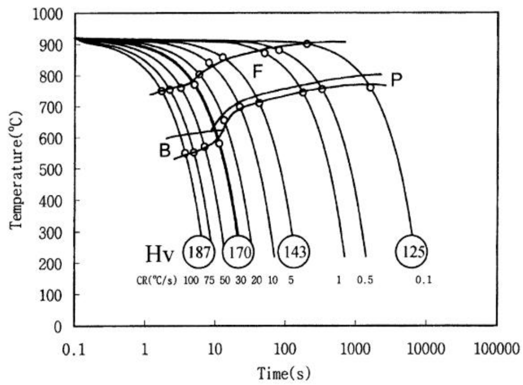

(b)

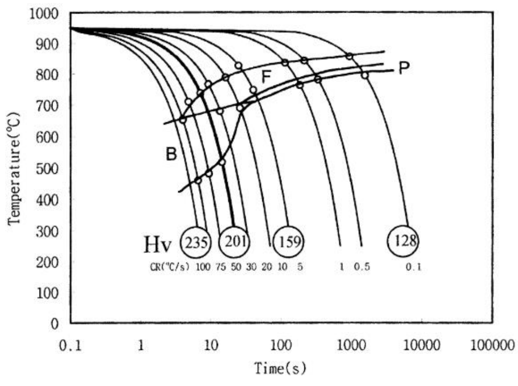

(c)

Figure 2.10 The effect of Mo on 0.3 wt% HSLA steel: (a) 0.03Nb, (b) 0.03Nb-0.3Mo, and (c) 0.03Nb-0.6Mo (Lee *et al.*, 2002).

Small increments of molybdenum and niobium improve the yield strength of HSLA steel (Lee *et al.*, 2002), while the additions of molybdenum and vanadium improve resistance to SCC in steels (Nasirpouri, Alizadeh, and Hosseingholizadeh, 2011). Molybdenum and vanadium are unresolved at temperatures below 860°C and may reduce grain growth (Avner, 1998), resulting in finely dispersed carbides that retard austenite growth (Zajac, 1999). Molybdenum and vanadium carbides are stable at temperatures below 910°C but form respective carbides.

Vanadium carbides decompose at about 950°C and therefore do not restrict austenite grain growth at higher temperatures (Annan, 2015). Vanadaium also has higher solubility in austenite compared to other alloying elements (Golden, 2017). Vanadium precipitates form at relatively low temperatures, indicating that the driving force for vanadium carbide precipitation in austenite is low. Apart from hardening the material, vanadium also induces secondary hardening effects during tempering (Goulas, 2019). Additionally, vanadium has been used as a micro-alloying element for HSLA steels since the 1950s (Sage, 1984).

Carbide-forming elements improve hardenability when dissolved in austenite and increase wear resistance (Totten, 2006). Additionally, the large measure of hardness is improved by the carbide size and distribution. Chromium carbides readily dissolve in austenite (Ardehali Barani, Ponge, and Raabe, 2006), while iron carbides, or cementite (Fe_3C), require minimum temperatures of about 723°C to dissolve. These carbides become nucleation sites during phase transformation, resulting in the TTT curve shifting to the right, as shown in Figure 2.11. Austenitisation of spring steel is undertaken at 850°C ± 30°C, therefore, the carbide will stimulate nucleation during phase transformation.

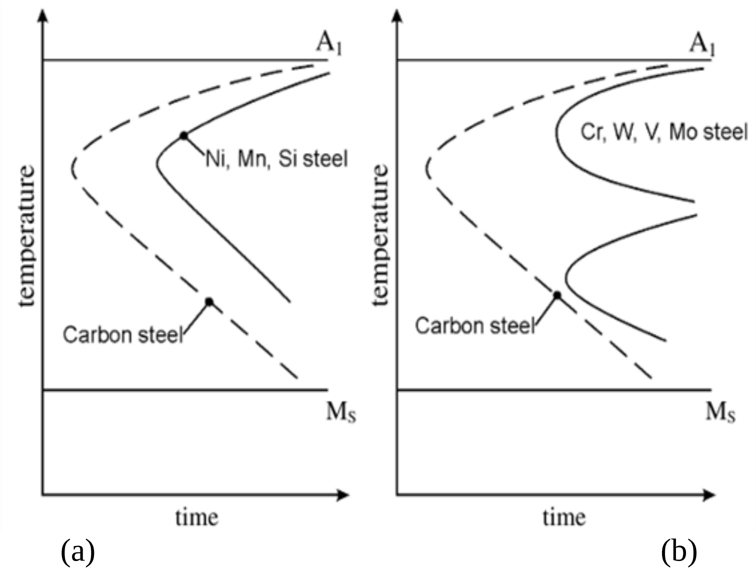

(a) (b)

Figure 2.11 TTT diagrams of the effect of alloying elements on steel: (a) steel alloyed with Ni, Si, and Mn and (b) steel alloyed with Cr, W, V, and Mo (Kobasko *et al.*, 2009).

2.1.3.2 Material selection

Helical compression springs are exposed to high stress levels, severe atmospheric conditions, and corrosive raw materials (Zhu, Wang, and Huang, 2014a). Hence, suitable material properties are essential (Fragoudakis *et al.,* 2014). Therefore, this section focuses on the factors to consider when selecting materials for springs. Firstly, the uses of the springs, as well as the conditions and environments that the springs will be used in, should be considered, as they play a significant role in the corrosion rate of different steel types and may influence the spring's durability (Komazaki *et al.,* 2005). For example, materials used to build a wagon that transports coal or iron ore should be able to withstand the corrosive environment and properties associated with these commodities.

Secondly, design requirements such as deflection, lifespan, and load need to be considered as they dictate material quality and type (Reddy and Reddy, 2013). The increase in freight traffic volumes could lead to an increase in the payload. Therefore, the materials used must have the necessary properties to carry the load over many cycles (Rajakumar and Karthiyaraj, 2021). The different types of loads include impact load, repeated load, and static load (Abidin *et al.,* 2013). Helical coil springs experience all three loading conditions at various stages during train movement.

Additionally, the material grade, mechanical properties, shape, and size of the spring, as well as the chemical composition, ductility, strength, and stiffness, are vital in the spring material selection as they are all important factors in the durability and performance of heavy-duty springs. Lastly, the manufacturability of the material should be considered to achieve the required properties.

2.1.3.3 Material properties

2.1.3.3.1 <u>Elasticity of material</u>

Material characteristics are used as crucial design parameters of springs (Hertzberg, 1996). The most important of these are the elasticity, elongation, tensile strength, and yield strength of steel. This study seeks to highlight mechanical properties, as well as illustrate the effect of estimated elasticity on the design life of springs. Determining the elasticity of the steel assists in effective material selection. Therefore, Young's modulus, or modulus of elasticity, is fundamentally important (Yetna N'Jock *et al.*, 2013) and can be obtained by determining the slope of the stress-strain curve within the elastic region of the steel (Saad, 2017).

Most designers estimate the modulus of elasticity. However, before doing so, it is important for them to understand the microstructure and crystal structure of the steel. The modulus of elasticity is shown using Equations 2.5 and 2.6, where σ = the stress and ε = the strain, L_0 = the equilibrium distance, and σ_{max} = UTS. Equation 2.7, also referred to as Hooke's law, defines the linear behaviour of the material within the elastic range. The elasticity of the material is dependent on the nature of the interatomic bond and distance, as shown in Equations 2.8, where F = force, k = spring constant, and x = associated displacement. Figure 2.12 also illustrates this.

$$E = \frac{\sigma}{\varepsilon} \qquad 2.5$$

$$E = \frac{L_0 \pi \sigma_{max}}{2L} \qquad 2.6$$

$$\sigma = \left[\frac{\sigma_{max}\pi}{2L}\right] x \qquad 2.7$$

$$F = kx \qquad 2.8$$

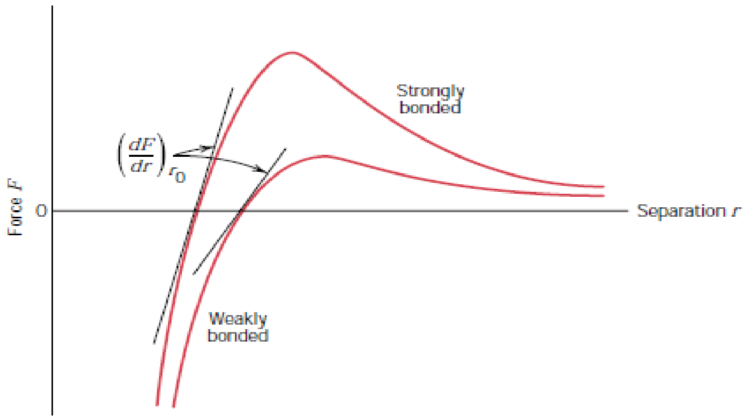

Figure 2.12 The force required to separate two atoms (Callister, 2001).

2.1.3.3.2 <u>Deformation behaviour of material</u>

One of the most crucial yet underrated properties of material is the strain hardening exponent, which includes elongation, strength, and toughness (Xu *et al.*, 2012). Determining the strain hardening exponent is vital in material selection as it is helpful in understanding the deformation behaviour of materials (Šebek *et al.*, 2016). The specific deformation behaviour of spring steel is a focus in this study. When stress is axially applied on a body, it may experience elastic or plastic deformation (Dieter and Bacon, 1962).

Elastic deformation refers to when the body returns to its original shape, while plastic deformation refers to permanent deformation. Bogie springs rely on elastic deformation to carry a load within any given range without plastic deformation (Das *et al.,* 2007b). The flow stress of material is determined from the plastic deformation zone before necking occurs (Hertzberg, 1996). A log-log plot of the plastic deformation zone will create a straight gradient, in which the strain hardening exponent can be determined (Yetna N'Jock *et al.,* 2013).

The plastic deformation zone can also be expressed by the Hollomon relationship to predict the flow stress, as presented in Equation 2.9, where K = the strength coefficient and n = the strain hardening exponent (Afrin *et al.*, 2007). The ration of UTS and yield strength signifies the hardening capacity (Luo *et al.*, 2006). The strain hardening exponent can be determined by plotting the true stress-strain curve, which can be calculated using Equations 2.10 and 2.11, where σ_T = the true stress, S = the engineering stress, e = the engineering strain, and n = the strain hardening exponent.

$$\sigma = K\varepsilon^n \quad 2.9$$

$$\sigma_T = S\,(e + 1) \quad 2.10$$

$$\varepsilon_T = \ln\,(e + 1) \quad 2.11$$

2.1.3.4 Alternative materials for SAE 1560 spring steel

Historically, the South African railway industry used SAE 5160 spring steel to manufacture springs. However, the steel grade is no longer popular since the local steel mill is unable to generate enough orders to keep the production line of the steel going. The availability of the recommended material therefore became a concern, and the local steel mill notified its customers to find alternative materials. Additionally, the South African government enacted local content legislations to encourage the localisation of skills and technology, which are not easily available in the country. Steel was deemed as a local product by the Department of Trade, Industry, and Competition.

As a result, implausible exemptions had to be approved that the required material and alternative materials were unavailable in the country. Therefore, three locally available dissimilar spring steel grades were identified for the development of the springs. The materials are equivalent to BS EN 10089:2002 grades 55Cr3, 54SiCr6, and 52CrMoV4. 55Cr3 is a rolled steel alloyed with approximately 0.90% chromium, 54SiCr6 is largely alloyed with 1.60% silicon, and 52CrMoV4 is a rolled steel alloyed with molybdenum and vanadium. The chemical compositions of the equivalent steel grades are shown in Table 2.1.

Table 2.1 Equivalent steel grades to the identified experiment samples (BS EN 10089, 2002).

Identity/Elements	**Specifications**		
	55Cr3	**54SiCr6**	**52CrMoV4**
Carbon (%)	0.52 – 0.59	0.51 – 0.59	0.48 – 0.56
Silicon (%)	0.40 max	1.20 – 1.60	0.40 max
Manganese (%)	0.70 – 1.00	0.50 – 0.80	0.70 – 1.10
Phosphorus (%)	0.025 max	0.025 max	0.025 max
Sulphur (%)	0.025 max	0.025 max	0.025 max
Chromium (%)	0.70 – 1.00	0.50 – 0.80	0.90 – 1.20
Molybdenum (%)	*	*	0.15 – 0.30
Vanadium (%)	*	*	0.10 – 0.20

The three selected steel grades are versatile and can achieve the desired properties by optimisation of the heat treatment process. In order to optimise the mechanical properties of various steels effectively, the exact processing parameters become important.

2.1.4 Spring design

Historically, failure investigations have shown that premature failure of springs occurred due to metallurgical aspects of spring steel, spring manufacturing, and corrosion (Murtaza and Akid, 2000). Consequently, the design and structural integrity of the springs are often neglected. However, a better understanding of surface fatigue cracks in high-strength spring steel cannot be limited to manufacturing and material properties alone and should include spring design and structural integrity as well.

The main reason for spring design is to obtain a spring that is economical for a suited application. Additionally, it must fit within the set configurations governed by dimensional constraints such as deflection, diameter, free length, solid length, and number of coils – the number of coils can be restrictive, particularly when there is a solid length specification (Hattingh, 1998). The design details and terminologies of helical compression springs are shown in Figure 2.13.

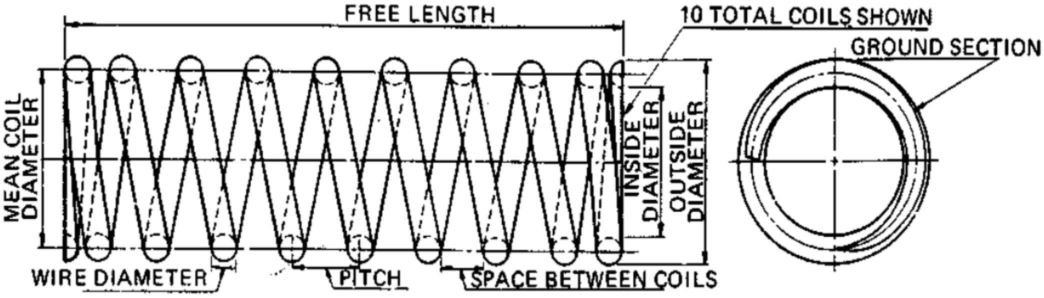

Figure 2.13 Helical coil compression spring information and terms (SAE AE-11, 1982).

Helical coil compression springs are designed to handle compressive and tensile loads (Tamada, 2020) and are usually loaded with an axially compressive force along their centreline. If the springs are not designed properly, this might cause the coils to come into contact when overloaded, resulting in spring buckling. This phenomenon could be due to poor spring stiffness (Pop *et al.*, 2018). Spring buckling causes contact patches, which eventually act as stress-raisers and result in a shortened lifespan of the springs (Reddy and Reddy, 2013; Ling *et al.*, 2017).

Therefore, pitch angle plays an important role in the design of bogie springs and has an effect on the fatigue life of the springs. Pitch angle is the angle between the coils and base of a spring and must be precise for springs to be structurally acceptable (Ghate, Shankapal, and H, 2012). The challenge of inaccurate pitch angle is that when the pitch angle is too large, the fatigue cycles of the springs are significantly reduced. The classical notion that spring instability is based on the buckling of an equivalent column during fatigue testing is discussed in the case studies (de Crescenzo and Salvini, 2019).

To evaluate the effectiveness of the proposed design for a certain loading condition, material selection, heat treatment experiments, and numerical simulations, i.e. FEA, were performed. In this study, detailed mathematical calculations were carried out to determine shear stress and the projected number of fatigue cycles. Solid models were generated and used to conduct a FEA simulation based on the structural integrity assessment of the springs. Furthermore, failure investigations were used to solve the technical challenges to improve the quality of the springs

(Vukelic and Brcic, 2016). The findings of this research will be used to improve the fatigue life of bogie springs.

2.1.5 Spring manufacturing

In the last century, efforts have been made to manufacture high-performance springs with the intention of increasing the spring lifespan and load. The average lifespan of bogie springs is approximately 20 years (‘ZEJ120-Co, 2014). The springs are manufactured using SAE 5160 spring steel, which is equivalent to BS EN 10089:2002 grade 51CrV4 spring steel (BS EN 10089, 2002). The specification chemistry range is shown in Table 2.2 and the current spring manufacturing process, which is also the focus of this study, is detailed in Figure 2.14, along with the research questions (RQ).

Table 2.2 SAE J404 grade 5160 chemical composition specification (in wt%) (SAE J404 standard, 1980).

Elements	C	Cr	Mn	P	Si	S
SAE 5160	0.56 – 0.64	0.70 – 0.90	0.75 – 1.00	0.035*	0.15 – 0.35	0.045*

*Maximum

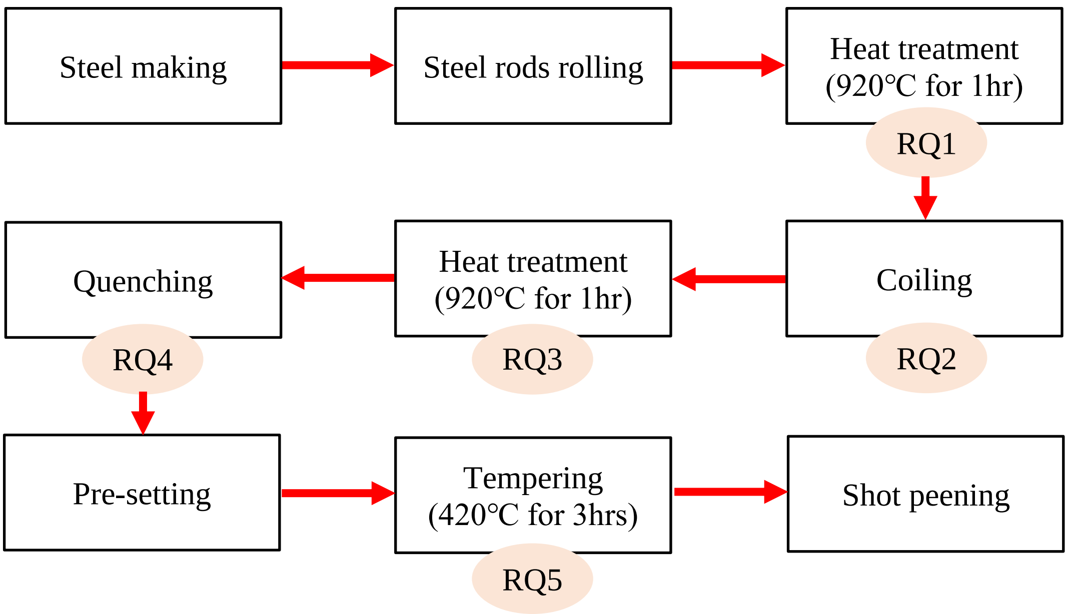

Figure 2.14 Spring manufacturing process flow.

The manufacturing process of the springs entails high temperature coiling, hardening, and tempering (Fedin and Borts, 2009). The steel rods received from the mill are charged in a heat treatment furnace and soaked at 920°C for an hour. The rods are then placed on a rotating holding reel and coiled by drive rollers on a coiling machine in a normalising atmosphere. After the coiling process, the coiled rods are re-heated to 920°C for an hour, followed by oil quenching at 60°C.

The quenching process is followed by tempering at 420°C for three hours, which completes the heat treatment process. The springs are then shot blasted to clean the oxide scale that forms during the heat treatment process. Although the process of manufacturing functional springs exists, the optimum process is unknown. This section covers the manufacturing processes used to create the desired spring shape and attain satisfactory mechanical properties.

2.1.5.1 Heat treatment

Heat treatment is the process of heating and cooling metals in a solid state to achieve the desired mechanical properties through modifying the crystal structure (Pohjonen *et al.*, 2021). The main objective of the heat treatment is to improve the hardness, strength, and toughness of the steel. The various stages of the heat treatment process include heating the metal to a specified temperature, soaking the metal for a specific time period, and cooling the metal to room temperature and are shown in Figure 2.15.

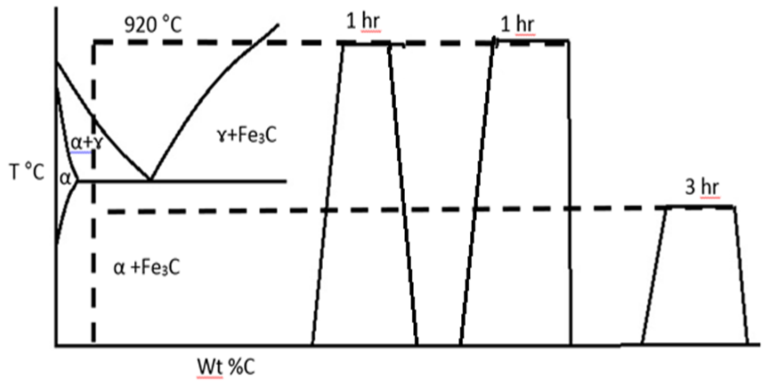

Figure 2.15 Spring shop alloy and heat treatment cycle.

Moreover, the heat treatment of springs entails normalising and coiling the steel at 850°C to 880°C, followed by austenitising the steel for an hour at 860°C to 880°C. The steel is then quenched in quenching oil at 40°C and tempered for three hours at 430°C to 450°C. Controlled quenching ensures fine grains and the lowest amount of oxidation and decarburisation; therefore, it is a necessity in the heat treatment of steels (Prawoto *et al.*, 2008). Additionally, the tempering process benefits steel by providing the maximum elastic limit and toughness by decreasing distortion and increasing the lifespan and reliability of the springs (Rakhshtadt, 1967).

2.1.5.1.1 Austenitisation

Austenitisation, which is the process of heating steel to a temperature at which the microstructure changes from the pearlite phase to austenite and homogenizes over time (Mandal *et al.,* 2016). The lowest temperature to fully obtain austenite is generally indicated by the A_{C3} line at various carbon concentrations. The austenitising temperature and soaking time of steel have adverse effects on the properties of the steel due to grain growth, oxidation, and decarburisation (Grzegorz, 2019). Therefore, high austenitising temperatures and longer soaking times must be controlled to avoid grain growth and quench cracking (Liu *et al.*, 2017). Austenite grain growth can also be limited by the additions of molybdenum and vanadium in small quantities (Annan, 2015).

2.1.5.1.2 Quenching

Quenching is the process of cooling steel from the solution treating temperature, using quenching media like oil or water (Totten, 2006). Buczek and Telejko (2013) referred to it as the thermal process where materials are immersed in a quenching media to achieve certain mechanical properties and microstructures. Quenching is an important stage of the heat treatment process because it improves the strength of spring steel, as well as creates compressive stresses on the surface (Kobasko, 2021). Compressive surface stresses may improve fatigue properties when the heat treatment is controlled (Šolić, Podgornik, and Leskovšek, 2018). However, when the quenching parameters are not controlled, most spring materials often develop quench cracks during the hardening process.

Usually the cracks are fine on the surface and are only detectable by dye penetrant testing. The main cause of quench cracks is severe cooling rates and subsequent development of tensile stress on the surface of the spring (Lingamanaik and Chen, 2014). Tensile stress is increased by volumetric martensite expansion during phase transformation and can be reduced by selecting a quenchant with slower cooling rates that still promote martensite transformation (Ravi Kumar *et al.,* 2000). The purpose of this study was to determine if quenching would be able to achieve martensite without causing quench cracks or other microstructural deficiencies using specific quenching oils. There are several factors that influence the selection of a quenchant and anticipate performance attained from the quenching process.

The quenching process is used to dissipate energy that is absorbed during the heating process (Avner, 1998). The cooling rate curve is indicative of the different stages of the quenching process. Quenchants such as oil and water usually occur in three stages, i.e. vapour blanket, nucleate boiling, and convection cooling (Totten, Sarmiento, and Gaston, 2011). Each heat transfer mechanism or stage has distinct characteristics, as illustrated in Figures 2.16 and 2.17.

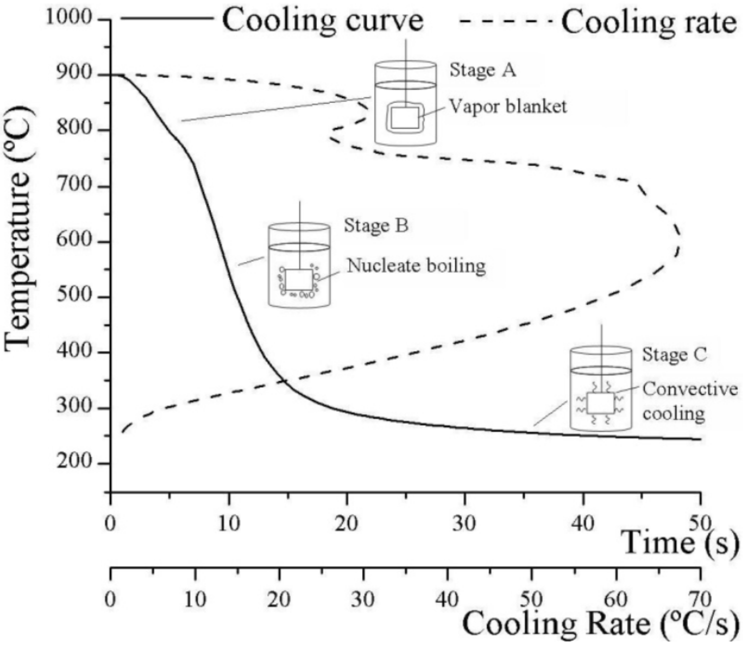

Figure 2.16 Heat dissipation mechanisms (Totten, Sarmiento, and Gaston, 2011).

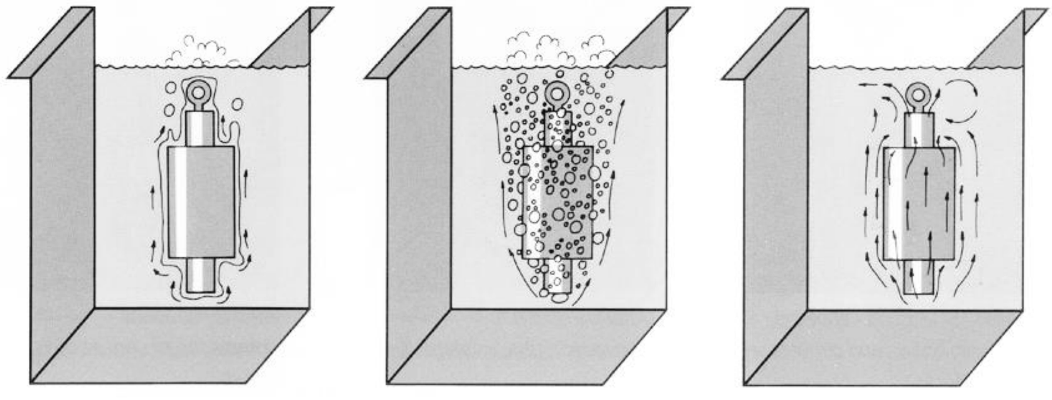

Figure 2.17 A schematic representation of the three quenching stages: (a) Vapour blanket, (b) Nucleate boiling, and (c) Convection cooling (Mackenzie, 2009).

Vapour blanket is the first stage in the quenching process and happens upon early immersion after austenitisation (Smallman and Bishop, 1999). The initial interaction between the hot metal surface and quenching media generates a layer of vapour. Cooling in this stage occurs as a function of conduction and radiation through a gaseous film. Vapour is a poor conductor of heat; therefore, cooling is relatively slow (Avner, 1998). As the steel cools, the vapour blanket breaks down at certain temperatures and the start quenchant boils aggressively against the workpiece (Ma, 2002).

This stage is regarded as nucleation boiling. Cooling is faster during this stage, with the cooling rate sometimes double the highest magnitude during the vapour blanket stage. Heat is removed rapidly from the surface of the workpiece due to the latent heat of vaporisation (Avner, 1998). When the workpiece is cooled below the boiling temperature of the quenching media, slow cooling occurs by convection and conduction (Ma, 2002). Cooling rates during this stage are slow and are largely dependent on the quenchant's viscosity (Avner, 1998). Higher cooling rates are relative to lower viscosity, while lower cooling rates are relative to higher viscosity.

Many researchers have studied the characteristics and behaviours of different quenchants, however, knowledge of the effect of the quenching media on specific steels is still lacking. Additionally, Atkins (1980) presented the effect of quenchant cooling rates on material transformation per part size, however, he did not specify the quenching media. Therefore, this study focusses on the selection of the most suitable quenching media for specific outcomes. There are numerous grades of quenching oils with different capabilities and characteristics, as shown in Figure 2.18.

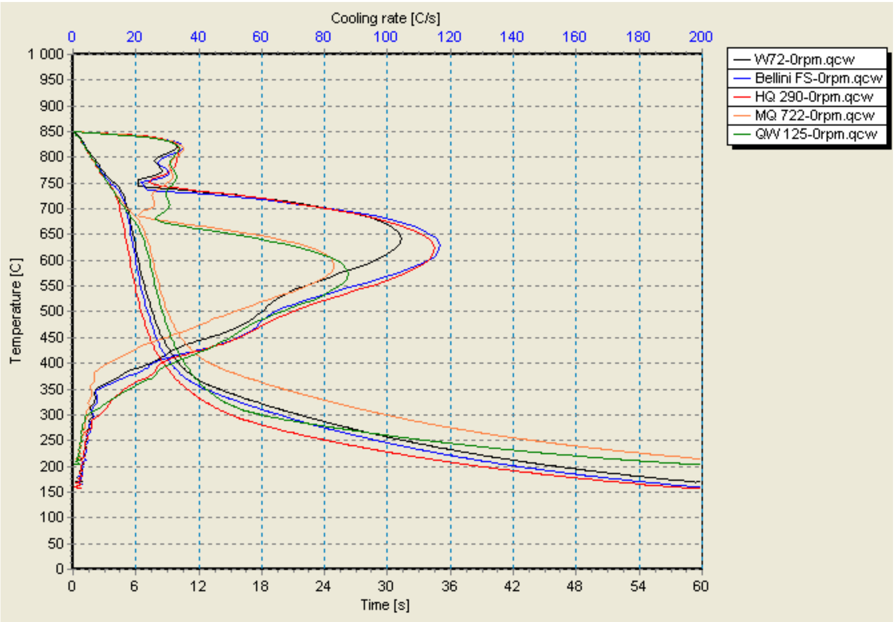

Figure 2.18 Cooling rates and convection curves for different types of quenching oils (Bodin and Segerberg, 2005).

Each quenchant has its own benefits and shortcomings (Hou *et al.*, 2012). For instance, water is widely used as a quenchant, however, due to its fast cooling rate at lower temperatures, it may induce cracking in certain steels (Zhang *et al.*, 2017). Steel cracking results in poor product quality. To avoid cracking and undesirable microstructures, the quenching media's heat transfer coefficient and cooling rates must be known and form a basis of the quenching media selection (Hasan *et al.*, 2011). There is a specific cooling rate for each steel grade to achieve full hardening.

The microstructure and hardness of materials cooled at specific rates can be predicted by using CCT diagrams (Totten, 2006). The criteria for the selection of a suitable quenchant will be largely based on the specific steel CCT diagram similar to the one shown in Figure 2.19, and the convection curve will be aligned to the CCT. The CCT curves of spring steel are shown in Figure 2.19. The letters displayed on the CCT diagram represent the microstructural phases, i.e. B: Bainite, F: Ferrite, P: Pearlite, M: Martensite, and Ms: Martensite start.

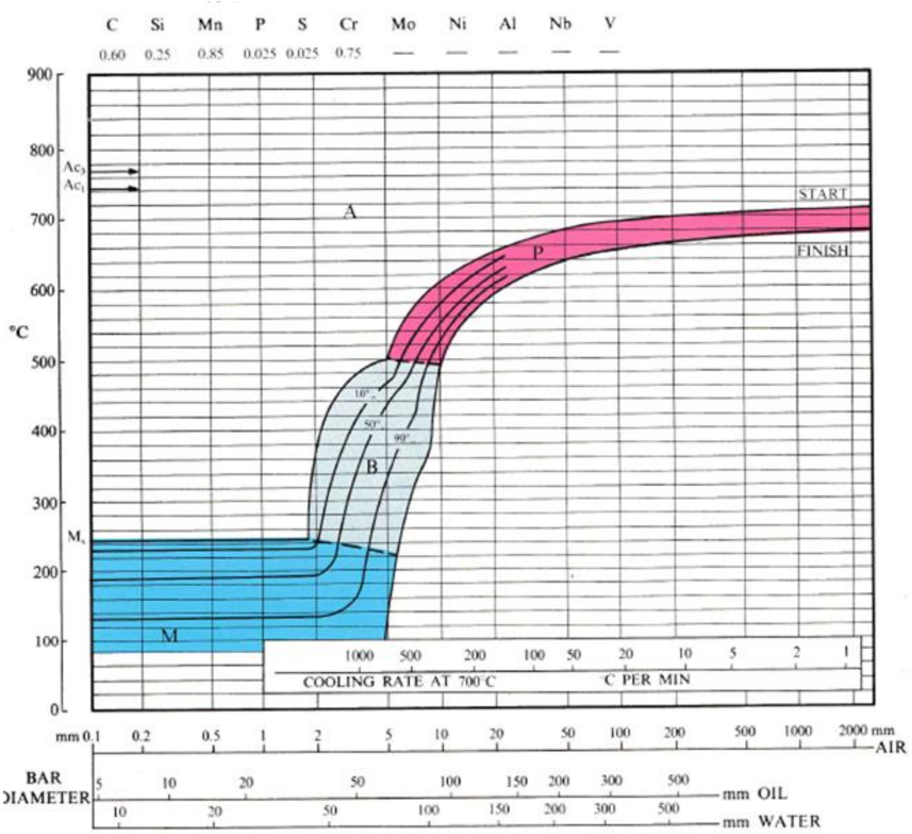

Figure 2.19 The modified CCT curve for SAE 5160 steel equivalent (Atkins, 1980).

2.1.5.1.3 Tempering

Because martensite is metastable and decomposes when subjected to continuous heating above austenitisation temperatures, the martensitic structure achieved during the quenching process is hard and brittle (Totten, 2006). Consequently, steel in the quenched condition has high strength but poor ductility (Matjeke *et al.,* 2018). This is undesirable for engineering purposes. Furthermore, attaining the ultimate balance between strength and ductility in spring production is critical. Therefore, steel requires further heat treatment in the form of tempering, as tempering improves the ductility and toughness of the steel, however, it also reduces strength, as seen in Figure 2.20.

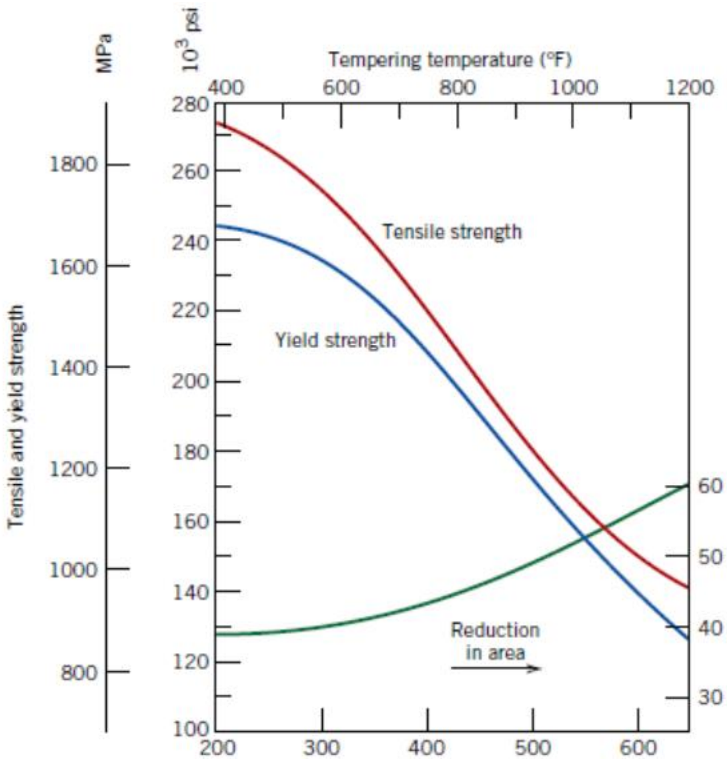

Figure 2.20 The effect of tempering temperature on the mechanical properties of steel (Özdem *et al.*, 2013).

During the tempering process, the temperature of the sample is raised to a value below the eutectoid temperature, held there for an extended period of time, and then cooled (Reed-Hill, 1973). Tempering is a vital step in the heat treatment process as spring steel is of little engineering relevance after the solution treatment, i.e. austenitisation and hardening, despite the importance of the process (Reed-Hill, 1973). However, tempering must be carefully regulated as it may result in undesirable microstructures and properties known as temper embrittlement (Dieter, 1988). A significant number of spring failures are attributed to temper embrittlement.

Over-tempering and temper embrittlement can reduce spring steel strength to unacceptably low levels for the application. Therefore, it is important to find the optimal tempering temperature and time to achieve the ultimate mechanical properties. Porter and Easterling (1992) claimed that tempering of some steels at a range of 350°C to 575°C can lead to embrittlement. However, Croft (1981) and other scholars observed temper embrittlement of high-strength steel at temperatures ranging from 250°C to 350°C.

When temper embrittlement is observed, it adversely affects the toughness of the material (Mukwevho, 2016). Toughness is a critical property of springs. The reduction in toughness does not essentially relate linearly with the increase in strength. Temper embrittlement can be detected by testing for the effect of tempering temperature on room temperature impact energy with a Charpy test (Belov *et al.,* 1976). The effect of temper embrittlement is shown in Figure 2.21.

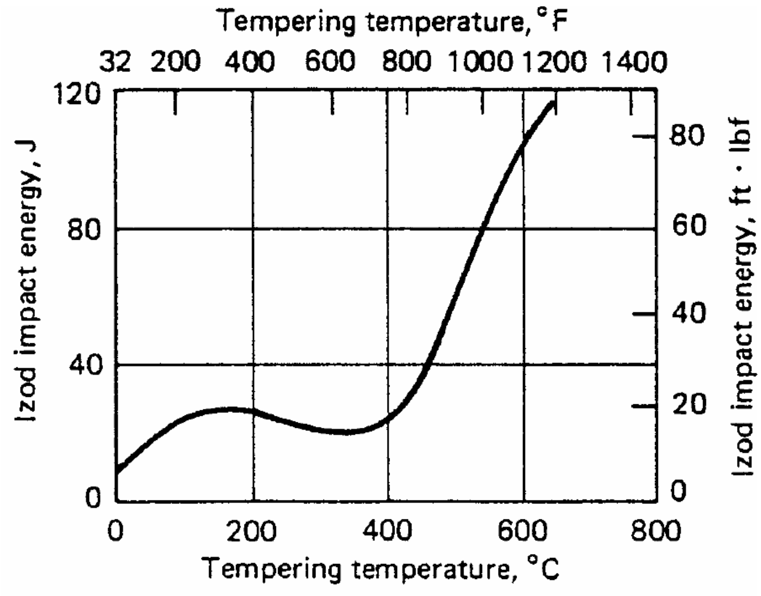

Figure 2.21 The effect of temper embrittlement as a function of temperature (Capus and Mayer, 1960).

There is a general understanding that strength decreases, while tempering temperature increases, as shown in Figure 2.22. However, the phenomenon of secondary hardening debunks the theory to a certain extent. Hence, a thorough understanding of steel behaviour during heat treatment becomes necessary.

Steel with a significant presence of phosphorus may suffer from temper embrittlement (Gorni, 1976). Iron carbides generally have no solubility for phosphorus. Phosphorus is largely rejected to the interface boundaries of iron carbides and ferrite, resulting in a weaker cohesion of boundaries or ferrite-carbide networks. Likewise, steels containing considerable amounts of chromium and manganese are also prone to temper embrittlement (Szymczak, Gumienny, and Pacyniak, 2015).

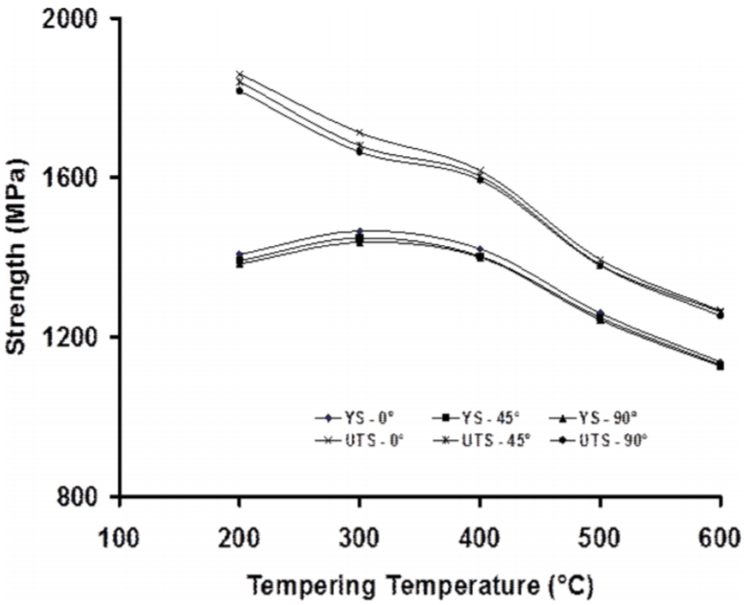

Figure 2.22 The effect of tempering temperature on the mechanical properties of high-strength steel (Jena *et al.*, 2014).

A significant presence of silicon shifts the embrittlement temperature range higher. On the other hand, the addition of molybdenum reduces susceptibility to embrittlement but does not completely eliminate it (Razavi, Rizi, and Zadeh, 2013). All these permutations call for a thorough optimisation of the heat treatment process in order to avoid the embrittlement phase and to achieve desired spring performance. In order for the heat treatment process to be optimised, the precise parameters have to be determined (Matjeke *et al.*, 2018).

2.1.5.1.4 Phase transformation and critical transformation temperature

During the heat treatment process, phase transformation occurs, which changes the crystalline structure and dramatically influences the mechanical and metallurgical properties of the steel (Meigui *et al.,* 2017). Additionally, phase transformation takes place at a specific temperature and can be determined when alloyed steels are subjected to heating and cooling (Xian, 2013). Therefore, information of phase transformation must be developed to ensure efficient metallurgical operations. It is also important to know the phase transformation temperatures to determine the optimal heat treatment process and its effect on the structure of specific spring steels.

The microstructure, hardness, and strength of spring steel are generally a function of chemical composition and cooling rate (Reed-Hill, 1973). To improve the mechanical properties of the springs, the manufacturing process needs to be optimised. Therefore, a detailed understanding of the critical transformation temperatures and behaviour of the selected spring steel grades is necessary. The spring steels that were selected in this investigation for the optimisation of bogie spring manufacturing are categorised by BS EN 10089:2002 grades 55Cr3, 54SiCr6, and 52CrMoV4.

The key steps of manufacturing hot coiled springs is the austenitisation and quenching process (Liu *et al.,* 2010). The acceptable hardened microstructure for the steel grades is martensite. Martensite is a diffusionless transformation that occurs by habit plane shear when the steel is rapidly cooled from the austenitic range (Peng *et al.,* 2019). The transformation involves the compression of the body cantered tetragonal (BCT) lattice parameter along the c-axis and the extension of the a-axis. Carbon atoms are trapped within the BCT structure.

Martensite is dependent on the lower critical temperature (Ac1), upper critical temperature (Ac3), and martensite start (Ms) temperature (Fedin and Borts, 2009; Khovova *et al.,* 2010). Ac1 and Ac3 are regarded as the beginning of austenite phase transformation and the end of austenite formation during heating. Martensite phase transformation depends on the stability of the austenite phase, which is largely dependent on heating above Ac1 and Ac3 (Wu *et al.,* 2013). Andrew’s equation is widely used for predicting Ac1, Ac3, and Ms temperature (Maisuradze and Ryzhkov, 2019).

Austenite transformation plays a significant role in terms of mechanical properties, followed by the chemical composition and cooling rate (Guerra-Fuentes *et al.,* 2016). According to the binary Fe_3C phase diagram presented in Figure 2.23, the start of austenite transformation during heating begins at 723°C (Ac1). Complete austenite transformation is achieved when the Ac3 transformation line is reached. The martensite structure is achieved when the steel is rapidly cooled from the austenite range. Austenite (ɤ) and ferrite (α) phases have face cantered cubic (FCC) crystal structures, respectively, while martensite has a BCT crystal structure.

CCT diagrams are unique and only provide limited information regarding the heat treatment process, while thermal analysis techniques are used to determine how material composition changes heat flow. Usually, the underlying reaction and transformation kinetics of steels are studied with DSC, a thermal analysis technique (Petrovic *et al.,* 2012). Calorimetry is one of the most accurate and suitable methods for analysing materials and does so by determining the heat flow rate as a function of temperature and time. Calorimetry bases its measurements on endothermic and exothermic processes (Mukherjee and Rosolen, 2013).

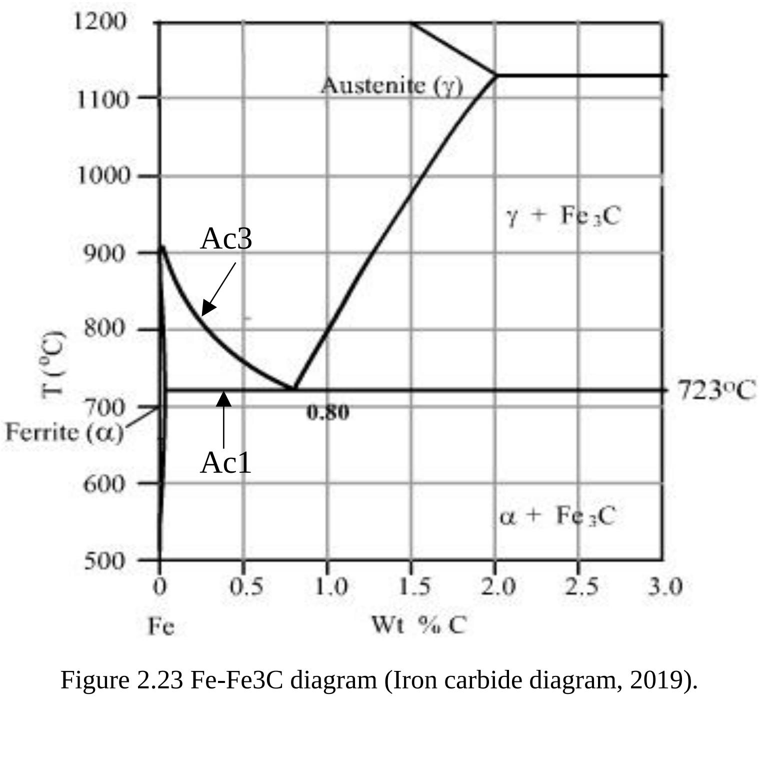

Figure 2.23 Fe-Fe3C diagram (Iron carbide diagram, 2019).

The phase transformation kinetics of the phases are known and understood, however, this study aimed to predict the optimum transformation characteristics for the specific steel grades. For instance, the martensite microstructure is reached when high-strength spring steel is supercooled from the austenitic region (Shin, Lee, and Hwa Ryu, 1999; Xu, Chen, and Sun, 2018). However, it is often difficult to achieve 100 percent martensite on spring steel without causing quench cracks (Ji *et al.,* 2013; Matjeke *et al.,* 2018). Steel is susceptible to quench cracking and microstructural deficiencies when quenching is not controlled (Matjeke *et al.,* 2018). As a result, the hardened microstructure usually has small percentages of either retained austenite, pearlite, or bainite.

A material's ability to harden is largely influenced by the chemical composition and quenching capacity of the quenching media. The phase transformation characteristics of the three selected spring steels were determined using DSC measurements to understand the behaviour of material when subjected to heat treatment. Additionally, the aim of the study was to determine the exact transformation temperatures of the selected steels. The empirical data generated from the JMatpro simulation software show the critical transformation temperatures of 54SiCr6 to be significantly lower than that predicted using Andrew's equation (Atkins, 1980).

An earlier study by Matjeke *et al.* (2019) showed that there is no agreement between the JMatPro simulation software and Andrew's equation in determining the Ms temperature of 54SiCr6. The unreliability in the Ms temperature warranted for the heating and cooling characteristics of the three grades to be investigated. Dilatometry was used to accurately measure the critical transformation temperatures to be considered during the heating and cooling procedures (Mohapatra, Sommer, and Mittemeijer, 2007; Motyčka and Kövér, 2012). The purpose of this study was to determine the effect of the cooling rate on the mechanical properties and microstructure of spring steel.

2.1.5.1.5 Austenite to martensite phase transformation

Steel is known to harden when rapidly cooled from the austenitic range to room temperature without eutectoid diffusion (Porter and Easterling, 1992). For spring steel to remain in an elastic state, high-yield strength is required, which can only be obtained by the formation of martensite. To improve these spring steel properties, it is imperative to achieve martensite structure during the heat treatment. Therefore, steel has to be heated to temperatures where carbon will be completely in solution for the required amount of time. This is schematically represented in Figure 2.24.

The degree of martensite formation or hardenability depends on the size of the component, the composition of the steel, the type of quenchant, and the cooling rate (Reed-Hill, 1973). Figure 2.25 shows the effect of the cooling rate at the surfaces and centre of a rod.

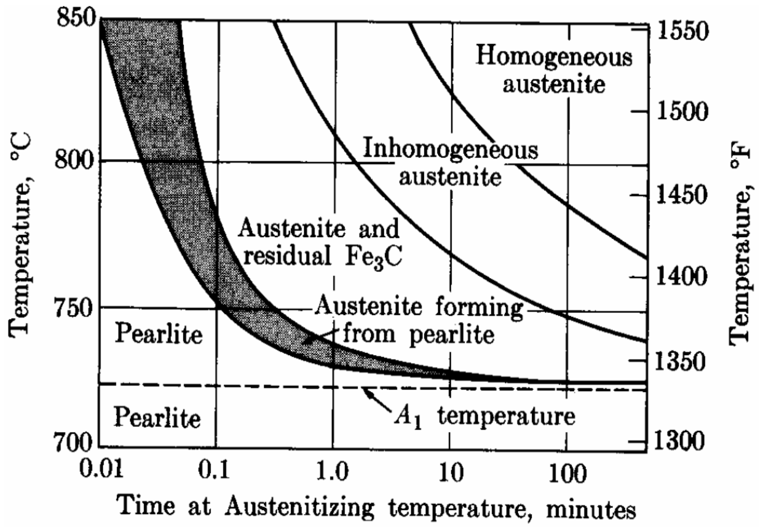

Figure 2.24 A schematic representation of the time required for carbon to be in austenite solution (Manuel and Cerda, 2017).

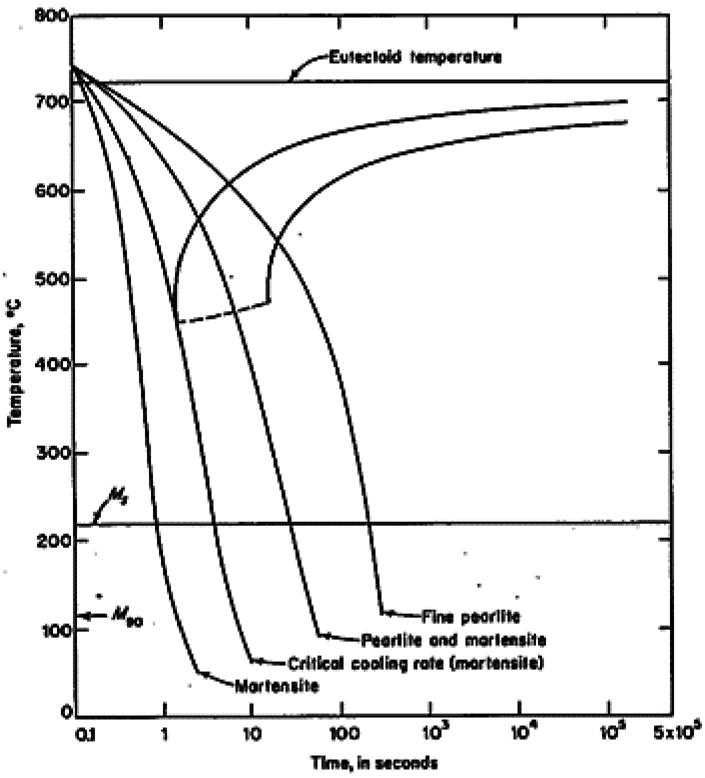

Figure 2.25 The effect of cooling rate on a cylindrical steel bar (Reed-Hill, 1973).

Depending on the rod diameter and quenchant, it is possible to fully transform to martensite, as shown in Figure 2.26. However, fully transforming to martensite comes with the risk of quench cracking.

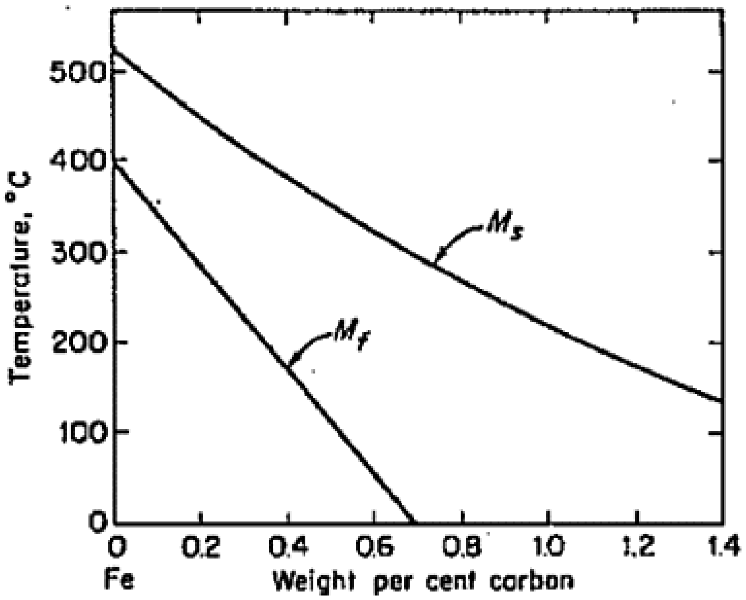

Figure 2.26 The effect of carbon on martensite start and finish temperatures (Reed-Hill, 1973).

Iron is an allotropic metal that can exist in more than one phase at different temperature ranges (Reed-Hill, 1973). Within the austenitic range, iron atoms arrange themselves into FCC, while below A_{C1} they transform to either BCC or BCT (Kundu, 2007). The A_{C1} and A_{C3} are estimated using Andrew's Equations 2.12 and 2.13 (Atkins, 1980).

$$A_{C1}(°C) = 723 - 20.7[\%Mn] - 16.9[\%Ni] - 29.1[\%Si] + 16.9[\%Cr] + 290[\%As] + 6.38[\%W] \quad 2.12$$

$$A_{C3}(°C) = 910 - 209\left[\sqrt{C}\right] - 15.2[\%Ni] + 44.7[\%Si] + 104[\%V] + 31.5[\%Mo] + 13.1[\%W] \quad 2.13$$

Martensite forms when rapidly cooled from the FCC phase (austenite), which is stable at high temperatures, and transforms in the metastable BCT crystalline. The carbon atoms do not have sufficient time to diffuse out of the interstitial spacing austenite structure during rapid cooling, therefore, the crystal structure transforms into a BCC ferrite structure. The FCC unit cell that is stable at high temperatures is shown in Figure 2.27. The crystallographic axes lie at right angles; however, the BCT lattice dimensions of the lattice constant differ from the two equal constants (Reed-Hill, 1973).

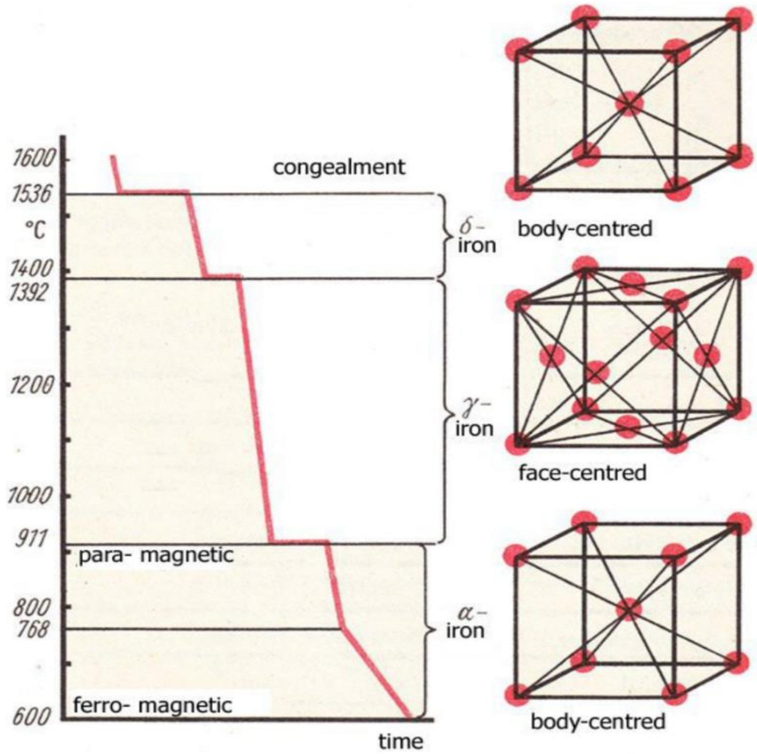

Figure 2.27 A schematic illustration of allotropic phases (Steel allotropic phase, 2020).

There is a relationship between the microstructure and strength of steel. Martensite is the desired microstructure for bogie springs as it offers higher strength than bainite and pearlite microstructures (Mesplont, 2003; Fragoudakis *et al.*, 2014). A large constituent of bainite and pearlite will negatively affect the homogeneity and strength of the steel. The strength of a martensitic structure decreases with increasing volume fractions of bainite and pearlite phases (Sungkhaphaitoon and Plookphol, 2016). It is therefore desirable to keep the volume fraction of these phases very low. Figure 2.28 shows lath and plate martensite microstructures.

Sufficient undercooling is required for nucleation and shear displacement. Martensite is a hard and brittle metastable phase with limited use, unless further transformed to tempered martensite. Kobasko *et al.* (2009) stated that the transformation of martensite and other phases are influenced by the amount of carbon present in the steel. This relationship is also presented in Figures 2.26 and 2.29. Martensite start and finish temperatures are defined as the temperatures at which martensite starts to form and completes transformation, respectively (Zhang *et al.*, 2018). Martensite transformation of steel, with about 0.5% carbon, starts at 230°C and finishes at 20°C, which can be seen in the figure.

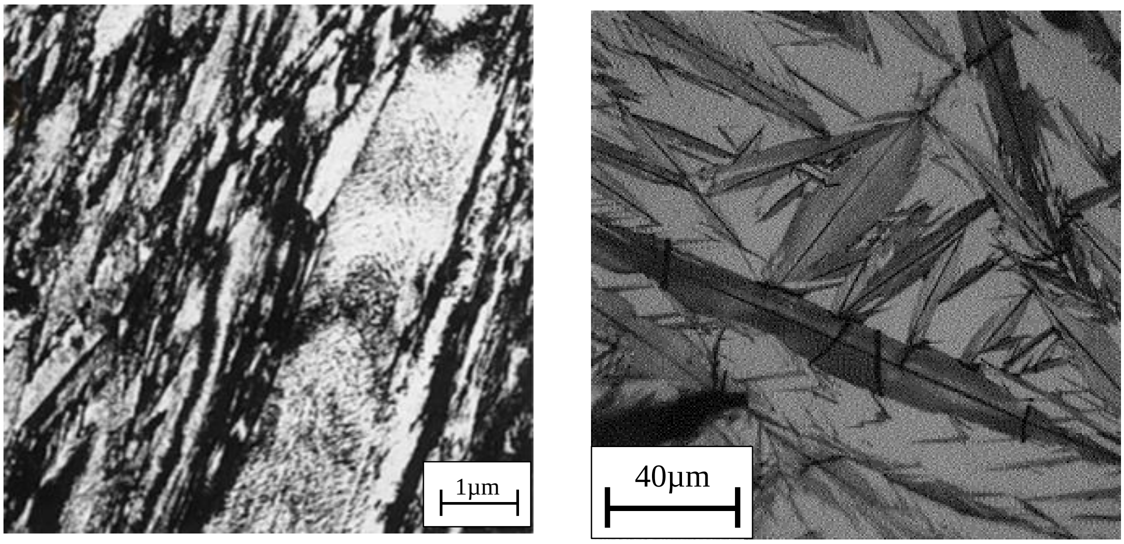

(a) (b)

Figure 2.28 (a)Typical illustrations of lath martensite microstructures and (b) plate martensite microstructures (Saad, 2017; Ahmed and Khanna, 2020).

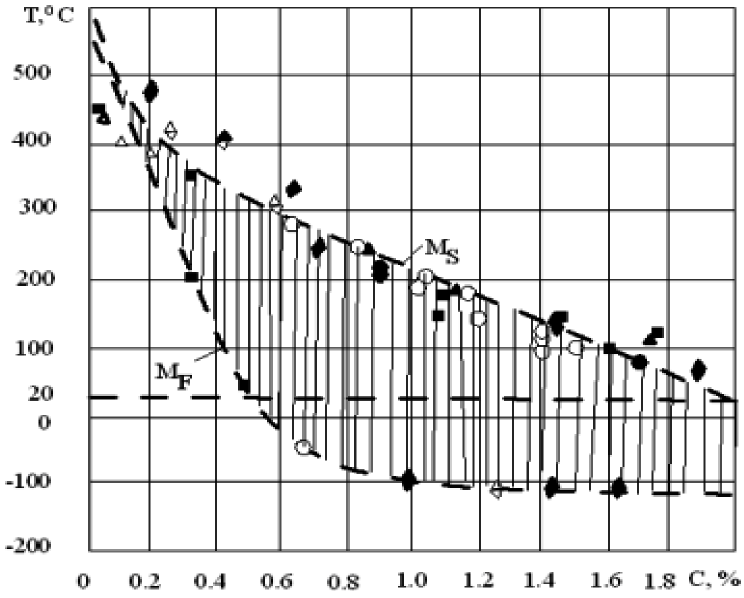

Figure 2.29 The effect of carbon on martensite start and finish temperatures (Kobasko *et al.*, 2009).

Martensite transformation occurs as a result of chemical free energy or Gibbs free energy when the critical driving force is equivalent or more than the Gibbs energy of austenite (Reed-Hill, 1973). In order to achieve the desired martensite fraction within the microstructure, the quenchant cooling rates for certain steel grades are important. During this transformation phase, the steel suffers a change in shape, which distorts the surrounding matrix. The martensitic transformation from austenite is eloquently described using the Bain distortion theory, which is shown in Figures 2.30 and 2.32. It is worth noting that Archie (2018) confused martensite BCT with austenite FCC in Figure 2.31.

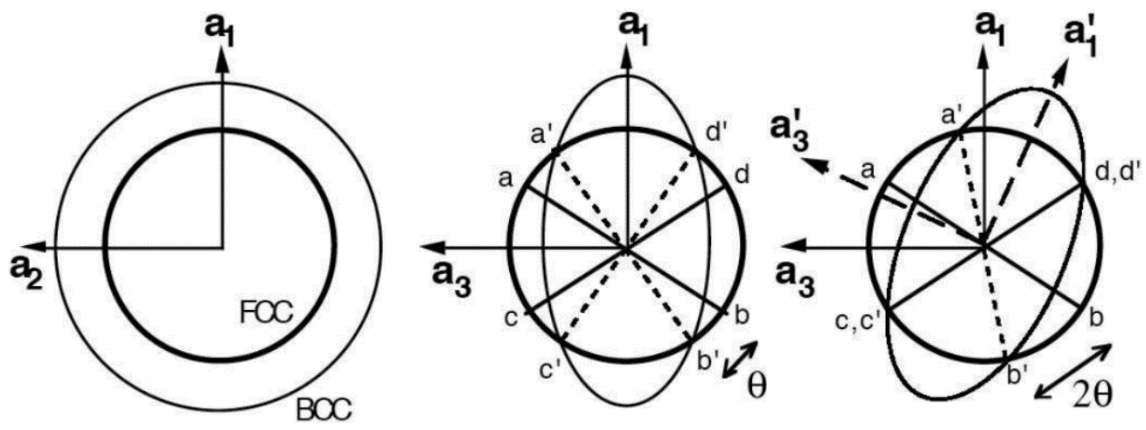

(a) (b) (c)

Figure 2.30 Bain distortion theory: (a) and (b) show the effect of Bain distortion on austenite and (c) shows the combined effect of Bain distortion on a rigid body (Kundu, 2007).

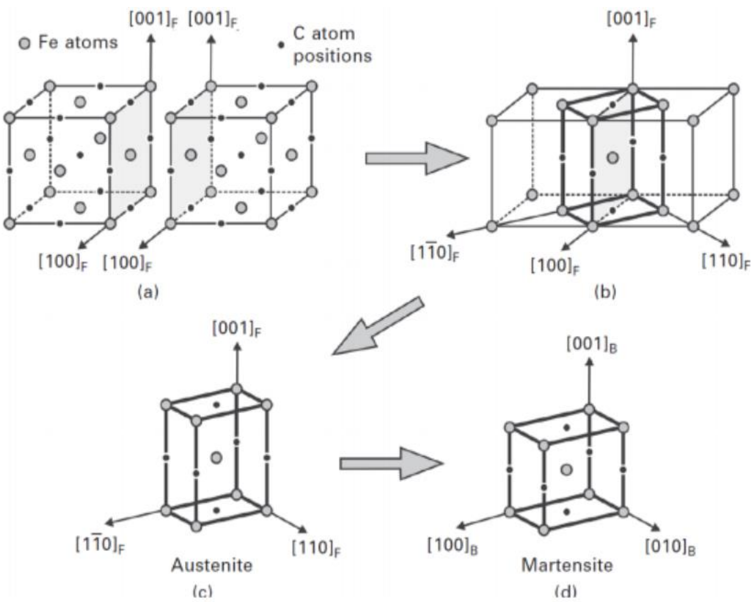

Figure 2.31 Bain distortion theory for steel: (a) shows a FCC unit cell, (b) shows a pair of FCC joined to form BCT, (c) shows a BCT unit cell (Martensite), and (d) shows a FCC unit cell (Austenite) (Archie, 2018).

When the Gibbs free energy of martensite exceeds that of austenite, austenite becomes unstable and martensite phase transformation occurs. This can be expressed as: $\Delta G^{\gamma\rightarrow m} = \Delta H - T\Delta S$, where $\Delta G^{\gamma\rightarrow m}$ = the driving force required to transform austenite to martensite, H = enthalpy, T = the absolute temperature, and S = the entropy of the system. For martensite to form from austenite, it requires a critical free energy difference. Figure 2.32 shows that austenite is more stable above T_0 temperature.

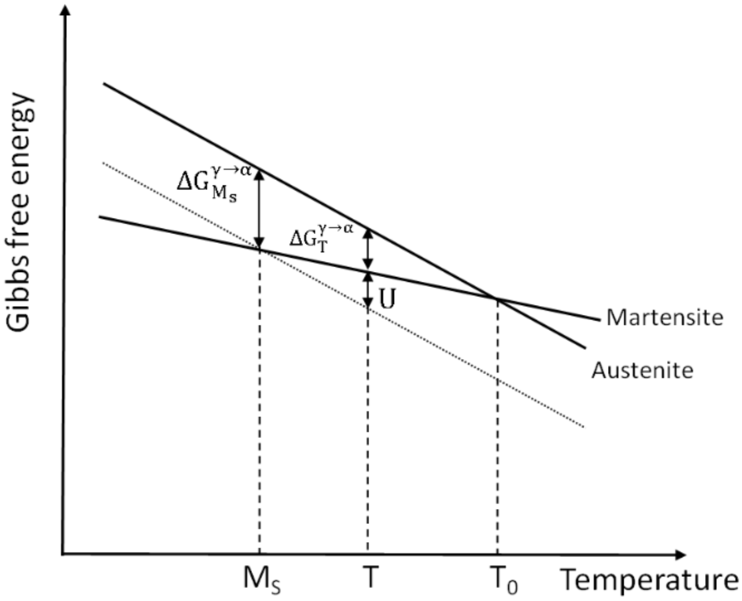

Figure 2.32 A Gibbs free energy schematic drawing of the variation of austenite and martensite (Gupta, 2014).

Gibbs free energy decreases with increasing temperature. At T_0, the free energy equilibrium is equal for both martensite and austenite, therefore, $\Delta G^{\gamma\rightarrow m}$ is zero. Beyond T_0, austenite is more stable than martensite, while below $T_{0,}$ stability favours martensite. Suitable nucleation sites for martensite are usually non-equilibrium defects such as dislocations, excess vacancies, free surfaces, grain boundaries, inclusions, and stacking faults (Wang, Van der Wolk, and Van der Zwaag, 2018).

2.1.5.2 Shot peening

Shot peening is the final step in the spring manufacturing process and is done to improve the surface properties of the spring. Shot peening entails subjecting the spring body to high velocity streams of shots (Yamanda, 2007), which introduces particularly beneficial compressive stresses on the spring surface (Scuracchio, de Lima, and Schön, 2013). Tests have shown that when shot peening, specifically micro-shot peening, is done properly, the fatigue life and resistance of the spring is improved (Harada *et al.*, 2014). This is achieved by the introduction of hoop stresses, countering the anticipated tensile stresses on the surface layer.

When shot peening is not implemented, surface defects can become the predominant origin of spring failure under the high-cycle fatigue regime (Murakami, Kanezaki, and Sofronis, 2013;

Reed-Hill, 1973). Knowledge of each factor of shot peening is important, e.g. type of shots, exposure time, and velocity. The effect of shot peening is illustrated in Figure 2.33 and the efficiency of shot peening is illustrated in Figure 2.34. The spring steel endurance limit curve stabilises at about 2 x 10^6 cycles (BS EN 13906-1, 2002), which is a region in which infinite life is expected.

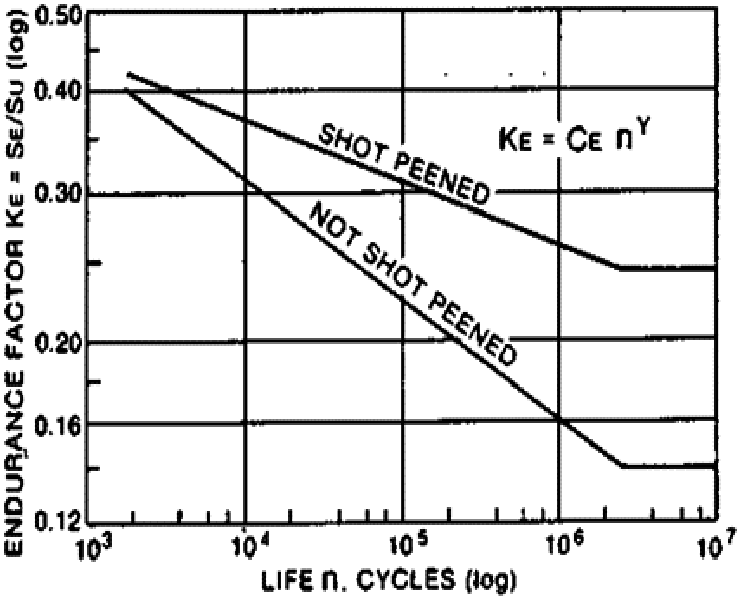

Figure 2.33 SN-curve for helical springs (SAE AE-11, 1982).

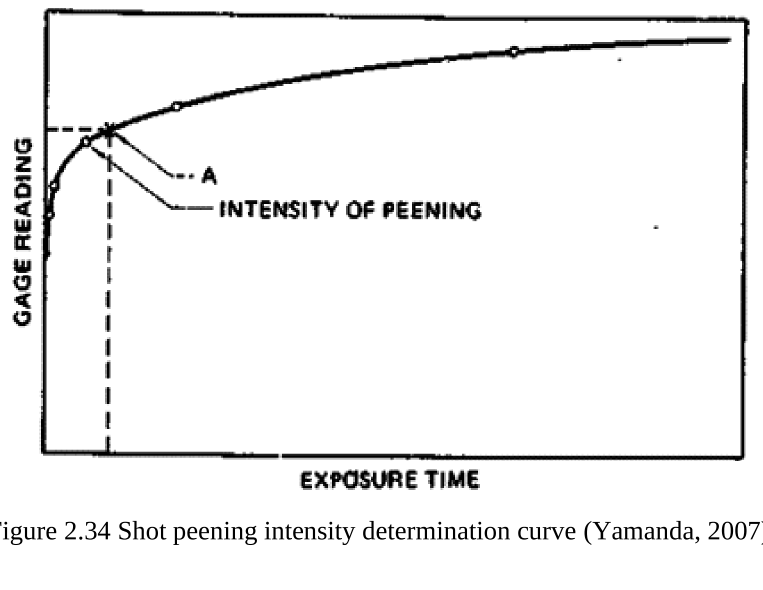

Figure 2.34 Shot peening intensity determination curve (Yamanda, 2007).

2.1.6 Surface properties of material

Alloying and heat treatment are the most important ways of improving the mechanical properties of spring steel. However, the performance of springs and properties of spring steel over extended periods of time also rely on surface properties. Figure 2.35 shows that a helical compression spring experiences the highest stress on the surface during deflection.

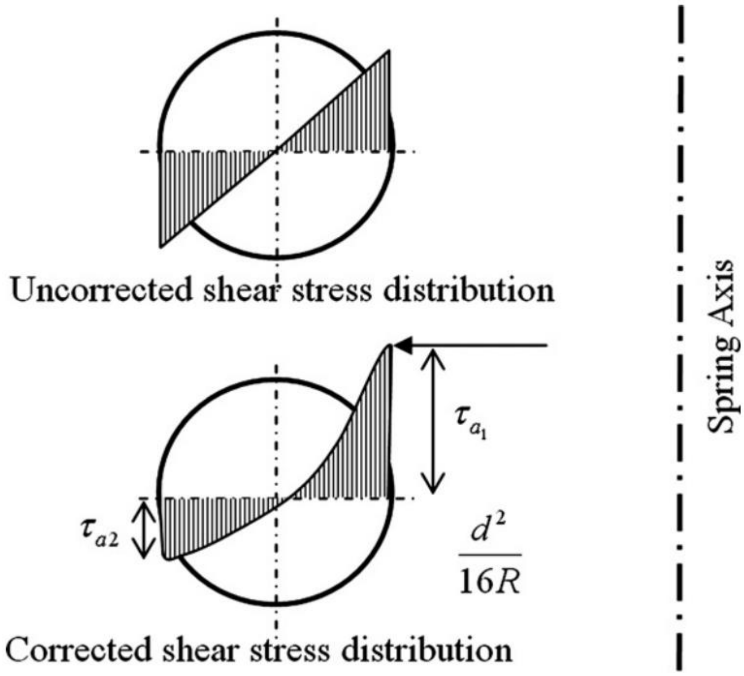

Figure 2.35 Rod section illustrating stress distribution (Prawoto *et al.*, 2008).

When a compression spring is loaded, the coils experience torsion. When subjected to torsional and bending stresses, springs are likely to yield (Rakhshtadt, 1975). However, the presence of surface defects such as decarburisation and surface roughness can become stress-raisers. In-service corrosion has negative impacts on spring performance. Fedin *et al.* (1987) showed that when spring rods are heated in gas furnaces, a thick decarburisation layer develops on the surfaces of the rods, which are detrimental to the fatigue strength of the springs (Mackenzie, 2008).

Therefore, special efforts must be made to prevent decarburisation during the production and heat treatment of the springs, which can be accomplished through shot peening. It has been observed that if the inner side of a coil spring is shot peened, the stresses on the surface inside the coils reduce and, as a result, the fatigue life increases (SAE AE-11, 1982). The corrosion rate of springs operating inland and coastally vary significantly (Zainal, 2010). Those operating in coastal environments experience accelerated corrosion. Many railway operators apply surface coatings to deter the corrosion rate, while others prefer to use it to prevent corrosion and hydrogen embrittlement (Vukelic and Brcic, 2016).

However, mechanical damages to the surface paint often result in accelerated localised corrosion (Dakhore and Bissa, 2013). The selection of the coating is crucial as the spring steel must be more noble than the coating to avoid accelerated galvanic corrosion in the event of coating damage (Kain, 2012). It is worth noting that the coating of bogie springs is a worthless effort due to the probability of coating removal as a result of mechanical damage or fretting. In the event of coating damage, SCC will be accelerated. For SCC to occur there must be a susceptible material, a corrosive environment, and stress.

This phenomenon causes degradation in mechanical properties of steel (Merson *et al.,* 2012) and results in a loss of material and reduction of strength and ductility of the steel (Popoola *et al.,* 2013). Alloying elements such as chromium are known to improve corrosion resistance in steel (Niu *et al.,* 2018). The current work investigated the susceptibility of the three spring steels to corrosion using electrochemical methods. The study is concerned with the interaction of corrosion and mechanical stress with the surface properties of the springs in order to prevent premature spring failure caused by SCC. Furthermore, efforts to predict SCC was attempted using slow strain rate testing (SSRT) techniques.

The susceptibility to SCC was determined as a function of elongation and time to fracture. Hydrogen-enhanced stress corrosion is notorious in high-strength steel and is detrimental to the surface properties of the steel. Since the surface finish of a spring influences the service lifespan, the surface is often shot peened to prolong the lifespan. The optimisation of spring steel mechanical properties is intended to increase the lifespan of springs.

2.1.7 Thermal characteristics of material

2.1.7.1 Thermogravimetric behaviour

Bogie springs are manufactured from high-strength spring steel that has to be accurately heat treated (Liu, Liu, and Liu, 2010). The general manufacturing process of springs entails hot coiling steel rods, followed by cooling and reheating the steel to austenitic temperatures for hardening purposes (Rakhshtadt, 1967; Hattingh, 1998). The hardened steel is then tempered to improve the toughness of the spring. The coiling of the springs is regarded as metal forming at 860°C, which entails time strain and relaxation. This section focuses on the thermogravimetric characteristics of the steels during heat treatment specifically relating to oxidation and decarburisation.

The heat treatment process entails the development phase when steel is heated and cooled at determined rates (Barbacki and Mikołajski, 1998). During the heat treatment process, the steel surface oxidises and forms scales when exposed to air (Chang and Wei, 1989). The surface also decarburises during the heat treatment process. These two processes deteriorate the spring's surface properties, which adversely affects the fatigue life of the spring (Ganesh *et al.,* 2012). A large body of work is available on the thermogravimetric analysis (TGA) of various metals but not really on that of spring steels.

The oxidation and decarburisation of steels have also been extensively investigated, as well as various steel chemistries and conditions (Gutiérrez, 2014). However, there is limited information on the oxidation rates, as well as the exact chemistries and conditions, of specific spring steels. Shi *et al.* (2013) evaluated the sensitivity of various spring steels to oxidation and decarburisation but did not show the relationship between them. In pursuit to understand how decarburisation of steel can be reduced, Zorc *et al.* (2019) conducted a study of oxidation and decarburisation of non-alloyed C45 steel at various temperatures. The prediction of thermomechanical properties and deformation behaviour of spring steels is of great interest to spring manufacturers.

2.1.7.2 Thermomechanical behaviour

Although general steel behaviour is known, the exact thermomechanical behaviour such as deformation and relaxation for specific grades are not. Therefore, a focus of this study was on the thermomechanical behaviour of the selected spring steels during quenching to maintain optimum design dimensions. The cooling capacity of viable quenching oils was studied in order to improve the appropriate oil selection to provide optimum mechanical steel properties (Maisuradze, Ryzhkov, and Yudin, 2015). In this study, deformation was affected by uniaxial compression using a dilatometer.

The cooling rates that were used were those that would sufficiently produce the necessary mechanical properties and martensite structure without causing quench cracking. It is well known that high temperature deformation results in grain refinement. In the current study, three alloyed spring steels were heat treated and evaluated against oxidation and decarburisation. A fair amount of attention was given to the oxidation rates and decarburisation of the steels in air at atmospheric pressure. The study also focused on the experimental heat treatment results to validate the high temperature oxidation rate.

Thermomechanical treatment (TMT) is essential for the production of high-strength spring steel and is the most effective way of increasing resistance to plastic deformation and relaxation. TMT should be extensively carried out on products such as finished springs.

2.1.8 Spring parameters

Helical coil compression springs offer resistance to compressive forces and are usually cold or hot coiled depending on the rod diameter. Springs are hot coiled when the diameter exceeds 16mm (BS EN 13906, 2002). They are generally made of various forms and shapes of wire depending on the purpose and use.

Though it is imperative that they employ rectangular or square wires in some cases, the use of round wires has been the most preferred. Tolerances in spring manufacturing are important as they affect the load-deflection characteristics of bogie springs. The spring designer must stipulate the load, mean diameter, pitch, solid length, and spring rate, as shown in Equations 2.14 to 2.18.

$$D = \frac{(D_o - D_i)}{2} \qquad 2.14$$

$$L_o = (n_t - 0.3)d_{max} \qquad 2.15$$

$$p = \frac{L_o - d}{n_t} \qquad 2.16$$

$$P = \frac{Gd^4F}{8D^3N_a} \qquad 2.17$$

$$R = \frac{P}{F} = \frac{Gd^4}{8D^3N_a} \qquad 2.18$$

When a spring is subjected to dynamic loading, a stress correction factor should be included when calculating the torsional shear stress. The stress correction factors were calculated from Equations 2.19 and 2.20. The fatigue life expectancy of the springs is to be evaluated according to SAE HS 795, using Equations 2.19 to 2.32.

$$K_w = \frac{4C-1}{4C-4} = \frac{0.615}{C} \quad 2.19$$

$$C = \frac{D}{d} \quad 2.20$$

$$K_{s1} = \frac{kS}{UTS} \quad 2.21$$

$$K_{s2} = A + BK_{s1} \quad 2.22$$

$$\frac{P_1}{P_2} = \frac{K_{s1}}{K_{s2}} \quad 2.23$$

$$K_E = \frac{K_U(K_{S2} - K_1)}{2K_U - (K_{S2} + K_{S1})} \quad 2.24$$

$$n = \frac{C_E^{\frac{1}{-y}}}{K_E} \quad 2.25$$

The fatigue strength parameters for the hot coiled helical compression springs manufactured from carbon steel bars that were shot peened and pre-set are given in Table 2.3 (K_U = 0.740, C_E = 0.830, M = -0.0215, and Y = -0.130.) and are presented in the Goodman-Haigh diagram in Figure 2.36 (SAE AE-11, 1982).

$$K_w = \frac{4C-1}{4C-4} = \frac{0.615}{C} \quad 2.26$$

$$C = \frac{D}{d} \quad 2.27$$

$$K_{s1} = \frac{kS}{UTS} \quad 2.28$$

$$K_{s2} = A + BK_{s1} \quad 2.29$$

$$\frac{P_1}{P_2} = \frac{K_{s1}}{K_{s2}} \quad 2.30$$

$$K_E = \frac{K_U(K_{S2} - K_1)}{2K_U - (K_{S2} + K_{S1})} \quad 2.31$$

$$n = \frac{C_E^{\frac{1}{-y}}}{K_E} \quad 2.32$$

Table 2.3 Parameters for calculating the fatigue strength of hot coiled springs (SAE AE-11, 1982).

Cycles n	Max K_{S2}	K_E	A	B
1000	0.715	0.737	0.738	0.002
10000	0.681	0.546	0.628	0.151
100000	0.648	0.405	0.523	0.293
1000000	0.617	0.300	0.427	0.423
2500000	0.605	0.266	0.392	0.471

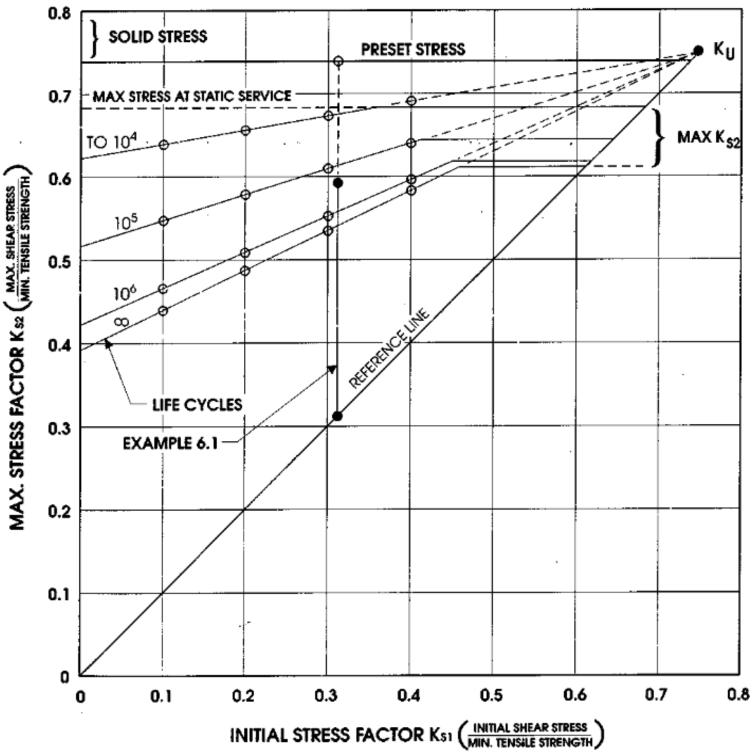

Figure 2.36 Goodman-Haigh diagram representing a B-10 fatigue life (90% probability of survival) (SAE AE-11, 1982).

2.1.9 Knowledge gap

Safe and reliable rail freight is crucial for global economic success due to large mass transportation. Therefore, bogie springs are critical elements of the structural system of rolling stock (Sayyaadi and Shokouhi, 2009) and are responsible for the dynamic stability and safe operation of trains (Ji-lin and Kai-hong, 2013). In the USA, the springs are subjected to scheduled inspections every two years to establish their roadworthiness (Porteiro, 2010). However, once installed, thorough routine inspection of bogie springs is difficult to carry out due to the inaccessibility of the springs. The springs are generally designed to have an infinite lifespan, but if they reveal uniform or pitting corrosion, they are removed from service to avoid catastrophic derailments.

The design of fit-for-purpose bogie springs is based on a combination of operational conditions such as loading and unloading, operational environments such as coastal or industrial environments, and manufacturability. However, high-end engineered springs require detailed knowledge of the materials, processes, and behaviour of steels at each stage of the manufacturing process. As a result, it is critical that the design is based on the properties of the selected material. A thorough grasp of the production process and its impact on material qualities is understood and controlled. The problem was defined using system thinking, which identified specific focus points that are outlined in the objectives.

Although the quenching process of steels has been properly studied for many years, the goal of this research is to choose the best quenching oil from a catalogue of industrial quenching oils to determine the exact influence of the quenching media on a specific grade of material. The impact of decarburising and heat-related oxidation on the heat treatment was the first step in optimisation. Although it is well understood that different grades of materials measure varying decarburisation and oxidation rates, the research on selected spring steel grades quantification is particularly limited.

The goal of this research was to determine the decarburisation and oxidation rates of the chosen spring steel grades to select a unique and optimal heat treatment for each grade. The next step was to determine what the critical transformation temperatures were for each steel grade. Thereby producing a body of knowledge for these specific spring steel grades, which is not available from literature.

The critical transition temperature, which impacts the outcome of mechanical properties, was a vital aspect of the optimisation process. It is also widely accepted that tempering temperature and soaking time have an impact on the ultimate mechanical properties of steel. Nevertheless, the optimum tempering temperature for the steels under investigation is unknown in literature.

SCC is more common in some spring steel grades than in others. All of these elements, including application, design, processing, and manufacturing, must be considered as a whole to have an acceptable lifespan and capacity of springs.

Chapter 3 : Methodology

The primary goal of this research was to address a potential industrial problem of limited material in the near future. Identifying three grades of spring steel to experiment with was the first step to addressing the problem. Because of the similarities in the manufacturing process and the prevalence of SAE 5160 steel-related failures in the past, a holistic system thinking approach was taken as part of the investigation. System elements such as spring design, austenitising, quenching, and tempering were identified and analysed as part of the root causes. The first part of the study looked at a list of notable failures as part of the problem statement, while the investigation makes up the second part.

The structural integrity of the springs was optimised using FEA as part of the design element of the study. The structural integrity analysis aimed at showing the effect of the pitch angle on the fatigue life of the spring. The material properties will be improved by determining suitable heat treatment processes to produce complete springs and entails thorough mechanical testing and metallographic examination. The three local materials identified for this research were 55Cr3, 54SiCr6, and 52CrMoV4. The candidate devised a heat treatment programme on his own and tested different temperatures as part of the optimisation process.

3.1 Background

A flood of bogie spring failures have caused grave concern for railway operators in South Africa. The first section of this study covered one of the investigations of spring failure that is representative of many similar failures, while the second section focuses on quenching and optimisation experimental exercises. Bogie springs are manufactured using hard-drawn steel rods that are hot coiled into a spring shape, followed by quenching, tempering, and shot peening. The springs are first normalised and hot coiled at 850°C to 880°C, followed by austenitising at 860°C to 880°C for one hour, quenching in oil at 40°C, and then tempering at 430°C to 450°C for three hours. The quenching oil properties are summarised in Table 3.1.

The prominent spring failures that were investigated were surface micro-cracks and mechanical damages caused by coil contact under load. Majority of the micro-cracks could only be detected after in-service failure because the existing non-destructive testing such as magnetic particle inspection and dye penetrant testing could not detect the cracks. In events where the cracks were detected because of their size, they were classified as the 'as receipt' from the mill defects and attributed as part of the rod manufacturing process. Due to accessibility difficulties, bogie springs are only inspected and monitored for fatigue cracks during maintenance intervention cycles, which are every four years during heavy lifting.

Table 3.1 Physical and chemical properties of the quenchant.

Appearance	Liquid
Flash point (°C)	>204°C
Density (g/cm^3)	0.854
Pour point (°C)	-15°C
Viscosity (m^2/s at 40°C)	20

The springs under investigation were one of many that failed in-service and another that failed fatigue testing. The spring that failed in-service could only survive a maximum of 1200 km over a period of one month. The spring that failed during the fatigue testing was part of a set of nine springs that were subjected to dynamic loading testing of 56 kN with a frequency of 3 Hz. The spring that failed fatigue testing recorded 203 800 cycles before complete failure at a frequency of 3 Hz.

The cyclic and mean load were 13.044 and -43.48 kN, respectively. All the tested sets failed to reach the minimum threshold, which stipulates that hot coiled springs must survive 2.5 x 10^6 cycles of dynamic loading at rated load (SAE AE-11, 1982). The typical failure of these springs can be described as fatigue failure, which progressed between 20% and 25% before the final brittle failure. The crack initiation point was always located on the inner radius of the springs.

The required microstructure of the spring steel was tempered martensite with a minimum hardness of 50 Rockwell C. The springs were manufactured out of SAE J404 grade 5160 spring steel with a rod diameter ranging from 25 mm to 35 mm and were fitted onto heavy-haul locomotives. The bogies consist of 12 dual spring sets, i.e. four dual springs per axle, and carries a maximum load of 22 tons per axle. This load is far less than the rated spring load. The load is transmitted directly from the bolster to the subframe to the springs to compress.

3.2 Experimental procedures

3.2.1 Root cause analysis

A case study of two failed inner springs was conducted. The as-received failed components were visually examined, and images of the failed components were taken. A spectrometer was used to determine the composition of the spring materials and the microstructures were analysed using an optical microscope and high magnification imaging with a scanning electron microscope (SEM). The phase analysis of the quenched steel rods was determined using X-ray diffraction (XRD) and the quenching capacity of the oil was determined using ivf Smart Quench. The hardness properties were determined using a micro-Vickers hardness tester. Details of the methods are covered in the sections below.

3.2.2 Structural integrity assessment

The aim of this section is to optimise the spring design, understand the stress distribution throughout the springs, and determine the Goodman-Haigh diagram for the springs. The structural integrity assessments of the springs were conducted using FEA and were determined using first principal calculations according to BS EN 13906 standards. In the past, pitch angle has not been considered to be an important parameter of spring design. However, the inconsistent pitch observed on the failed springs inspired an investigation of the pitch angle effect on the fatigue life of springs. The pitch angle was varied using the original spring design as reference.

The following three dual spring set configurations were considered:

1. Dual spring set with the original pitch angle and the loads applied evenly on the spring.
2. Dual spring set with the original pitch angle and the loads applied unevenly on the spring.
3. Dual spring set with the modified pitch angle and the loads applied evenly on the spring.

3.2.3 Chemical analysis

The chemical composition of the rods was determined with the Q4 TASMAN Advanced CCD-Based Optical Emission Spectrometer. The samples were prepared by cutting and grinding the mounted sample, the tests were carried out at room temperature and an average of three measurements were taken per sample. The results were analysed and compared to the relevant grades of BS EN 10089:2002 standards.

3.2.4 Heat treatment

The three identified steel rods were subjected to various heat treatment processes to optimise the mechanical properties. A heat treatment programme was devised with a range of temperatures to optimise the process. The heat treatment cycles are shown in Table 3.2.

Table 3.2 Experimental heat treatment cycles.

Steels	**Heat treatment processes**						
	Coiling		**Austenitising**		**Tempering**		
	Temp. (°C)	Time (min)	Temp. (°C)	Time (min)	Temp. (°C)	Time (h)	
55Cr3	880	60	880	60	410	2	3
54SiCr6	880	60	880	60	450	2	3
52CrMoV4	880	60	880	60	470	2	3

The heat treatment experiment only focused on 25 mm diameter spring steel rods. Three heat treatment furnaces with temperatures ranging from 0°C to 1200°C were used to carry out the austenitising, and tempering. The furnaces were set to the required temperatures and the samples were placed inside once the temperature had stabilised. The soaking timer was started once the furnace doors were closed. After the set time expired, the samples were removed and quenched.

The rods were heated to 860°C and isothermally soaked for an hour before normalising. The rods were then re-heated to 860°C and isothermally soaked for another hour, followed by oil quenching. The quenched rods were further optimised by tempering at various temperatures and soaking times. The received material was analysed with a spectrometer and were heat treated thereafter. The heat-treated material was then subjected to mechanical testing and a thorough microscopical examination.

The steels were subjected to the heat treatment process in a controlled furnace to evaluate the decarburisation and oxidation behaviour of the materials. The heat treatment entailed austenitising, at 860°C for one-hour, subsequent oil quenching, and then tempering at 450°C for three hours. Before the heat treatment, the three rods were machined to a depth of 1 mm to remove any possible decarburised surface layers. Transverse sections were then polished to 1 μm surface and then finished and etched with picric acid for the purpose of microstructural analysis.

3.2.5 Sample preparation

The samples were sectioned with a band saw and a water-cooled abrasive cutting machine. The saw was used to reduce the 5 m length rods to 450 mm sections, which were easy to handle and could fit easily into the furnace. The water-cooled abrasive cutting machine was used to cut small samples that were prepared for metallographic examination.

The cut samples were then deburred by rough grinding, followed by the mounting process using Bakelite and thermoplastic resin. The samples were ground and polished using an automatic Struers Tegramin polisher and a Struers CitoPress was used for the mounting. The maximum temperature for the mounting was 140°C. The grinding and polishing steps and parameters are presented in Table 3.3.

Table 3.3 Grinding and polishing steps and parameters.

Steps	**Grinding**		**Polishing**		
Surface finish	320 grit	1200 grit	9 μm cloth	3 μm cloth	1 μm cloth
Lubricant	Water	Water	9 μm	3 μm	1 μm
Speed (rpm)	300	150	150	150	150
Force (N)	30	30	15	10	10N
Time (min)	2	5	5 – 10	5	5

Each grinding and polishing step removes surface scratches, while etching is used to reveal the microstructure of the steel. Etching was done on the polished surface using 3% Nital and 2% picric reagent.

3.2.6 Testing

3.2.6.1 Quench testing

Quenching is a critical aspect of the heat treatment process. The selection of a wrong quenchant may result in detrimental effects on the steel. A quench analysis test was carried out to analyse quenchant characteristics that would induce the appropriate cooling rates along with the ability to produce the desired microstructure without causing cracking. A portable ivf Smart Quench system shown in Figure 3.1 was used.

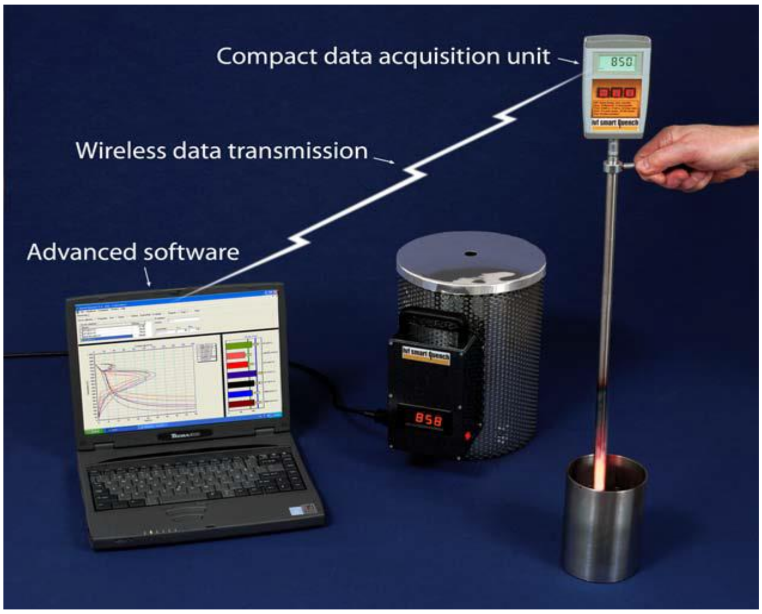

Figure 3.1 ivf Smart Quench setup (Bodin and Segerberg, 2005).

The ivf Smart Quench system consists of a probe manufactured according to the ISO 9950 standard, a furnace, and a computer equipped with data acquisition software. An Inconel 600 probe with a 12.5 mm diameter and 60 mm length and containing a thermocouple was used. A beaker was used to pour the quenchants for testing. The probe was heated to 860°C using the furnace, held at that temperature for 20 minutes, and then quenched using a different quenchant.

The quenching temperature was monitored and restricted to a maximum of 60°C during the heat treatment. The probe was cleaned in an ultrasonic bath before and after testing. The cooling rates and temperatures during quenching were recorded by the data acquisition system and analysed. The selected quenching oils for the experiment were then tested. The results of the most suitable oils are presented in the results section of this thesis.

3.2.6.2 Corrosion testing

The corrosion rate and premature failure of springs in-service have preoccupied rail operators worldwide. It is paramount to understand the corrosion resistance of the material before deploying it in a specific environment. The three identified materials were tested for corrosion resistance under severe atmospheric conditions similar to those across the country. The materials were exposed to a pH level of 4 and a 3.5% sodium chloride solution. Furthermore, the electrochemical characteristics of the three spring materials were determined to measure the effect of coating on the electrochemical potential and corrosion rate.

3.2.6.3 Slow strain-rate testing

Slow strain-rate testing was used to determine SCC at a strain rate of 1 x 10^{-6} s^{-1} and was carried out at 25°C according to ISO 7539-7 (ASTM E8). The environment consisted of water with 3.5% sodium chloride at a pH of 4. Small-sized specimens proportional to the standard specimen according to the American Society for Testing and Materials (ASTM) Standard E8 for cylindrical tensile test specimens were used, with a diameter of 4 mm and a reduced section length of 22.5 mm (slightly longer than the standard, which is 19.0 mm). A schematic drawing of the tensile specimen is shown in Figure 3.2.

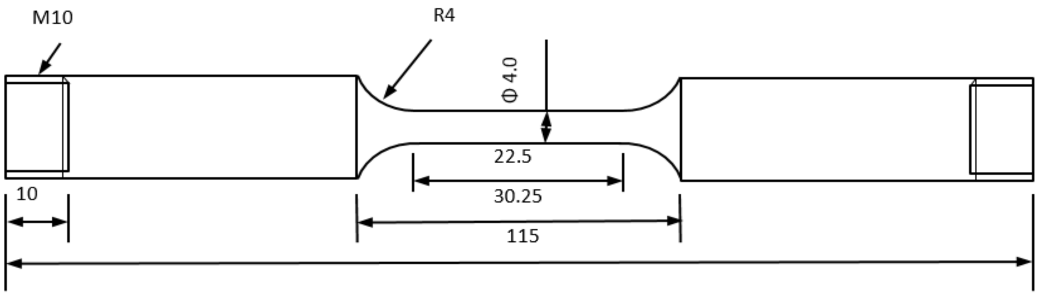

Figure 3.2 Approximate details of the tensile specimen used.

3.2.6.4 Tensile testing

Tensile strength gives an indication of the strength and ductility of materials. The results of these tests may be used to establish other critical parameters, such as the strain hardening exponent and Young's modulus. The tensile testing samples were machined to the dimensions specified in Figure 3.3.

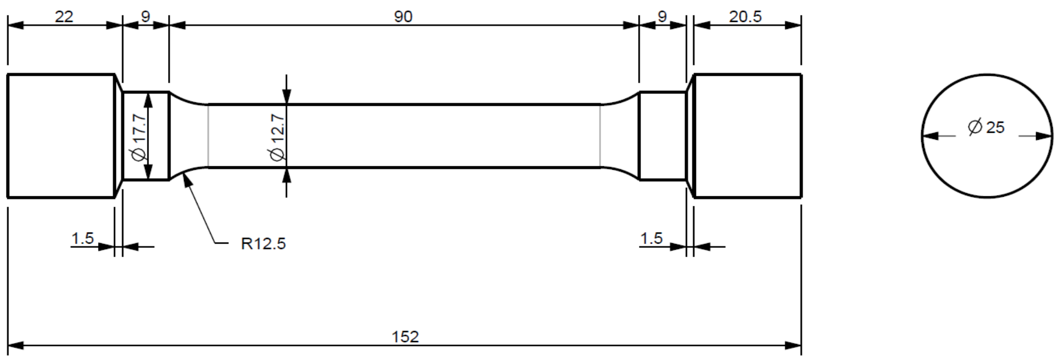

Figure 3.3 Tensile testing of a geometric sample.

The samples were taken from the centre of the rods. Tensile testing was performed in accordance with ASTM E8-00 using a 100 kN load cell MTS machine (Avner, 1998) and was carried out at room temperature. The initial diameter and gauge lengths were measured, and the engineering stress-strain curve was plotted.

3.2.6.5 Hardness testing

Hardness testing can be used to determine the hardenability of materials. The hardness tests were conducted on flat polished samples using an INNOVATEST Vickers hardness tester and Rockwell hardness tester. A micro-Vickers hardness test, with 0.5 kg.f, was used for microhardness and the test profile was carried out across the sample diameter at 100 µm intervals. The Rockwell hardness tester was used to measure hardness on a macroscale.

3.2.6.6 Impact strength testing

Impact strength testing, or Charpy testing, is generally used to study the temperature-dependent ductile to brittle transition of the materials. A Charpy impact machine was used to determine the impact strength of the spring steel and a 750 pound hammer was used to conduct the testing. A 10 x 10 x 60 mm sample was machined from the centre of the rod and tested at -20°C, -7°C and 25°C.

3.2.6.7 Microscopic analysis

An optical microscope was used to evaluate the microstructures of the samples. The samples were cut and prepared for metallographic examination by grinding and polishing to about 1 µm surface finish. The samples were then evaluated in the polished condition for non-metallic inclusions and etched to evaluate the developed microstructure. A SEM, which is equipped with energy-dispersive X-ray spectroscopy, was used to examine the samples at high magnification. The fracture surfaces of tensile test samples were also evaluated using a SEM.

3.2.6.8 Differential scanning calorimetry

SDT Q600 V20.9 Build 20 DSC equipped with DSC-TGA module was used for experimental thermal analysis. Sample preparation entailed grinding fine particles from the three materials. Each material was weighed with the instrument before the analysis began. The chamber temperature was ramped up to 850°C at 120°C per minute and held there for two minutes before cooling at the same rate.

All three materials experienced a similar heating and cooling cycle under air atmospheric conditions. Furthermore, the oxidation rates were determined by holding the samples isothermally after they were heated to 860°C while purging the steel with argon gas. The samples were then isothermally held at 860°C for one hour under atmospheric conditions.

3.2.6.9 Dilatometric testing

The three selected spring steels were prepared for dilatometry to conduct thermal analysis and evaluate the impact of cooling rates on mechanical properties and microstructures. The dilatometric samples were machined to a 5 mm diameter and a 10 mm length. The dilatometric test samples for each spring steel grade were heated to 860°C followed by soaking them at the same temperature before cooling them at various rates.

The constant cooling rates were used to generate dilatometric data for the steels. The critical transformation temperatures were determined by measuring the dilation using thermal expansion against temperature. The heat treatment parameters are shown in Table 3.4.

Table 3.4 Dilatometric parameters used on the three materials.

Temperature (°C)	**Cooling rate (°C/s)**	**Heating rate (°C/s)**	**Soaking time (h)**
860	0.01	10	45
860	0.1	10	45
860	1	10	45
860	10	10	45
860	20	10	45
860	30	10	45
860	100	10	45

The heat-treated dilatometric test samples were mounted and prepared for microscopic examination by grinding and polishing them to a 1 µm finish. The samples were etched with 2% nitric reagent prior to the metallographic examination using both the optical microscope and the SEM. The samples were further subjected to micro-Vickers hardness testing to determine the hardness of the materials relative to the microstructure. The CCT curves for the three steels were generated from the dilation curves. The Ms temperature was determined with a cooling rate of 100°C per second.

3.2.6.10 Thermomechanical testing

The three selected spring steels were prepared for thermomechanical testing using a dilatometer. The samples were machined to a 5 mm diameter and a 10 mm length and were subjected to heating followed by compression deformation to 0.02 strain before cooling. A strain of 0.02 is regarded as a point where permanent deformation starts while conducting tensile testing at room temperature. The experimental parameters and variables are presented in Tables 3.5 and 3.6.

Table 3.5 Deformation and soaking of the three materials.

Temperature	**Isothermal soaking**	**Strain**	**Strain rate**	**Cooling rate**	**Cooling media**
860°C	45 min	0.02 mm /mm	5/s	0.47°C/s	Air

Table 3.6 Deformation and quenching of the three materials.

Sample	**Temperature (°C)**	**Isothermal soaking (min)**	**Strain (mm/mm)**	**Quenching media**
55Cr3	860	45	0.02	Oil A
54SiCr	860	45	0.02	Oil B
52CrMoV4	860	45	0.02	Oil A

The first batch of samples were cooled in conditions simulated to be still air. The cooling rate of 0.4°C per second was aimed at mimicking the normalising process after coiling the springs. The second batch of samples were quenched in oil whereby the quenching characteristic of the oil was used. The quenching capacity and cooling rates of the oil were determined using a smart quench system. The introduction of quenching after coiling was to assess the relaxation ability upon rapid cooling.

The smart quench system was equipped with an Inconel probe, furnace, and computer that has data acquisition software. The two selected oils were poured into a beaker for testing and were labelled Oil A and Oil B. Oil A was designated to 55Cr3 and 52CrMoV4, while Oil B was designated to 54SiCr6. The probe was heated to 850°C and soaked for 20 minutes before it was quenched in the respective oils.

The determined quenching capacity data that was collected included the oil cooling rates, which were inserted as parameters in the dilatometer to mimic the cooling capacity of the respective oils. The dilatometer used helium gas for rapid cooling. The heat-treated samples were prepared for microscopic examination by grinding, polishing, and etching with 2% Nital. Microscopic examination was determined using an optical microscope.

3.2.6.11 X-ray diffraction

XRD was used to investigate and characterise the microstructure of the steel. With XRD, the samples are scanned at an angle (∅), while the detector simultaneously moves at 2∅. Rietveld analysis was used to quantify the XRD results to characterise the crystallographic phases, which were analysed and quantified.

3.2.7 Manufacturing of bogie springs

Full-scale prototype springs were produced at an unnamed spring manufacturing facility. The coiling was done as per FEA report recommendations. The manufacturing of springs entails hot coiling, quenching, and tempering. The springs were shot peened in the same facility as a final process.

Chapter 4 : Results

The results are separated according to root cause analysis and experimental results.

4.1 Root cause analysis

4.1.1 Visual examinations

Visual examinations of the spring that failed in-service due to micro-cracking are shown in Figure 4.1 and 4.2. The failure of these springs can be described as fatigue failure that began on the surface of the spring. The fractured surface of the spring in Figure 4.1 reveals a dull area followed by approximately 13% of fatigue beach marks from the dark area before brittle failure. Figure 4.2 reveals a dull area that appeared as a pre-existing crack that oxidised during the heat treatment. The dark area is identified as the initiation point of the fatigue crack.

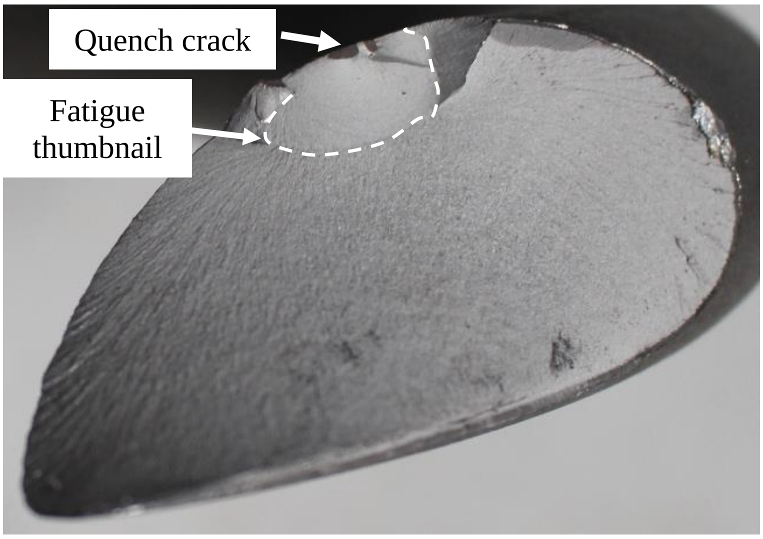

Figure 4.1 Complete spring fracture surface.

A visual examination of the spring that failed during fatigue testing is shown in Figure 4.3. The spring failed at coil number 5. The fracture surface of the spring revealed fatigue cracks that progressed approximately 20% of the spring. The fracture surfaces of the spring are shown in Figures 4.4 and 4.5.

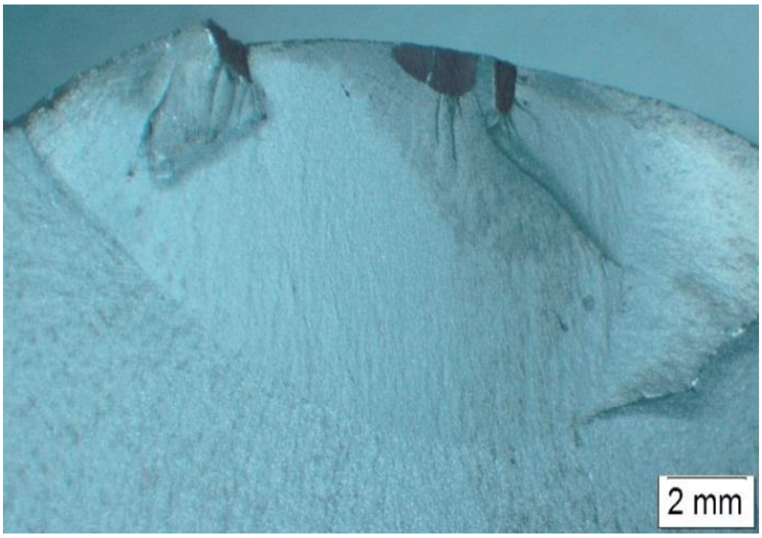

Figure 4.2 A cropped image of the initiation point in

.

Figure 4.3 Spring that failed during fatigue testing.

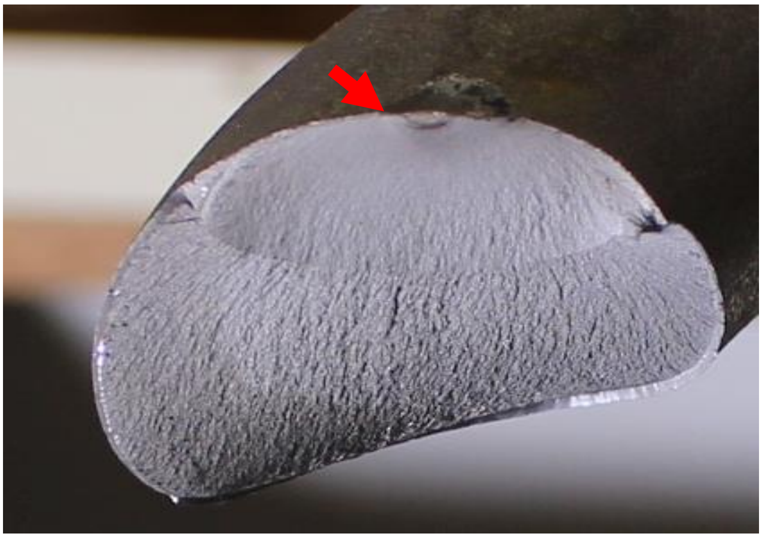

Figure 4.4 Facture surface and initiation point of the failed spring.

Figure 4.5 Top view of the failed spring.

4.1.2 Scanning electron microscope

The origin of the fatigue crack on the sample that failed in-service was examined by means of a SEM. The initiation point featured a mixture of transgranular and intergranular cracking typical of quench cracking. The surface of the failure origin was covered with what appears to be heat-related iron oxide scales. Oxidation occurred during further heat treatment processes, i.e. tempering. A SEM image of the origin of the crack is presented in Figure 4.6.

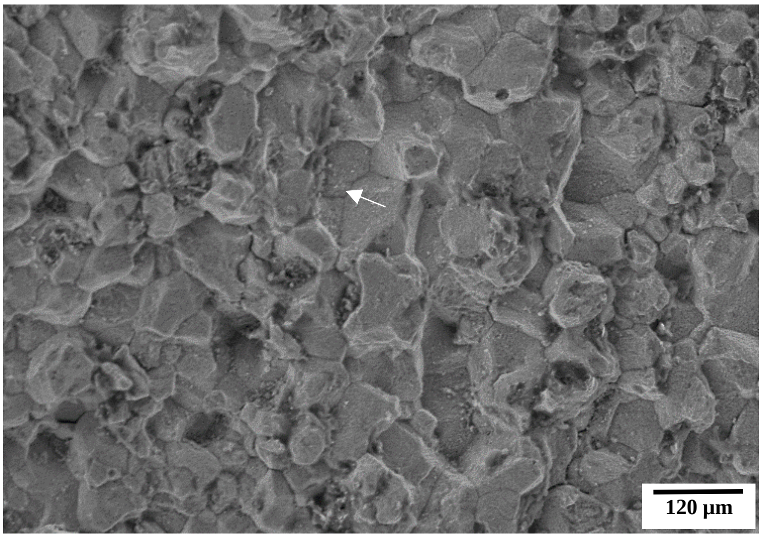

Figure 4.6 A SEM image of the failure origin.

4.1.3 Chemical composition

The chemical composition of the spring that failed in-service was conducted by means of optical emission spectrometry in element weight percentage and the results are presented in Table 4.1. The composition of the failed spring complied with the requirements of SAE 5160 spring steel, which is classified as hardenable high-carbon steel.

Table 4.1 Chemical composition results of the failed spring.

Elements	%C	%Si	%Mn	%P	%S	%Cr
Failed spring	0.60	0.28	0.84	0.013	0.004	0.78
SAE 5160 steel	0.56-0.64	0.15-0.35	0.75-1.00	0.04 max	0.03 max	0.70-090

4.1.4 Quench test

The oil sample that was used to produce the failed springs was collected from the quench tank for quench test analysis. An additional sample of the unused oil was also taken for analysis. The oil samples were taken in clean separate containers for testing and were tested using a portable quenchant test system, i.e. ivf Smart Quench. The quench test results are presented in Table 4.2 and are plotted in graphs shown in Figures 4.7 and 4.8.

Table 4.2 Quench test results.

Properties	Unused oil	Used oil
Maximum cooling rate (°C/s)	61.6	78.9
Temperature at maximum cooling rate (°C)	526.0	515.9
Temperature at start of boiling (°C)	619.9	615.3
Temperature at start of convection (°C)	331.9	240.1
Cooling rate at 300°C (°C/s)	7.3	19.0
Time to 600°C (s)	10.9	9.8
Time to 400°C (s)	15.8	13.1
Time to 300°C (s)	41.3	15.1
Time to 200°C (s)	49.8	27.2
Theta 1 (°C)	616.3	612.3
Theta 2 (°C)	398.6	326.3
Hardening Power-IVF (Oil)	271.2	756.3

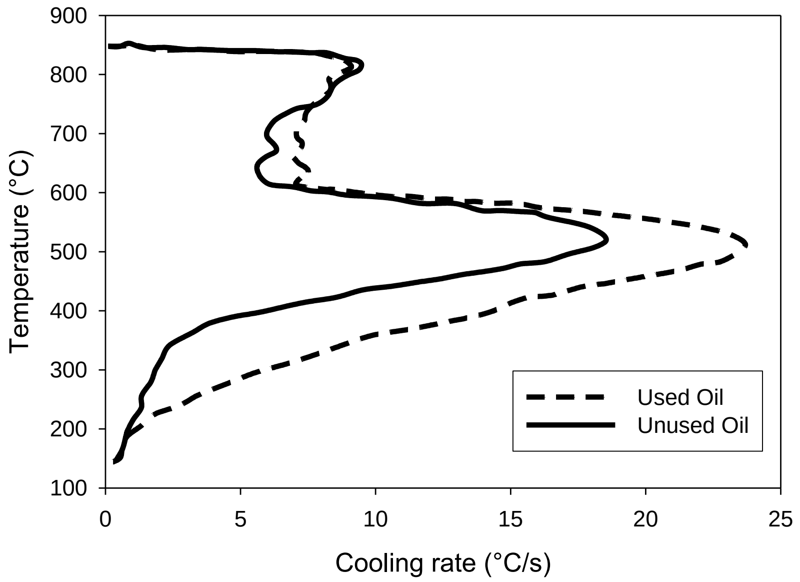

Figure 4.7 Oil properties: cooling rates.

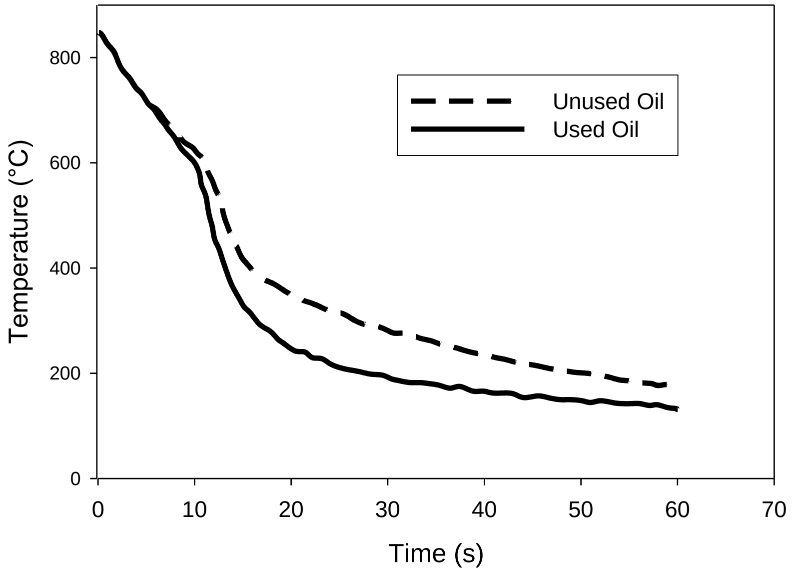

Figure 4.8 Oil properties: convection curves.

The used oil showed deterioration and as a result had a faster cooling rate at the martensitic start range. The cooling rates of the used oil were severe at critical temperatures of 280°C and 300°C. The harmonisation of the SAE 5160 CCT curve is shown in Figure 4.9. The CCT curve in the figure was generated using JMatPro software and shows full martensitic transformation.

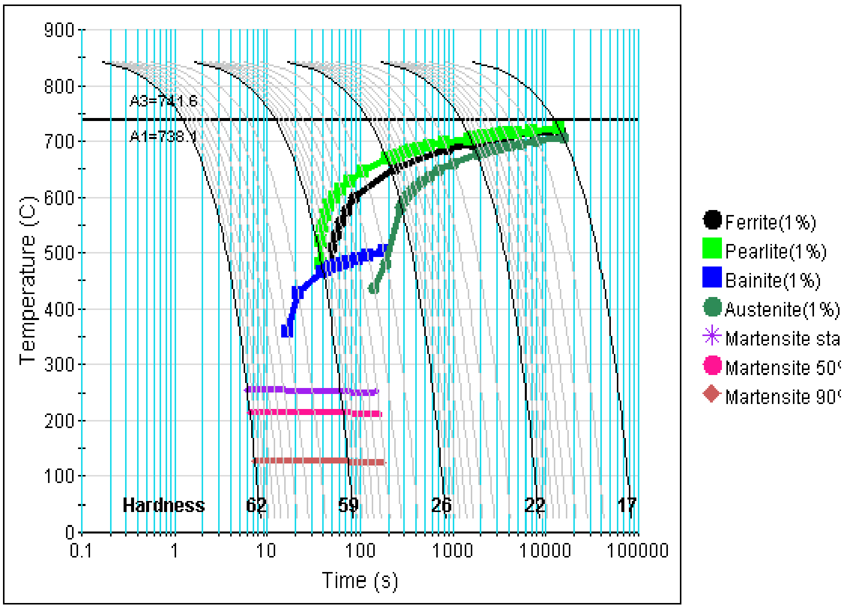

Figure 4.9 SAE 5160 steel CCT diagram.

4.1.5 Heat treatment validation experiments

To validate the findings of the discussed oil quenching capacity, hardening experiments were undertaken to simulate the spring heat treatment process. The SAE 5160 steel sample was heated to 860°C and quenched in the Unused oil and the used oil, respectively.

4.1.5.1 Microscopic examination results

The microstructure of the steel that was quenched with the Unused oil revealed a matrix of martensite and bainite formations, while the microstructure of the steel quenched with the used oil revealed fully transformed martensite with a crack running through. The microstructural images are shown in Figures 4.10 and 4.11.

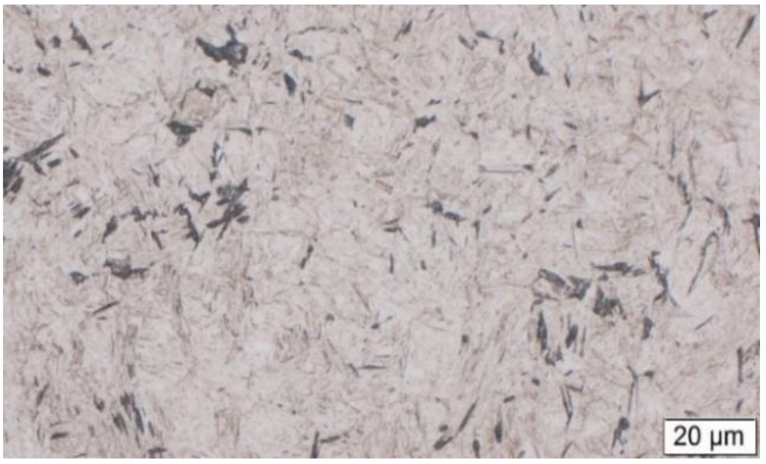

Figure 4.10 Microstructure of the steel after quenching in the Unused oil.

Figure 4.11 Microstructure of the steel after quenching in the used oil.

4.1.5.2 Hardness results

The hardness profile measurements were carried out using the Vickers hardness tester and was done from one edge to the other at a 1 mm interval. The steel that was quenched with the used oil revealed higher hardness compared to the Unused oil. The hardness average and profile results are shown in Table 4.3 and Figures 4.12 and 4.13.

Table 4.3 Average hardness measurements.

Quenchant	Average	Standard deviation	Standard error
Unused oil	780.9	23.3	4.6
Used oil	866.8	13.9	2.8

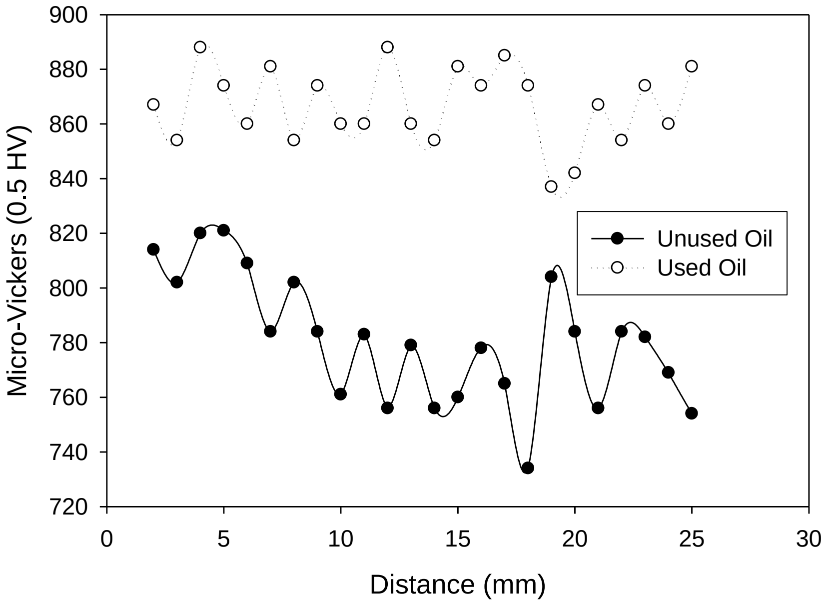

Figure 4.12 Hardness profile measurements.

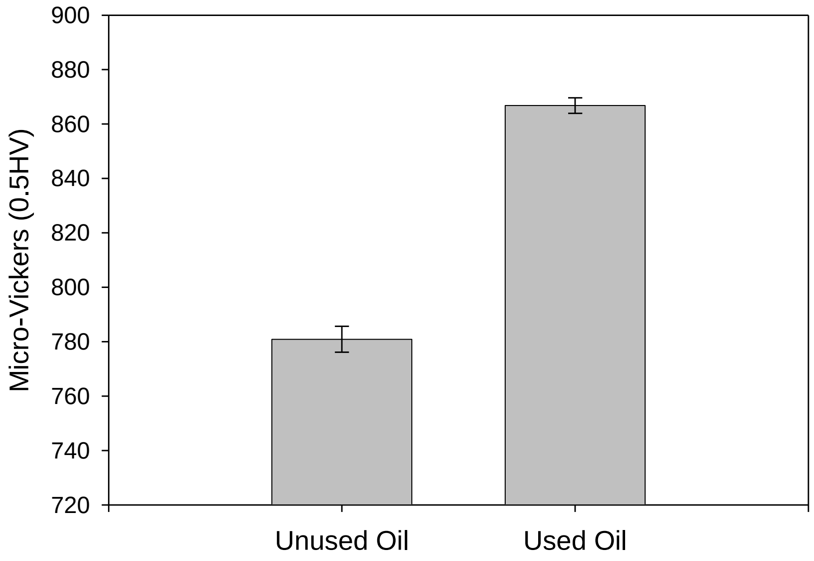

Figure 4.13 Hardness measurements average.

4.1.5.2.1 X-ray diffraction results

A XRD analysis was conducted on the samples that were quenched with the Unused oil and used oil. The XRD spectrums are shown in Figures 4.14 and 4.15. The quantitative analysis showed that the sample quenched in the used oil had more martensite transformation than the sample quenched in the Unused oil. This confirms that the deterioration of oil has an impact on the cooling rates of the oil. Phase quantification, as shown in Table 4.4, was conducted using the Rietveld method.

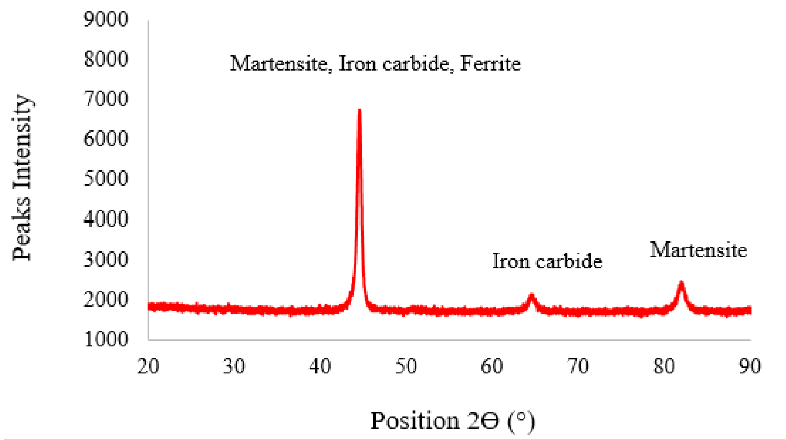

Figure 4.14 XRD spectrum: Unused oil sample.

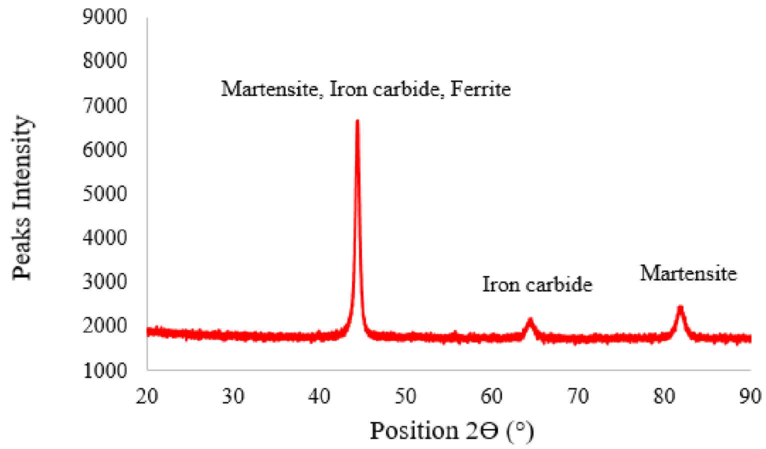

Figure 4.15 XRD spectrum: used oil sample.

Table 4.4 Quantified phase analysis.

Phases	Unused oil	Used oil
Martensite (%)	67.4	77.7
Cementite (%)	31.7	21.1
Ferrite (%)	0.9	1.1

4.2 Design optimisation

This section looks at optimising the spring design to solve the problem of spring coil contact stated in the root cause analysis. Although the spring set up is a dual configuration, the focus of this study is developing an optimum pitch angle for the inner spring.

4.2.1 Spring information

The designed spring dimensions of the dual spring sets are given in Table 4.5. The pitch and pitch angle of the springs were calculated using Equations 2.16 and 4.1.

$$\lambda = \tan^{-1}\left(\frac{p}{\pi D}\right) \tag{4.1}$$

4.2.2 Structural integrity assessment

The inconsistent pitch observed on the failed spring inspired the investigation of the effect of pitch angle on the fatigue life of springs. These investigations involved varying the pitch angle using the original design as reference. The structural integrity of both dual spring sets was evaluated when compressed to solid length and subjected to dynamic loading. The influence on the fatigue life expectancy when the dual spring set was loaded unevenly with the original pitch angle was then evaluated. The structural integrity was conducted with the pitch angle, as shown in Tables 4.6 and 4.7.

Table 4.5 Spring dimensions.

Spring information	**Spring set with original pitch angle**	
	Outer spring	**Inner spring**
Number of coils	5.7	7.9
Number of active coils	4.2	6.4
Mean coils diameter (mm)	243	165
Nominal wire diameter (mm)	35	25
Free length (mm)	367.6	367.6
Length at rated load (mm)	252.5	252.5
Solid length (mm)	189.0	190.0
Pitch (mm)	79.2	53.5
Pitch angle (°)	5.9	5.9

Table 4.6 Torsional shear stresses of the outer spring when subjected to solid compression.

Pitch (mm)	**Pitch angle (°)**	**Shear stress (MPa)**	**Corrected stress (MPa)**	**Deflection (mm)**
72	5.4	571	643	166
79	5.9	630	709	179
83	6.2	661	745	179
85	6.3	673	758	179
87	6.5	694	782	179
152	11.2	1207	1359	179

Table 4.7 Torsional shear stresses of the inner spring when subjected to solid compression.

Pitch (mm)	**Pitch angle (°)**	**Shear stress (MPa)**	**Corrected stress (MPa)**	**Deflection (mm)**
45	5.4	582	656	148
54	5.9	637	717	178
56	6.2	668	752	178
57	6.3	679	765	178
59	6.5	703	791	178
100	10.9	1188	1338	178

The corrected and uncorrected torsional shear stresses were determined using Equations 4.2 and 4.3.

$$\tau = \frac{Gds}{\pi n D^2} \qquad 4.2$$

$$\tau_{k,shear} = k\tau \qquad 4.3$$

The spring design calculations were done according to the requirements of the following standards:

- EN 13906-1: 2013. Cylindrical helical springs made from round wire and bar - Calculation and design - Compression springs - Part 1: Compression springs (BS EN 13906-1, 2002).
- DIN 2096-1: 1981. Helical compression springs made of round wire and rod; Quality requirements for hot formed compression springs (DIN 2096, 1981).
- SAE HS 795: 1990. Spring design manual - Part 2: Design and application of helical and spiral springs (SAE AE-11, 1982).

4.2.3 Theoretical calculations

The theoretical calculations for torsional stress were conducted in accordance with the spring drawing and BS EN 13906 compliance criteria and are presented in Table 4.7. SAE HS 795, 1990, p. 2.60 states that the maximum allowable uncorrected torsional shear stress in a spring that is manufactured from an oil-tempered alloy steel is 50% of the material tensile strength. SAE J404 5160 steel has a nominal UTS of 1400 MPa. This suggests that the maximum allowable uncorrected torsional shear stress is 700 MPa.

The calculated results of the outer spring show that the pitch angle can only be varied between 5.9° and 6.5° without causing structural problems. However, the pitch angle of the inner spring can be varied between 5.9° and 6.3°. The theoretical forces required to reach solid compression for the outer spring, inner spring, and dual spring set with the original pitch (5.9°) and modified pitch (5.4°) are presented in Figures 4.16 and 4.17.

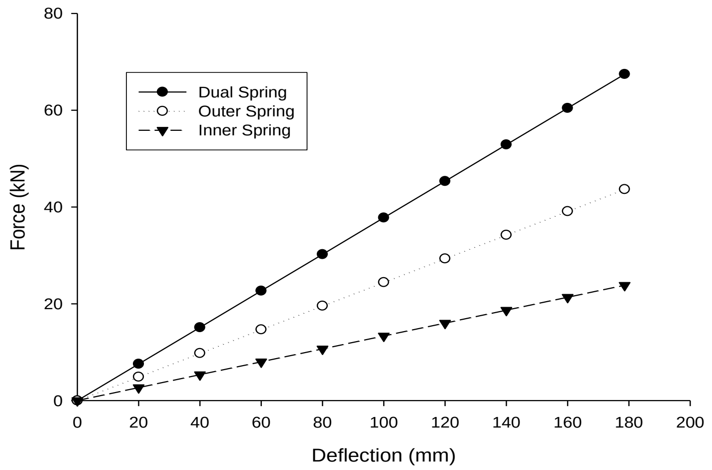

Figure 4.16 Theoretical forces required to reach solid compression of the dual spring set with a pitch angle of 5.9°.

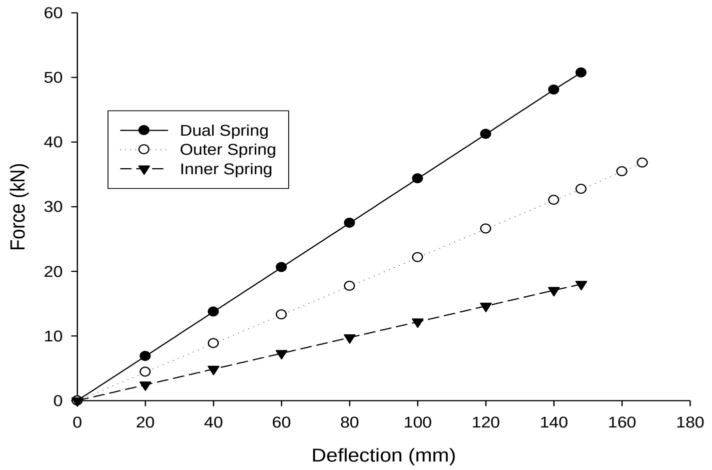

Figure 4.17 Theoretical forces required to reach solid compression for the dual spring set with a pitch angle of 5.4°.

A theoretical spring force of 50.7 kN is required to compress the modified pitch angle of 5.4° of the dual spring set to solid length, which is less than the maximum dynamic load of 56.5 kN. The spring deflection was calculated using Equation 4.4 and the results are summarised in Table 4.6. The results of the modified pitch angle of 5.4° with an expected spring deflection of 178 mm will achieve solid compression at a deflection of 149 mm, suggesting that the spring with the modified pitch angle is not suitable for this application.

$$s = \frac{8D^3nF}{Gd^4} \qquad 4.4$$

4.2.4 Finite element model

A FEA was carried out to confirm the corrected and uncorrected torsional stresses that were calculated in Table 4.6 and 4.7. Three solid models of dual spring sets were generated with different pitch angles using the parameters given in Table 4.5. The respective pitch angles were 5°, 5.9°, and 11°, as illustrated in Figure 4.18.

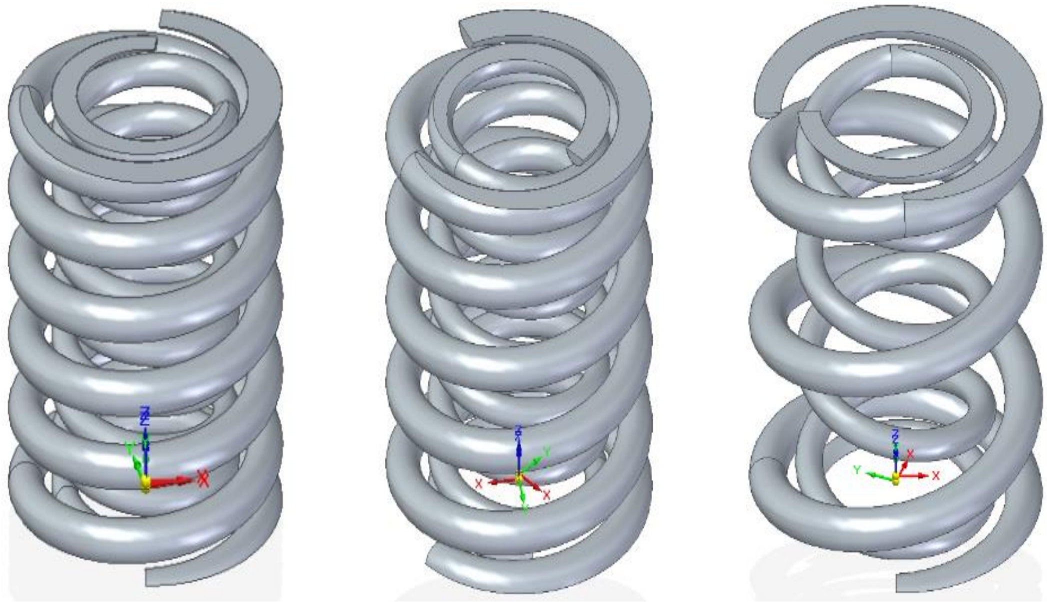

(a) (b) (c)

Figure 4.18 A solid model of the dual springs set with the original pitch angle (b) 5.9° and modified pitch angles (a) 5° and (c) 11°.

These solid models were imported into MSC Patran where the solid bodies were meshed with TET10 solid elements and were then exported to MSC Marc. Two contact bodies were created for each dual spring set, namely the inner spring and outer spring. The finite element model (FEM) of the dual spring set with the original pitch angle is presented in Figure 4.19, where two contact bodies are indicated. Two geometric surfaces were generated – one touching the bottom of the two springs and the other touching the top.

4.2.4.1 Boundary conditions

Touching surfaces with a friction coefficient of 0.3 was specified between the surfaces and springs, as well as self-contact between the spring coils. The top surface was connected to a control node that was used to apply the relevant boundary conditions. The control node was constrained for translation and rotation in all directions except for translation along the z-axis (axial direction of the spring), as shown in Figure 4.20.

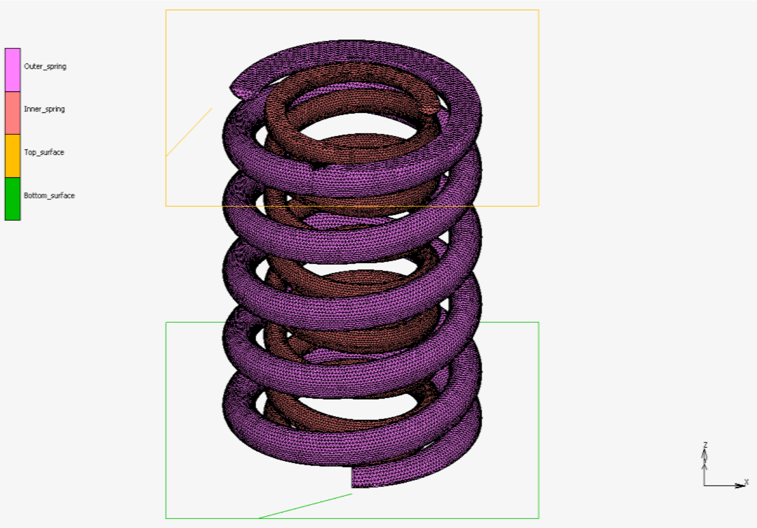

Figure 4.19 A FEM of the dual spring set with the original pitch angle.

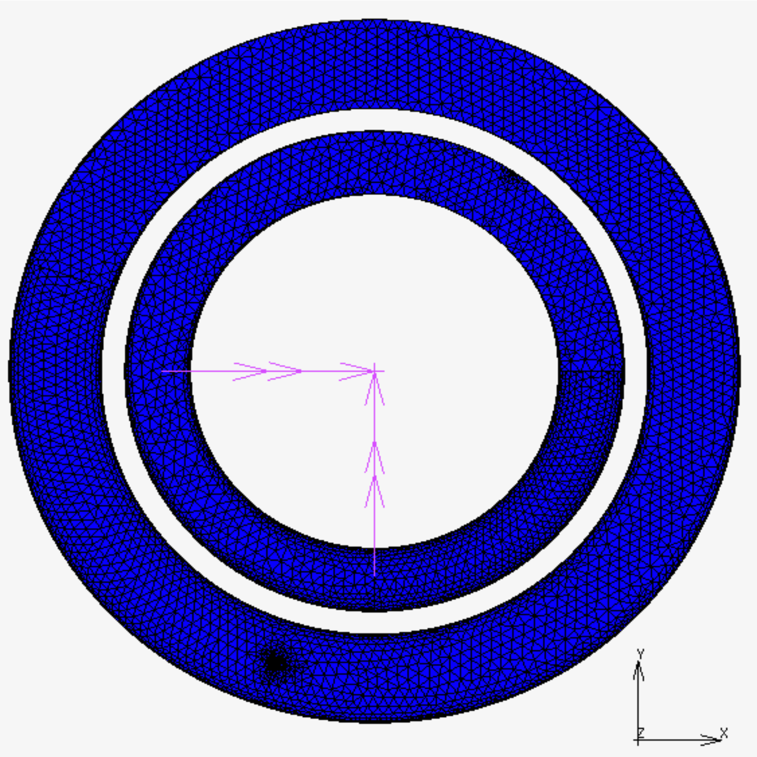

Figure 4.20 Boundary conditions applied to the control node that is attached to the geometric surface above the springs.

Either a fixed displacement or point load was applied to the control node. Two nodes at the bottom end of each spring were constrained for translation along the x-axis and y-axis to keep the springs from rotation, as shown in Figure 4.21. The same boundary conditions were applied to both dual spring sets.

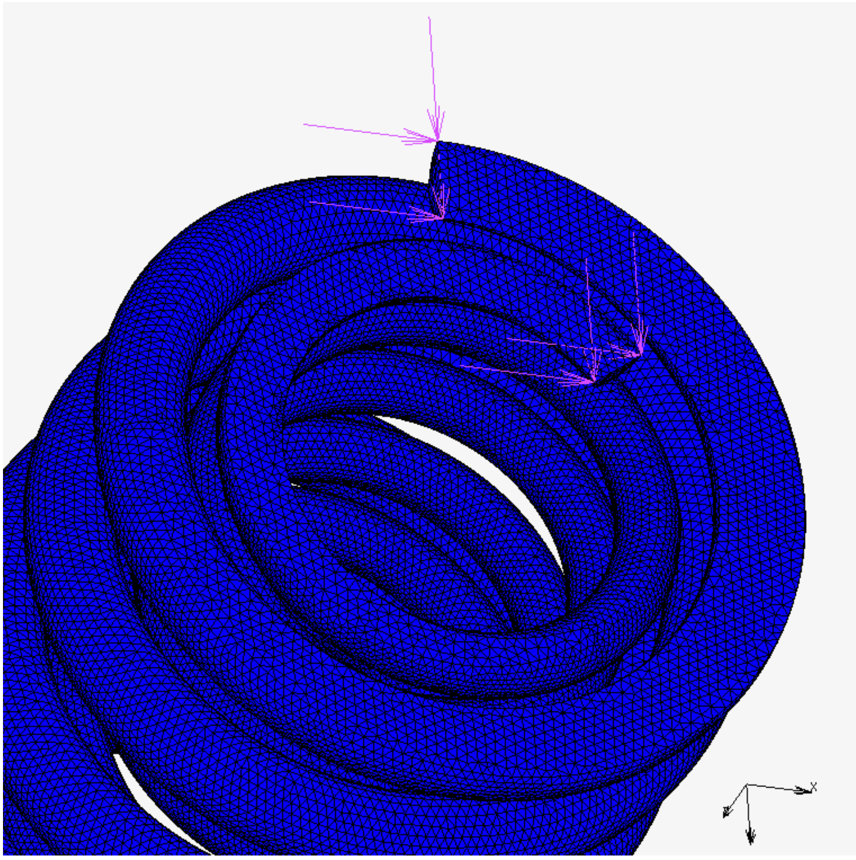

Figure 4.21 Two nodes at the bottom end of each spring constrained for translation.

4.2.4.2 Load cases

The following two load cases were assessed:

- Load Case 1: During this load case, a displacement with a magnitude equal to the free length subtracted by the solid length of the dual spring set was applied to the geometric surface above the springs.
- Load Case 2: During this load case, a point load was applied to the geometric surface above the springs in four increments, where increments 2, 3, and 4 had magnitudes equal to the minimum, mean, and maximum dynamic loads on the dual spring sets, respectively.

4.2.4.3 Constitutive model

The dual spring sets were modelled with linear elastic isotropic material properties in MSC Marc. The properties are shown in Table 4.8.

Table 4.8 Material properties of spring steel used in the finite element analysis.

Description	Value
Density (kg/m^3)	7 850
Modulus of elasticity (GPa)	206
Shear modulus of elasticity (GPa)	78.5
Poisson ratio	0.31

4.2.4.4 Dual spring set with the original pitch angel of 5.9°

4.2.4.4.1 <u>Solid compression</u>

The major principal shear stress and equivalent von Mises stress for Load Case 1, where the dual spring set was compressed to its solid length, are shown in Figures 4.22 and 4.23, respectively.

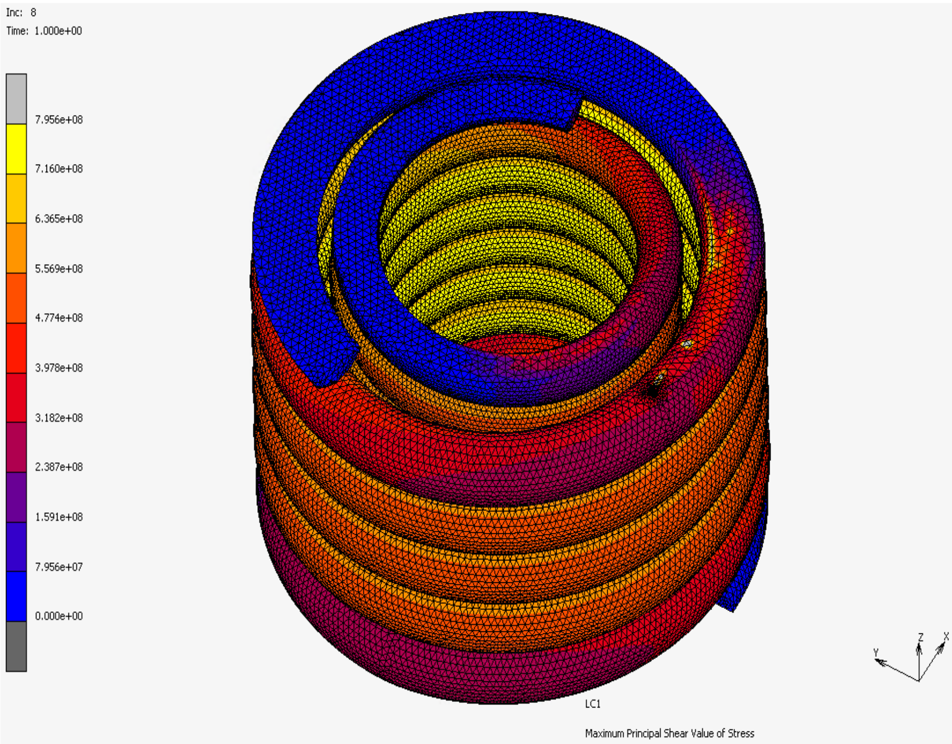

Figure 4.22 Maximum shear values of stress on the dual spring set for Load Case 1.

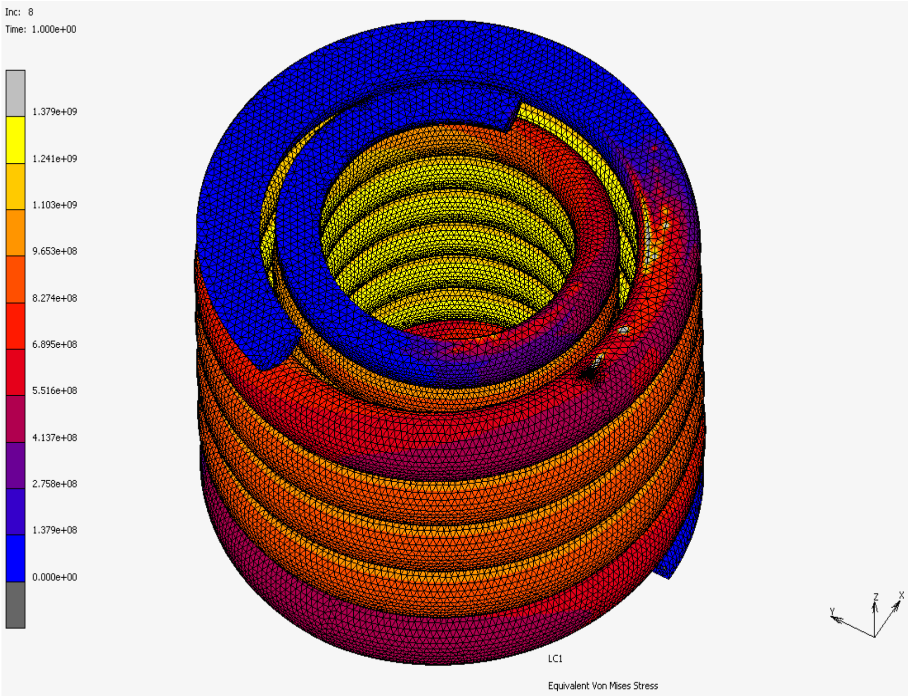

Figure 4.23 Equivalent von Mises stress on the dual spring set for Load Case 1.

A maximum shear value of stress of 765.6 MPa and a maximum equivalent von Mises stress of 1328 MPa were calculated on the outer spring, while a maximum shear value of stress of 795.6 MPa and a maximum equivalent von Mises stress of 1379 MPa were calculated on the inner spring. The maximum stresses were found on the inner surfaces of both springs.

4.2.4.4.2 Dynamic loading

A summary of the maximum shear values of stress and the maximum equivalent von Mises stress on the outer and inner springs for Load Case 2 are presented in Table 4.9.

Table 4.9 Maximum stresses on the outer and inner springs for Load Case 2.

Description	**Maximum shear stress values**		**Equivalent von Mises stress**	
	Outer spring	**Inner spring**	**Outer spring**	**Inner spring**
Minimum load (MPa)	366.9	373.0	636.7	646.8
Mean load (MPa)	523.9	534.7	908.9	927.2
Maximum load (MPa)	659.8	678.9	1 145	1 177

The maximum shear value of stress on the outer spring varies between 366.9 MPa and 659.8 MPa, while that on the inner spring varies between 373.0 MPa and 678.9 MPa. The maximum shear values of stress on the dual spring set are presented in Figure 4.24 for the maximum load.

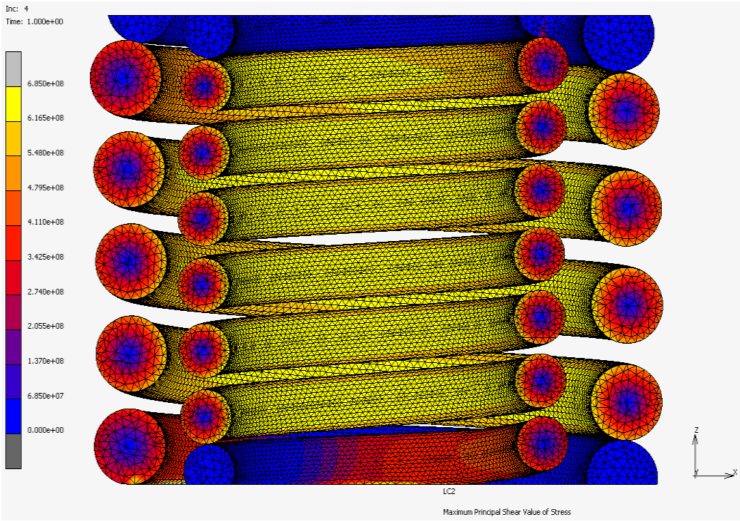

Figure 4.24 Maximum shear values of stress on the dual spring set for Load Case 2.

4.2.4.5 Dual spring set with a modified pitch angle of 5°

4.2.4.5.1 Solid compression

The results for Load Case 1, where the dual spring set was compressed to its solid length, indicated a maximum shear value of stress of 541.9 MPa and a maximum equivalent von Mises stress of 939.9 MPa on the outer spring. A maximum shear value of stress of 564.4 MPa and a maximum equivalent von Mises stress of 978.2 MPa was calculated on the inner spring. The maximum stresses are found on the inner surfaces of both springs, as shown in Figure 4.25. It was noted that the inner spring deformed unevenly to the one side. The equivalent von Mises stress on the dual spring set with the modified pitch angle is shown in Figure 4.26.

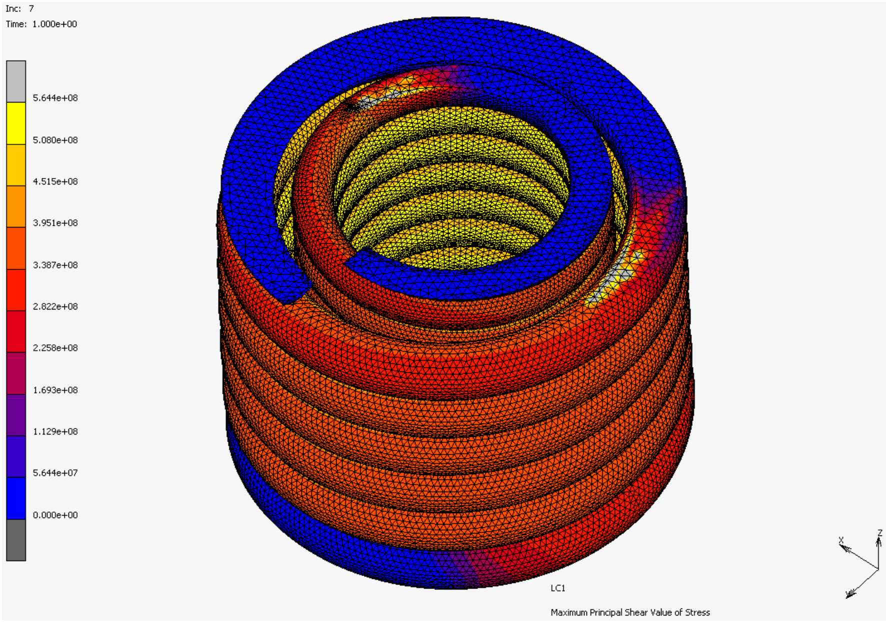

Figure 4.25 Maximum shear values of stress on the dual spring set for Load Case 1 (modified pitch angle).

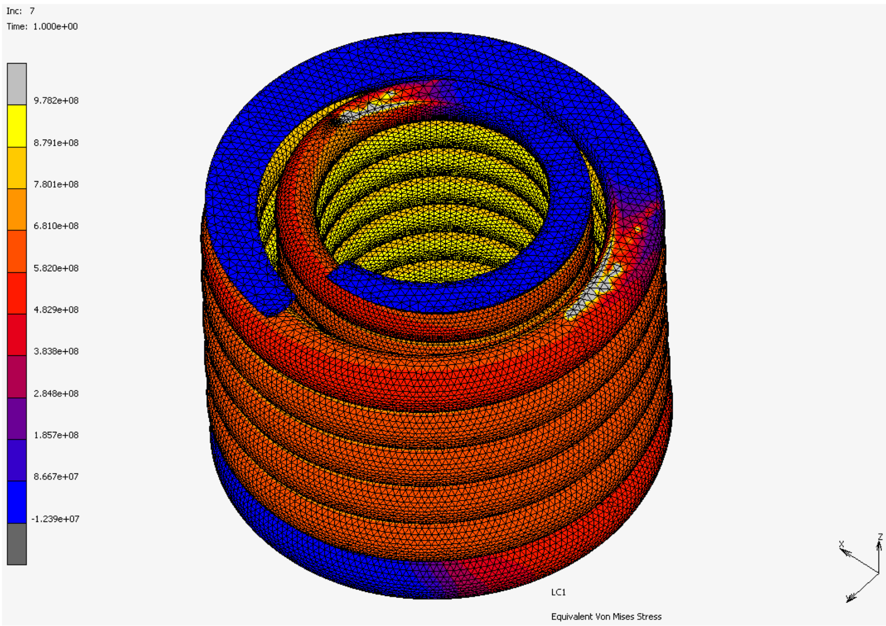

Figure 4.26 Equivalent von Mises stress on the dual spring set for Load Case 1 (modified pitch angle).

4.2.4.5.2 Dynamic loading

The results obtained from the FEA indicated that the dual spring set with the modified pitch angle reaches solid compression before the maximum load is reached. A summary of the maximum shear values of stress and the maximum equivalent von Mises stress on the outer and inner springs for the minimum and mean loads of Load Case 2 are presented in Table 4.10.

Figure 4.27 shows how the inner spring is completely compressed with the areas of contact shown in yellow.

Table 4.10 Maximum stresses on the outer and inner springs for Load Case 2 (modified pitch angle).

Description	**Maximum shear stress values**		**Equivalent von Mises stress**	
	Outer spring	**Inner spring**	**Outer spring**	**Inner spring**
Minimum load (MPa)	356.5	365.7	617.9	634.2
Mean load (MPa)	505.9	520.5	876.8	902.6

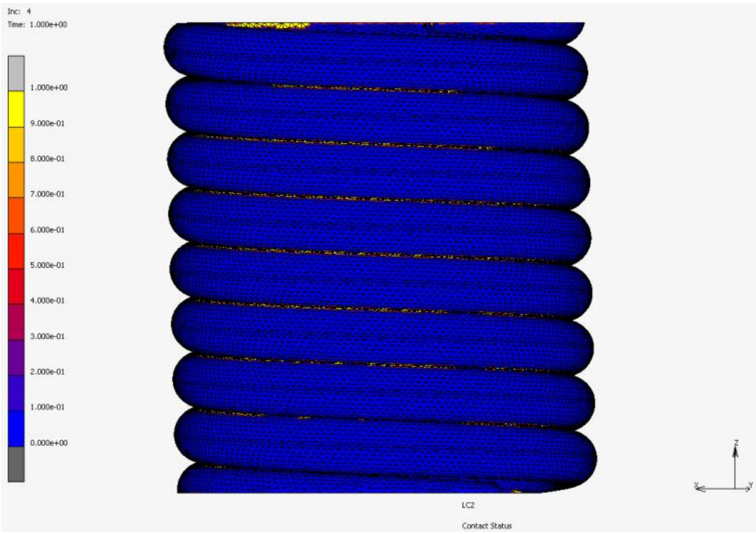

Figure 4.27 Contact status of the inner spring when subjected to the maximum dynamic force.

4.2.4.6 Dual spring set with a modified itch angle of 11°

4.2.4.6.1 <u>Solid compression</u>

The results for Load Case 1, where the dual spring set was compressed to its solid length, indicated a maximum shear value of stress of 1903 MPa and a maximum equivalent von Mises stress of 3312 MPa on the outer spring. A maximum shear value of stress of 1994 MPa and a maximum equivalent von Mises stress of 3473 MPa were calculated on the inner spring. The maximum stresses are found on the inner surfaces of both springs, as shown in Figure 4.28.

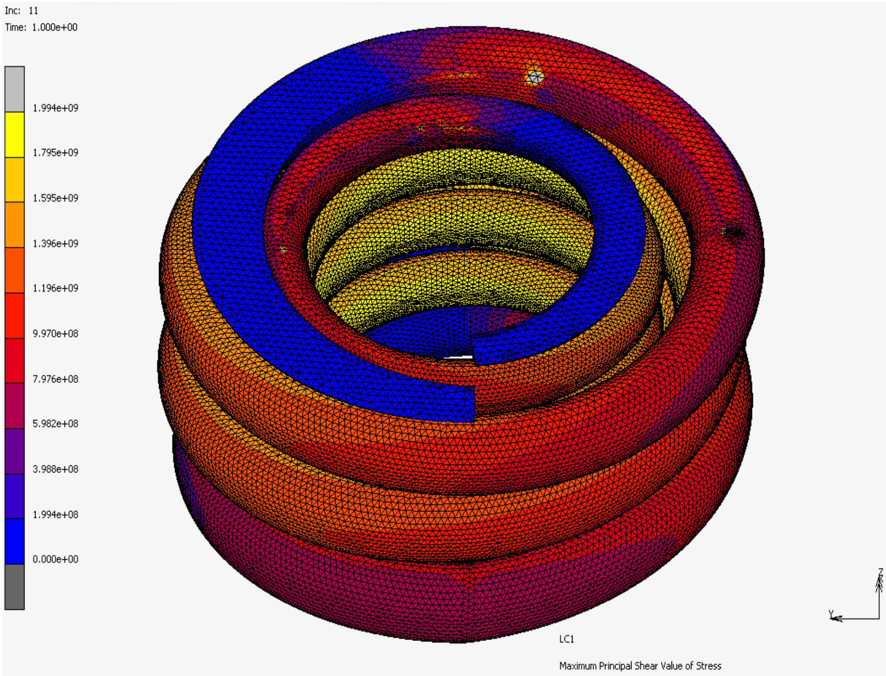

Figure 4.28 Maximum shear values of stress on the dual spring set for Load Case 1 (modified pitch angle).

It was noted that both springs deformed unevenly to the one side. The equivalent von Mises stress on the dual spring set with the modified pitch angle is shown in Figure 4.29.

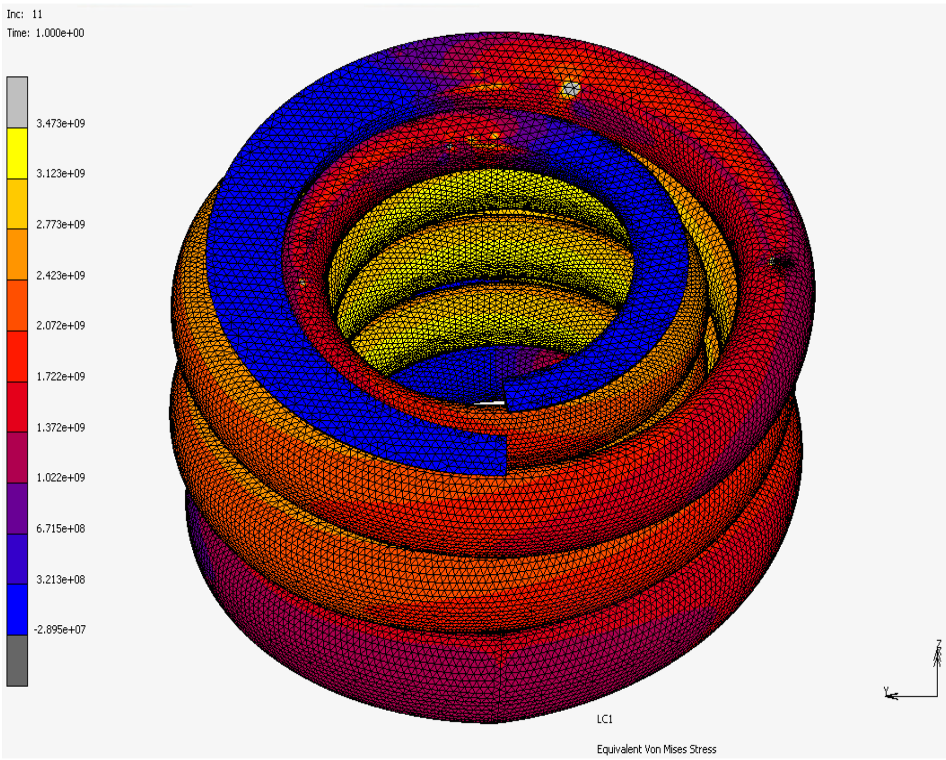

Figure 4.29 Equivalent von Mises stress on the dual spring set for Load Case 1 (modified pitch angle).

4.2.4.6.2 Dynamic loading

A summary of the maximum shear values of stress and the maximum equivalent von Mises stress on the outer and inner springs for Load Case 2 are presented in Table 4.11.

Table 4.11 Maximum stresses on the outer and inner springs for Load Case 2 (modified pitch angle).

Description	**Maximum shear stress values**		**Equivalent von Mises stress**	
	Outer spring	**Inner spring**	**Outer spring**	**Inner spring**
Minimum load (MPa)	392.6	389.4	684.1	678.5
Mean load (MPa)	575.5	559.9	1 003	975.2
Maximum load (MPa)	750.7	745.0	1 307	1 297

It was once again noted that both springs deformed unevenly to the one side and that the stress distribution is not uniform, as shown in Figure 4.30. The maximum shear value of stress on the outer spring varies between 392.6 and 750.7 MPa and varies between 389.4 and 745.0 MPa on the inner spring.

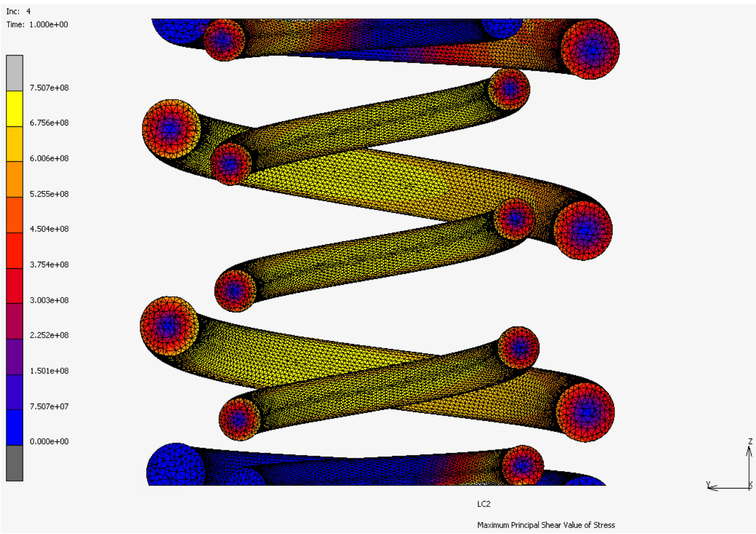

Figure 4.30 Maximum shear values of stress on the dual spring set for Load Case 2 (modified pitch angle).

4.2.4.7 Structural integrity of dual spring set when loaded unevenly

The additional scenario was evaluated wherein the dual spring set is loaded unevenly. Only the dual spring set with the original pitch angle and Load Case 2 was considered during this evaluation. To load the dual spring set unevenly, the geometric surface above the springs was rotated by 10°, as shown in Figure 4.31.

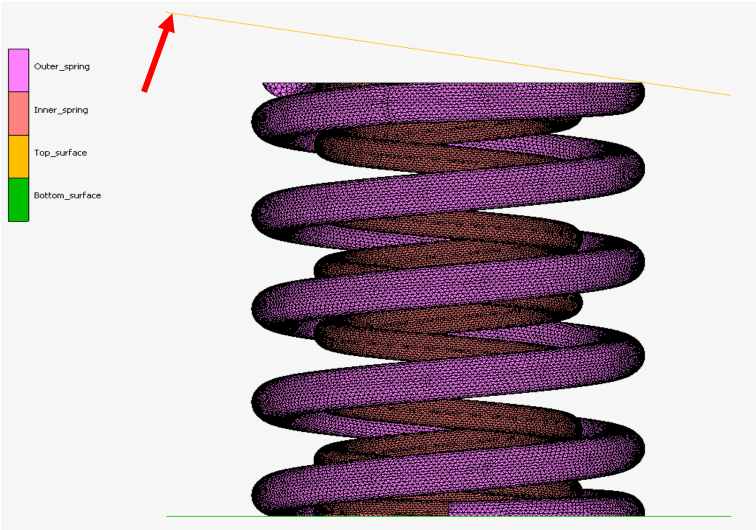

Figure 4.31 Geometric surface above the dual spring set rotated by 10° from the horizontal plane.

The same boundary conditions previously considered were applied to the FEM and the FEA was repeated. A summary of the maximum shear values of stress and the maximum equivalent von Mises stress on the outer and inner springs are presented in Table 4.12.

Table 4.12 Maximum stresses on the outer and inner springs for Load Case 2 (load applied unevenly).

Description	Maximum shear stress values		Equivalent von Mises stress	
	Outer spring	Inner spring	Outer spring	Inner spring
Minimum load (MPa)	476.8	527.5	826.2	915.2
Mean load (MPa)	614.3	711.8	1 065	1 236
Maximum load (MPa)	789.2	813.6	1 368	1 412

The maximum shear value of stress on the outer spring varies between 476.8 and 789.2 MPa and that on the inner spring varies between 527.5 and 813.6 MPa. The maximum shear values of stress on the two springs are presented in Figure 4.32.

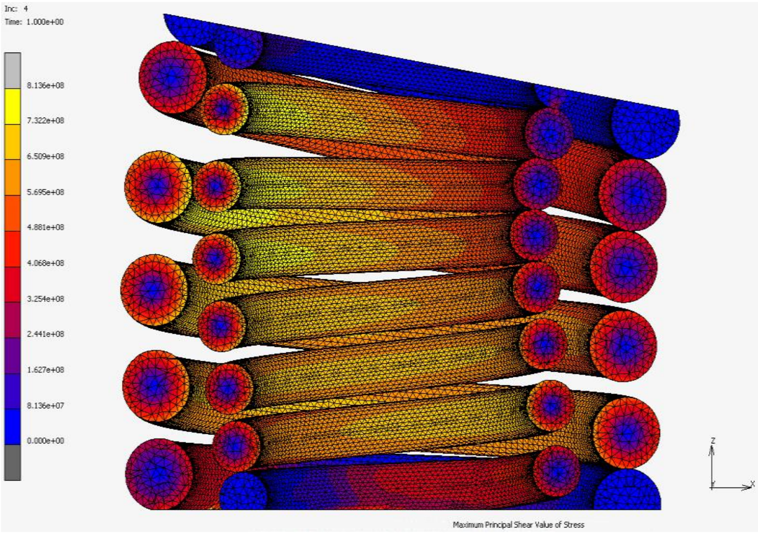

Figure 4.32 Maximum shear values of stress on the dual spring set for Load Case 2 (load applied unevenly).

4.2.4.8 Fatigue life expectancy according to SAE HS 795:1990

The fatigue life expectancy of the dual spring sets were evaluated according to SAE HS 795, using Equations 2.31 to 2.32 (SAE AE-11, 1982). The fatigue strength parameters for hot coiled springs that were shot peened and pre-set are given in Table 4.13. The fatigue life expectancy of both springs were calculated in Tables 4.14 and 4.15

.

Table 4.13 Stress correction factors for the outer and inner springs.

Description	**Symbol**	**Value**	
		Outer spring	**Inner spring**
Mean diameter of coil (mm)	D	243	165
Nominal diameter of wire (mm)	*d*	35	25
Spring index	*w*	6.94	6.60
Stress correction factor	*k*	1.22	1.23

Table 4.14 Outer spring fatigue life expectancy according to SAE HS 795.

Pitch angle (°)	**K_{S1}**	**K_{S2}**	**KE**	**No. of fatigue cycles**
5.9	0.4892	0.6224	0.2676	2412598
6.2	0.5137	0.6340	0.2678	2401549
6.3	0.5229	0.6383	0.2678	2396794
6.5	0.5393	0.6460	0.2680	2387173
5.4	0.4436	0.6009	0.2674	2428426

Table 4.15 Inner spring fatigue life expectancy according to SAE HS 795.

Pitch angle (°)	**K_{S1}**	**K_{S2}**	**KE**	**No. of fatigue cycles**
5.9	0.4946	0.6250	0.2676	2410354
6.2	0.5190	0.6364	0.2678	2398873
6.3	0.5276	0.6405	0.2679	2394173
6.5	0.5459	0.6491	0.2680	2382962
5.4	0.4522	0.6050	0.2674	2425815

The results indicate fatigue life expectancies that are below 2.5 million cycles for both springs, suggesting that both have a finite fatigue life. The fatigue life reduces when the pitch angle increases. The spring with a pitch angle of 5.4° shows a longer fatigue life, however, due to the notch caused by the contact, the fatigue life will be shorter. The initial and maximum stress factors for the inner and outer springs are almost the same and are shown in the Goodman-Haigh diagram in Figure 4.33. The two red lines intersect at the borderline of the finite fatigue life curve.

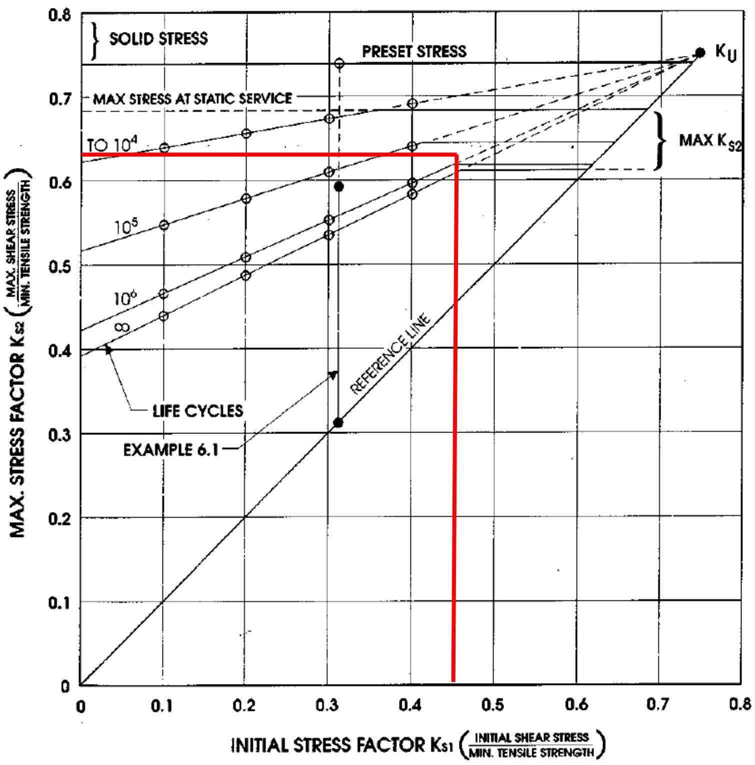

Figure 4.33 Goodman-Haigh diagram representing a B-10 fatigue life (90% probability of survival) (SAE AE-11, 1982).

4.3 Heat treatment optimisation

4.3.1 Chemical analysis

Chemical analysis was determined to characterise the composition of each spring steel grade. The composition was to be used to devise a unique heat treatment process and select a suitable quenching oil for each steel grade. The chemical evaluation results are presented in Table 4.16 and the prominent elements are discussed in detail.

The results comply with the respective material specifications. The presence of carbon, chromium, manganese, molybdenum, silicon, and vanadium contributes towards the improved strength and hardenability of steel. An increase in carbon improves the hardenability of steels during heat treatment, while chromium and silicon also improve corrosion resistance.

Table 4.16 Chemical composition of the springs.

Identity/ Element	Samples			BS EN 10089: 2002, Specifications		
	55Cr3	54SiCr6	52CrMoV4	55Cr3	54SiCr6	52CrMoV4
Carbon (%)	0.58	0.56	0.55	0.52-0.59	0.51-0.59	0.48-0.56
Silicon (%)	0.32	1.33	0.28	0.40 max	1.20-1.60	0.40 max
Manganese (%)	0.92	0.71	0.92	0.70-1.00	0.50-0.80	0.70-1.10
Phosphorus (%)	0.013	0.014	0.012	0.025 max	0.025 max	0.025 max
Sulphur (%)	0.004	0.002	0.007	0.025 max	0.025 max	0.025 max
Chromium (%)	0.79	0.75	1.05	0.70-1.00	0.50-0.80	0.90-1.20
Nickel (%)	0.06	0.01	0.01	*	*	*
Copper (%)	0.10	0.01	0.01	*	*	*
Molybd. (%)	0.01	0.00	0.19	*	*	0.15-0.30
Vanadium (%)	0.01	0.06	0.11	*	*	0.10-0.20

* = Not specified

All the materials are low alloy steels, with 54SiCr6 containing approximately 1.33% silicon, 55Cr3 containing 0.32% silicon, and 52CrMoV4 containing 0.28% silicon. The chromium in 55Cr3 was significantly higher compared to 54SiCr6, while the silicon was higher in 54SiCr6. On the other hand, 52CrMoV4 contains a significant percentage of chromium and molybdenum compared to 55Cr3 and 54SiCr6.

4.3.2 Continuous cooling transformation curves

The CCT curves of the three steel grades were simulated using JmatPro software by inserting the chemical composition of each steel grade shown in Figure 4.34 into the simulation software. The CCT curve was used to predict the heat treatment temperatures and cooling rates of the various steels and oils used in this research. According to Andrew's equation (Atkins, 1980), the Ms temperature of 55Cr3, 54SiCr6, and 52CrMoV4 would be 253.3°C, 271.3°C, and 265.6°C, respectively. The CCT diagrams for the three steel grades are presented in Figure 4.34 and assisted in selecting suitable quenching oil in the next section.

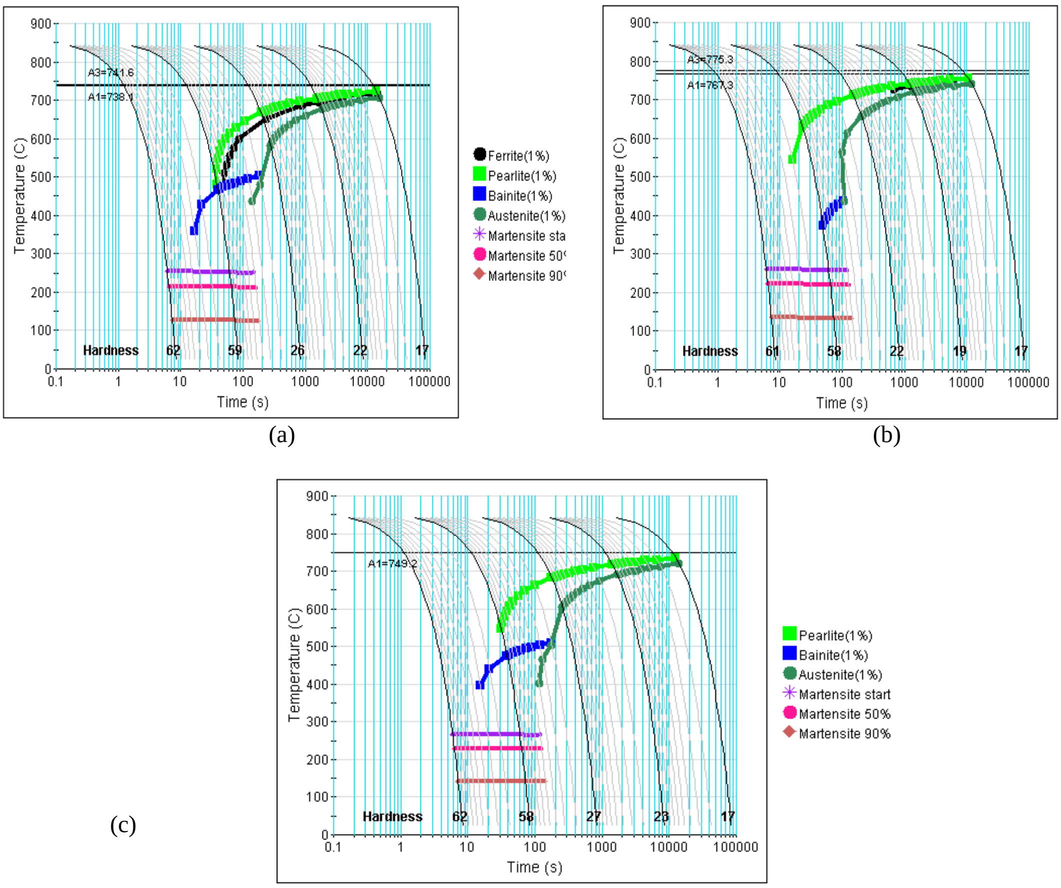

Figure 4.34 CCT curves generated using JMatPro of (a) 55Cr3, (b) 54SiCr6, and (c) 52CrMoV4.

4.3.3 Quenchant analysis

This section of the results presents the characteristics and properties of the selected quenchants. The three steels were quenched with various oils due to their different hardenability. The oils were labelled Oil A and Oil B to avoid mentioning brand names and were analysed to determine the cooling rates. Table 4.17 summarises the quenchants properties and Table 4.18 shows the characteristics of the selected oils.

Table 4.17 Quenching media properties.

Properties	**Oil A**	**Oil B**
Appearance	Liquid	Liquid
Fire point (°C)	270	220
Flash point (°C)	235	204
Density (g/cm^3)	0.884	0.854
Pour point (°C)	-12	-15
Viscosity (mm^2/s at 40 °C)	62	20

Table 4.18 Quench test results.

Properties	**Oil A**	**Oil B**	**Unit**
Maximum cooling rate	40.09	61.63	°C/s
Temperature at maximum cooling rate	548.00	526.02	°C
Temperature at start of boiling	603.00	619.94	°C
Temperature at start of convection	360.00	331.99	°C
Cooling rate at 300°C	6.22	7.27	°C/s
Time to 600°C	9.89	10.96	s
Time to 400°C	22.98	15.79	s
Time to 300°C	48.23	41.27	s
Time to 200°C	60.18	49.83	s
Theta 1	563.45	616.25	°C
Theta 2	299.28	398.63	°C

Oil A illustrated slower cooling rates that are able to harden 54SiCr6 without causing quench cracks but is unable to sufficiently harden 55Cr3 and 52CrMoV4. The characteristics of Oil A were predicted to be suitable for achieving the desired microstructure, i.e. martensite, and mechanical properties to produce springs from 54SiCr6 steel. On the other hand, Oil B showed more desirable characteristics to produce springs out of 55Cr3 and 52CrMoV4 steel. The graphs displaying the cooling rates and convection curves are presented in Figures 4.35 and 4.36. Martensite is achieved at cooling temperatures below 300°C for all three steels.

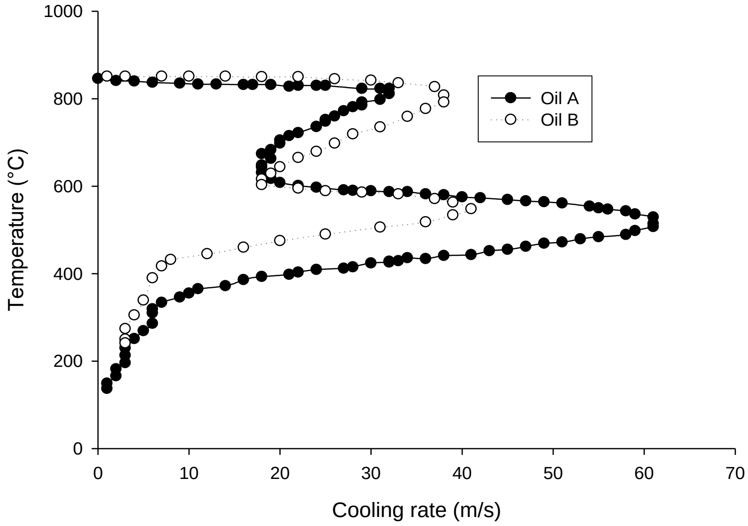

Figure 4.35 Quenching media cooling rate plots.

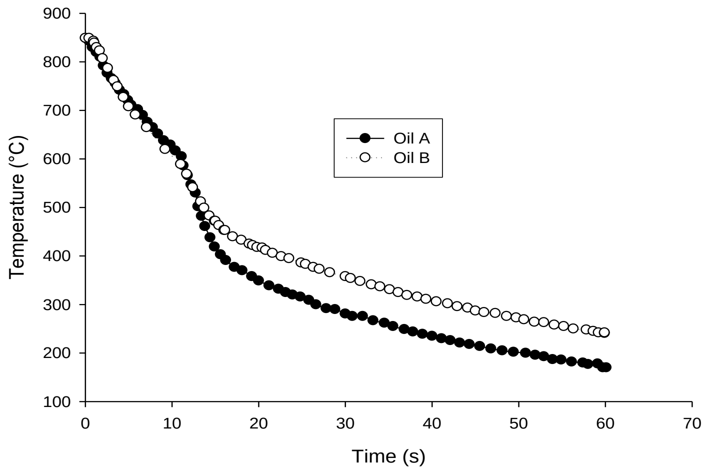

Figure 4.36 Quenching media convection curves.

4.3.4 Thermal analysis

The DSC measurements shown in Figure 4.37 indicate three curves that have an endothermic and exothermic peak, representing the eutectoid temperatures of the three samples.

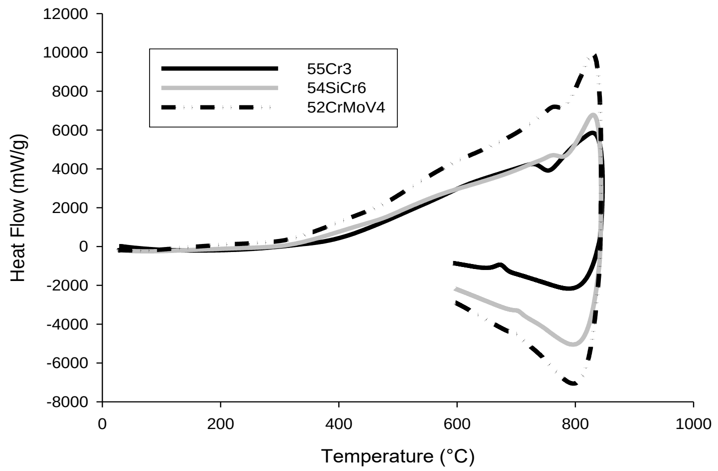

Figure 4.37 Heat flow vs temperature plots.

The heating and cooling peak information is summarised in Table 4.19. The steels showed distinct thermal properties with 55Cr3 requiring a lower heat flow than 54SiCr6 and 52CrMoV4. In addition, the eutectoid temperature of 55Cr3 was lower compared to 54SiCr6 and 52CrMoV4.

Table 4.19 Endothermic and exothermic reaction details.

Samples	**Heating**			**Cooling**		
	Time (min)	**Eutectoid temperature (°C)**	**Heat flow (mW/g)**	**Time (min)**	**Eutectoid temperature (°C)**	**Heat flow (mW/g)**
55Cr3	6.18	729.58	4246	11.98	689.23	1297
54SiCr6	7.70	761.82	4702	12.65	713.93	3566
52CrMoV4	7.76	766.08	7201	12.81	709.67	4769

Figure 4.38 presents the required heat flow over time. The trends of the graphs show that 52CrMoV4 requires a significantly higher heat flow to achieve the eutectoid temperature at approximately the same time as 55Cr3 and 54SiCr6.

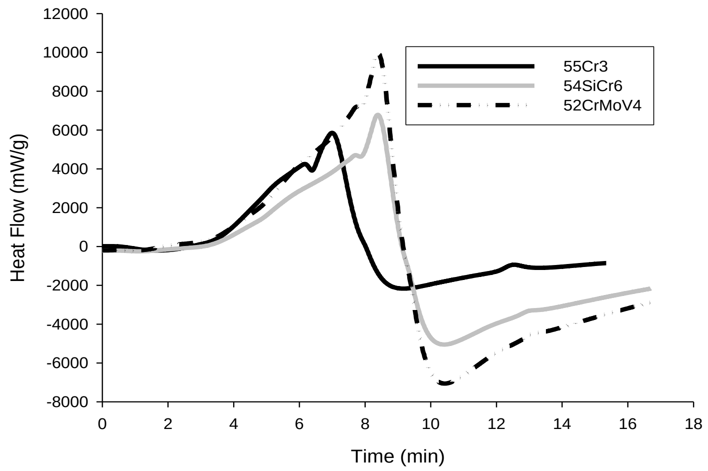

Figure 4.38 Heat flow vs time plots.

Figure 4.39 shows the behaviour of the three materials during heating while purging them with argon, followed by isothermal treatment for one hour under atmospheric conditions. The graph for 52CrMoV4 fell between those of 55Cr3 and 54SiCr6.

Table 4.20 shows the sample weight before analysis and after heating and atmospheric exposure. Figure 4.40 shows the weight gain due to heating and atmospheric exposure.

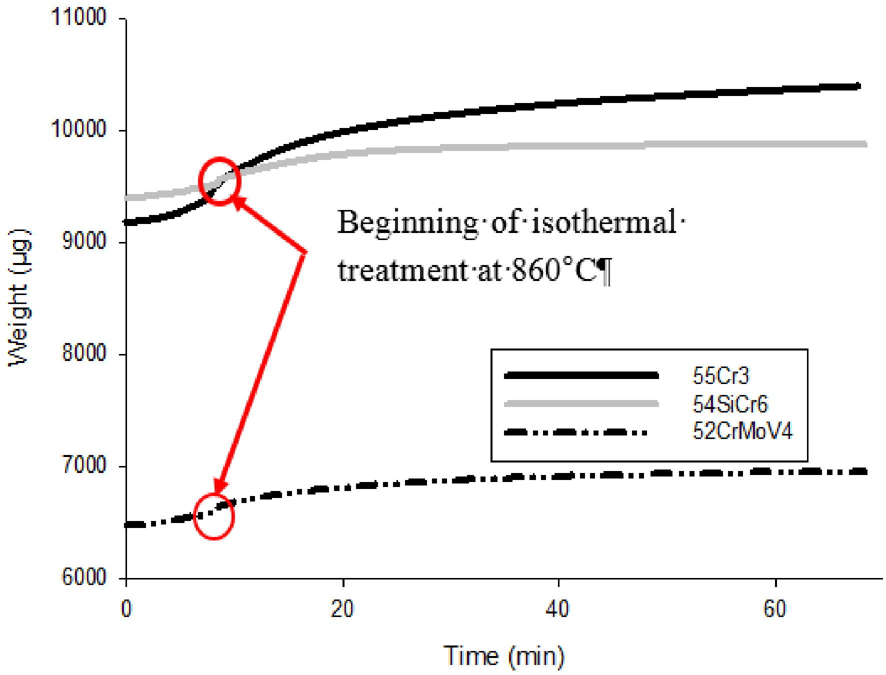

Figure 4.39 Oxidation in weight percentage vs temperature.

Table 4.20 Oxidation characteristics.

Samples	Initial weight (µg)	Final weight (µg)	Oxidation (%)	Oxidation rate (µg/min)
A	9178	10384	11.6	131587
B	9393	9794	4.1	18054
C	6465	6954	7.0	28154

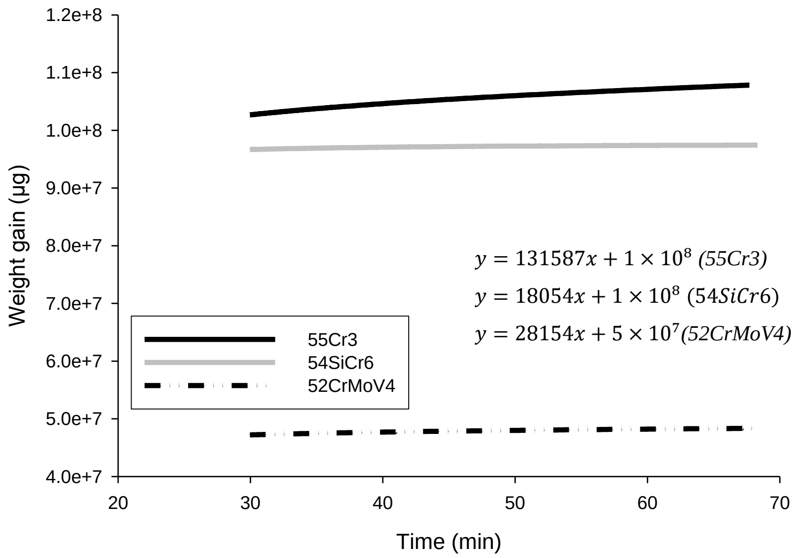

Figure 4.40 Oxidation rate at 860°C.

The oxidation rates were determined by plotting the gradient once the graph stabilised. 55Cr3 showed higher oxidation rates, while 54SiCr6 was more resistant to oxidation. Despite the slightly smaller weight, the oxidation rate of 52CrMoV4 is less than 55Cr3 but higher than 54SiCr6.

4.3.5 Critical transformation temperatures

Dilatometric and DSC testing were conducted to establish the exact phase transition temperatures for the purpose of process optimisation. Figure 4.41a and 4.41b show the dilation characteristics of the three steels.

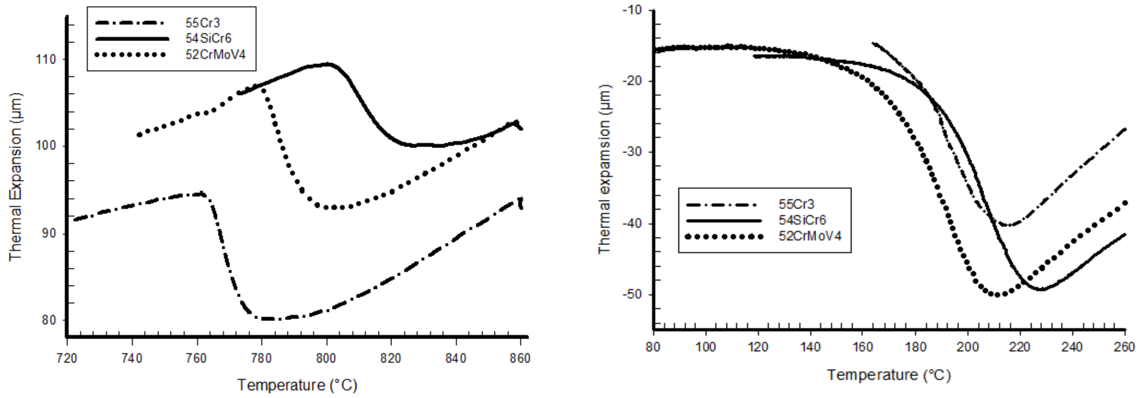

(a) (b)

Figure 4.41 Critical transformation temperatures for the three steels: (a) Ac1 and Ac3 and (b) Ms temperature.

The dilation was determined by evaluating the thermal expansion against the temperature, while the DSC relied on the heat flow. The measured critical transformation temperatures are presented in Table 4.21.

Table 4.21 Critical transformation temperatures.

Identity	**Andrew's equation**			**Dilatometer**			**DSC**		**JMatPro**		
Transition temperature	Ac_1	Ac_3	Ms	Ac_1	Ac_3	Ms	Ac_1	Ms	Ac_1	Ac_3	Ms
55Cr3	726	740	255	753	818	218	751	225	738	741	253
54SiCr6	759	945	271	793	846	235	777	235	767	775	260
52CrMoV4	727	909	264	772	823	216	762	227	749	750	266

The DSC measurements verified the dilatometer results. The actual thermal test measurements were compared to the JMatPro estimations and Andrew's equation results and it was found that there was no unanimity between them. The optimisation of the heat treatment parameters is largely dependent on the Ac1, Ac3, and Ms temperature. A higher Ac1 means a longer cooling time.

It is evident from the results that a general approach would be ineffective to optimise the heat treatment parameters for the three steel grades. According to the dilation results, 55Cr3 would require the least amount of time to start forming martensite, followed by 52CrMoV4. It is worth noting that 54SiCr6 is the most hardenable due to a higher Ms temperature. The austenite critical transformation temperature for 54SiCr6 is higher compared to 55Cr3 and 52CrMoV4, however, it takes less time for austenite to stabilise.

The rule of thumb is that for complete austenitisation, the length of time required for steel to be homogeneous is one hour for a 25 mm diameter (Manuel and Cerda, 2017). Carbon and other alloying elements require time to be completely in solution (Avner, 1998). It can be observed from Figure 4.42 that there is a change in the length of the different steels during isothermal treatment at 860°C.

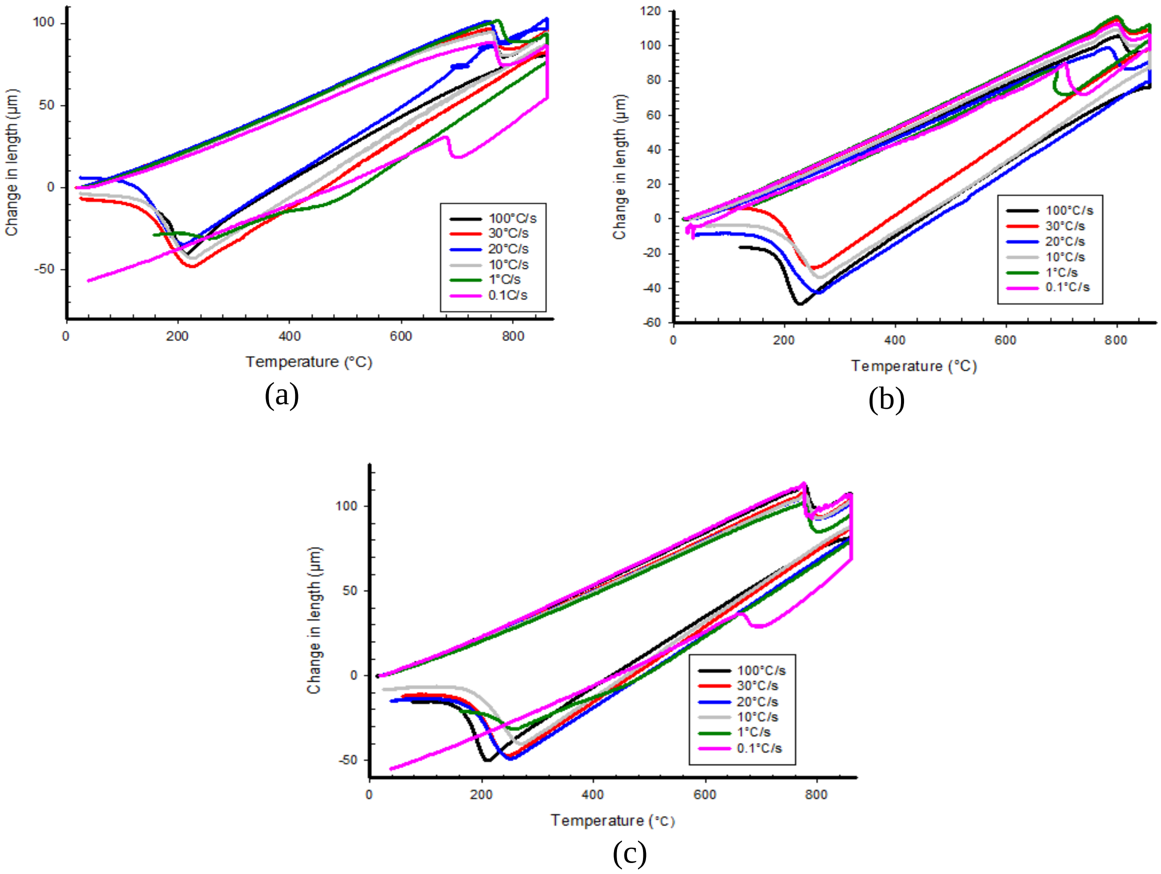

Figure 4.42 Dilatometric graphs of (a) 55Cr3, (b) 54SiCr6, and (c) 52CrMoV4 at various cooling rates.

The change in length can be describe as phase transformation from a BCC phase to a smaller FCC phase. This change in length stabilises over time, however, the rate of stabilisation varies from one steel to another. Figure 4.43 shows that the thermal expansion of 54SiCr6 stabilised approximately 30 minutes after soaking, while 52CrMoV4 did not stabilise after 45 minutes of soaking. This proves that complete austenitisation does not only depend on time but also on composition. Therefore, the Ac1 and Ac3 temperatures and the austenite stabilisation time are to be carefully considered during the heat treatment optimisation process. Figure 4.44 shows the martensite start for each grade of spring steel at various cooling rates.

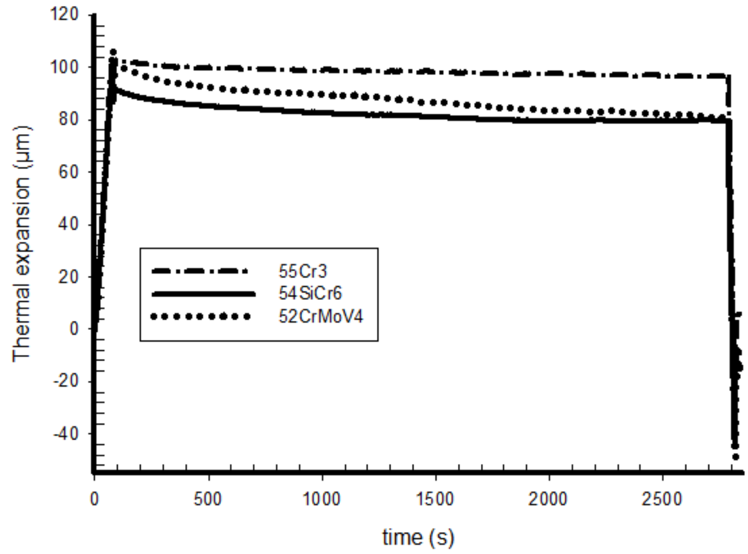

Figure 4.43 Thermal expansion rates for the three spring steel grades.

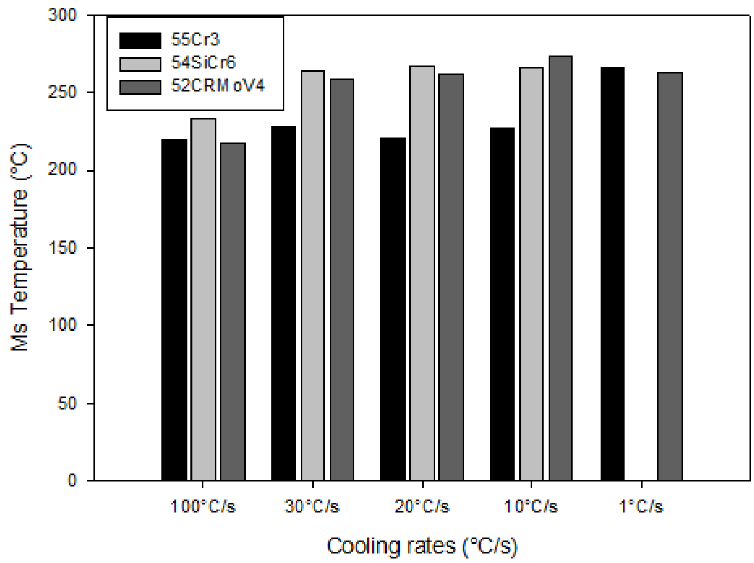

Figure 4.44 Effect of cooling rates on Ms temperature.

4.3.6 The effect of normalisation on stress relaxation

Deformation and stress relaxation of steels are important functions of spring manufacturing. Springs are coiled to a precise pitch angle and the spring steel stress relaxation behaviour may alter the pitch angle during cooling, which may result in deficient springs. The true stress-true strain behaviour of the three steels was determined at 860°C, as shown in Figure 4.45.

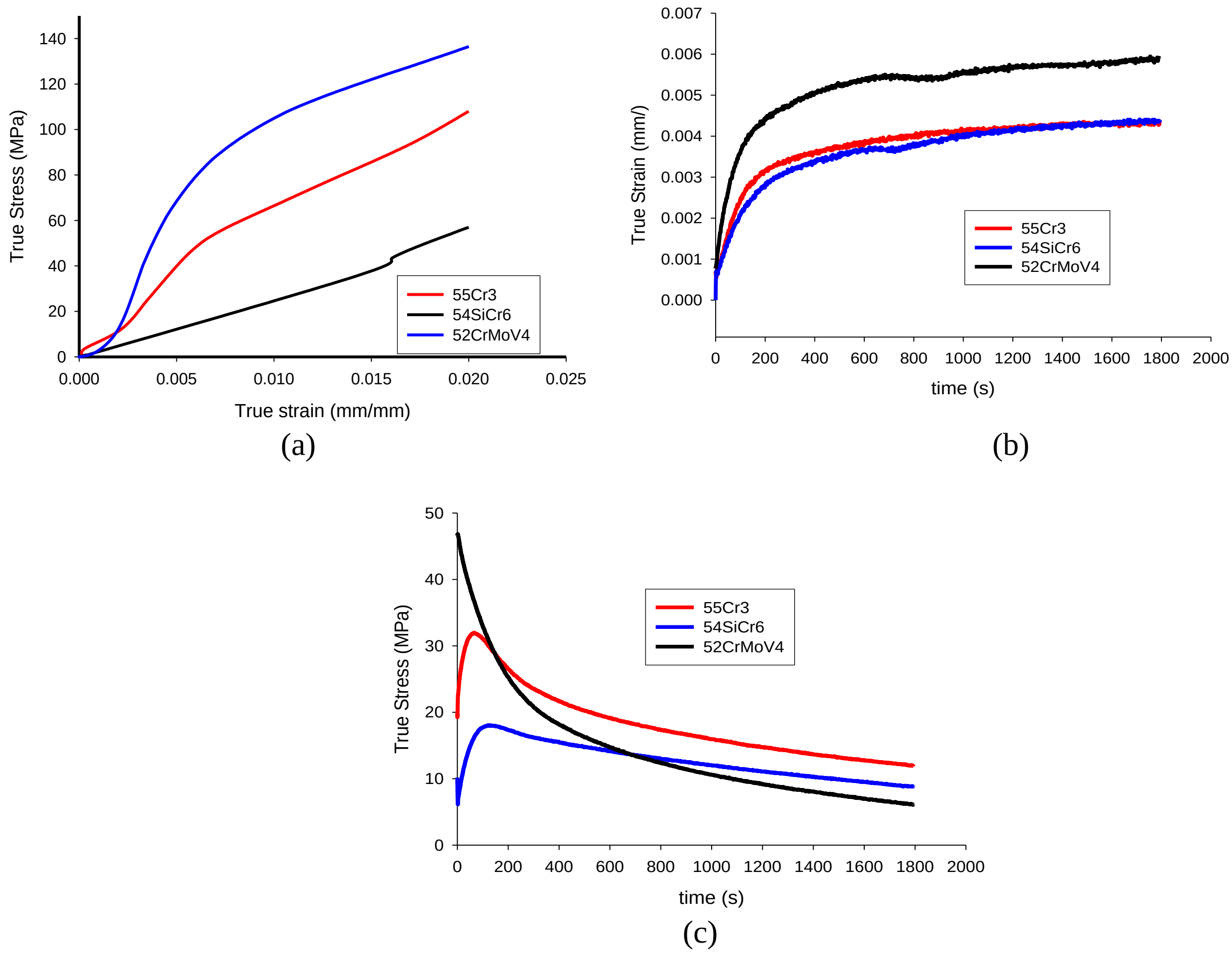

Figure 4.45 Deformation behaviour: (a) True stress-true strain curve, (b) air-cooled relaxation behaviour, and (c) stress behaviour during cooling.

52CrMoV4 required higher deformation force, while 54SiCr6 required the least amount of force to deform.

Figure 4.45a and b show that 55Cr3 and 54SiCr6 yielded within the earlier stages of normalisation cooling, while 52CrMoV4 resembled gradual reduction of thermal expansion related force. The relaxation abilities of the three steels can be observed in Figure 4.45c. The 55Cr3 and 54SiCr6 strain ability were comparable, while 52CrMoV4 has proven to strain more. This information becomes particularly important for the spring coiling and cooling stage optimisation.

4.3.7 The effect of rapid cooling on stress relaxation

The three steels were deformed and rapidly quenched to achieve martensitic transformation. Figure 4.46a illustrates that the stress relaxation and phase transformation was completed within 20 seconds. The cooling characteristics of the quenching media used for the steel grades are presented in Figure 4.46b.

Stress relaxation was found to be minimal when the steels were quenched rapidly. Figure 4.46b also shows that the strain is approximately zero after oil quenching. This proves that rapid cooling will result in minimal or no geometrical change of the coiled springs.

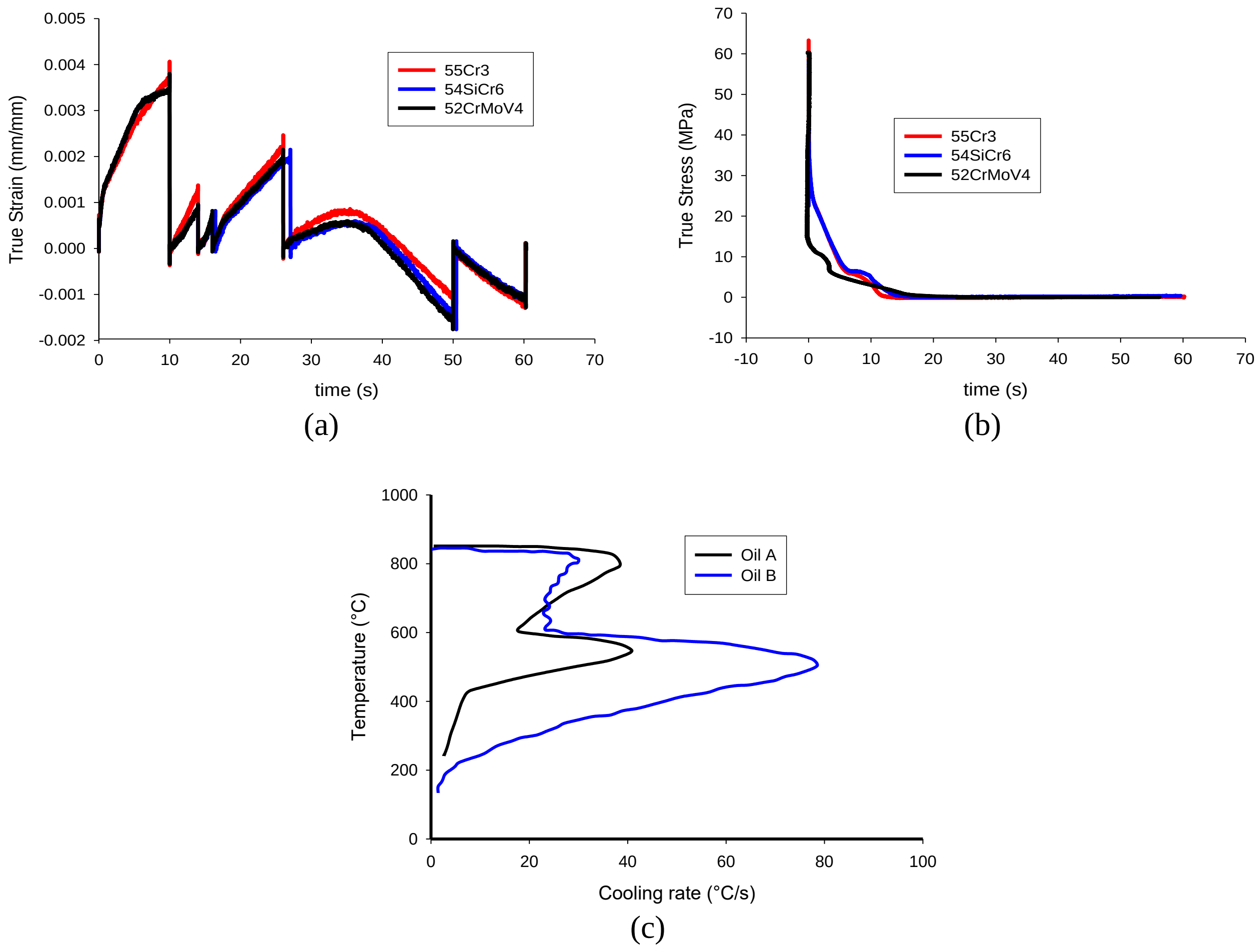

Figure 4.46 Relationship behaviour during quenching: (a) relaxation during quenching, (b) stress behaviour during quenching, and (c) quenching media cooling rates.

4.3.8 Metallographic examination

Microscopic examinations were done to evaluate the microstructure of the three heat treated materials and measure the effect of the various heat treatment experiments. The as-etched samples were examined using a light metallurgical microscope. The first part of the metallographic examination covers the microstructures of the raw steel rods received from the steel mill. The general microstructure of the steel rods was that of a pearlitic nature as shown Figure 4.47. 55Cr3 revealed a coarser grain structure compared to 54SiCr6 and 52CrMoV4.

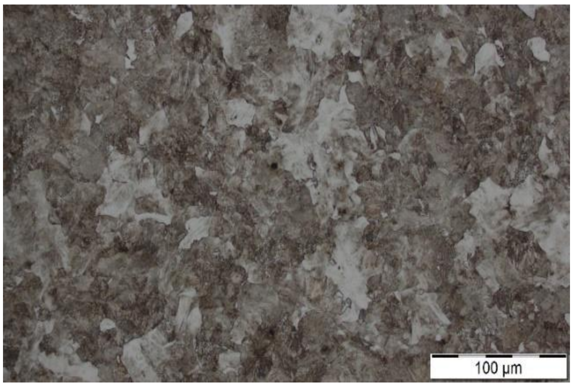

(a)

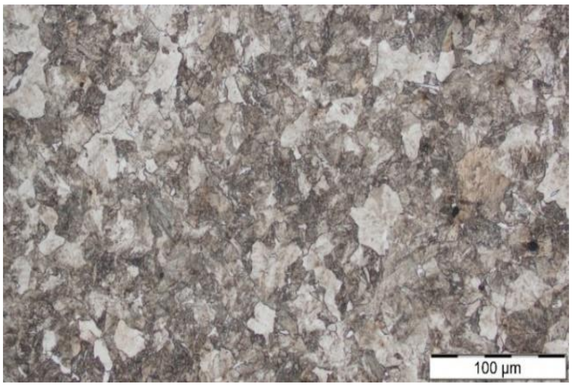

(b)

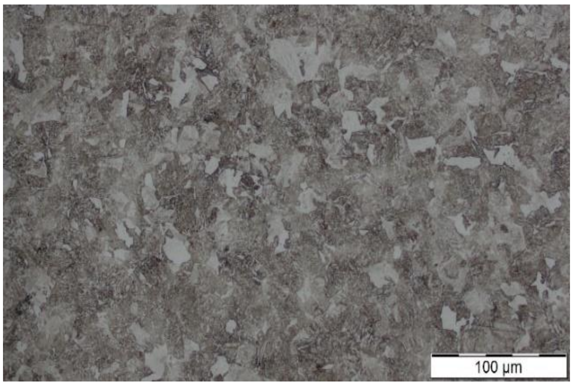

(c)

Figure 4.47 The microstructures of the non-heat treated steel rods: (a) 55Cr3, (b) 54SiCr6, and (c) 52CrMoV4.

4.3.9 The effect of cooling rates on phase transformation

The thermal dilatometric treatment microstructures are presented in Figures 4.48 to 4.50. These microstructures were achieved by varying the cooling rates. The overall microstructure for the cooling rate of 20°C per second to 100°C per second for the three steels was martensite. The micrographs of 55Cr3 and 52CrMoV4, with a 10°C per second cooling rate, presented mainly martensite and bainite microstructures. The bainite microstructure shown in Figure 4.48d was coarser compared to that observed in Figure 4.50d, showing the negligible presence of the bainite microstructure. Figure 4.48e and Figure 4.50e indicated a significant percentage of bainite and martensite present, while Figure 4.49e had a pearlitic microstructure with a presence of pro-eutectoid ferrite. The percentage of bainite in Figure 4.48e was approximately equal to that of martensite, while martensite constituted a larger fraction in Figure 4.50e. Figure 4.48f showed pearlitic structures, while Figure 4.49f and Figure 4.50f were pearlitic with proeutectoid ferrite. The details of the microstructures were confirmed with a SEM. The SEM images are presented in Appendix A.

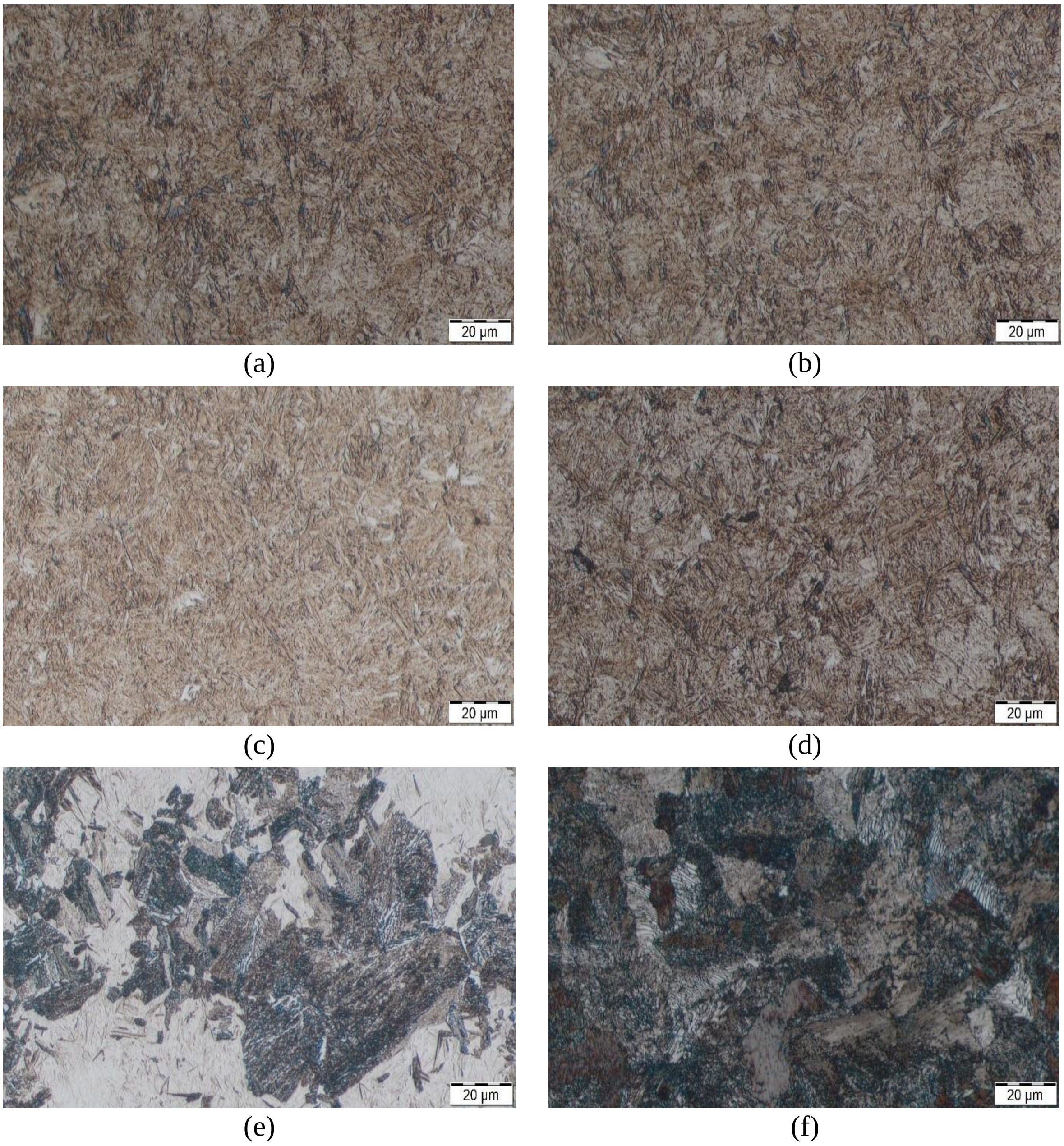

Figure 4.48 The optical micrographs of 55Cr3 cooled at (a) 100°C/s, (b) 30°C/s, (c) 20°C/s, (d) 10°C/s, (e) 1°C/s, and (f) 0.1°C/s.

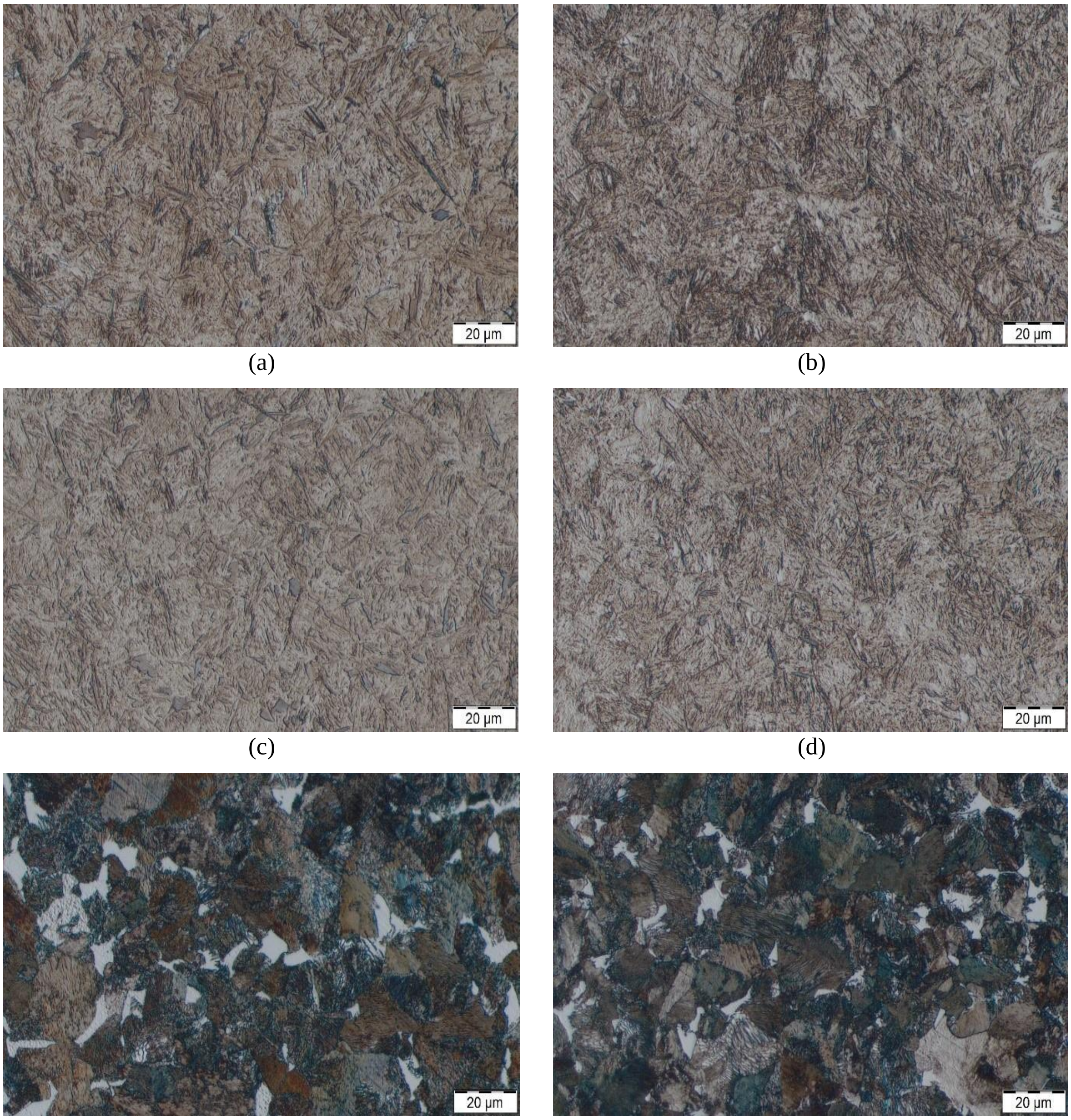

(a) (b)

(c) (d)

(e) (f)

Figure 4.49 The optical micrographs of 54SiCr6 cooled at (a) 100°C/s, (b) 30°C/s, (c) 20°C/s, (d) 10°C/s, (e) 1°C/s, and (f) 0.1°C/s.

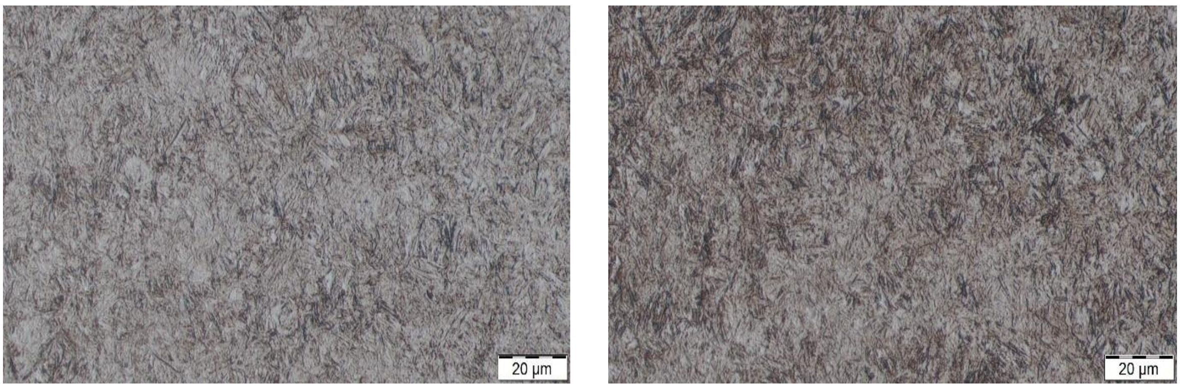

(a) (b)

(c) (d)

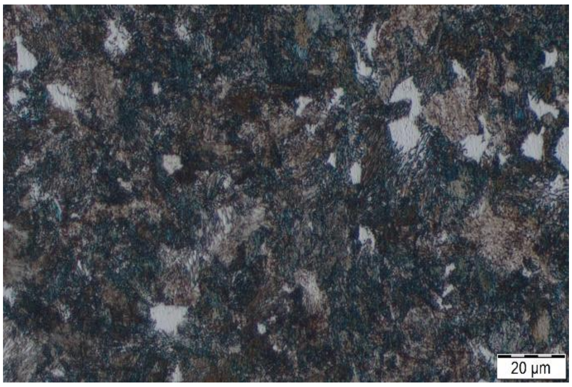

(e) (f)

Figure 4.50 The optical micrographs of 52CrMoV4 cooled at (a) 100°C/s, (b) 30°C/s, (c) 20°C/s, (d) 10°C/s, (e) 1°C/s, and (f) 0.1°C/s.

4.3.10 Characterisation of surface microstructural properties

The general microstructures of the three steels were heat treated in order to validate the oxidation results that were performed using the DSC and are presented in Figure 4.51. The tempered martensite with a degree of decarburisation at the edges can be observed in Figure 4.51a, 4.51b, and 4.51c. Decarburisation occurred on all three samples but mostly on 54SiCr6. However, 55Cr3 and 52CrMoV4 showed similar microstructures, which is indicative of a lower extent of decarburisation. This observation showed that there is a relationship between oxidation and decarburisation.

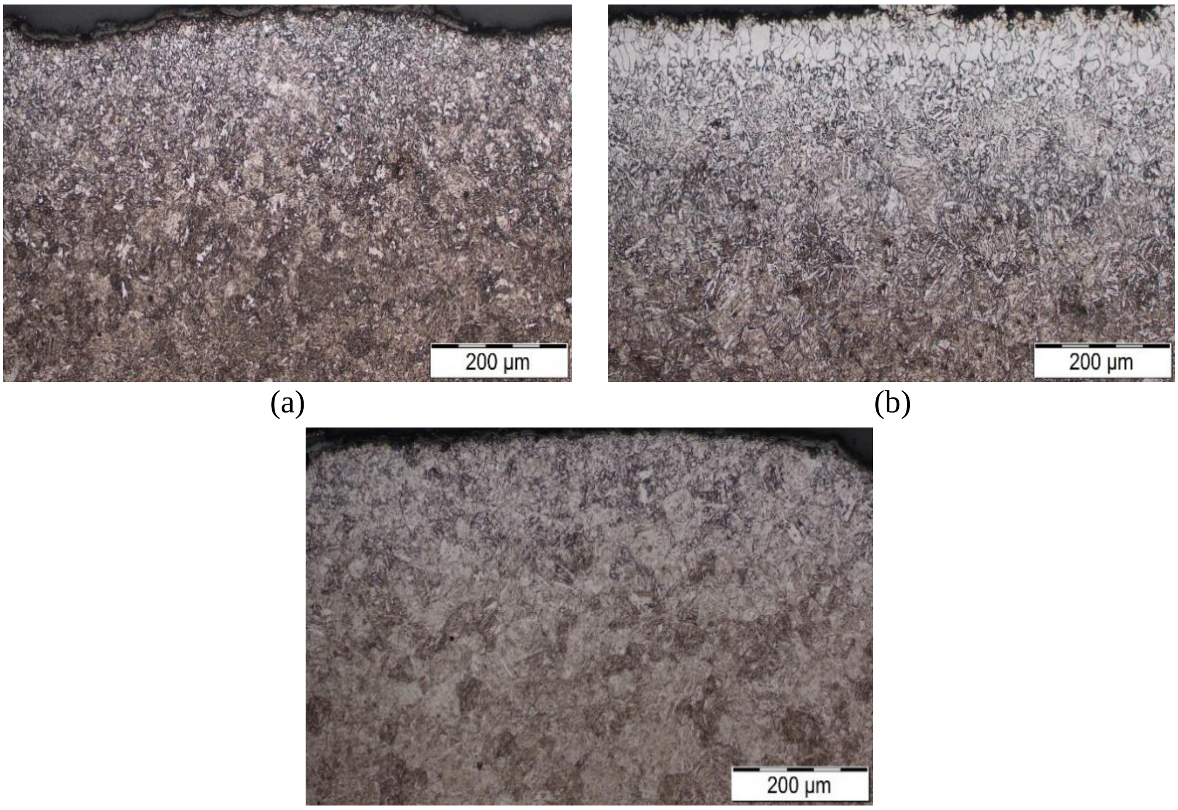

(a) (b)

(c)

Figure 4.51 The microstructures of (a) 55Cr3, (b) 54SiCr6, and (c) 52CrMoV4.

4.3.11 The effect of quenching oil on the microstructures of the three steel grades

This section of the metallographic examination covers the as-quenched microstructures, which are presented in Figure 4.52. All three microstructures predominately consist of martensite lath morphology with a smaller fraction of other phases, which are identified and quantified in the XRD section. The structure of 55Cr3 featured finer lath compared to the structures of 54SiCr6 and 52CrMoV4. The as-quenched microstructure XRD spectrums of the three materials are shown in Figure 4.53 to 4.55, while the phase analysis is presented in Table 4.22.

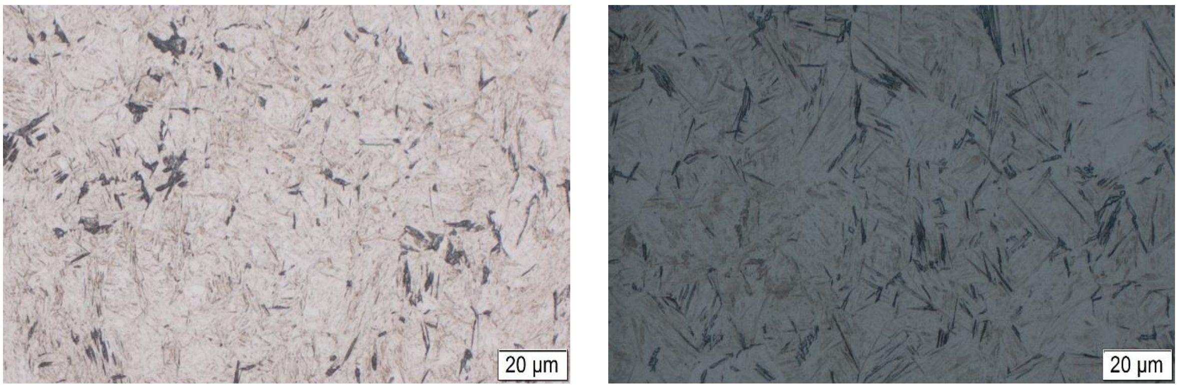

(a) (b)

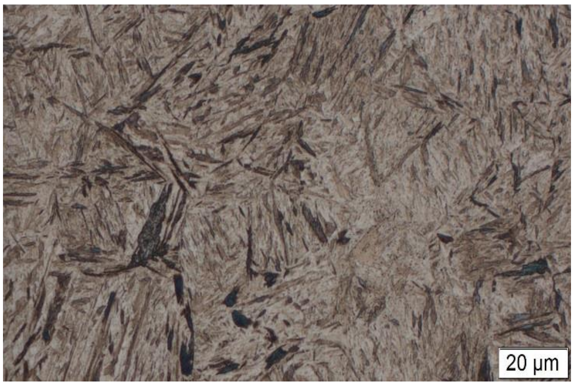

(c)

Figure 4.52 The as-quenched microstructure of (a) 55Cr3, (b) 54SiCr6, and (c) 52CrMoV4.

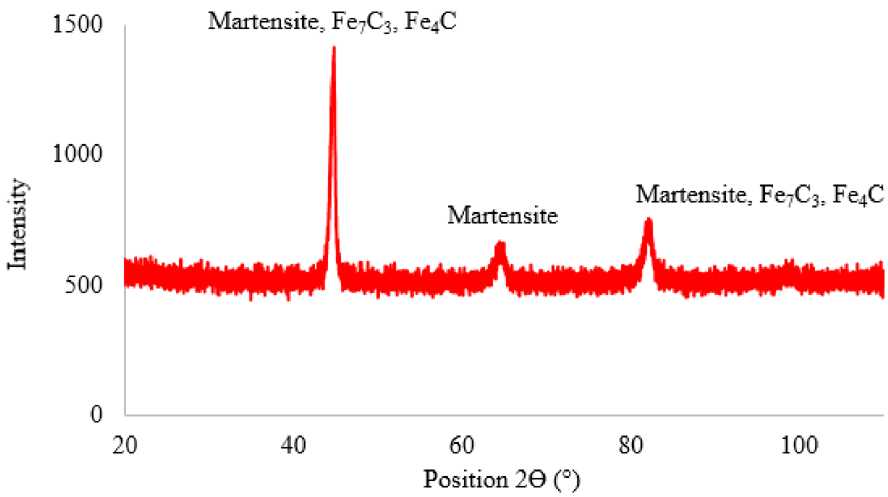

Figure 4.53 XRD spectrums of 55Cr3.

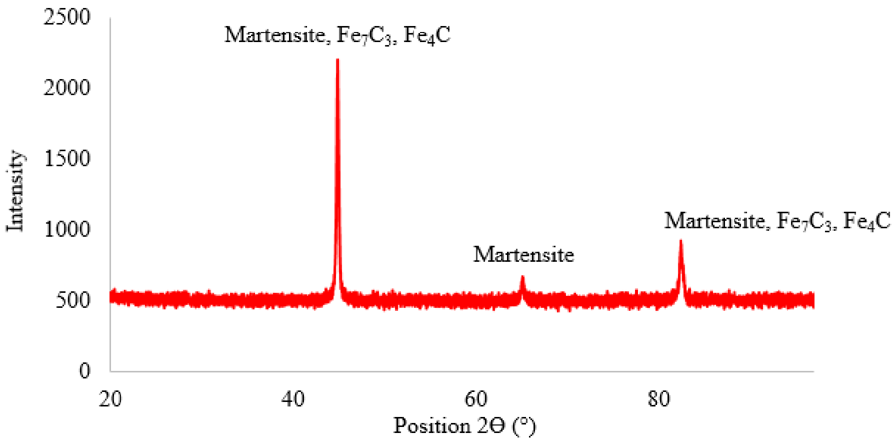

Figure 4.54 XRD spectrums of 54SiCr6.

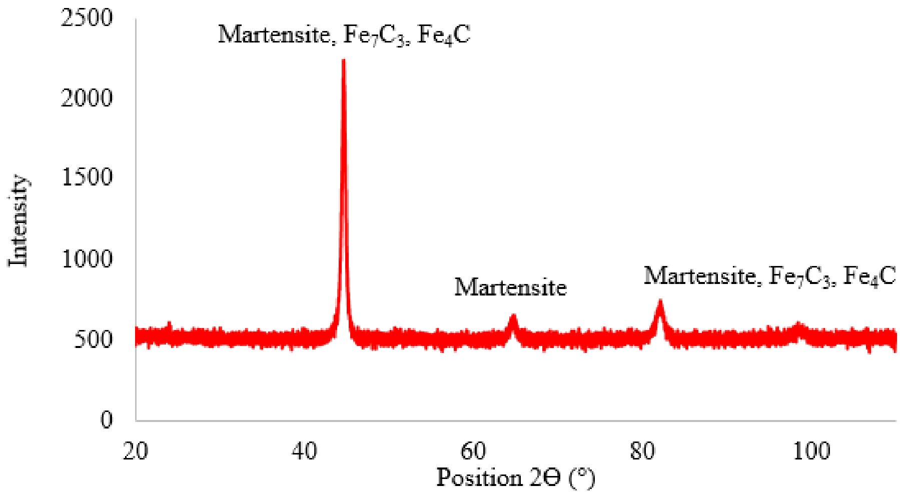

Figure 4.55 XRD spectrums of 52CrMoV4.

Table 4.22 The as-quenched phase analysis.

Phases	Tetragonal	Hexagonal	Cubic
55Cr3	$C_{0.12}Fe_{1.88}$ (87%)	Fe_7C_3 (7%)	Fe_4C (6%)
54SiCr6	$C_{0.12}Fe_{1.88}$ (92%)	Fe_7C_3 (5%)	Fe_4C (3%)
52CrMoV4	$C_{0.12}Fe_{1.88}$ (84%)	Fe_7C_3 (11%)	Fe_4C (5%)

4.3.12 The effect of tempering temperature and soaking time on the microstructures of the three steels

This section of the metallographic examination covers the tempered microstructures of the three steels at various temperatures and soaking times. Figure 4.56 presents the microstructures of the steels tempered at 410°C for two hours. The general microstructure of the steels was tempered martensite, however, 55Cr3 and 52SiCr6 had features of untempered martensite lath visible, while 52CrMoV4 had a fully tempered microstructure.

(a)

(b)

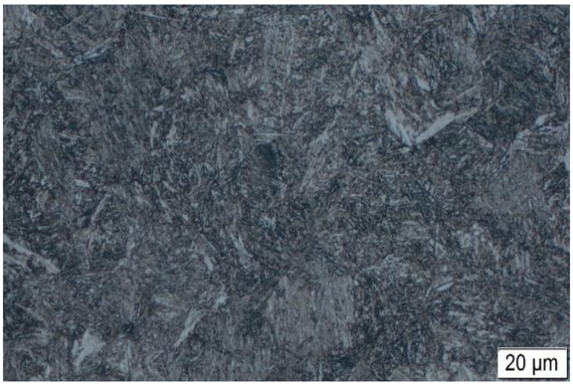

(c)

Figure 4.56 (a) 55Cr3, (b) 54SiCr6, and (c) 52CrMoV4 tempered at 410°C for two hours.

Figure 4.57 shows the microstructures of the three steels tempered at 410°C for three hours. The general microstructure of the steels was fully tempered martensite. The rod-like shaped iron carbides were shorter and finer in 55Cr3 than 54SiCr6 and 52CrMoV4.

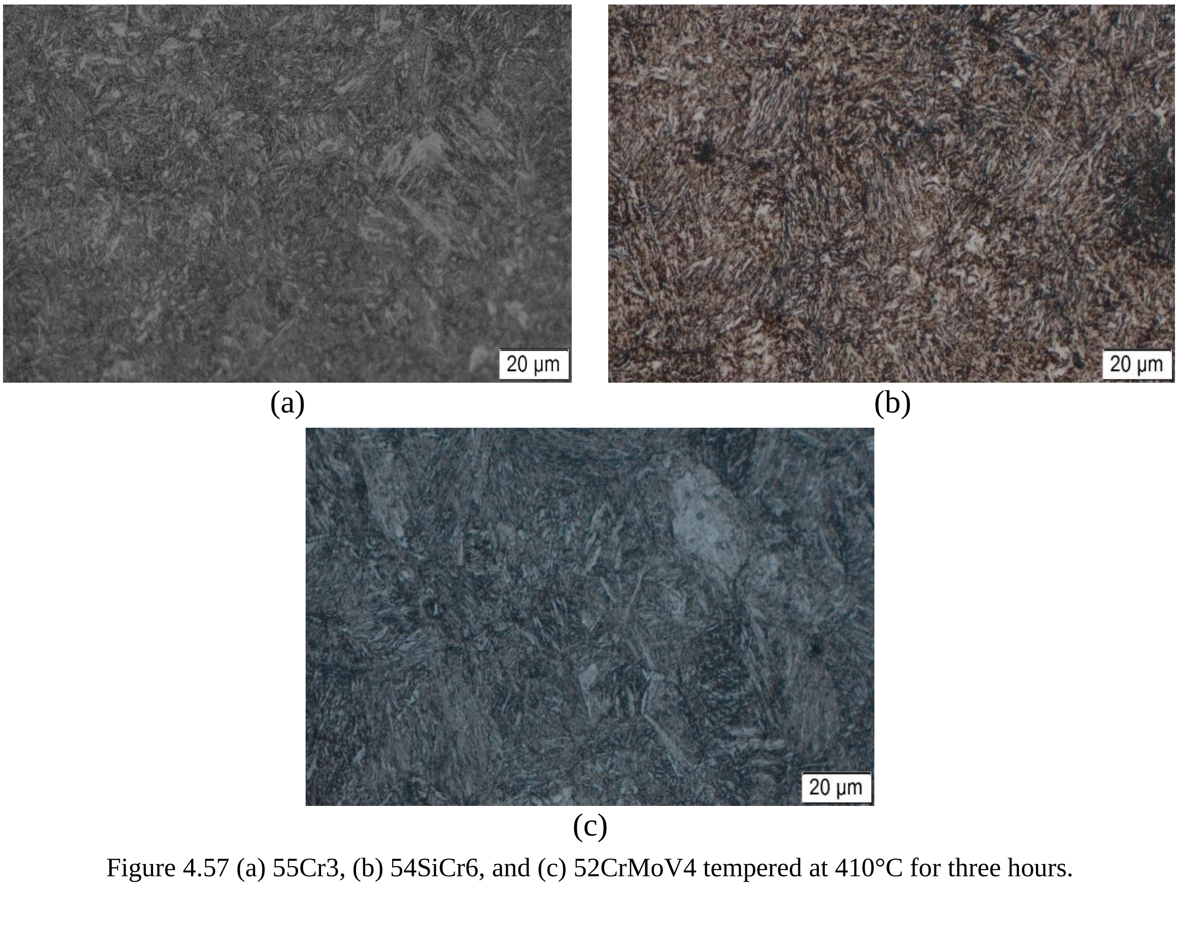

(a) (b)

(c)

Figure 4.57 (a) 55Cr3, (b) 54SiCr6, and (c) 52CrMoV4 tempered at 410°C for three hours.

Figure 4.58 shows the microstructures of the three steels tempered at 450°C for two hours. The general microstructure of the steels was tempered martensite. However, 54SiCr6 and 52CrMoV4 revealed coarser iron carbides than 55Cr3.

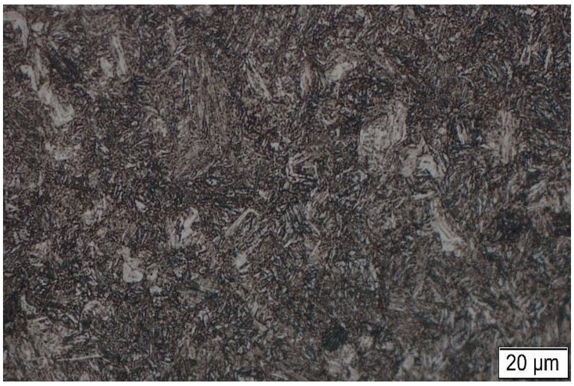

(a)

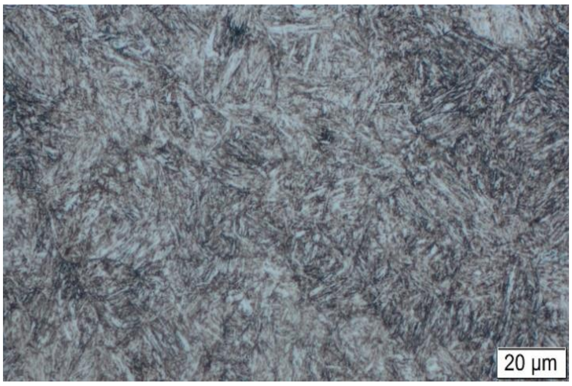

(b)

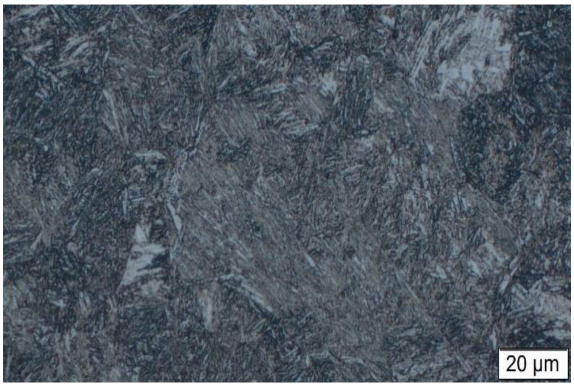

(c)

Figure 4.58 (a) 55Cr3, (b) 54SiCr6, and (c) 52CrMoV4 tempered at 450°C for two hours.

Figure 4.59 presents the microstructures of the three steels tempered at 450°C for three hours. The microstructure of the steels was tempered martensite. 55Cr3 revealed finer iron carbide needles than 54SiCr6 and 52CrMoV4.

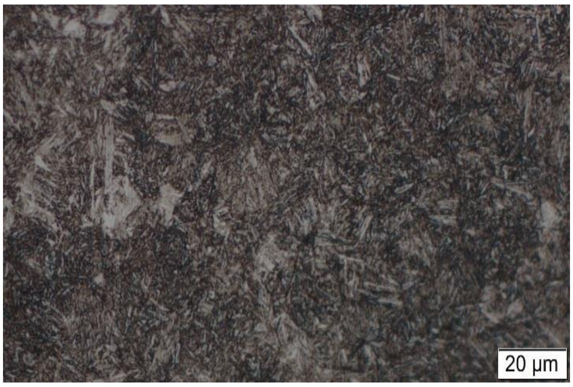

(a)

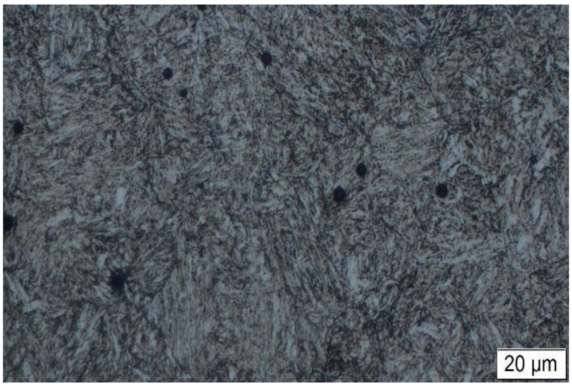

(b)

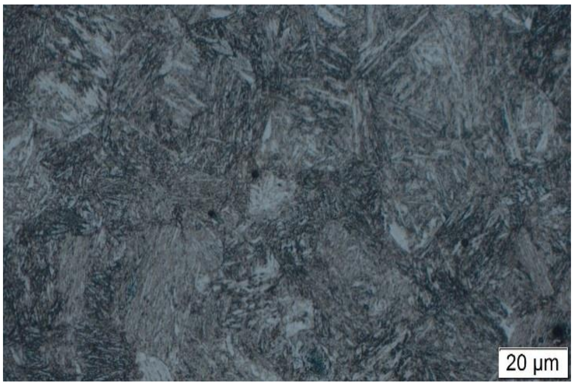

(c)

Figure 4.59 (a) 55Cr3, (b) 54SiCr6, and (c) 52CrMoV4 tempered at 450°C for three hours.

Figure 4.60 presents the microstructures of the three steels tempered at 470°C for two hours. The general microstructure of the steels was tempered martensite. 55Cr3 showed finer iron carbides compared to 54SiCr6 and 52CrMoV4.

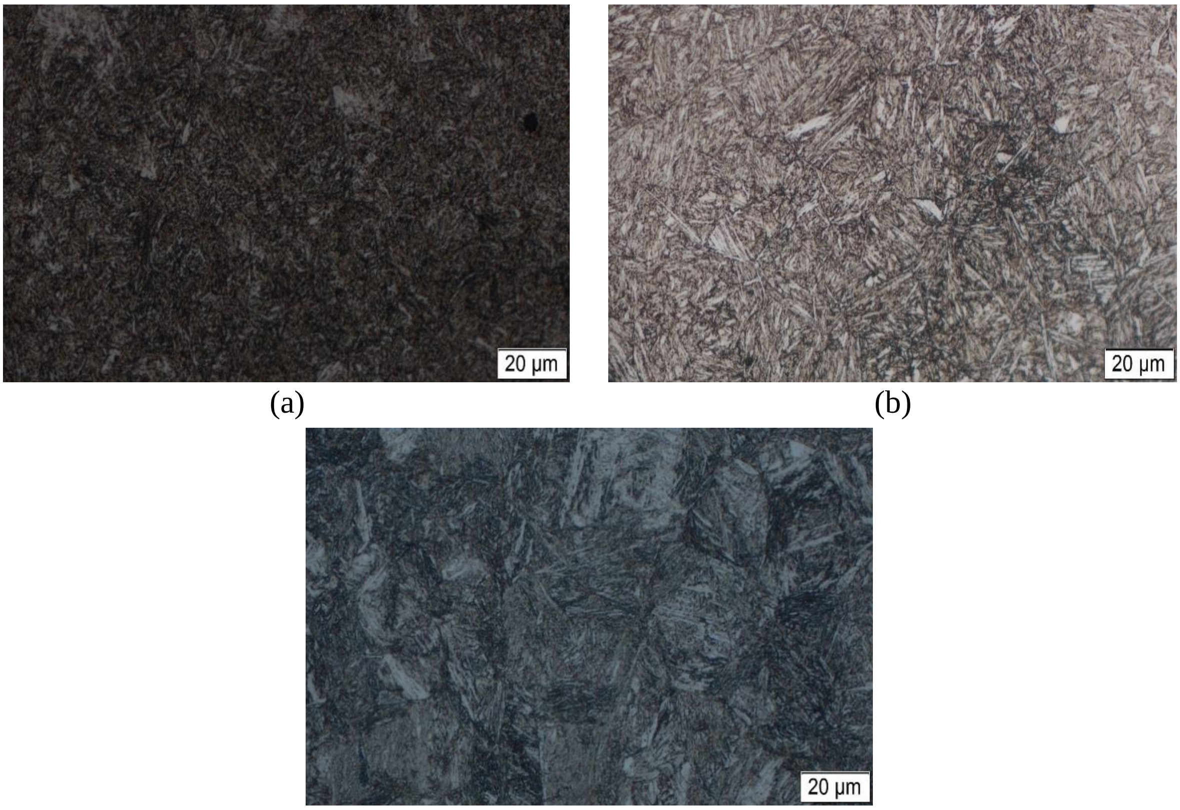

(c)

Figure 4.60 (a) 55Cr3, (b) 54SiCr6, and (c) 52CrMoV4 tempered at 470°C for two hours.

Figure 4.61 presents the microstructures of the three steels tempered at 470°C for three hours. The general microstructure of the steels was tempered martensite. The ferrite structure was more pronounced in all three materials.

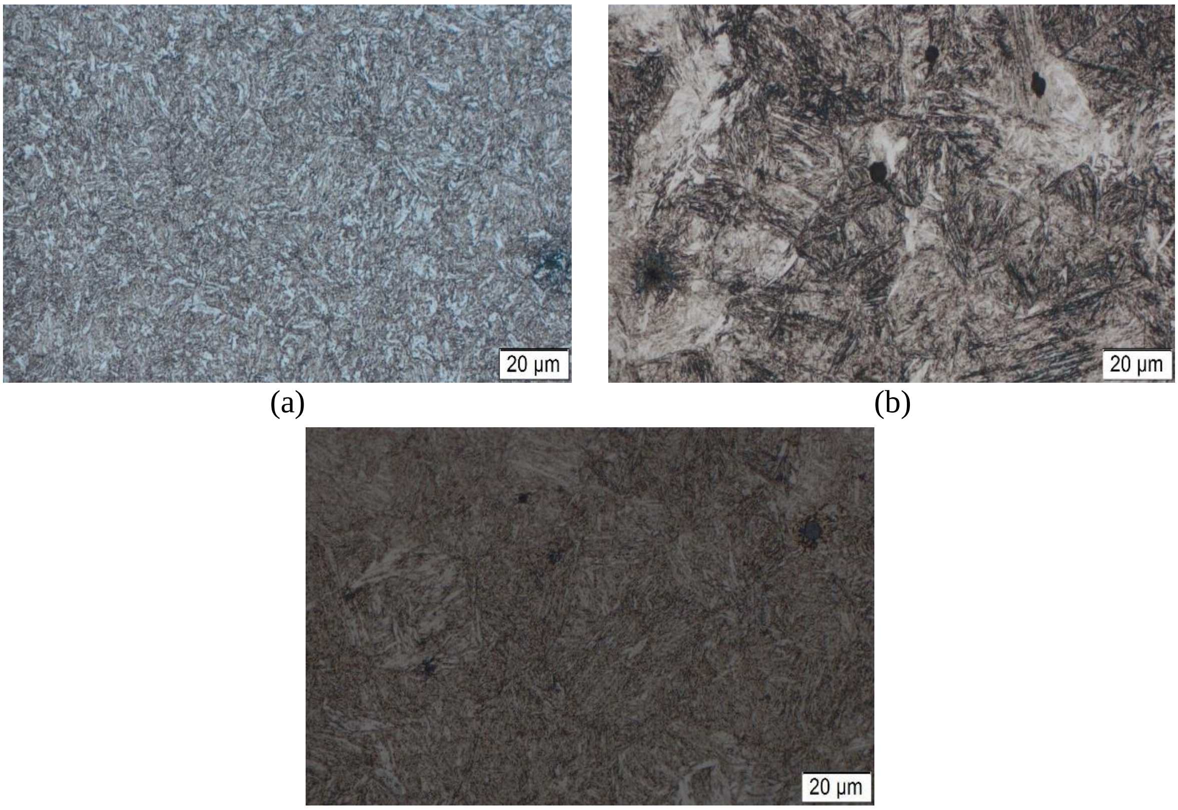

Figure 4.61 (a) 55Cr3, (b) 54SiCr6, and (c) 52CrMoV4 tempered at 470°C for three hours.

The microstructures were further characterised by the SEM at higher magnification to evaluate the details of the structures. The general microstructure was that of tempered martensite. All the materials showed that with the increase in tempering temperature and soaking time, there was a disappearance of martensite lath boundaries and an increase in ferrite. The SEM images of 55Cr3, 54SiCr6, and 52CrMoV4 are presented in Figure 4.62 to 4.64.

4.3.12.1 55Cr3 Steel

55Cr3 showed that the steel tempered for two hours revealed alternating rod-like carbides, while the steel tempered for three hours revealed some sort of periodisation of the iron carbides. From 450°C, the microstructure started to reveal carbide precipitates on the martensite lath.

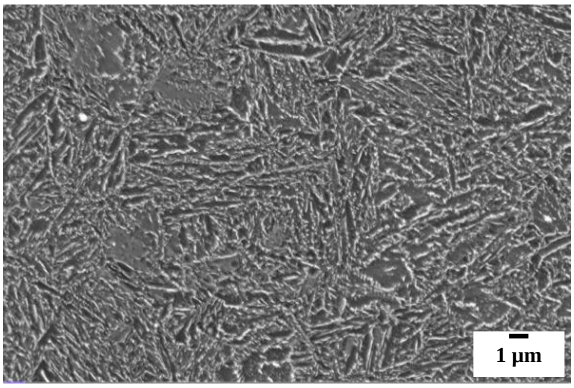

410°C for two hours

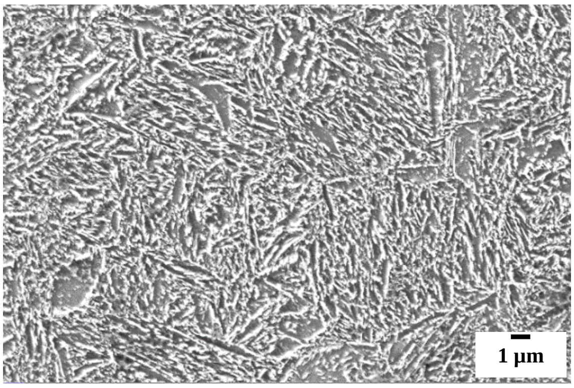

410°C for three hours

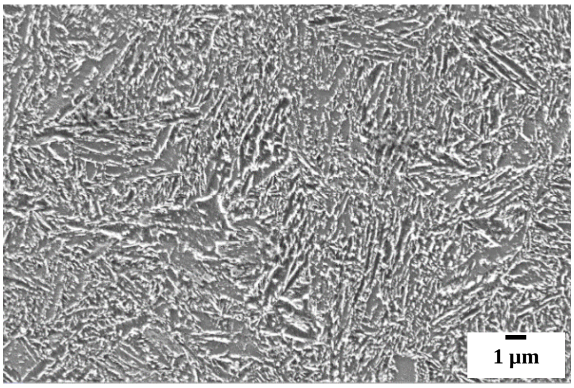

450°C for two hours

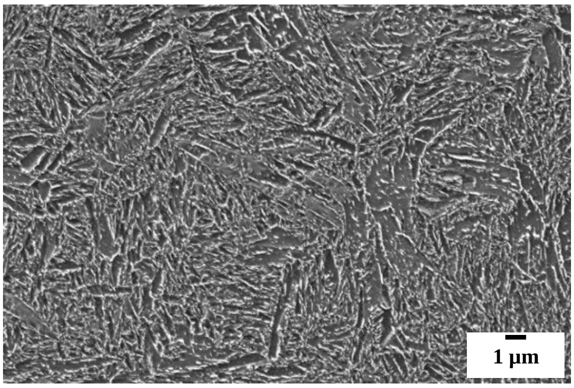

450°C for three hours

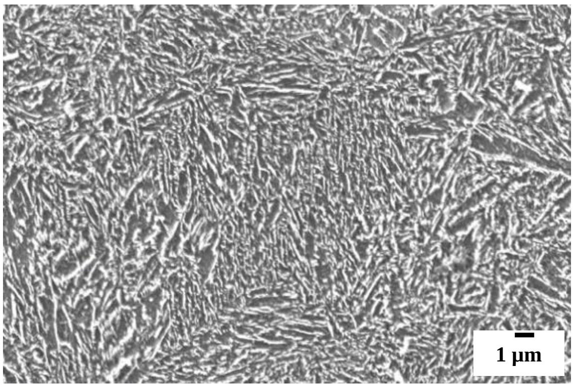

470°C for two hours

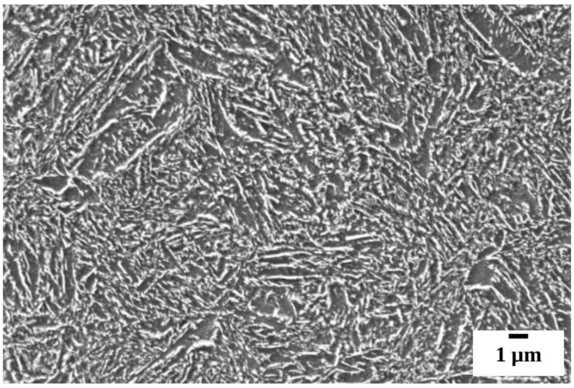

470°C for three hours

Figure 4.62 The tempered microstructures of 55Cr3.

4.3.12.2 54SiCr6 Steel

54SiCr6 showed irregular-shaped carbides compared to the alternating rod-like-shaped carbides observed in 55Cr3. The structures were consistently characterised with silicon carbides, which impinged on the formation of the characteristic rod-like carbides. The iron carbides spheroidised with the increase in temperature and soaking time, while the silicon carbides became more pronounced.

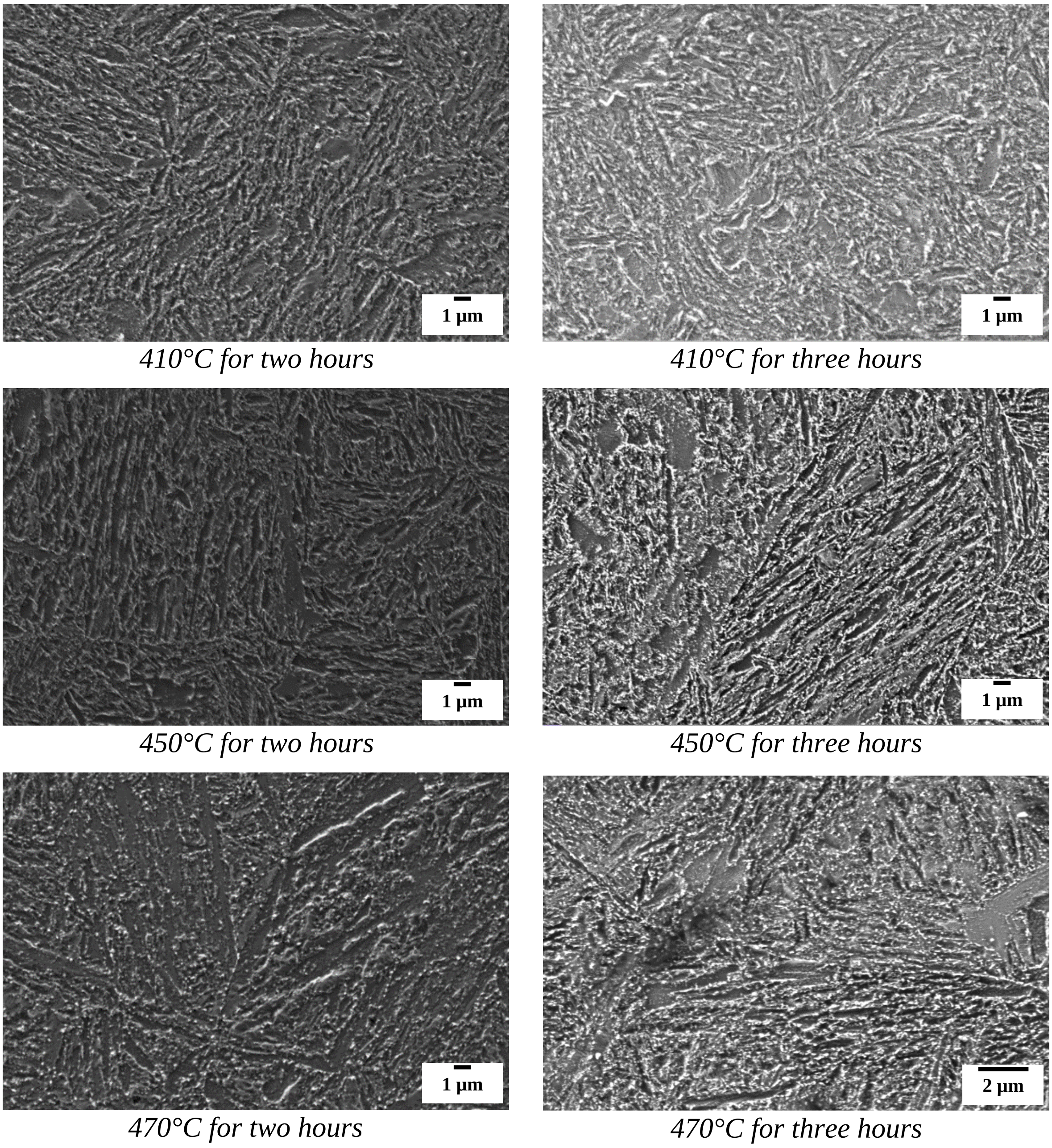

Figure 4.63 The tempered microstructures of 54SiCr6.

4.3.12.3 52CrMoV4 Steel

The images of the tempered microstructures of 52CrMoV4 revealed rod-shaped iron carbides layered around ferrite. With the increase in tempering temperature and soaking time, the structures revealed a mixture of rod-shaped and spherical iron carbides. The observation of the samples tempered for two hours was microstructures with rod-shaped carbides, while the samples tested for three hours showed pronounced spherical carbides. Figure 4.64 shows a structure of tempered martensite for the samples tempered at 470°C and is predominately made up of rod-shaped and spherical carbides. There was also a presence of needle-like carbides.

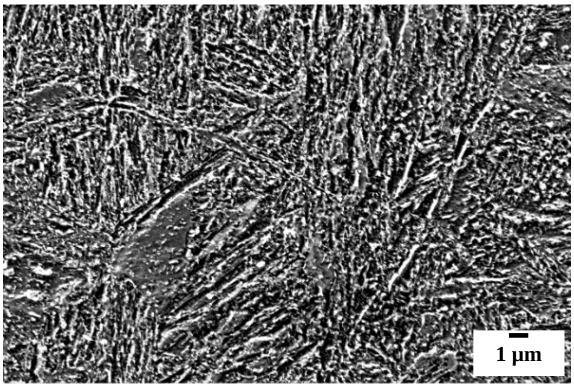

410°C for two hours

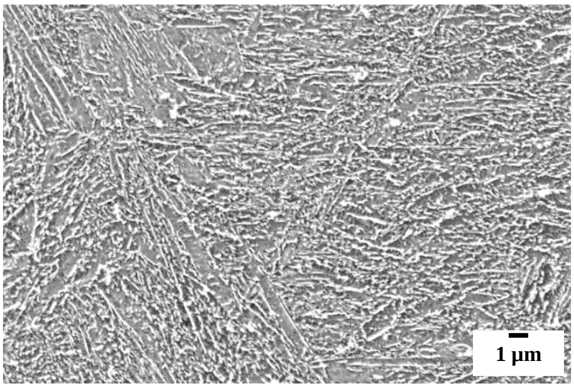

410°C for three hours

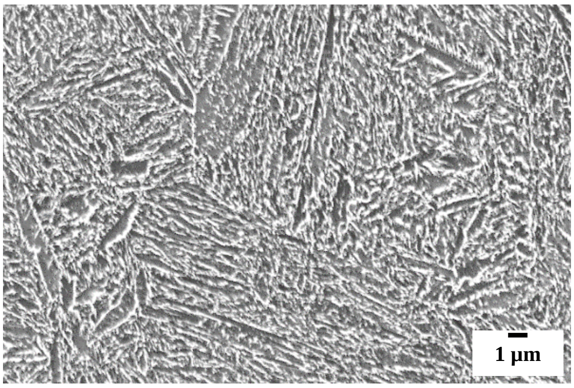

450°C for two hours

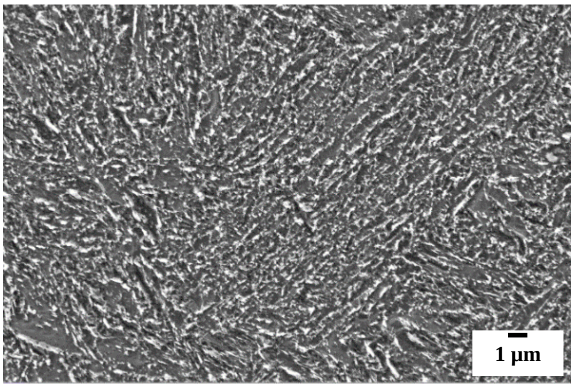

450°C for three hours

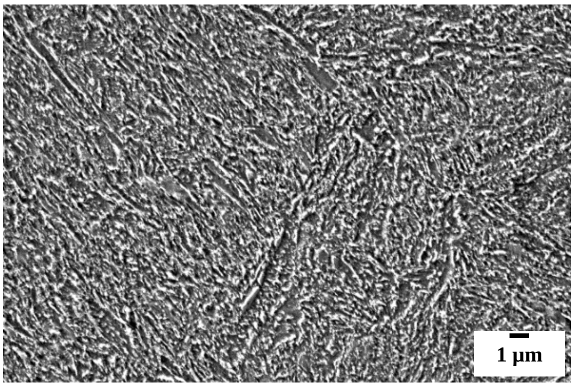

470°C for two hours

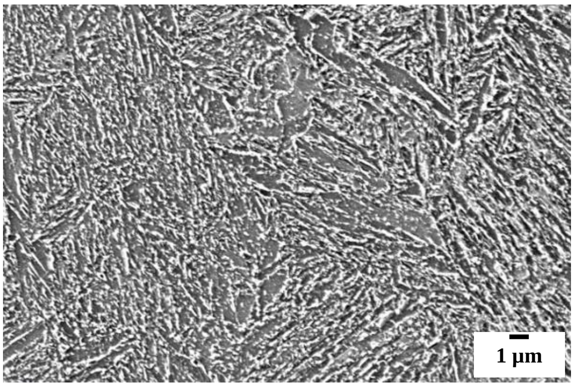

470°C for three hours

Figure 4.64 The tempered microstructures of 52CrMoV4.

4.3.13 Mechanical testing results

This section presents the mechanical test results of the three materials that underwent heat treatment as stipulated in the methodology. The tests covered are tensile testing, hardness testing, and impact strength testing.

4.3.13.1 Tensile testing results

The samples that were tempered at various temperatures and times were prepared for tensile testing, which was done to determine the effects of the various heat treatments on the materials. This was established by applying the required force to elongate the steel samples to breaking point. Tables 4.23 to 4.25 present a summary of the tensile test properties of the three materials.

Table 4.23 Tensile test results of 55Cr3.

Tempering parameters	**UTS (MPa)**	**YS (MPa)**	**Elongation (%)**
410°C for 2h	1675	1497	11
410°C for 3h	1615	1451	11
450°C for 2h	1619	1452	12
450°C for 3h	1580	1457	13
470°C for 2h	1545	1400	13
470°C for 3h	1427	1277	14

Table 4.24 Tensile test results of 54SiCr6.

Tempering parameters	**UTS (MPa)**	**YS (MPa)**	**Elongation (%)**
410°C for 2h	1682	1496	9
410°C for 3h	1614	1484	12
450°C for 2h	1391	1234	12
450°C for 3h	1339	1235	13
470°C for 2h	1361	1200	14
470°C for 3h	1290	1155	13

Table 4.25 Tensile test results of 52CrMoV4.

Tempering parameters	**UTS (MPa)**	**YS (MPa)**	**Elongation (%)**
410°C for 2h	1674	1633	9
410°C for 3h	1655	1608	10
450°C for 2h	1462	1424	11
450°C for 3h	1558	1516	12
470°C for 2h	1412	1343	12
470°C for 3h	1495	1420	13

Figure 4.65 shows the stress-strain curve of the three materials and Figure 4.66 shows that there is a gradual UTS decrease of 55Cr3 and 54SiCr6 with an increase in tempering temperature and time.

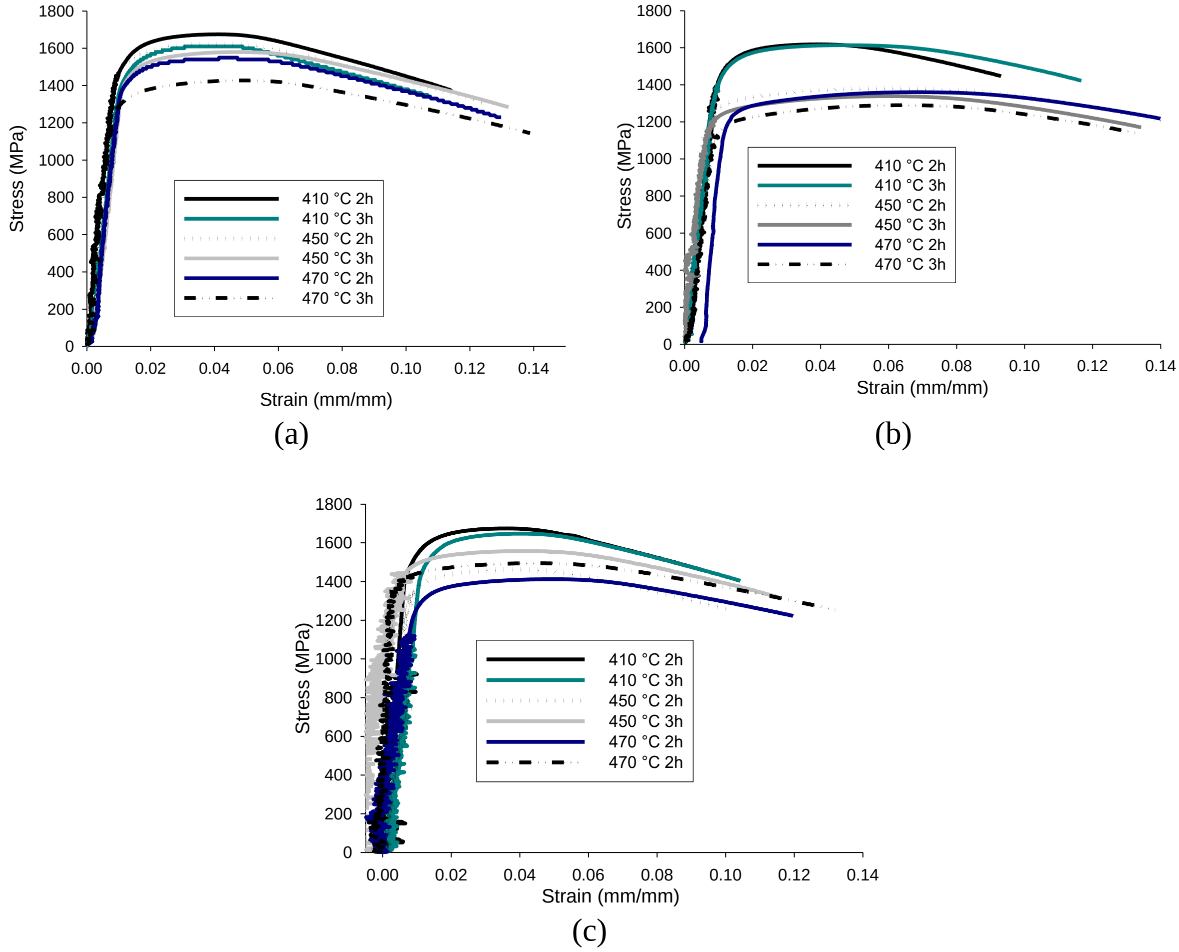

Figure 4.65 Tensile test stress-strain curves of (a) 55Cr3, (b) 54SiCr6, and (c) 52CrMoV4.

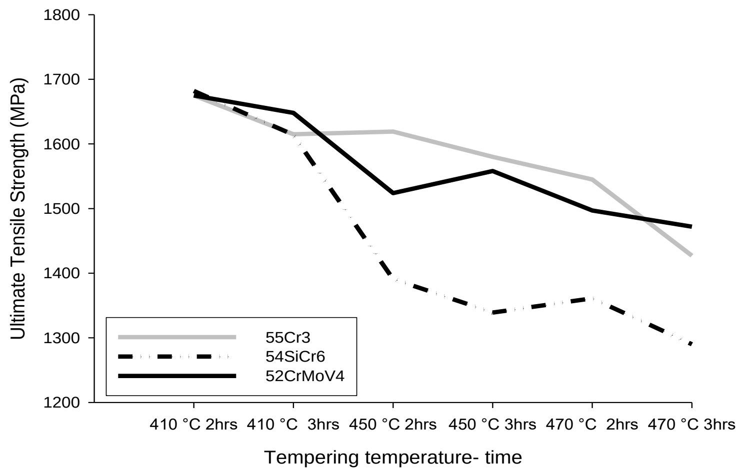

Figure 4.66 The UTS of the three-materials vs tempering temperature and time.

54SiCr6 showed a steady decrease in UTS at 410°C to 450°C, as well as evidence of insignificant secondary hardening at a tempering temperature of 470°C for two hours. 52CrMoV4 revealed what appears to be significant secondary precipitation hardening with an increase in tempering time. Figure 4.67 shows the yield strength profile versus the tempering temperature and time. 55Cr3 decreased in yield strength, while 52CrMoV4 showed a superior yield strength against 55Cr3 in contrast to the UTS. Secondary precipitation hardening is observed on the yield strength versus the tempering time of 52CrMoV4. 54SiCr6 decreased in yield strength between 410°C and 450°C, followed by a gradual decrease, and showed a lower UTS and yield strength compared to 55Cr3 and 52CrMoV4. Figure 4.68 shows the elongation percentage against tempering temperature and time.

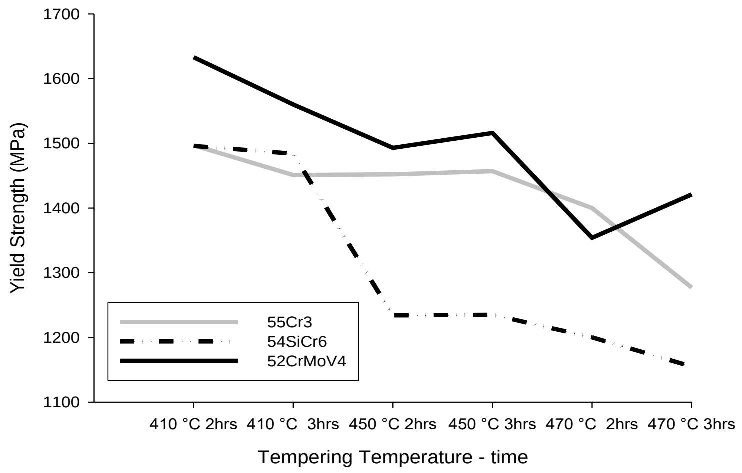

Figure 4.67 The yield strength of the three-materials vs tempering temperature and time.

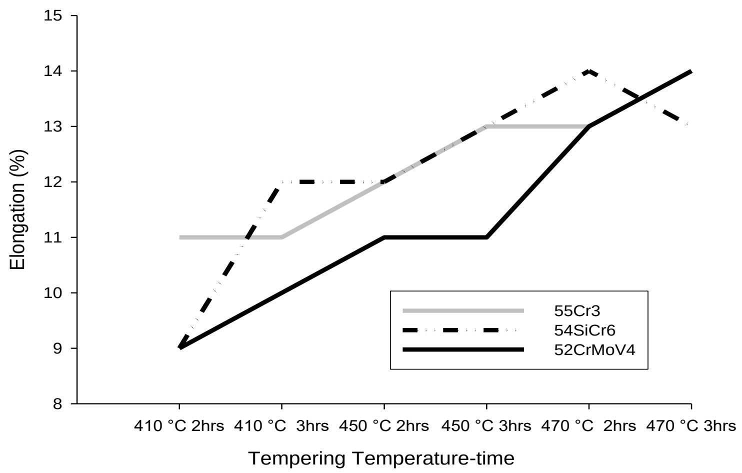

Figure 4.68 The elongation percentage of the three-materials vs tempering temperature and time.

The elongation percentage increased with the increase of tempering temperature and soaking time. However, 52CrMov4 showed the least percentage of elongation compared to 55Cr3 and 54SiCr6. 54SiCr6 showed superior ductility when compared to 55Cr3 except at the tempering temperatures of 410°C for two hours and 470°C for three hours. The YS:UTS ratio observed on the tensile test results are presented in Table 4.26.

Table 4.26 YS vs UTS ratios of the three materials.

Tempering parameters	**55Cr3**	**54SiCr6**	**52CrMoV4**
410°C for 2h	0.89	0.89	0.98
410°C for 3h	0.90	0.92	0.95
450°C for 2h	0.90	0.89	0.98
450°C for 3h	0.92	0.92	0.97
470°C for 2h	0.91	0.88	0.90
470°C for 3h	0.90	0.90	0.97

The YS:UTS of 55Cr3, 54SiCr6, and 52CrMoV4 gave average results of 0.9, 0.9, and 1.0, respectively. 55Cr3 and 54SiCr6 showed comparable hardening capacity, while 52CrMoV4 showed lower hardening capacity. Table 4.27 presents the strain hardening exponent of each material tempered at various temperatures. The detailed plots are captured in Appendix B.

Table 4.27 Tensile test mechanical properties.

Tempering parameters	**55Cr3**			**54SiCr6**			**52CrMoV4**		
	K	ε_{UTS}	**n**	**K**	ε_{UTS}	**n**	**K**	ε_{UTS}	**n**
410°C for 2h	2035	0.05	0.04	1961	0.05	0.05	2000	0.04	0.04
410°C for 3h	1931	0.05	0.05	2050	0.06	0.05	1940	0.05	0.04
450°C for 2h	1983	0.05	0.05	1811	0.07	0.07	1775	0.05	0.05
450°C for 3h	1970	0.06	0.06	1810	0.07	0.07	1940	0.05	0.05
470°C for 2h	1896	0.05	0.05	1821	0.08	0.08	1691	0.04	0.06
470°C for 3h	1802	0.06	0.06	1711	0.08	0.08	1873	0.06	0.05

The plastic behaviour of the tempered spring steels was characterised by evaluating the flow stress curve and determining the strain hardening exponent. While 55Cr3 and 52CrMoV4 were comparable, 54SiCr6 showed a higher ability to work harder. The R^2 was found to be above 0.99, which means that the Hollomon equation was applicable to determine plastic deformation behaviour.

On the other hand, the strength coefficient generally decreased with the increase of tempering temperature. The strength coefficient was determined by plotting a fitting curve and extrapolating the gradient line to intercept the true strain at 1 mm/mm. The strength coefficient graphs are plotted in Appendix C.

4.3.13.2 Hardness testing results

This section presents the hardness measurements of the three materials that were subjected to various tempering temperatures and times and includes the as-quenched micro-Vickers hardness results and the tempered Rockwell hardness measurements. Hardness tests were carried out to measure the effects of different heat treatment processes on the hardenability of the selected steels. The average hardness of the as-quenched results are shown in Table 4.28 and Figure 4.69.

Table 4.28 The as-quenched average micro-Vickers results.

Materials	Average	Standard deviation	Standard error
55Cr3	804.3	14.4	2.9
54SiCr6	826.5	13.5	2.7
52CrMoV4	803.7	15.2	3.0

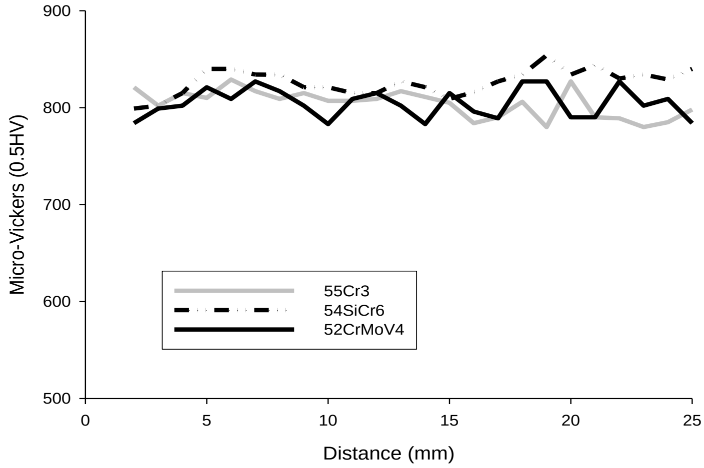

Figure 4.69 A graphical illustration of the as-quenched average hardness.

54SiCr6 showed superior hardness, while 55Cr3 and 52CrMoV4 were comparable. This phenomenon is attributed to 54SiCr6 having a greater ability to harden. Figure 4.70 shows the micro-Vickers hardness profile of the three materials. Tables 4.29 to 4.31 give a summary of the Rockwell hardness test of the three materials, while Figure 4.71 to 4.73 show the hardness profile measurements.

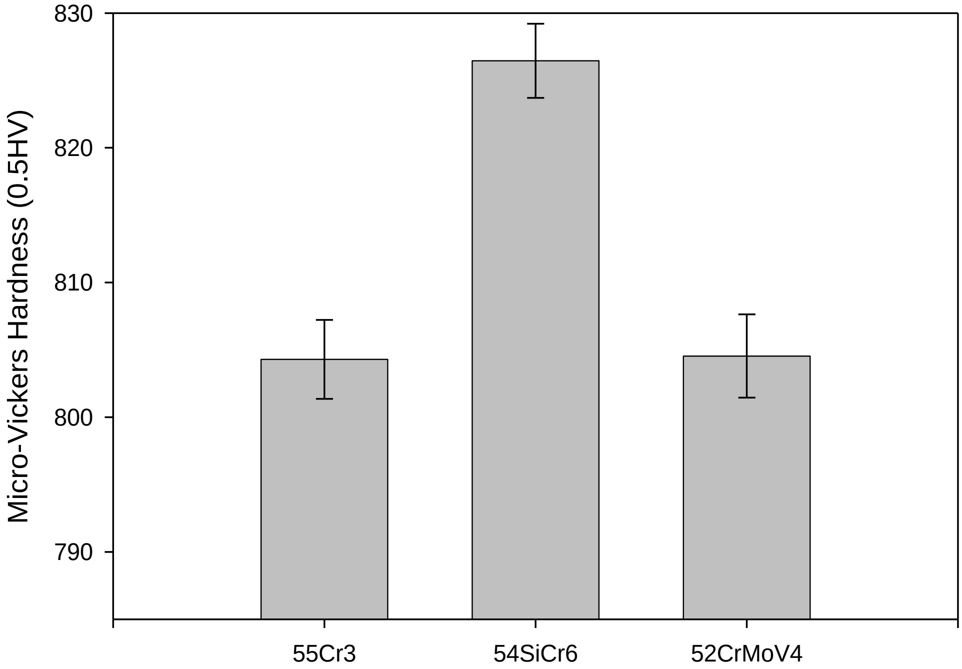

Figure 4.70 Micro-Vickers hardness profile results.

Table 4.29 The Rockwell macro-hardness measurements of 55Cr3.

Distance (mm)	**410°C 2h**	**410°C 3h**	**450°C 2h**	**450°C 3h**	**470°C 2h**	**470°C 3h**
2.3	48	49	47	45	43	41
4.6	51	50	48	45	43	41
6.9	50	49	48	46	45	41
9.2	49	50	49	46	45	41
11.5	50	50	48	46	46	42
13.8	51	51	48	46	42	42
16.1	51	50	48	46	44	42
18.4	51	50	48	46	44	42
20.7	52	50	48	46	44	41
23	51	50	48	46	45	42

Table 4.30 The Rockwell macro-hardness measurements of 54SiCr6.

Distance (mm)	**410°C 2h**	**410°C 3h**	**450°C 2h**	**450°C 3h**	**470°C 2h**	**470°C 3h**
2.3	46	46	43	43	42	42
4.6	46	46	44	43	44	43
6.9	46	46	43	44	42	42
9.2	45	46	44	42	43	42
11.5	45	45	43	42	41	42
13.8	45	45	44	42	41	41
16.1	46	46	44	42	42	41
18.4	47	46	44	42	43	42
20.7	47	46	44	43	43	41
23	46	46	44	43	43	43

Table 4.31 The Rockwell macro-hardness measurements of 52CrMoV4.

Distance (mm)	**410°C 2h**	**410°C 3h**	**450°C 2h**	**450°C 3h**	**470°C 2h**	**470°C 3h**
2.3	46	47	45	44	44	44
4.6	47	49	43	45	44	45
6.9	48	49	45	45	44	46
9.2	47	49	45	45	44	46
11.5	47	49	46	45	44	45
13.8	47	49	45	46	44	45
16.1	47	49	44	46	45	45
18.4	47	48	45	46	44	44
20.7	46	49	46	46	45	46
23	46	48	45	45	44	46

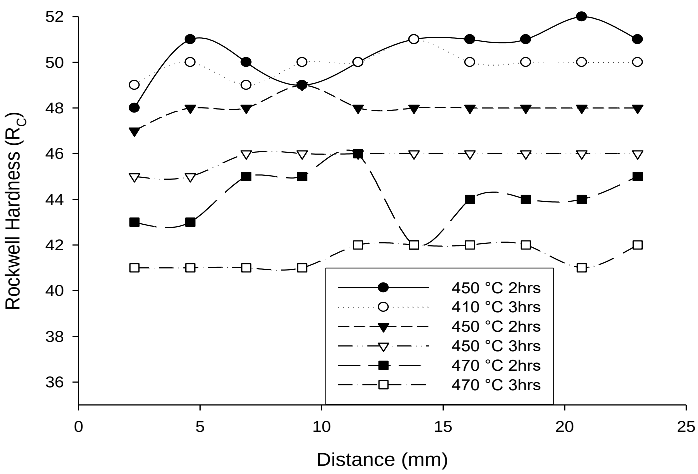

Figure 4.71 Hardness profile of 55Cr3.

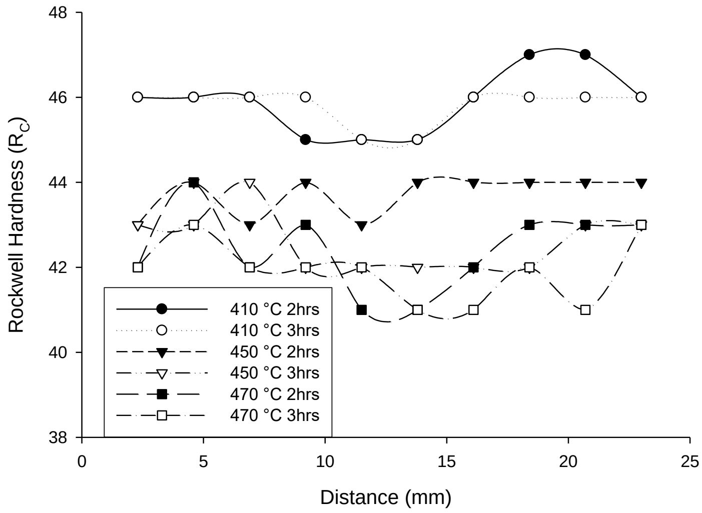

Figure 4.72 Hardness profile of 54SiCr6.

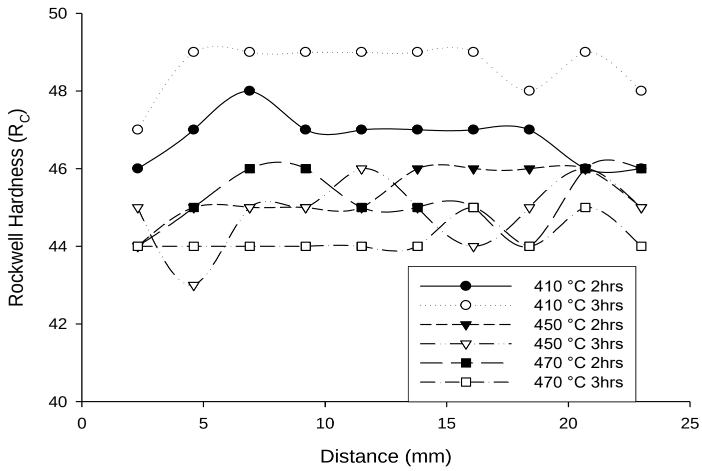

Figure 4.73 Hardness profile of 52CrMoV4.

Table 4.32 and Figure 4.74 show an overall comparison of hardness averages at different tempering temperatures and times. The hardness measurements of 55Cr3 showed a steep decrease with an increase of tempering temperature, while 54SiCr6 and 52CrMoV4 showed a gradual decrease. 54SiCr6 showed lower Rockwell hardness measurements consistent with its tensile strength and 52CrMoV4 revealed secondary precipitation hardening at three hour tempering soaking times.

Material hardness generally decreased with the increase in tempering temperature. However, the samples that were tempered for three hours showed evidence of secondary precipitation hardening compared to the materials tempered for two hours. The secondary hardening phenomenon observed on the tensile test results was reported by Vinet and Zhedanov (2010) and Totten (2006) and was a result of coalescence of Mo_3C and V_4C_3. On the other hand, the strength decreased, and the ductility increased with the increase of tempering temperature.

Table 4.32 The Rockwell hardness results of the three materials.

Tempering parameters	55Cr3			54SiCr6			52CrMoV4		
	Average	**Standard deviation**	**Standard error**	**Average**	**Standard deviation**	**Standard error**	**Average**	**Standard deviation**	**Standard error**
410°C for 2h	50	1.1	0.3	46	0.8	0.3	47	0.5	0.1
410°C for 3h	50	0.7	0.2	46	0.3	0.1	49	0.7	0.2
450°C for 2h	48	0.3	0.1	44	0.5	0.2	45	0.8	0.2
450°C for 3h	46	0.6	0.2	43	0.5	0.2	45	0.6	0.2
470°C for 2h	44	0.9	0.3	42	1.0	0.3	44	0.4	0.1
470°C for 3h	42	0.5	0.1	42	0.7	0.2	45	0.6	0.2

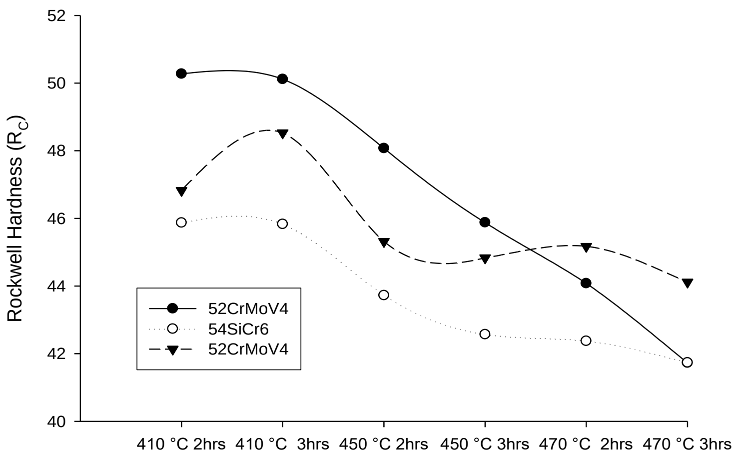

Figure 4.74 Rockwell hardness vs tempering temperature and time

4.3.13.3 Impact strength testing results

Each heat treatment process was tested at 23°C, -7°C, and -20°C. The main objective for this section is to illustrate the effect of lower temperatures on the impact strength of the materials. The impact strength results are presented in Table 4.33 to 4.35 and Figures 4.75 to 4.77. The results revealed an increase in impact strength with the increase in tempering temperature and soaking time.

52CrMoV4 proved to consistently have superior impact strength at ambient and cryogenic temperatures compared to 55Cr3 and 54SiCr6. The impact strength of 55Cr3 competitively improved with the increase in tempering temperature. Although the materials show a drop in impact strength with decreasing temperature, the ductile transition temperature was not obvious.

Table 4.33 Impact strength tested at 23°C.

Tempering parameters	**Testing temperature**	**Impact strength (J)**		
		55Cr3	**54SiCr6**	**52CrMoV4**
410°C for 2h	23°C	19.87	27.41	28.37
410°C for 3h	23°C	28.37	25.51	36.09
450°C for 2h	23°C	39.06	37.06	37.06
450°C for 3h	23°C	39.03	38.11	40.02
470°C for 2h	23°C	41.62	42.11	45.97
470°C for 3h	23°C	42.03	52.02	48.11

Table 4.34 Impact strength tested at -7°C.

Tempering parameters	**Testing temperature**	**Impact strength (J)**		
		55Cr3	**54SiCr6**	**52CrMoV4**
410°C 2h	-7°C	16.25	26.33	25.12
410°C 3h	-7°C	17.04	26.74	29.81
450°C 2h	-7°C	34.84	31.85	35.85
450°C 3h	-7°C	35.01	33.84	38.86
470°C 2h	-7°C	39.9	33.08	42.95
470°C 3h	-7°C	40.04	41.88	44.84

Table 4.35 Impact strength tested at -20°C.

Tempering parameters	Testing temperature	Impact Strength (J)		
		55Cr3	54SiCr6	52CrMoV4
410°C 2h	-20°C	15.20	18.90	19.32
410°C 3h	-20°C	17.08	19.14	23.62
450°C 2h	-20°C	27.88	29.24	30.28
450°C 3h	-20°C	29.27	31.11	30.33
470°C 2h	-20°C	33.01	29.32	41.01
470°C 3h	-20°C	32.38	32.38	38.04

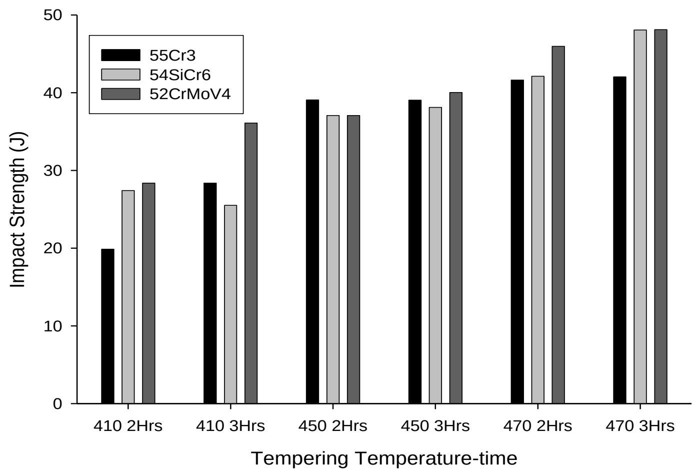

Figure 4.75 The average impact strength tested at 23°C.

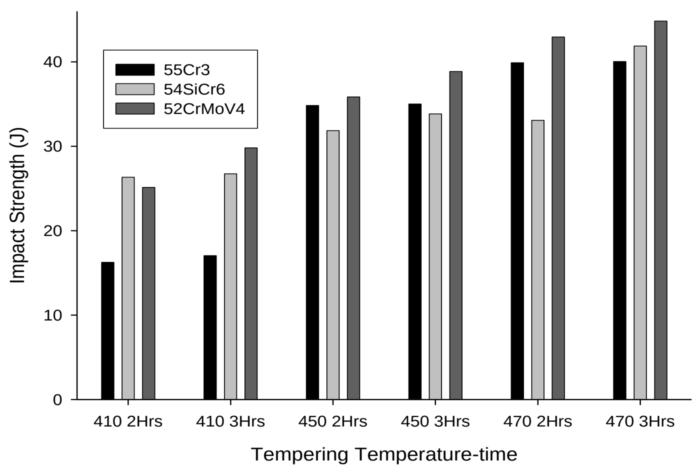

Figure 4.76 The average impact strength tested at -7°C.

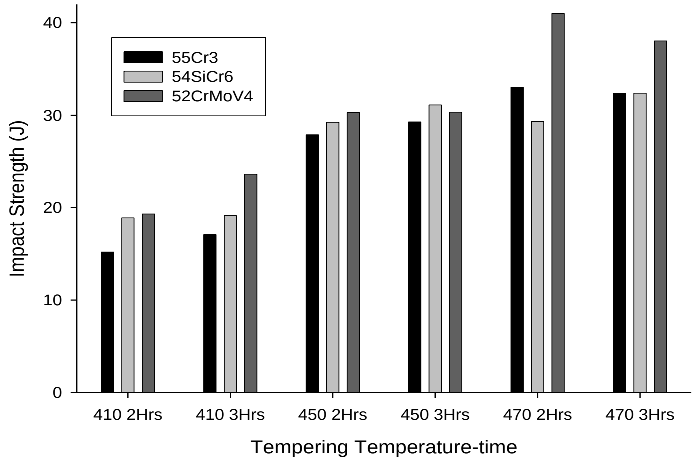

Figure 4.77 The average impact strength tested at -20°*C*.

4.3.14 Electrochemistry

The three materials were subjected to corrosion testing and were exposed to a solution of 3.5% sodium chloride. The corrosion characteristics were determined with an electrochemical test by first considering the open circuit potential for a short period of time. Thereafter, the electrochemical potential was scanned from an active potential to a more cathodic potential around the corrosion potential. Figure 4.78 shows the time dependence corrosion potential of the three materials that were subjected to the corrosion test.

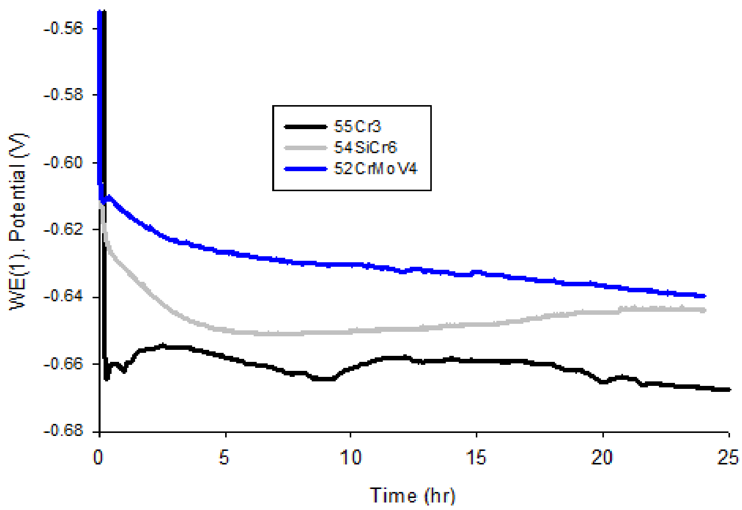

Figure 4.78 Time dependence potential.

In the initial period, the corrosion potential moved to the negative potential and gradually stabilised over time. It was observed that 55Cr3 achieved the lowest potential, while 52CrMoV4 achieved the highest potential over the 24-hour period trend. Additionally, 55Cr3 and 52CrMoV4 steadily decreased, while 54SiCr6 decreased and then steadily increased after five hours. The polarisation curves are shown in Figure 4.79 to 4.81.

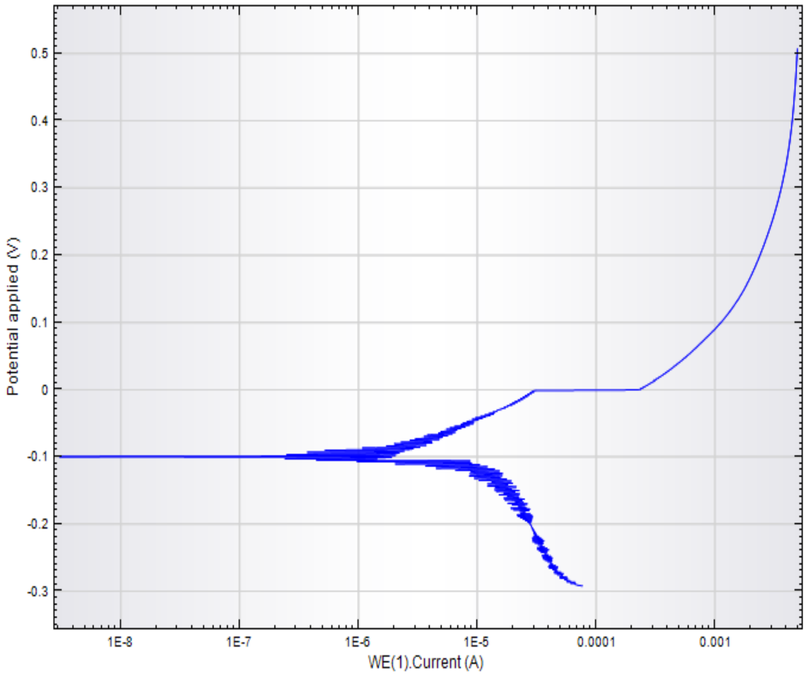

Figure 4.79 Polarisation diagrams of 55Cr3 at room temperature in 3.5% NaCl.

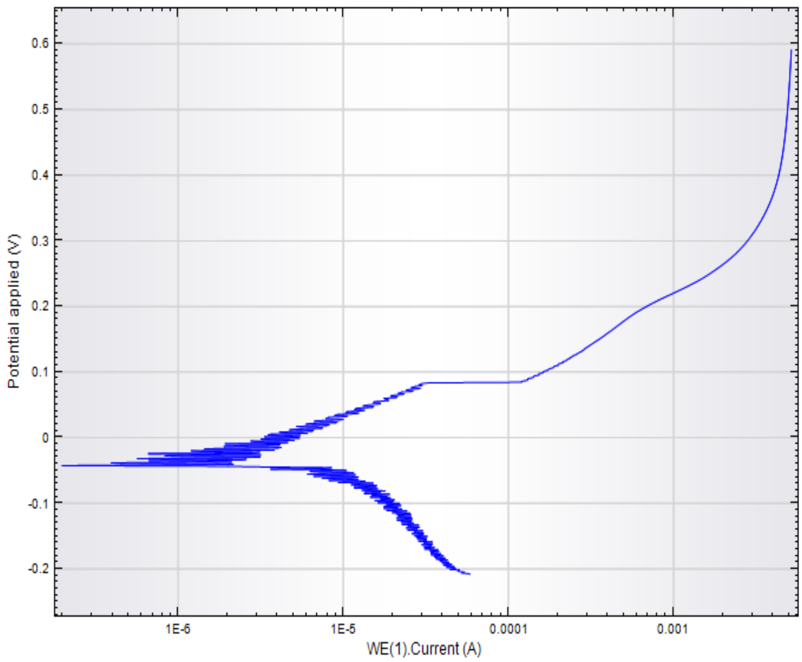

Figure 4.80 Polarisation diagrams of 54SiCr6 at room temperature in 3.5% NaCl.

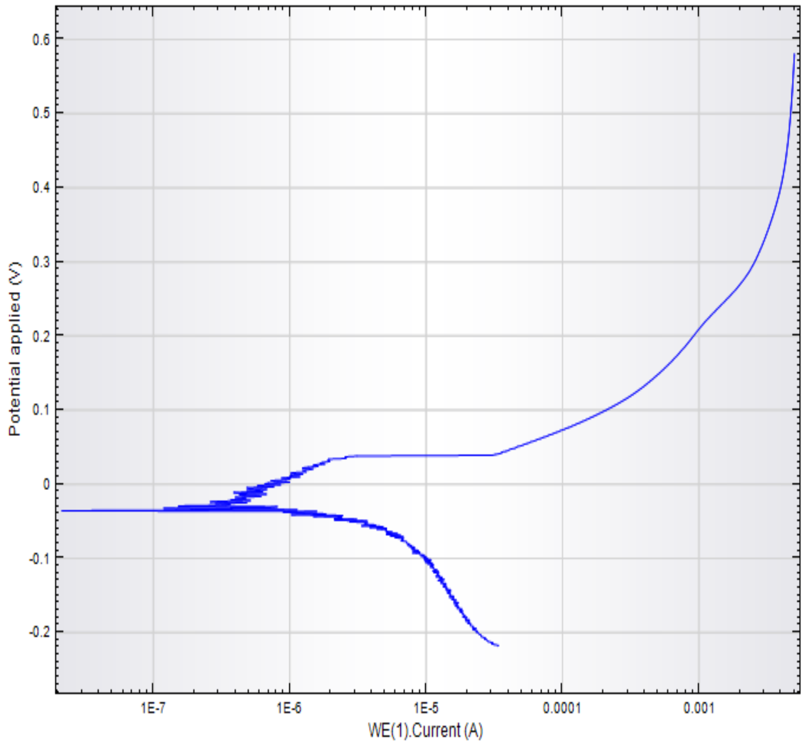

Figure 4.81 Polarisation diagrams of 52CrMoV4 at room temperature in 3.5% NaCl.

According to the polarisation curves, 55Cr3 shows the lowest corrosion current, while 52CrMoV4 shows a higher corrosion current. Corrosion rate is directly proportional to the corrosion current, therefore, 55Cr3 shows the lowest corrosion resistance and 54SiCr6 shows the highest corrosion resistance. The calculated corrosion resistance values are shown in Table 4.36.

Table 4.36 Corrosion resistance results.

Samples	**Corrosion rates (mm/year)**	**Current density** *(µA)*
55Cr3	0.1414	12.169
54SiCr6	0.91714	78.928
52CrMoV4	0.0044587	0.384

4.3.15 Slow strain rate testing

SSRT was conducted in order to evaluate the SSC on the heat treated steel rods. The SSRT results that were performed at a strain rate of 1 x 10^{6} s^{-1} are shown in Tables 4.37 to 4.39 and Figures 4.82 to 4.84. The general trends show that the elongation percentage and percentage reduction area increased with the tempering temperature and time for all the samples. Comparatively, 55Cr3 shows a lower elongation percentage, while 52CrMoV4 shows a superior elongation percentage. At 410°C tempering temperature, all the three steels showed embrittlement, however, at the tempering temperature were raised and soaking time were increased, the opposite effect was observed.

Table 4.37 SSRT strain measurements of 55Cr3.

Samples	**L_o**	**L_f**	**A_o**	**A_f**	**Elongation (%)**	**Area reduction (%)**
410°C 2h	32.00	32.01	10.75	10.46	0,03	2,70
410°C 3h	30.50	30.51	11.34	11.04	0,03	2,65
450°C 2h	32.00	32.01	11.64	11.34	0,03	2,58
450°C 3h	29.90	29.92	10.75	10.18	0,07	5,30
470°C 2h	31.90	31.92	11.04	9.62	0,06	12,86
470°C 3h	31.90	33.10	11.34	9.62	3.62	15,17

Table 4.38 SSRT strain measurements of 54SiCr6.

Samples	**L_o**	**L_f**	**A_o**	**A_f**	**Elongation (%)**	**Area reduction (%)**
410°C 2h	31.90	31.92	11.34	10.75	0,06	5,20
410°C 3h	31.90	31.92	11.34	10.75	0,06	5,20
450°C 2h	32.00	32.02	11.34	11.22	0,06	1,06
450°C 3h	32.00	32.02	11.34	10.75	0,06	5,20
470°C 2h	32.00	32.01	11.34	9.08	0,03	19,93
470°C 3h	32.00	32.03	11.95	9.62	0,09	19,50

Table 4.39 SSRT strain measurements of 52CrMoV4.

Samples	**L_o**	**L_f**	**A_o**	**A_f**	**Elongation (%)**	**Area reduction (%)**
410°C 2h	32.00	32.30	11.34	10.75	0,94	5,20
410°C 3h	27.50	27.90	13.20	12.57	1,45	4,77
450°C 2h	32.00	32.40	11.04	10.18	1,25	7,79
450°C 3h	31.90	32.31	11.34	9.40	1,29	17,11
470°C 2h	31.90	32.40	11.34	8.87	1,57	21,78
470°C 3h	32.00	32.90	11.34	9.08	2,81	19,93

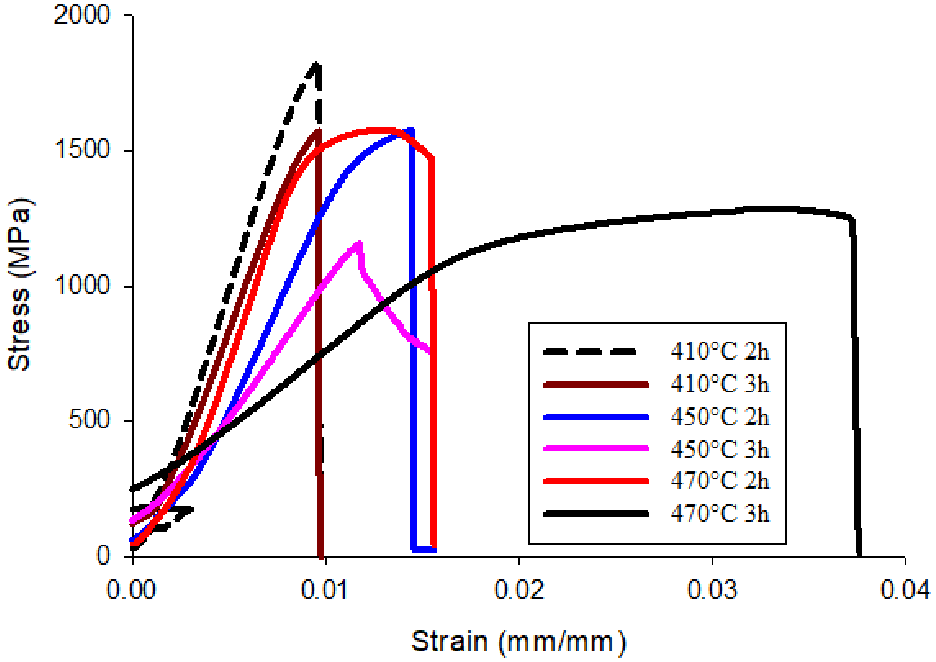

Figure 4.82 SSRT strain flow of 55Cr3.

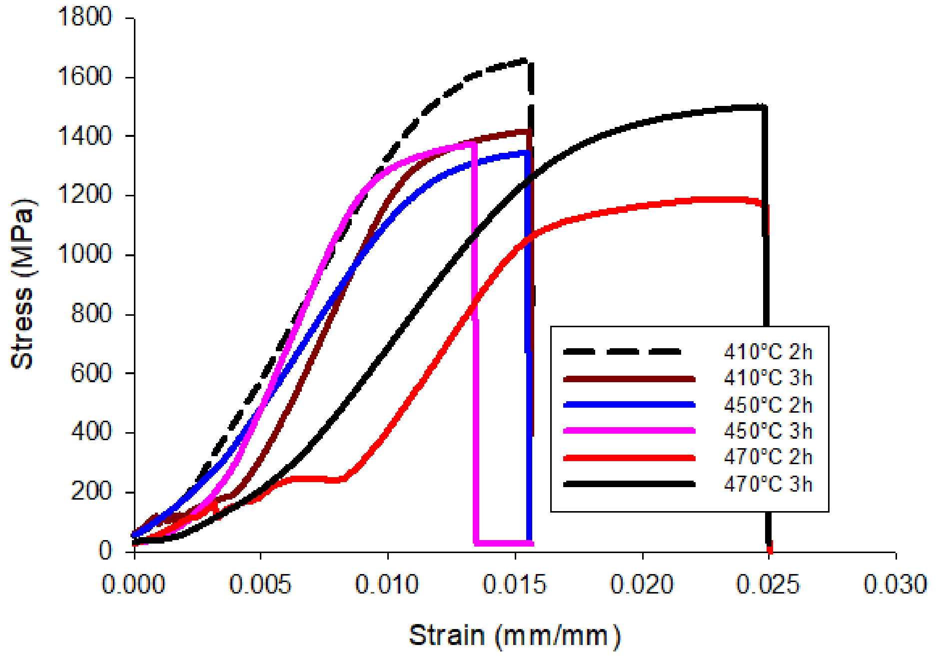

Figure 4.83 SSRT strain flow of 54SiCr6.

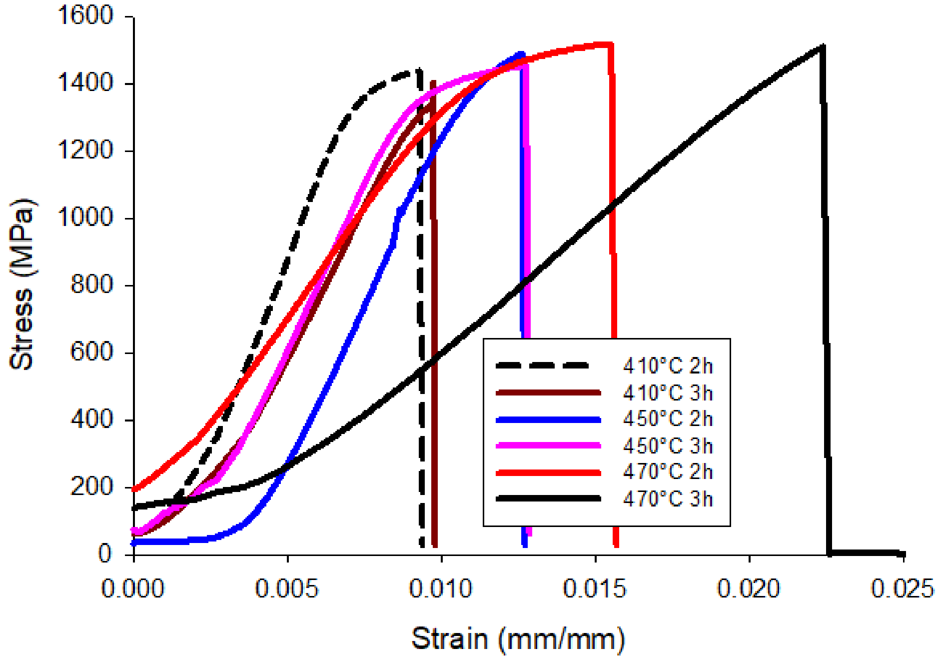

Figure 4.84 SSRT strain flow of 52CrMoV4.

The SSRT techniques largely focused on specimen fracture behaviour. Upon completion of the SSRT, the fracture surfaces of the samples were cleaned with 100 ml H_2O and 4 ml HCl solution in an ultrasonic bath. The fracture mechanisms shown in Figures 4.85 to 4.87 were observed and analysed under the SEM.

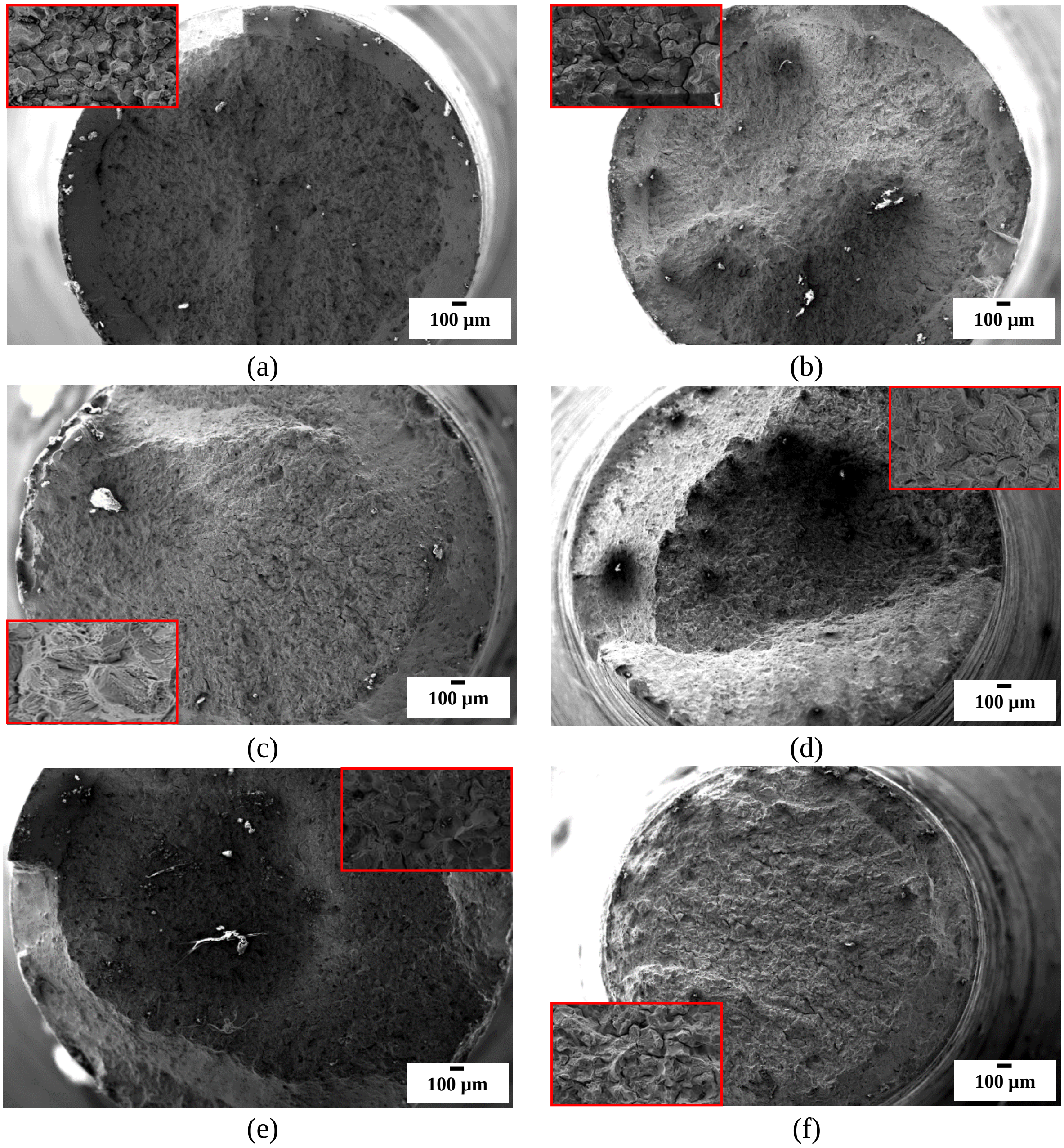

Figure 4.85 SSRT fracture surface of 55Cr3 tempered at (a) 410°C for 2 hours, (b) 410°C for 3 hours, (c) 450°C for 2 hours, (d) 450°C for 3 hours, (e) 470°C for 2 hours, and (f) 470°C for 3 hours.

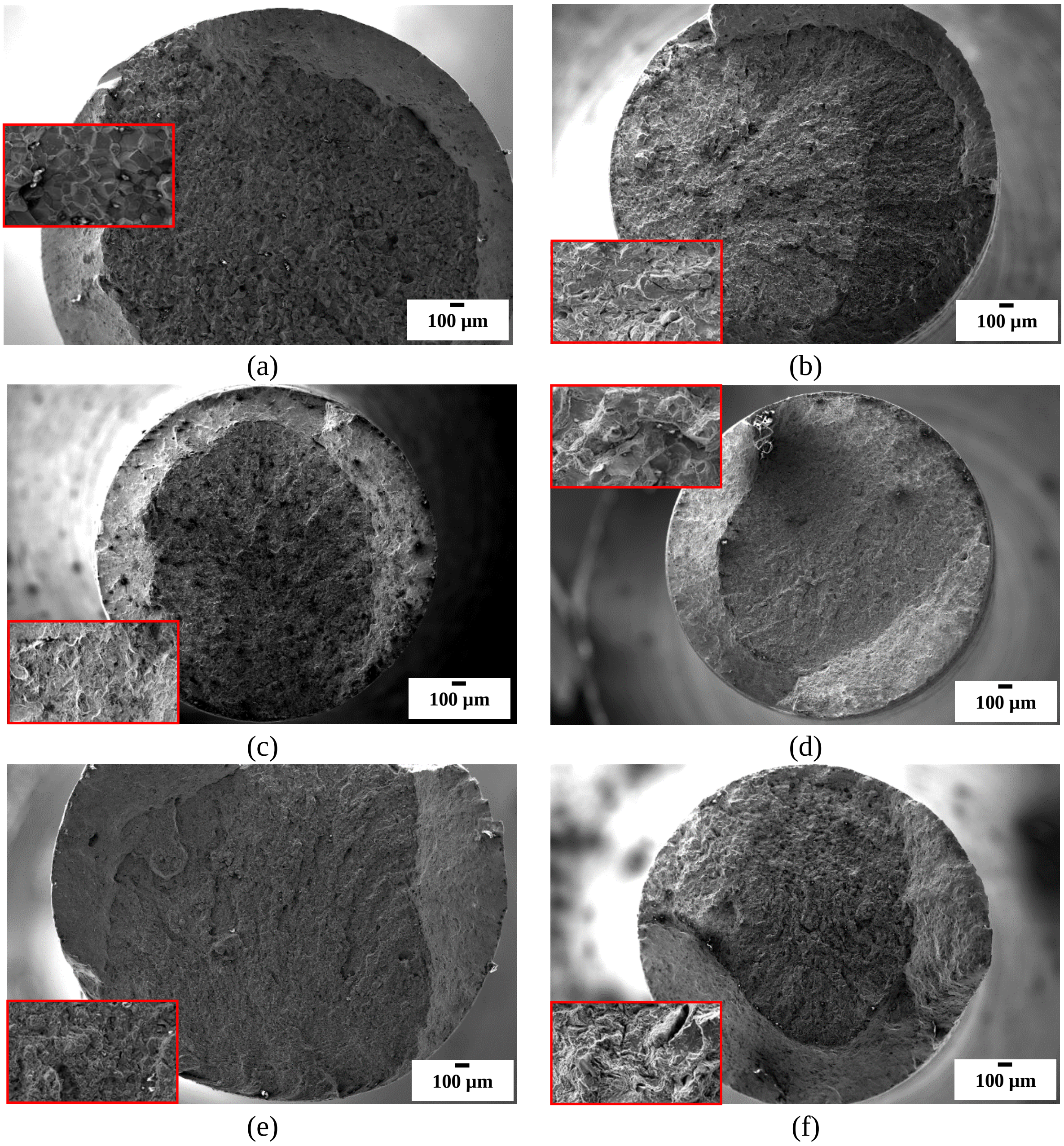

Figure 4.86 SSRT fracture surface of 54SiCr6 tempered at (a) 410°C for 2 hours, (b) 410°C for 3 hours, (c) 450°C for 2 hours, (d) 450°C for 3 hours, (e) 470°C for 2 hours, and (f) 470°C for 3 hours.

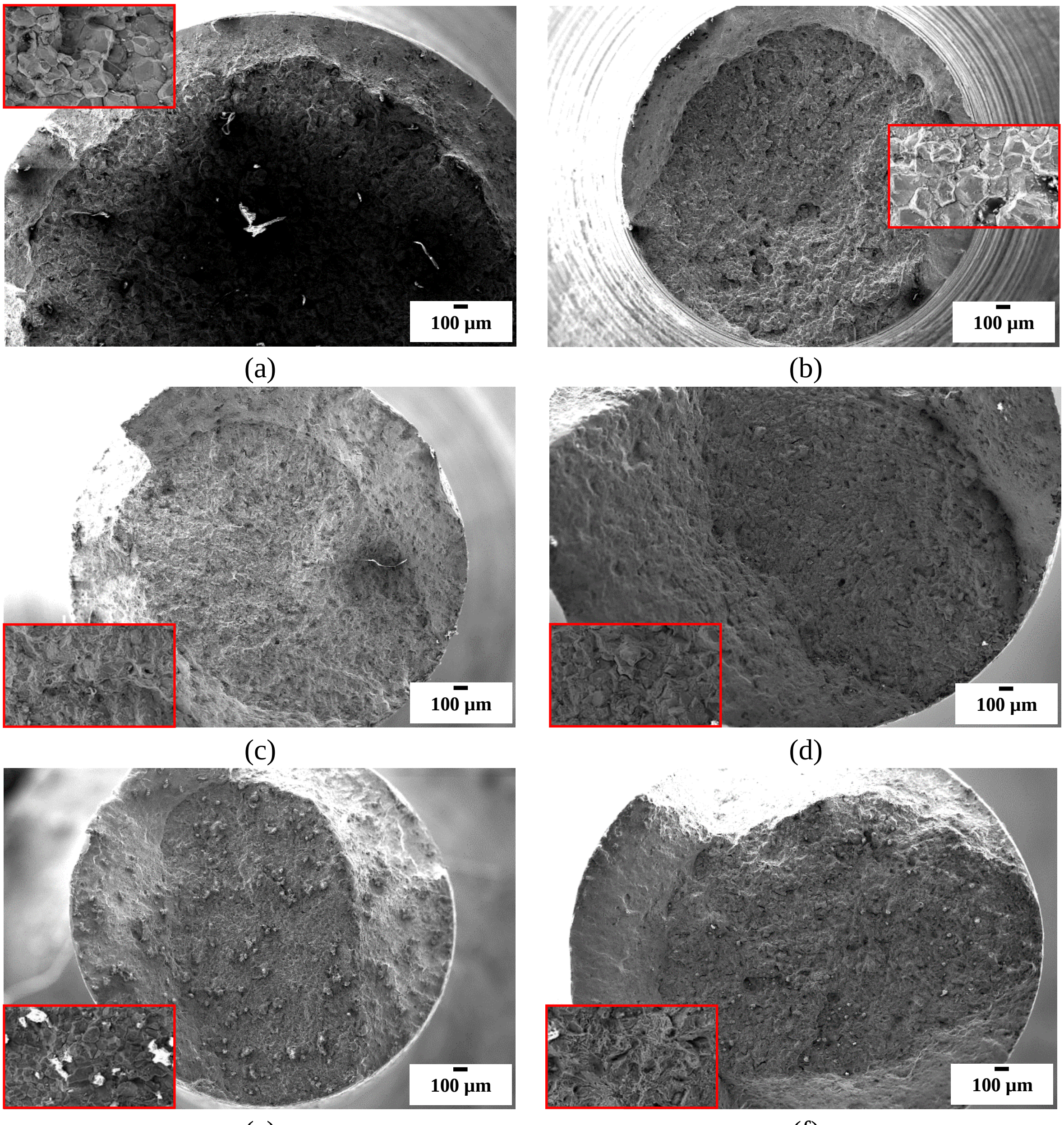

Figure 4.87 SSRT fracture surface of 52CrMoV4 tempered at (a) 410°C for 2 hours, (b) 410°C for 3 hours, (c) 450°C for 2 hours, (d) 450°C for 3 hours, (e) 470°C for 2 hours, and (f) 470°C for 3 hours.

The 55Cr3 fracture surfaces were characterised by brittle features such as intergranular cracking and cleavage facets. Intergranular cracking was more pronounced on the samples tempered at 410°C and reduced with the increase in tempering temperature. Intergranular cracking was not observed on the samples tempered at 470°C. However, cleavage facets and lamellar tearing were.

The 54SiCr6 fracture surfaces showed different fracture mechanisms compared to 55Cr3. Although the fracture mechanism of 54SiCr6 tempered at 410°C for two hours revealed intragranular fracture features, they were not as prominent as those observed in Figure 4.85. The rest of the fractures in Figure 4.86 and Figure 4.87 revealed a distinct kind of lamellar tearing without evidence of hydrogen cracking. In addition, the 52CrMoV4 SSRT samples that were tempered at 410°C showed intergranular cracking features, while the samples tempered at 450°C and 470°C revealed a mixture of ductile and quasi-cleavage fractures.

Chapter 5 : Discussion

5.1 Failure root cause analysis of springs that failed in-service and during fatigue testing

The findings of the spring failure root cause analysis revealed the following:

5.1.1 Spring that failed in-service

The spring that broke in-service failed as a result of microcracking that occurred during the heat treatment. The cracks were positively recognised as quench cracks, which developed during phase transformation. The quench cracks occurred due to uneven rapid cooling caused by the deteriorated quenching oil. The cracks had intergranular features and heat-related oxidation scales, indicating that the micro-crack had been exposed to high temperatures. The spring was only subjected to high temperatures during the austenitising and tempering processes.

High temperature oxidation on the fracture surface and intergranular cracking are characteristics that link the failure mode to quench cracking. This was further validated by simulating the quenching process in the laboratory using Unused oil and the old oil used to quench the failed spring a month prior. The steel rod that was quenched with the Unused oil had a significant considerable martensitic structure fraction and some bainite structure, whereas the steel rod that was quenched with the old oil had a martensitic structure with intergranular cracking.

The old oil cooling rates were found to be undesirable as they resulted in the formation of micro-cracks that led to the spring failure. The microstructure of the spring steel that was quenched with the Unused oil did not reveal defects, however, it did reveal a presence of bainite. Although the effect of bainite on the performance of SAE 5160 spring steel was unknown at the time, it was believed, as stated in Hypothesis 02, that the quenching oil cooling rates can affect the microstructure and properties, and thus the best quenching oil can be selected based on its quenching capacity and properties.

The immediate cause of quench cracks is severe cooling rates and subsequent development of tensile stress on the surface of the spring (Lingamanaik and Chen, 2014). The tensile stresses are increased by volumetric martensite expansion during phase transformation. The cracks are often fine on the surface and are only detectable by dye penetrant testing. The internal stresses that caused cracking can be reduced by selecting a quenchant with slower cooling rates that still promotes low martensite transformation (Kumar *et al.*, 2000).

There are several grades of quenching oils with different quenching capabilities and properties. Many researchers have studied the behaviours and characteristics of quenchants, however, the effect of the quenching media on selected steel grades is still lacking (Kumar *et al.*, 2000; Chen *et al.*, 2007). This commissioned a study to select a quenching oil by using the exact chemical composition of the spring steel, which will produce the optimum mechanical properties without causing quench cracks.

5.1.2 Spring that failed during fatigue testing

The spring that broke during fatigue testing, failed due to coil contact, which caused stress-raisers on the surface of the spring. The coil contact of the spring was caused by the pitch angle that was inadequately designed based on the mechanical properties of the spring steel used. The calculations further showed an increase in torsional stress with an increase in pitch angle. Therefore, the premature failure of the spring could be attributed to inadequate pitch angle. Furthermore, this study illustrated that there is a relationship between the pitch angle and the fatigue life of the spring, i.e. an increase of nominal pitch angle adversely affects the lifespan of the spring.

The FEA also showed that the shear stress exceeds the tensile strength of the spring material when the pitch angle varies by more than 0.4°. As a result, the pitch angle was optimised to ensure that the coils do not touch under the design load cases. It is important that designers stipulate the pitch tolerances, while spring manufacturers must be equipped with machinery that can constantly produce the springs as per requirement. It is paramount that the design requirements are fully met during manufacturing to avoid premature failures, as inspection and monitoring of cracking in-service are difficult due to the inaccessibility of the installed springs on the bogie.

The insufficient displacement capacity will result in impact forces during operation, which will reduce the fatigue life expectancy of the dual spring set. The magnitude of the impact forces and the extent to which it will reduce the fatigue life expectancy were not evaluated, as this is not within the scope of this project. The failure modes observed on both springs originated from the surface and progressed by fatigue before the final brittle failure.

5.1.3 Optimisation of the alternative materials

The unavailability of SAE 5160 spring steel in the near future and the increased payload necessitated the development of springs from alternative high-strength spring steel. In order to address the problem statement, the application, geometrical design, material selection, manufacturing process, parameters, and suitability of the spring were considered. A system thinking approach assisted with key learnings from the existing manufacturing process during the optimisation of the three identified spring steel grades to replace SAE 5160 spring steel.

It also assisted in defining the problem statement and in avoiding inherent defects associated with the manufacturing process. This is due to the adopted manufacturing process being similar but with different process parameters. The failure investigation makes some unique and overlooked but crucial findings.

5.1.4 Deformation behaviour of material

An important element of spring manufacturing that relates to material selection and management is the coiling and material response thereafter. Bogie springs are deformed into continuous coils at high temperatures to maintain the desired spring effect. The stress relaxation analysis revealed that 52CrMoV4 requires higher force to deform at 860°C, while 54SiCr6 requires the least amount of force. Even though the stress relaxation between 55Cr3 and 54SiCr6 was comparable, the relaxation for 52CrMoV4 was more over time. The experiments showed that relaxation could be countered by rapid cooling.

It was also found that a pitch angle of 0.4° above the nominal pitch angle results in lower fatigue life due to high stress. Additionally, one of the key findings of the research was that various spring steel grades have stress relaxation abilities during thermomechanical deformation and cooling. As a result, the pitch angle may be altered by stress relaxation that follows deformation and cooling. Furthermore, the designers of the springs should carefully consider the pitch angle and the thermomechanical properties of the material, and its effect on the fatigue life of the springs. A thorough understanding of the thermomechanical behaviour of spring steel is critical during the material selection of coiled springs.

5.1.5 Surface properties of material

Further to the internal microstructures and mechanical properties of the steel, the surface interaction with the heat treatment environment is important. The surface properties of the spring steel influence the fatigue life of the spring. It therefore, becomes important to understand the oxidation and decarburisation rates so that it can be managed during heat treatment. Depending on the heat treatment process and intentions, oxidation can be used to slow down decarburisation (Matjeke *et al.*, 2019). In that case, spring steel that readily forms an oxide scale during heat treatment must be selected.

Size reduction must also be considered in spring steel that forms high oxide scales. The information generated in this study may assist in the process of controlling and limiting oxidation. Heat treatment optimisation of various spring steels requires precise knowledge of the parameters and how they influence the behaviour of the spring steel during the heating and cooling processes. The DSC curves of the steels heated to 860°C showed high temperature endothermic peaks during heating and exothermic peaks during cooling in air. The achieved peaks for the different spring steel grades were measured at different temperatures.

The graphs show that 55Cr3 required 4606 mW/g heat flow to reach the eutectoid temperature, while 54SiCr6 and 52CrMoV4 required 5679 mW/g and 7200 mW/g, respectively. Therefore, the heat treatment process for the three grades of steel had to be varied according to their specific heat capacity. This is important with respect to economic production, as it will also influence the temperature and amount of time the spring steels spend within the furnace, i.e. energy consumption. Another significant observation made when conducting thermal analysis was the determination of the oxidation rate for each spring steel grade. Calorimetry analysis indicated a higher oxidation rate for 55Cr3, followed by 5SiCr6 and 52CrMoV4, respectively.

The microstructure of 54SiCr6 displayed severe decarburisation in comparison to 55Cr3 and 52CrMoV4. This was found after exposing the samples to 860°C for one hour, followed by tempering at 450°C for three hours. 54SiCr6 had a significantly higher silicon level compared to 55Cr3 and 52CrMoV4. 55Cr3 and 52CrMoV4 showed less decarburisation, which is attributed to protection offered by the thick oxidation scale. The observed behaviour is similar to that reported by Liu *et al.,* (2014).

Although oxidation may hinder decarburisation, the heat treatment and calorimetry revealed that the relationship between the oxidation rate and decarburisation is non-linear. With the cooling segment at 120°C per minute, the eutectoid temperature of each steel grade was found to be lower than the heating eutectoid temperature. The low temperature phase transformation peaks were predicted using CCT diagrams and Andrew’s equation. The Ms temperatures (generated from JmatPro and Andrew’s equation) were comparable to each other with the exception of 54SiCr6, which contained a significant silicon content. 54SiCr6’s behaviour is attributed to the fact that Andrew’s equation does not consider the amount of silicon present.

It is well known that the amount of carbon influences mechanical properties significantly; however, silicon can substantially influence hardenability. Carbon reduces iron oxide to form carbon monoxide and iron, thus causing decarburisation (Chen and Yuen, 2003). A stable oxide scale, which forms on the surface of the steel, hinders the progression of decarburisation. The addition of aluminium and silicon in steel retards oxidation by forming aluminium and silicon-rich scales, which prevent the diffusion of iron ions. Silicon readily oxidises to form silicon oxides at high temperatures (Abidin *et al.*, 2013).

Due to the inadequate cooling capability of the DSC instrument used, rapid quenching could not be carried out. However, phase transformation from austenite to martensite was predicted using JmatPro and Andrew’s equation. The established Ms temperature will aid in determining the critical cooling rate and consequently selecting an appropriate quenching media.

5.1.6 Heat treatment refinement: Quenching

To achieve the minimum required strength for the specific spring design, the alternative spring steel grades were subjected to a heat treatment refinement process. In order to develop a heat treatment refinement process, the exact critical transformation temperatures for the specific spring steel grades are key. Additionally, a large aspect of steel hardening involves selecting quenchants for the appropriate materials with the intention of achieving the desired metallurgical and mechanical properties without causing quench cracks. In line with

Hypothesis 02, selecting the quenching media for the specific spring steel grades based on the critical transformation temperatures can achieve the desired microstructure and mechanical properties without causing quench cracks.

Suitable quenchants were determined using CCT curves and dilatometric data, which were generated using the chemical composition of the selected steel grades, along with their cooling rates determined during the experiments. The quenchants were selected based on their quenching capabilities with respect to the three selected spring steel grades. Oil A was found to be suitable for quenching 54SiCr6, while Oil B was found to be appropriate for quenching 55Cr3 and 52CrMoV4. The additional information on critical transformation temperatures will form part of literature for future heat treatment developments.

The dilatometric measurements for 54SiCr6 showed that Ms temperature is high compared to 55Cr3 and 52CrMoV4. This is one of the reasons why Oil A was selected for quenching 54SiCr6. Oil B was selected to quench 55Cr3 and 52CrMoV4 due to its capability of achieving the desired microstructure between 180°C and 250°C without causing quench cracks. Another important aspect that was revealed by the dilatometric experiments was the stabilisation of austenite. 55Cr3 stabilises relatively easily when heated at 860°C compared to 52CrMoV4 and 54SiCr6. This is attributed to lower the Ac1 and Ac3 temperatures of 55Cr3.

54SiCr6 had the highest Ac1 and Ac3 temperatures, followed by 52CrMoV4. The different Ms temperatures of the three spring steel grades significantly influenced the materials' hardenability. The Ms temperature and CCT curve that are on the extreme right-hand side illustrate that 54SiCr6 was found to be more readily hardenable than 55Cr3 and 53CrMoV4. This is attributed to the substantial silicon content in 55SiCr6, which shifted the CCT curve to the right.

5.1.7 Critical transformation temperatures

To achieve the desired microstructures of spring steel, the exact Ac3 temperature must be known for solution treating purposes. Austenite solution treating at the wrong temperature may result in undesirable microstructures. Austenite treating at too high a temperature may result in larger microstructures prior to austenite grains, while austenite treating at too low a temperature may result in some of the carbon not being in solution. Therefore, knowing the exact critical transformation is a key step in the optimisation process.

The actual thermal test measurements were compared to the JMatPro estimations and Andrew's equation results. It was found that there was no unanimity between the test results, JMatpro, and Andrew's equation outputs. The optimisation of the heat treatment parameters is largely dependent on the Ac1, Ac3, and Ms temperature. A higher Ac1 means a longer cooling time. It is evident from the results that a general approach would be ineffective to optimise the heat treatment parameters for the three spring steel grades.

5.1.8 Optimisation experiments

The broad scope of this research was to improve the mechanical properties of bogie springs by optimising the heat treatment process parameters. The main objective of optimising the various spring steel grade properties is to increase the lifespan of the springs.

5.1.8.1 Quenching

According to Allen, Fletcher, and King, (1987), various quenching media qualities and performances have been studied in general terms. The use of the quenching oils deployed in this study introduced a premise that has never been investigated before, i.e. different types of quenching oils will achieve different quenching outcomes.

It is notable that the high cooling rates of Oil B were most likely to cause the quench cracks observed on the failed springs. This was discussed in the failure investigation. While the slow cooling rates of Oil A were unlikely to achieve the desired microstructure, there were no signs of quench cracking on all three spring steel grades. Based on different characteristics and behaviours, as observed in Figures 4.36 and 4.37, it is my view that different quenching oils will achieve different quenching outcomes in similar conditions.

The general microstructure of the as-quenched steel rods was martensitic and tempered martensite after tempering. This means that the selected quenchants were adequate to produce the desired microstructure.

5.1.8.2 Tempering temperature and soaking time

If the strength of the spring steel is not adequate, the spring may experience coil contact when loaded, which creates a stress-raiser on the surface and consequently, the fatigue life of the spring will be reduced. This phenomenon is illustrated in the case study presented in the second failure investigation. Therefore, due to the increase in the payload and speed of railway vehicles, it is paramount that the steel used for the springs has high strength and excellent ductility. This was achieved through optimising the heat treatment process by selecting the most appropriate austenitising temperature and experimenting with the tempering temperatures and soaking times.

The optimisation of heat treatment process parameters requires a delicate balance between tempering temperature and soaking time. This will influence the strength and elongation percentage of the spring steel. The findings of the heat treatment optimisation revealed that in terms of strength and ductility, the optimum tempering temperature for 55Cr3, 54SiCr6, and 52CrMoV4 is 450°C. 55Cr3 showed superiority, while 54SiCr6 showed the least strength of the three.

The higher the tempering temperature and soaking time proved to trade strength with ductility. However, that was not the case with respect to 52CrMoV4. This is attributed to secondary hardening on 52CrMoV4 introduced by the difference in the soaking temperatures, which is attributed to the presence of molybdenum and vanadium carbide precipitates. The stress-strain graph of 52CrMoV4 also showed an interesting behaviour within the elastic range. This phenomenon was not investigated further, however, it falls within the scope to be investigated in the future.

According to Afrin *et al.* (2007), the hardening capacity of material can be regarded as the ratio of yield strength and UTS. The yield strength is often regarded as the amount of stress predetermined for plastic deformation to occur. According to ASTM spring design manual (BS EN 13906-1, 2002), the UTS is a critical parameter in determining the fatigue resistance of a spring. 55Cr3 and 54SiCr6 showed a similar YS:UTS ratio. However, the strain hardening coefficient was inconsistent with each other for the same heat treatment cycle.

52CrMoV4 showed a higher YS:UTS ratio compared to 55Cr3 and 54SiCr6, and the strain hardening coefficient was comparable to that of 55Cr3. The strain hardening coefficient of 54SiCr6 was significantly higher than that of 55Cr3 and 52CrMoV4, which theoretically means that 54SiCr6 has good ductility compared to 55Cr3 and 52CrMoV4. Of the three materials, 54SiCr6 showed lower UTS, yield strength, and elongation percentage, with the exception of the cycle tempered at 410°C. The yield strength of 52CrMoV4 proved to be superior of the three materials, despite the UTS being dominated by that of 55Cr3. Even though there are substantial differences between the yield strength of 55Cr3 and 52CrMoV4, the elongation percentages are comparable.

Future studies regarding the use of UTS or yield strength as design parameters are necessary, given that 55Cr3 showed superior UTS, while 52CrMoV4 showed superior yield strength despite comparable elongation percentages. However, despite the SAE spring design manual calling for the UTS as a design parameter, designers use von Misses to determine the structural integrity of the spring, making the yield strength a significant part of the design parameter. On the contrary, Shin, Lee and Hwa Ryu, (1999) found that the fatigue properties of springs can be pre-estimated with tensile strength.

According to Dieter, (1988), there is an empirical relationship of the strength being 3.4 times the hardness. Despite 54SiCr6 showing superior micro-Vickers hardness properties, it responded to the heat treatment cycles with lower tensile and hardness properties after tempering. The hardness properties of 55Cr3 and 52CrMoV4 were consistent with the tensile properties.

Hertzberg (1996) stated that true plastic strain at necking instability is numerically equal to strain hardening exponents. The strain hardening exponent determined by plotting the log-log plot of the true stress-strain curve between the yielding point and UTS was comparative to the Hertzberg empirical method. Generally, the strain hardening exponent increased with the increase in tempering temperature. This study found that there is no relationship between Afrin's hardening capacity and the strain hardening exponent. It is my submission that the strain hardening exponent is influenced by heat treatment and chemical composition, however, further studies are required to follow up on this finding.

5.1.9 Corrosion

The design and tensile properties are not the only considerations when selecting spring material. Corrosion resistance and SCC should also be considered. Generally, corrosion reduces the fatigue life of steel by approximately 50% (Croft, 1981). It is for this reason that the properties of the three spring steel grades are optimised and evaluated against general corrosion and SSRT embrittlement.

52CrMoV4 was the most corrosive resistant, while 54SiCr6 showed the least corrosion resistance of the three steel grades. The superior corrosion resistance can be attributed to the 1.1% of chromium present in 52CrMoV4. Although 55Cr3 and 54SiCr6 had 0.8% chromium, respectively, the presence of 0.1% nickel and 0.9% manganese influenced the corrosion resistance of 55Cr3 to be more than that of 54SiCr6. These are important considerations as it could mean an additional corrosion protection process, as well as an increase in the cost of the spring and future maintenance.

With respect to SSRT, 410°C tempering temperature showed prominent susceptibility, while the risk reduced with the increase in tempering temperature. This can be observed with a gradual increase in elongation percentage when increasing temperatures. It is worth noting that 54SiCr6 showed superior resistance of the three steel grades, followed by 55Cr3. In all cases, the SSRT degraded the elongation properties of the three steels. However, 55Cr3 and 54SiCr6 were more susceptible.

Weather conditions where the spring will operate under stresses is another area of focus. Some bogie springs operate in the coast while others operate inland; in a South African climate that rarely reaches -4°C in winter. The impact strength at 23°C, -7°C, and -20°C were evaluated. The results at 23°C and -7°C showed little difference. However, the difference was substantial at -20°C. The number of samples tested are a limitation.

Chapter 6 : Conclusions

The study was able to overcome the problem of material shortage and resolve potential manufacturing-related defects that could shorten the lifespan of bogie springs. The initial task was to solve material scarcity by designing tests to optimise three carefully selected spring steel grades manufactured by a local steel mill. Optimising each step of the spring development in detail added to the complexity that comes with balancing the system's elements, such as geometric design, material selection, quenching oil selection, and process parameters. In the end, all of these factors were weighed together. Having considered the microstructures, strength, and ductility, the ultimate tempering parameter for the three steels tempered at 450°C were considered to be the most structurally suitable and durable for the specific spring design.

Another factor to consider when developing bogie springs is the operational environment, as well as value-adding by coating the surface of the spring to protect it from corrosion. Of the three steels, 52CrMoV4 is the most suitable for usage in a coastal environment due to its good corrosion and SCC resistance. It is important to note that while coating the springs is a beneficial practice for preserving them from corrosion, care must be given to minimise mechanical damage to the coating as the damaged coating can accelerate galvanic corrosion. The three steels are suitable for use in inland environments, with 55Cr3 being the most suggested due to its superior strength and ductility. In the inland environment, no value-adding coating is required.

From a manufacturing perspective, 54SiCr6 was more resistant to oxidation but it was more susceptible to undesirable decarburisation. The other two steels showed some resistance to decarburisation, yet they had high oxidation rates. The oxidation can be countered by specifying the desirable rod size from the mill to accommodate the material loss. The effect of oxidation during manufacturing and decarburisation may have detrimental effects on the surface properties of the material. It should be highlighted that more research is needed to reach a point where material loss due to oxidation is known in relation to the design rod size. Decreased decarburisation on 55Cr3 was attributed to a high oxidation scale.

54SiCr6 showed less oxidation and high decarburisation attributed to a significant amount of silicon. Decarburisation introduces metallurgical notch effects; therefore, it is undesirable, and designers can accommodate oxidation by carefully selecting the rod dimensions. In terms of energy consumption and production time, 54SiCr6 will take longer to homogenize austenite than 55Cr3 and 52CrMoV4 due to higher Ac1 and Ac3. Steel grade 55Cr3 will spend the least time in the furnace of the three. These are some of the additional information that this study can contribute to the unavailable knowledge of these specific steels.

The three steels were optimised by tailor-making the heat treatment process and selecting the appropriate quenching media to be fit for purpose. This study further proves that optimum mechanical properties can be achieved by selecting quenching media with the most appropriate cooling rates for the steel grade. The most suitable quenching oils were selected for the specific steel grades that will produce desired microstructures without causing quench cracking. The failure of the springs was caused by surface quench cracking, which acted as a precursor for fatigue cracking and subsequent failure. The immediate cause of spring failure was found to be micro-quench cracking caused by rapid cooling attributed to the deterioration of the quenching media.

The quenching oil that was initially suitable for the specific spring steel degraded and lost its original properties over time. It is, therefore, important that the quenching oil properties are regularly monitored to avoid using degraded oil for quenching operations due to crack formation. In another case study, the immediate cause of premature spring failure was found to be inconsistent pitch angle, which occurred during the coiling process. The study found that pitch angle reduces the fatigue life of the spring when there is a deviation from the design pitch angle. The immediate cause of premature spring failure was found to be inconsistent pitch angle, which occurred during the coiling process.

References

Abidin, M. I. Z., Mahmud, J., Latif, M. J. A., & Jumahat, A. (2013). Experimental and numerical investigation of SUP12 steel coil spring. *Procedia Engineering*, *68*, 251–257. https://doi.org/10.1016/j.proeng.2013.12.176

Adasooriya, N. D., Hemmingsen, T., & Pavlou, D. (2017). Fatigue strength degradation of metals in corrosive environments. *IOP Conference Series: Materials Science and Engineering*, *276*(1). https://doi.org/10.1088/1757-899X/276/1/012039

Afrin, N., Chen, D. L., Cao, X., & Jahazi, M. (2007). Strain hardening behavior of a friction stir welded magnesium alloy. *Scripta Materialia*, *57*(11), 1004–1007. https://doi.org/10.1016/j.scriptamat.2007.08.001

Ahmed, S. R., & Khanna, S. (2020). Heliyon Investigation into features of fracture toughness of a transparent E-glass fi ber reinforced polyester composites at extreme temperatures. *Heliyon*, *6*, e03986. https://doi.org/10.1016/j.heliyon.2020.e03986

Ahn, S. H., Heo, J., Kim, J., Hwang, H., & Cho, I. S. (2020). The effect of baking heat treatment on the fatigue strength and life of shot peened 4340M landing gear steel. *Materials*, *13*(24), 1–11. https://doi.org/10.3390/ma13245711

Allen, F. S., Fletcher, A. J., & King, S. (1987). On the quenching characteristics of polyalkylene glycol solutions in water. *Materials Science and Engineering*, *95*(C), 247–257. https://doi.org/10.1016/0025-5416(87)90516-7

Al-Oqla, F. M., & Sapuan, S. M. (1971). Materials Selection. *Metal Progr*, *99*(1). https://doi.org/10.4324/9780203475034_chapter_7

Annan, K. (2015). The study of austenite grain growth in Nb-Ti-V microalloyed steels after reheating, during and after rough hot rolling. *Thesis,* University of Pretoria.

Archie, F. (2018). Damage nucleation in DP-steels: experimental characterization of the contributing microstructural parameters. *Thesis*, Rheinisch -Westfälischen Technischen Hochschule Aachen. https://doi.org/10.18154/RWTH-2018-229075

Ardehali Barani, A., Ponge, D., & Raabe, D. (2006). Refinement of grain boundary carbides in a Si-Cr spring steel by thermomechanical treatment. *Materials Science and Engineering A*, *426*(1–2), 194–201. https://doi.org/10.1016/j.msea.2006.04.002

Artaraz, F., & Sánchez Beitia, S. (1991). An unsuitable residual stress state in train springs originated by shot peening. *International Journal of Fatigue*, *13*(2), 165–168. https://doi.org/10.1016/0142-1123(91)90009-N

ASM Technical Books (2008). Elements of Metallurgy and Engineering Alloys. (First edit) ASM Intarnational. https://doi.org/10.31399/asm.tb.emea.9781627082518

Atkins, M. (1980). Atlas of continous cooling transformation diagrams for engineering steels. Second edit, *American Society for Metals.*

Avner, S. H. (1998). Introduction to Physical Metallurgy. Student edit, *MCGraw Hill*

Baek, S. G., Shin, B., Lee, S. W., Choi, Y. S., Kim, J., & Koo, J. C. (2013). Optimization of high speed EMU suspension parameters for vibration reduction. *Journal of Mechanical Science and Technology*, *27*(2), 305–311. https://doi.org/10.1007/s12206-012-1246-1

Barbacki, A., & Mikołajski, E. (1998). Optimization of heat treatment conditions for maximum toughness of high strength silicon steel. *Journal of Materials Processing Technology*, *78*(1–3), 18–23. https://doi.org/10.1016/S0924-0136(97)90457-X

Belov, B. G., Zakharov, E. K., Zubova, L. V., & Smirnova, A. V. (1976). Structure and properties of a spring alloy for operation at low temperatures *(3).* Plenum Publishing Corporation.

Bodin, J., & Segerberg, S. (2005). IVF SmartQuench– Application Examples and New Functions. *Presentation*, 1–34. http://www.thermoprocess.fr/documents/presentation_new_tool_for_calculation_of_heat_transfer_coefficients_microstructure_and_hardness_from_the_cooling_curve_berlin_2007.pdf

Boysen, H. E. (2010). Developments in railway freight transportation between scandinavia and germany. *6th South North Axis University Think Tank Conference*, *April*.

BS EN 10089: (2002) Hot rolled steels for quenched and tempered springs — Technical delivery conditions.

BS EN 13906-1. (2002). Cylindrical helical springs made from round wire and bar calculation and design.

Buczek, A., & Telejko, T. (2013). Investigation of heat transfer coefficient during quenching in various cooling agents. *International Journal of Heat and Fluid Flow*, *44*, 358–364. https://doi.org/10.1016/j.ijheatfluidflow.2013.07.004

Cahn, R. W., & Haasen, P. (1996). Physical Metallurgy (Fourth edi). North Holland.

Cain, T. (1984). Hardening, tempering, and heat treatment (First edit). Argus books.

Callister, W. (2001). Fundamentals of Materials Science and Engineering: An Introduction. (Seventh edit), John Wiley & Sons, Inc.

Capus, J. M., & Mayer, G. (1960). Metallurgia. *Metallurgical Transactions A*, *62*(7), 133. https://doi.org/10.1007/BF02664814

Chang, Y.-N., & Wei, F.-I. (1989). Review High temperature oxidation of low alloy steels. *Journal of Materials Science*, *24*, 14–22. https://doi.org/10.1007/BF00660927

Chatterjee, S. (2006). Transformations in TRIP-assisted Steels: Microstructure and Properties. *Thesis*, University of Cambridge.

Chen, N., Han, L., Zhang, W., & Hao, X. (2007). Enhancing mechanical properties and avoiding cracks by simulation of quenching connecting rods. *Materials Letters*, *61*(14–15), 3021–3024. https://doi.org/10.1016/j.matlet.2006.10.078

Croft, N. H. (1981). Fracture characteristics and mechanisms. *Thesis*, University of Sheffield.

Crompton, R., Fessehaie, J., Kaziboni, L., & Zengeni, T. (2017). Railway Locomotives and Transnet: A Case Study. *SSRN Electronic Journal*, *January*. https://doi.org/10.2139/ssrn.2970938

Dakhore, M., & Bissa, B. (2013). Failure analysis of locomotive suspension. *International Monthly Refereed Journal of Research In Management & Technology*, *II*, 96–104. ISSN – 2320-0073.

Das, S. K., Mukhopadhyay, N. K., Kumar, B. R., & Bhattacharya, D. K. (2007). Failure analysis of a passenger car coil spring. *Engineering Failure Analysis*, *14*(1), 158–163. https://doi.org/10.1016/j.engfailanal.2005.11.012

Daudpoto, J., Soother, D. K., Shaikh, S. A., Hussain, T., & Memon, Z. A. (2021). Fatigue failure of SUP-9 spring steel. *Materials Research Express*, *8*(6), 066509. https://doi.org/10.1088/2053-1591/ac0773

de Crescenzo, F., & Salvini, P. (2019). Two-dimensional discrete model for buckling of helical springs. *Procedia Structural Integrity*, *24*(2019), 28–39. https://doi.org/10.1016/j.prostr.2020.02.003

Dieter, G. E. (1988). Mechanical Metallurgy. (SI metric edit) *McGraw-Hill Book* Company.

Dieter, G. E., & Bacon, D. (1962). Mechanical metallurgy. *Journal of the Franklin Institute* (Vol. 273, Issue 4, p. 338). https://doi.org/10.1016/S0016-0032(62)91145-6

Eom, B. G., Kang, B. B., & Lee, H. S. (2013). A study on running stability assessment methods for 1/5 small scaled bogie of saemaul using small-scaled derailment simulator. *International Journal of Precision Engineering and Manufacturing*, *14*(4), 589–598. https://doi.org/10.1007/s12541-013-0079-x

Fedin, V. M., & Borts, A. I. (2009). Heat treatment and thermoplastic treatment. *Metal Science and Heat Treatment*, *51*, 544–552.

Fedin, V. M., Devyatkin, V. P., Strok, L. P., & Latyshkova, P. (1987). Improving the quality and extending the life of springs for railroads rolling stock. 42–45, *Plenum Publishing Corporation.*

Fragoudakis, R., Karditsas, S., Savaidis, G., & Michailidis, N. (2014). The effect of heat and surface treatment on the fatigue behaviour of 56SiCr7 spring steel. *Procedia Engineering, 74*, 309–312. https://doi.org/10.1016/j.proeng.2014.06.268

Fragoudakis, R., Savaidis, G., & Michailidis, N. (2017). Optimizing the development and manufacturing of 56SiCr7 leaf springs. *International Journal of Fatigue*, *103*, 168–175. https://doi.org/10.1016/j.ijfatigue.2017.05.016

Frazier, R. H., Boulger, F. W., & Lorig, C. H. (1956). Influence of silicon and aluminum on the properties of hot-rolled steel. *J. Metals,* (*8*)*,* 1269–1276. https://doi.org/10.1007/BF03377864

Ganesh, P., Sundar, R., Kumar, H., Kaul, R., Ranganathan, K., Hedaoo, P., Tiwari, P., Kukreja, L. M., Oak, S. M., Dasari, S., & Raghavendra, G. (2012). Studies on laser peening of spring steel for automotive applications. *Optics and Lasers in Engineering*, *50*(5), 678–686. https://doi.org/10.1016/j.optlaseng.2011.11.013

Ghate, P., Shankapal, S. R., & H, M. G. M. (2012). Failure Investigation of a Freight Locomotive Suspension Spring and Redesign of the spring for durability and ride index. *SASTECH journal*. *11*(2), 23–29.

Glebov, A. G., Arabey, A. B., Lutsenko, A. N., Pikunov, M. V., & Nemtinov, A. A. (2010). Role of silicon in the macro- and microstructure of high-strength steel. *Steel in Translation*, *40*(5), 398–406. https://doi.org/10.3103/S0967091210050025

Golden, A. (2017). The effect of heat treatment on the through thicknesss properties of vanadium microalloyed forging steel. *Thesis,* Colorado School of Mines.

Gorni, A. A. (1976). Steel Forming and Heat Treating Handbook (First edit). *McGraw-Hill Book Company.* https://doi.org/10.1016/S0026-0576(03)90166-8

Goulas, C. (2019). Developing novel heat treatments for automotive spring steels : Phase transformations , microstructure and performance. *Thesis,* Delft University of Technology https://doi.org/10.4233/uuid

Grajcar, A., Zalecki, W., Burian, W., & Kozłowska, A. (2016). Phase equilibrium and austenite decomposition in advanced high-strength medium-mn bainitic steels. *Metals*, *6*(10), 1–14. https://doi.org/10.3390/met6100248

Grzegorz, G. (2013). The effect of austenitizing temperature on prior austenite grain size in martensitic cast steel. *Solid state phenomena 197, 53 - 5*. https://doi.org/10.4028/www.scientific.net/SSP.197.53

Guerra-Fuentes, L., Deaquino Lara, R., Hernandez-Rodriguez, M. A. L., Salinas-Rodriguez, A., & Garcia-Sanchez, E. (2016). Thermal stability and phase transformations of a FV535 steel. *Journal of Thermal Analysis and Calorimetry*, *123*(1), 27–33. https://doi.org/10.1007/s10973-015-4948-7

Gupta, S. (2014). Micromechanical modeling of martensitic phase transformation in steels based on non-local crystal plasticity. *Thesis,* Ruhr-Universität Bochum.

Gutiérrez, I. (2014). Effect of microstructure on the impact toughness of high strength steels. *Revista de Metalurgia, 50(4).* http://dx.doi.org/10.3989/revmetalm.029.

Harada, Y., Tanaka, S., Itoh, M., & Nakatani, M. (2014). Effect of microshot peening on fatigue life of spring steel SUP9. *Procedia Engineering*, *81,* 1493–1498. https://doi.org/10.1016/j.proeng.2014.10.179

Hasan, H. S., Peet, M. J., Jalil, J. M., & bhade. (2011). Heat Transfer Coefficients during Quenching of Steels. *Heat mass transfer. 47(3):*315-321 doi: 10.1007/S00231-010-0721-4.

Hattingh, G. D. (1998). The fatigue propertiesof spring steel. *Thesis,* University of Plymouth.

Hertzberg, R. W. (1996). Deformation and fracture mechanics of engineering materials. . (Fourth edi). *John Wiley & Sons, Inc., ISBN 0-471-01214-9.*

Hou, L., Cheng, H., Li, J., Li, Z., Shao, B., & Hou, J. (2012). Study on the cooling capacity of different quenchant. *Procedia Engineering*, *31*, 515–519. https://doi.org/10.1016/j.proeng.2012.01.1061

Ibrahim Al-Zuhairi, H. M., Hamza, A. K., Mahdi, B. S., & Al-Alkawi, H. J. M. (2020). Effect of Heat Treatment on Toughness and Fatigue Behavior Strength of Steel CK45. *IOP Conference Series: Materials Science and Engineering*, *881*(1). https://doi.org/10.1088/1757-899X/881/1/012069

Izadi, A., Nabipour, M., & Titidezh, O. (2020). Cost Models and Cost Factors of Road Freight Transportation : A Literature Review and Model Structure. *Fuzzy Information and Engineering*, *0*(0), 1–22. https://doi.org/10.1080/16168658.2019.1706960

Jena, P. K., Organisation, D., & Kumar, K. S. (2014). Effect of Tempering Temperature on Microstructure , Texture and Mechanical Properties of a High Strength Steel. *International Journal of Manufacturing, Materials, and Mechanical Engineering, 4(3)* 33 - 49. https://doi.org/10.4018/ijmmme.2014070102

Ji-lin, L. I., & Kai-hong, Z. (2013). The Effects of Nodulizer on the Microstructure and Mechanical Properties of Austempered Ductile Iron. *Tehnički vjesnik 25(2*), 635-642. https://doi.org/10.17559/TV-20170124120729

Ji, S., Huang, H., Huang, G., Qin, X., & Shui, G. (2013). Experimental study on fatigue damage of train K6 spring. *Przegląd elektrotechniczny (3),* 131–133. ISSN 0033-2097, R. 89 NR 3b/2013.

Joshi, R., Chaudhari, S., Choudhari, D., & Chaugule, P. (2015). Failure investigation of axle box spring of railway 16-ton coaches. *International Journal of Research in Engineering and Technology, 04 (04)* 442–446.

Juvinall, R. C. (1967). Engineering considerations of stress, strain, and strength. (First edit). McGraw Hill.

Kain, V. (2012). Corrosion-resistant materials. *Functional Materials*. https://doi.org/10.1016/B978-0-12-385142-0.00012-X

Kasonde, M. (2005). Optimising the mechanical properties and microstructure of armoured steel plate in the quenched and tempered condition. *Thesis,* University of Pretoria.

Khalifeh, A. (2019). Stress Corrosion Cracking Damages. *Failure Analysis*, https://doi.org/10.5772/intechopen.80826

Khovova, O. M., Piskunova, E. N., Dumanskii, I. O., & Plokhikh, A. I. (2010). A study of the properties of spring alloy 36nkhtyu after rapid quenching and combined aging. *Metal Science and Heat Treatment*, *52 (5*) 243 - 250. doi: 10.1007/s11041-010-9265-y

Kobasko, N. I. (2021). Quench Process and Steel Chemistry Optimization to Prevent Quench Cracking during Hardening of Splined Semi – Axles. *European Journal of Applied Physics*, *3*(2), 23–28. https://doi.org/10.24018/ejphysics.2021.3.2.60

Kobasko, N. I., Aronov, M. A., & Powell, J. A. (2009). Intensive Quenching of Steel Parts : Equipment and Method Intensive Quenching of Steel Parts : Equipment and Method. *7th IASME / WSEAS International Conference on heat transfer, thermal engineering and environmen*t. doi: 10.13140/RG.2.2.17040.56328

Kobelev, V. (2020). Delayed presetting of helical springs. *Mechanics Based Design of Structures and Machines*, *48*(1), 122–132. https://doi.org/10.1080/15397734.2019.1669457

Koch, G. H. (2001). Tests for stress-corrosion cracking. *Advanced Materials and Processes, 159*(8), 36–38.

Komazaki, S. I., Kobayashi, K., Misawa, T., & Fukuzumi, T. (2005). Environmental embrittlement of automobile spring steels caused by wet-dry cyclic corrosion in sodium chloride solution. *Corrosion Science*, *47*(10), 2450–2460. https://doi.org/10.1016/j.corsci.2004.10.008

Kostryzhev, A., Singh, N., Chen, L., Killmore, C., & Pereloma, E. (2018). Comparative Effect of Mo and Cr on Microstructure and Mechanical Properties in NbV-Microalloyed Bainitic Steels. *Metals*, *8*(2), 134. https://doi.org/10.3390/met8020134

Kubit, A., Bucior, M., Zielecki, W., & Stachowicz, F. (2016). The impact of heat treatment and shot peening on the fatigue strength of 51CrV4 steel. *Procedia Structural Integrity*, *2*, 3330–3336. https://doi.org/10.1016/j.prostr.2016.06.415

Kumar, B. Ravi., Bhattacharya, D. K., Das, S. K., & Chowdhury, S. G. (2000). Premature fatigue failure of a spring due to quench cracks. *Engineering Failure Analysis*, *7*(6), 377–384. https://doi.org/10.1016/S1350-6307(99)00048-5

Kumbhalkar, M. A., Yenarkar, P. Y. L., & Grover, A. K. (2011). Failure Analysis of Inner Suspension Spring of Railway Engine : A Case Study. *Proc. of Int. Conf. on Advances in Robotic, Mechanical Engineering and Design*. doi: 02.ARMED.2011.01.22.

Kundu, S. (2007). Transformation Strain and Crystallographic Texture in Steels. *Thesis*, University of C ambridge.

Leach, L. J. (2013). The role of Cr and Mo alloying element additions on the kinetics and effects of Upper Bainite formation in quench and tempered plate steels. *Thesis* University of Pretoria.

Lee, W. B., Hong, S. G., Park, C. G., & Park, S. H. (2002). Carbide precipitation and high-temperature strength of hot-rolled high-strength, low-alloy steels containing Nb and Mo. *Metallurgical and Materials Transactions A: Physical Metallurgy and Materials Science*, *33*(6), 1689–1698. https://doi.org/10.1007/s11661-002-0178-2

Li, Z., Pradeep, K. G., Deng, Y., Raabe, D., & Tasan, C. C. (2016). Metastable high-entropy dual-phase alloys overcome the strength–ductility trade-off. *Nature*, *534* 227–230. https://doi.org/10.1038/nature17981

Lingamanaik, S. N., & Chen, B. K. (2014). Microstructural and thermo-mechanical analysis of quench cracking during the production of bainitic-martensitic railway wheels. *Engineering Failure Analysis*, *40*, 25–32. https://doi.org/10.1016/j.engfailanal.2014.02.010

Ling, L., Li, W., Foo, E., Wu, L., Wen, Z., & Jin, X. (2017). Investigation into the vibration of metro bogies induced by rail corrugation. *Chinese Journal of Mechanical Engineering*, *30*(1), 93–102. https://doi.org/10.3901/CJME.2016.1018.121

Liu, M., Wang, C. H., Dai, Y. C., Li, X., Cao, G. H., Russell, A. M., Liu, Y. H., Dong, X. M., & Zhang, Z. H. (2017). Effect of quenching and tempering process on sulfide stress cracking susceptibility in API-5CT-C110 casing steel. *Materials Science and Engineering A*, *688*(November 2016), 378–387. https://doi.org/10.1016/j.msea.2017.01.067

Liu, S. Y., Liu, D. Y., & Liu, S. C. (2010). Effect of heat treatment on fatigue resistance of spring steel 60Si2CrVAT. *Metal Sci Heat Treat Engl Tr, 52*(1–2), 57–60.

Liu, Y. L., Xie, B., Zhang, Z., Zheng, Q. S., & Xu, Z. P. (2012). Mechanical properties of graphene papers. *J. Mech. Phys. Solids*, *60*(4), 591–605. https://doi.org/10.1016/j.jmps.2012.01.002

Liu, Y., Zhang, W., Tong, Q., & Wang, L. (2014). Effects of Temperature and Oxygen Concentration on the Characteristics of Decarburization of 55SiCr Spring Steel. *ISIJ International*, *54*(8), 1920–1926. http://dx.doi.org/10.2355/isijinternational.54.1920.

Loganathan, K. (2019). Testing of helical spring under compression test. *International Journal of Management, Technology And Engineering 8(11)*.

Luo, J., Mei, Z., Tian, W., & Wang, Z. (2006). Diminishing of work hardening in electroformed polycrystalline copper with nano-sized and uf-sized twins. *Materials Science and Engineering A*, *441*(1–2), 282–290. https://doi.org/10.1016/j.msea.2006.08.051

Mackenzie, D. S. (2009). The chemistry of oil quenchants. *Heat treating progress*

Mackenzie, S. (2008). Overview of the mechanisms of failure in heat treated steel components. *Failure Analysis of Heat Treated Steel Component.*

Maisuradze, M. v., & Ryzhkov, M. A. (2019). Phase transformations and microstructure of advanced engineering steels. *Materials Today: Proceedings*, *19*, 1985–1989. https://doi.org/10.1016/j.matpr.2019.07.057

Maisuradze, M. v., Ryzhkov, M. A., & Yudin, Y. v. (2015). Rapid Evaluation of the Cooling Capacity of Quenching Media. *Metal Science and Heat Treatment*, *57*(7–8), 515–518. https://doi.org/10.1007/s11041-015-9914-2

Mandal, G., Ghosh, S. K., Bera, S., & Mukherjee, S. (2016). Effect of partial and full austenitisation on microstructure and mechanical properties of quenching and partitioning steel. *Materials Science & Engineering A*, *676*(2016), 56–64. https://doi.org/10.1016/j.msea.2016.08.094

Manna, R. (2012). Heat Treatment. *Class Notes(presentation),* Banaras Hindu University

Manuel, F., & Cerda, C. (2017). Third Generation Advanced High Strength Steels via Ultrafast Heating. *Thesis,* Ghent University.

Ma, S. (2002). Characterization of the performance of mineral oil based quenchants using the CHTE Quench Probe System. *Thesis,* Worcester Polytechnic Institute.

Matjeke, V. J., Mukwevho, G., Maleka, A., & van der Merwe, J. W. (2018). Effect of heat treatment on strength and ductility of 52CrMoV4 spring. *IOP Conference Series: Materials Science and Engineering*. https://doi.org/10.1088/1757-899X/430/1/012044

Matjeke, V. J., van de Merwe, J. W., Mukwevho, G., & Phasha, J. M. (2019). Thermal characteristics of spring steels used in railway bogies. *SN Applied Sciences*, *October*. https://doi.org/10.1007/s42452-019-1546-5

Meigui, O., Chunlin, Y., Jie, Z., Qifan, X., & Huina, Q. (2017). Influence of Cr content and Q–P–T process on the microstructure and properties of cold-coiled spring steel. *Journal of Alloys and Compounds*. https://doi.org/10.1016/j.jallcom.2016.12.134

Merson, E. D., Krishtal, M. M., Merson, D. L., Eremichev, A. A., & Vinogradov, A. (2012). Effect of strain rate on acoustic emission during hydrogen assisted cracking in high carbon steel. *Materials Science and Engineering A*, *550*, 408–417. https://doi.org/10.1016/j.msea.2012.04.094

Mesplont, C. (2003). Phase transformations and microstructure - mechanical properties relations in Complex Phase high strength steels. *Thesis*, Universiteit Gent.

Mishra, A., & Aggarwal, M. L. (2020). Comparative deflection analysis of conical compression spring with standard constant rate helical spring. *IOP Conference Series: Materials Science and Engineering*, *804*(1). https://doi.org/10.1088/1757-899X/804/1/012010

Mohapatra, G., Sommer, F., & Mittemeijer, E. J. (2007). Calibration of a quenching and deformation differential dilatometer upon heating and cooling: Thermal expansion of Fe and Fe-Ni alloys. *Thermochimica Acta*, *453*(1), 31–41. https://doi.org/10.1016/j.tca.2006.11.007

Motyčka, P., & Kövér, M. (2012). Evaluation methods of dilatometer curves of phase transformations. *Recent Trends in Structural Materials (conference)*.

Mukherjee, I., & Rosolen, M. (2013). Thermal transitions of gelatin evaluated using DSC sample pans of various seal integrities. *Journal of Thermal Analysis and Calorimetry*, *114*(3), 1161–1166. https://doi.org/10.1007/s10973-013-3166-4

Mukhopadhyay, N. K., Das, S. K., Ravikumar, B., Ranganath, V. R., & Ghosh Chowdhury, S. (1997). Premature failure of a leaf spring due to improper materials processing. *Engineering Failure Analysis*, *4*, 161–170. https://doi.org/10.1016/S1350-6307(97)00013-7

Mukwevho, G. (2016). Failure investigation of 22E locomotive springs. *Report* Transnet

Murakami, Y., Kanezaki, T., & Sofronis, P. (2013). Hydrogen embrittlement of high strength steels: Determination of the threshold stress intensity for small cracks nucleating at nonmetallic inclusions. *Engineering Fracture Mechanics*, *97*(1), 227–243. https://doi.org/10.1016/j.engfracmech.2012.10.028

Martin, D.S., Caballero, F. G., Capdevila, C. & García de Andrés, C (2006). A contribution to the modelling of the austenitisation process in steels. *Metal Conference.*

Murtaza, G., & Akid, R. (2000). Empirical corrosion fatigue life prediction models of a high strength steel. *Engineering Fracture Mechanics*, *67*(5), 461–474. https://doi.org/10.1016/S0013-7944(00)00057-6

Nasirpouri, F., Alizadeh, H., & Hosseingholizadeh, M. (2011). Failure analysis of a carbon steel screw under the service in the presence of hydrogen sulphide. *Engineering Failure Analysis*, *18*(8), 2316–2323. https://doi.org/10.1016/j.engfailanal.2011.07.001

Naveen, S., Kiran, C. P., Das, M. P., Dilip, P. N., & Bharathi, V. V. P. (2014). Study on Bogie and Suspension System of an Electric Locomotive. *Internatinal Journal of Modern Engneering Research*, *4*,(4) 1–14.

Niu, G., Chen, Y. li, Wu, H. bin, Wang, X., & Tang, D. (2018). Corrosion behavior of high-strength spring steel for high-speed railway. *International Journal of Minerals, Metallurgy and Materials*, *25*(5), 527–535. https://doi.org/10.1007/s12613-018-1599-2

Özdem, Z., Özdem, T., Aksoy, Z., & Eruslu, S. Ö. (2013). An examination of different heat treatment effects to the fracture parameters of connecting rod made from C70S6 steel. *Fen Bilimleri Dergisi*, *25*(2), 75–90.

Pandit, A. S. (2011). Theory of the Pearlite Transformation in Steels. *Thesis*, University of Cambridge.

Pang, J. C., Li, S. X., Wang, Z. G., & Zhang, Z. F. (2013). General relation between tensile strength and fatigue strength of metallic materials. *Materials Science and Engineering A*, *564*, 331–341. https://doi.org/10.1016/j.msea.2012.11.103

Parkins, R. N. (1992). Mechanisms of Stress-corrosion Cracking. *Corrosion Science*. https://doi.org/10.1016/B978-0-08-052351-4.50064-9

Peng, F., Xu, Y., Han, D., & Gu, X. (2019). Kinetic models of multiple-stage martensite transformation and subsequent isothermal bainite formation excluding ε -carbide precipitation in intercritical quenching and partitioning steels. *Materials & Design*, *183*, 108183. https://doi.org/10.1016/j.matdes.2019.108183

Petrovic, D. S., Pirnat, M., Klancnik, G., Mrvar, P., & Medved, J. (2012). The effect of cooling rate on the solidification and microstructure evolution in duplex stainless steel A DSC study. *Journal of Thermal Analysis and Calorimetry*, *109*(3), 1185–1191. https://doi.org/10.1007/s10973-012-2370-y

Podgornik, B., Torkar, M., Burja, J., Godec, M., & Senčič, B. (2015). Improving properties of spring steel through nano-particles alloying. *Materials Science and Engineering A, 638,* 183–189. https://doi.org/10.1016/j.msea.2015.04.082

Pohjonen, A., Javaheri, V., Paananen, J., & Pyykkönen, J. (2021). Semi-Automatic Optimization of Steel Heat Treatments for Achieving Desired Microstructure. *Proceedings of The 61st SIMS Conference on Simulation and Modelling SIMS 2020, September 22-24, Virtual Conference, Finland*, *176*, 139–145. https://doi.org/10.3384/ecp20176139

Pop, D., Cluj-napoca, U. T., Haragas, S., Cluj-napoca, U. T., Popa, D., & Cluj-napoca, U. T. (2018). Helical spring with variable wire diameter. *Appl. Mechanics, 62 (3)*. Technical University of Cluj-Napoca, Roman

Popoola, L., Grema, A., Latinwo, G., Gutti, B., & Balogun, A. (2013). Corrosion problems during oil and gas production and its mitigation. *International Journal of Industrial Chemistry*, *4*(1), 35. https://doi.org/10.1186/2228-5547-4-35

Porteiro, J. L. (2010). Spring design optimization with fatigue. *Thesis,* University of South Florida.

Porter, D. A., & Easterling, K. E. (1992). Phase Transformations in Metals and Alloys. (Third edit) *CRC press*.

Prakash, T. L., Hara, J. O., & Malik, A. U. (1999). Studies on the stress corrosion cracking (SCC) behavior of various metals and alloys used in the desalination and power plants. *Technical report WSTA 4th Gulf Conference*.

Prawoto, Y., Ikeda, M., Manville, S. K., & Nishikawa, A. (2008). Design and failure modes of automotive suspension springs. *Engineering Failure Analysis*, *15*(8), 1155–1174. https://doi.org/10.1016/j.engfailanal.2007.11.003

Pyttel, B., Brunner, I., Kaiser, B., Berger, C., & Mahendran, M. (2014). Fatigue behaviour of helical compression springs at a very high number of cycles - Investigation of various influences. *International Journal of Fatigue*, *60*, 101–109. https://doi.org/10.1016/j.ijfatigue.2013.01.003

Rajakumar, S., & Karthiyaraj, M. (2021). Static structural analysis of helical compression spring materials. *International Journal of Engineering Development and Research*, 9(1).

Rakhshtadt, A. G. (1975). The problem of improving the properties of spring steels and alloys. *Plenum Publishing Corporation.*

Rakhshtadt, A. G. (1991). Structure and properties of carbon-containing spring steels after high-speed hardening and tempering. *Plenum Publishing Corporation, 7,* 57–63.

Rashid Khan, H. U., Siddique, M., Zaman, K., Yousaf, S. U., Shoukry, A. M., Gani, S., Sasmoko, Khan, A., Hishan, S. S., & Saleem, H. (2018). The impact of air transportation, railways transportation, and port container traffic on energy demand, customs duty, and economic growth: Evidence from a panel of low-, middle-, and high -income countries. *Journal of Air Transport Management*, *70*, 18–35. https://doi.org/10.1016/j.jairtraman.2018.04.013

Razavi, G. R., Rizi, M. S., & Zadeh, H. M. (2013). Effect of a Mo addition on the properties of high-Mn steel. *Materiali in Tehnologije*, *47*(5), 611–614.

Reddy, M. S., & Reddy, B. M. (2013). The Study of Premature Failure of Springs Used In Railway Coaches. *Journal of Mechanical and Civil Engineering (IOSR-JMCE) 8*(5), 19–28.

Reed-Hill, R. E. & Abbaschian, R. (1973). Physical_Metallurgy_Principles. (Third edit) PWS-KENT

Rui, Y. (2021). Research on the Correlation between Freight Transportation and National Economic Development. *E3S Web of Conferences* 253, *01008*, 1–5. https://doi.org/10.1051/e3sconf/202125301008.

Saad, A. A. (2012). Cyclic plasticity and creep of power plant materials. *Thesis*, University of Nottingham.

SAE AE-11. (1982). *:*Spring Design Manual. *Specification*

SAE J404 standard. (1980). Chemical composition of SAE alloy steels.

Sage, A. M. (1984). Vanadium in structural steels. *J. S. Afr. Inst. Min. Metall.*, *84*(5), 138–146.

Salihu, S. A. (2016). Assessment of Advanced High Strength Steels used in Auto Industry – A Review. *IJSRSET |2*(4), 565–571.

Sayyaadi, H., & Shokouhi, N. (2009). A new model in rail-vehicles dynamics considering nonlinear suspension components behavior. *International Journal of Mechanical Sciences*, *51*(3), 222–232. https://doi.org/10.1016/j.ijmecsci.2009.01.003

Scuracchio, B. G., de Lima, N. B., & Schön, C. G. (2013). Role of residual stresses induced by double peening on fatigue durability of automotive leaf springs. *Materials and Design*, *47*, 672–676. https://doi.org/10.1016/j.matdes.2012.12.066

Šebek, F., Kubík, P., Hůlka, J., & Petruška, J. (2016). Strain hardening exponent role in phenomenological ductile fracture criteria. *European Journal of Mechanics, A/Solids*, *57*, 149–164. https://doi.org/10.1016/j.euromechsol.2015.12.006

Shin, J. C., Lee, S., & Hwa Ryu, J. (1999). Correlation of microstructure and fatigue properties of two high-strength spring steels. *International Journal of Fatigue*, *21*(6), 571–579. https://doi.org/10.1016/S0142-1123(99)00010-9

Shi, R.-X., Yao, C.-F., & Hui, W. (2008). Effect of Si on behavior of oxidation and decarburization of medium carbon spring steels. *Spec. Steel, 29*

Shi, X.-B., Zhao, L.-Y., Wang, W., Zeng, B., Zhao, L.-J., Shan, Y.-Y., Shen, M.-G., & Yang, K. (2013). Decarburization sensitivities of several spring steels used for high-speed trains. *Cailiao Rechuli Xuebao/Transactions of Materials and Heat Treatment*, *34*(7), 47–52.

Smallman, R. E., & Bishop, R. J. (1999). Modern Physical Metallurgy and Materials Engineering. (Sixth edit), Butterworth-Heinemann 320–350. https://doi.org/10.1016/B978-075064564-5/50010-0

Šolić, S., Podgornik, B., & Leskovšek, V. (2018). The occurrence of quenching cracks in high-carbon tool steel depending on the austenitizing temperature. *Engineering Failure Analysis*, *92*(May), 140–148. https://doi.org/10.1016/j.engfailanal.2018.05.008

Spisák, B., & Szávai, S. (2019). Mechanisms of Stress Corrosion Cracking. *International Multidisciplinary Scientific Conference.* https://doi.org/10.26649/musci.2019.052

Stone, D., Dedmon, S., Pilch, J., & Cummings, S. (2010). Vertical Split Rim Wheels. *16 International Wheelset Congress*, 5.

Sungkhaphaitoon, P., & Plookphol, T. (2016). Effect of cooling rate on the microstructure and mechanical properties of Sn-0.7wt.%Cu solder alloy. *Key Engineering Materials*, *675–676*(2), 513–516. https://doi.org/10.4028/www.scientific.net/KEM.675-676.513

Szymczak, T., Gumienny, G., & Pacyniak, T. (2015). Effect of Vanadium and Molybdenum on the Crystallization , Microstructure and Properties of Hypoeutectic Silumin. *Archives of foundry engineering*, *15*(4), 81–86.

Tamada, U. (2020). Design and Static Analysis on a Helical. *A Journal Of Composition Theory*, ISSN : 0731-6755

Totten, G. E. (2006). *Steel heat treatment* (Second edi). Taylor & Francis Group. LLC.

Totten, G.E., Sarmiento, S., & Gaston, A. (2011). Computational modeling of heat treating processes by use of ht-mod and abaqus. *Latin American Applied Research, 224*, 217–224.

Van Bohemen, S. M. C. (2012). Bainite and martensite start temperature calculated with exponential carbon dependence. Materials Science and Technology 28(4), 487–495. https://doi.org/10.1179/1743284711Y.0000000097

Varshney, A., Sangal, S., Gouthama, Pramanick, A. K., & Mondal, K. (2017). Microstructural evidence of nano-carbides in medium carbon high silicon multiphase steels. *Materials Science and Engineering A*. https://doi.org/10.1016/j.msea.2017.09.088

Vinet, L., & Zhedanov, A. (2010). Pricipal effects of Mo in HSLA steels and cross effects with microalloying elements. *International Seminar in Applications of Mo in Steels*, 1–18. https://doi.org/10.1088/1751-8113/44/8/085201

Vukelic, G., & Brcic, M. (2016). Failure analysis of a motor vehicle coil spring. *Procedia Structural Integrity*, *2*, 2944–2950. https://doi.org/http://dx.doi.org/10.1016/j.prostr.2016.06.368

Walentek, A. (2007). Quantitative characterization of microstructure of two phase materials *Thesis*, Katholieke Universiteit Leuven.

Wang, J., Van der Wolk, P. J., & Van der Zwaag, S. (2018). Determination of Martensite Start Temperature in Engineering Steels Part I . Empirical Relations Describing the Effect of Steel Chemistry. *Materials Transactions*. https://doi.org/10.2320/matertrans1989.41.761

Wrigley, R. I., Fawcett, S. W. J., & Brown, T. J. (1996). Flexible manufacturing technology for coil and helical spring products. *Report*

Wu, Q. S., Zheng, S. H., Huang, Q. Y., Liu, S. J., & Han, Y. Y. (2013). Continuous cooling transformation behaviors of CLAM steel. *Journal of Nuclear Materials*, *442*(1-3 SUPPL.1). https://doi.org/10.1016/j.jnucmat.2013.03.072

Xian-, S. H. I. (2013). Decarburization sensitivities of several spring steels used for high-speed trains Decarburization sensitivities of several spring steels used for high- speed trains. *Transactions of Materials and Heat Treatment*, *34*, 7.

Xu, L., Chen, L., & Sun, W. (2018). Effects of soaking and tempering temperature on microstructure and mechanical properties of 65Si2MnWE spring steel. *Vacuum*. https://doi.org/10.1016/j.vacuum.2018.05.029

Xu, T., Feng, Y., Jin, Z., Song, S., & Wang, D. (2012). Determination of the maximum strain-hardening exponent. *Materials Science and Engineering A*, *550*, 80–86. https://doi.org/10.1016/j.msea.2012.04.027

Yamanda, Y. (2007). Materials for springs. (Japanese edit) Springer Berlin Heidelberg New York.

Yetna N'Jock, M., Chicot, D., Decoopman, X., Lesage, J., Ndjaka, J. M., & Pertuz, A. (2013). Mechanical tensile properties by spherical macroindentation using an indentation strain-hardening exponent. *International Journal of Mechanical Sciences*, *75*, 257–264. https://doi.org/10.1016/j.ijmecsci.2013.07.008

Zajac, S. (1999). Role of vanadium in microalloyed steels. *Article in Scandinavian Journal of Metallurgy*, *109*, 690.

Zeineddine, F. (2021). Stress Corrosion Cracking and Mechanisms. *Presentation Submitted to : Dr . Ramazan Asmatulu ME* 0–19. https://doi.org/10.13140/RG.2.2.15187.71204

ZEJ120-Co*:* (2014). Technical specification for primary spring set of ZEJ120-C0 type bogie.

Zhang, L., Chen, K., Du, D., Gao, W., Andresen, P. L., & Guo, X. (2017). Characterizing the effect of creep on stress corrosion cracking of cold worked Alloy 690 in supercritical water environment. *Journal of Nuclear Materials*, *492*, 32–40. https://doi.org/10.1016/j.jnucmat.2017.05.018

Zhang, R., Zheng, W., Veys, X., & Huyberechts, G. (2018). Prediction of Martensite Start Temperature for Lightweight Fe-Mn-Al-C Steels. *Journal of Phase Equilibria and Diffusion*, *39*(5), 476–489. https://doi.org/10.1007/s11669-018-0660-1

Zhu, Y., Wang, Y., & Huang, Y. (2014a). Case Studies in Engineering Failure Analysis Failure analysis of a helical compression spring for a heavy vehicle ' s suspension system. *Biochemical Pharmacology*, *2*(2), 169–173. https://doi.org/10.1016/j.csefa.2014.08.001

Zhu, Y., Wang, Y., & Huang, Y. (2014b). Failure analysis of a helical compression spring for a heavy vehicle's suspension system. *Case Studies in Engineering Failure Analysis*, *2*(2), 169–173. https://doi.org/10.1016/j.csefa.2014.08.001

Zia-Ebrahimi, F., & Krauss, G. (1984). Mechanisms of tempered martensite embrittlement in medium-carbon steels. *Acta Metallurgica*, *32*(10), 1767–1778. https://doi.org/10.1016/0001-6160(84)90233-5

Zorc, M., Nagode, A., Bizjak, M., & Zorc, B. (2019). Decarburization of the Carbon Steel C45 During Annealing in Air Razogljičenje ogljikovega jekla C45 med žarjenjem na zraku. 167–178. https://doi.org/10.2478/rmzmag-2019-0005

Zubov, V., & Grachev, S. V. (1957). Effect of preliminary plastic deformation on the properties of heat treated spring strip. Plenum Publishing Corporation.

Appendix A: Tempered spring steel SEM images

This section contains SEM images at higher magnification in order to show the microstructural details as observed in Figure 4.48 to 4.51.

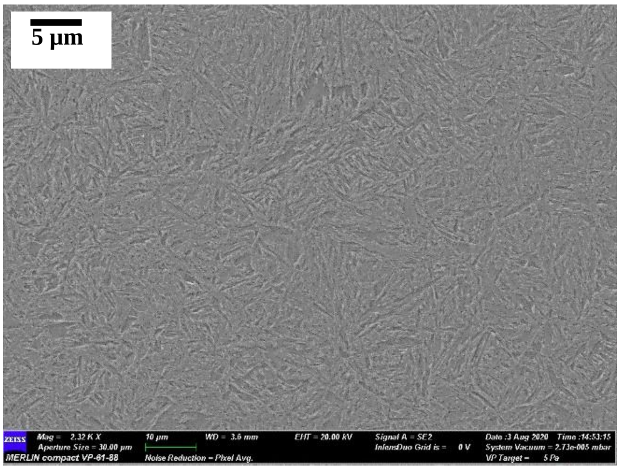

(a)

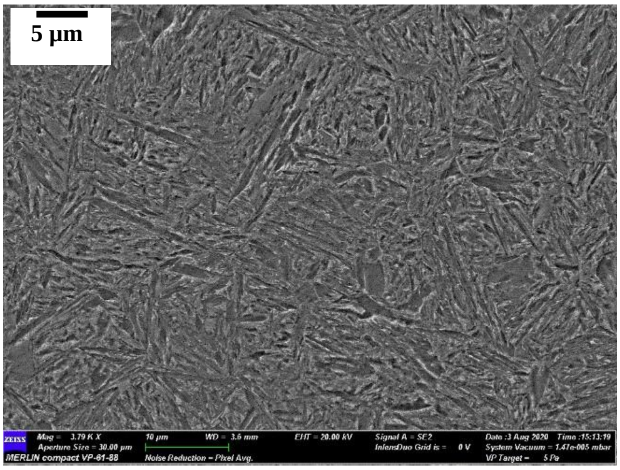

(b)

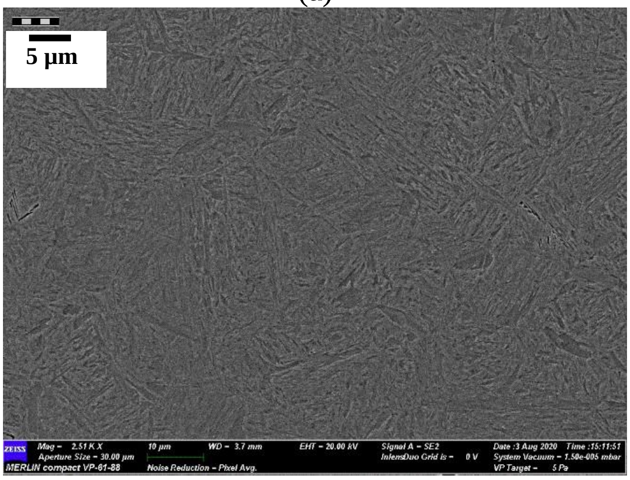

(c)

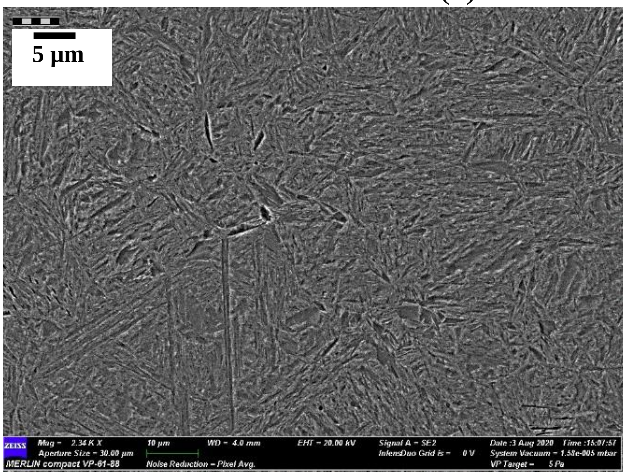

(d)

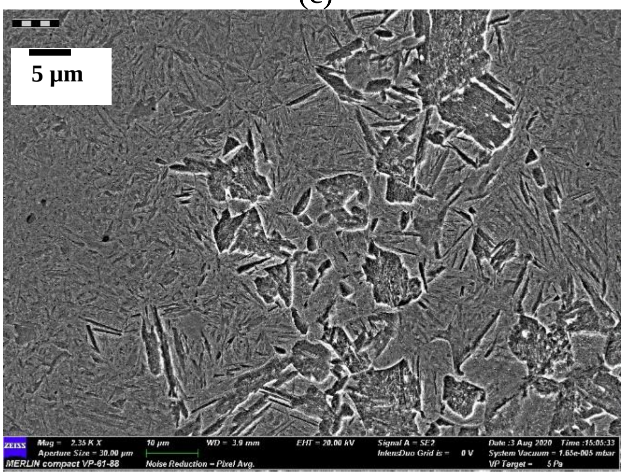

(e)

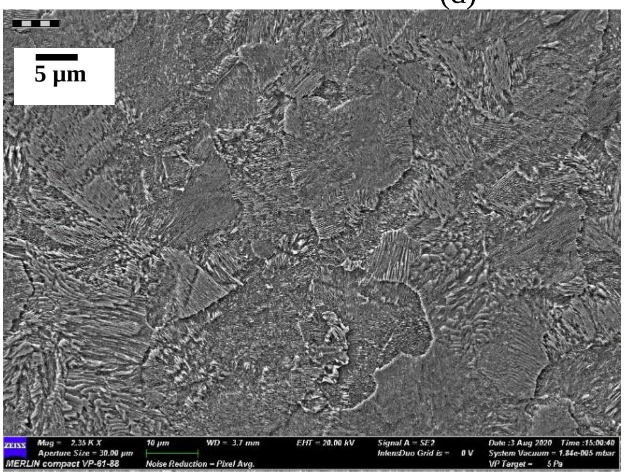

(f)

Figure A. 1 55Cr3 SEM images of the microstructure cooled at (a) 100 °C/s, (b) 30 °C/s, (c).20 °C/s, (d) 10 °C/s, (e) 1 °C/s, and (f) 0.1 °C/s.

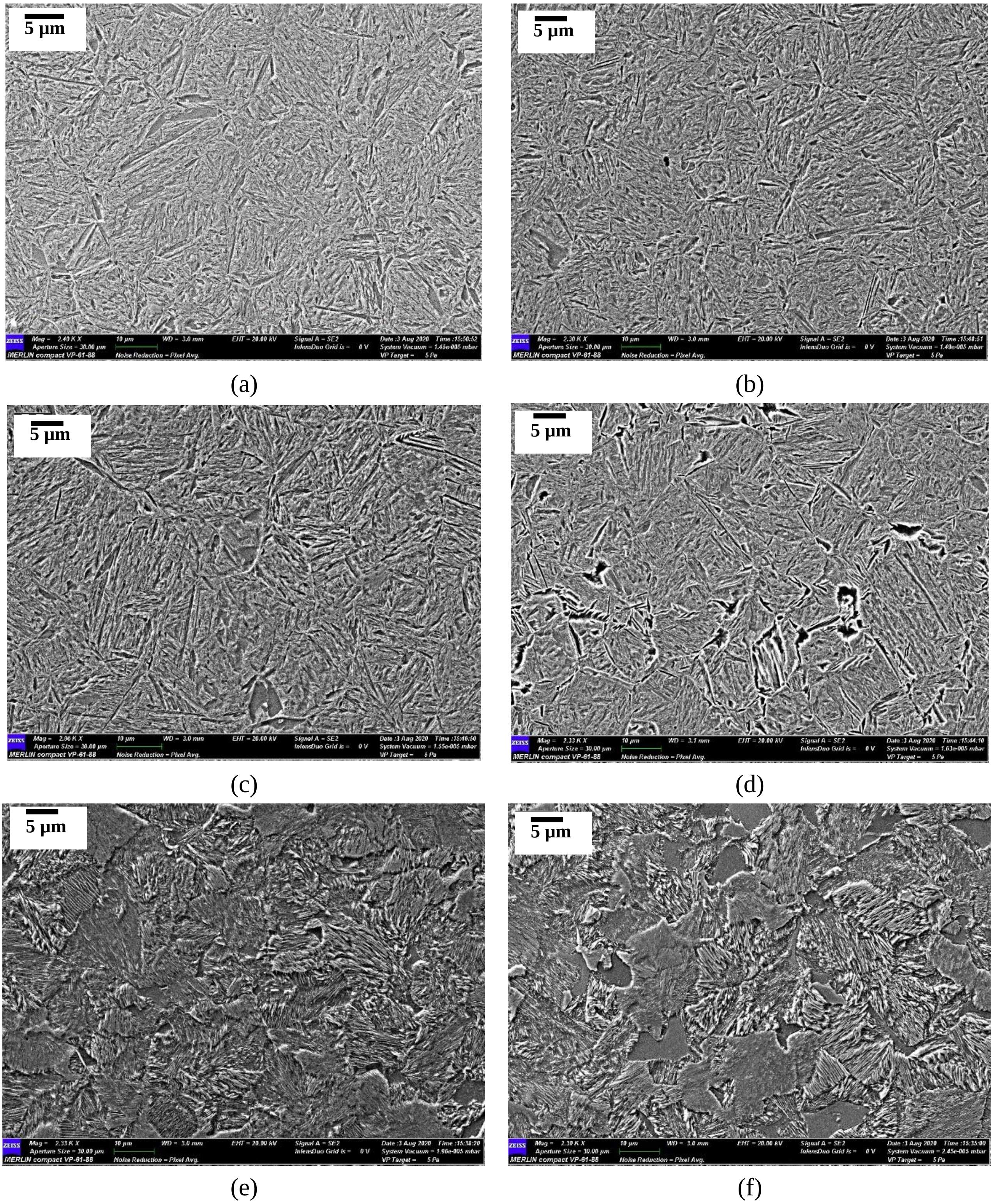

Figure A. 2 54SiCrMoV4 SEM images of the microstructure cooled at (a) 100 °C/s, (b) 30 °C/s, (c) 20 °C/s, (d) 10 °C/s, (e) 1 °C/s, and (f) 0.1 °C/s.

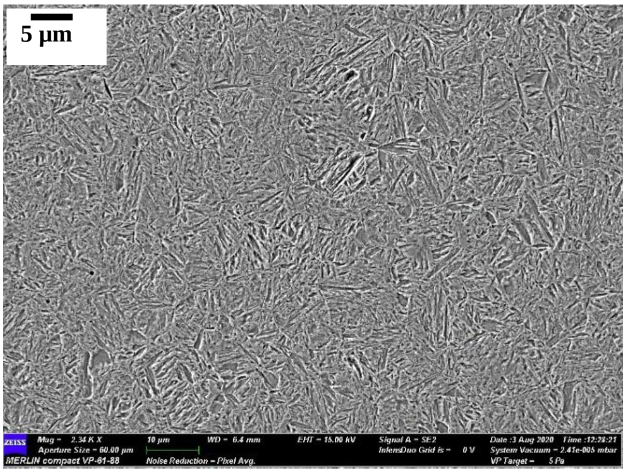

(a)

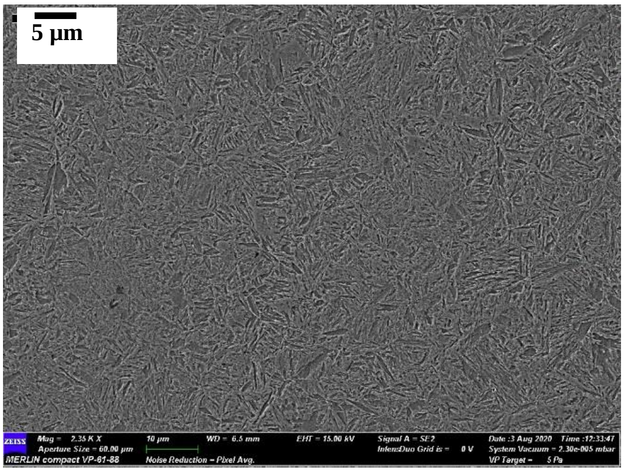

(b)

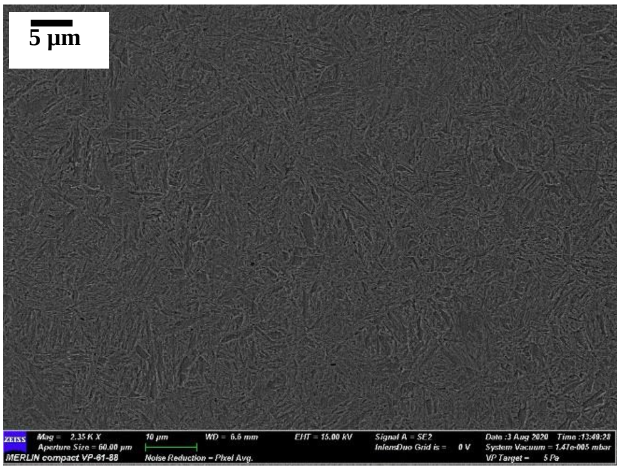

(c)

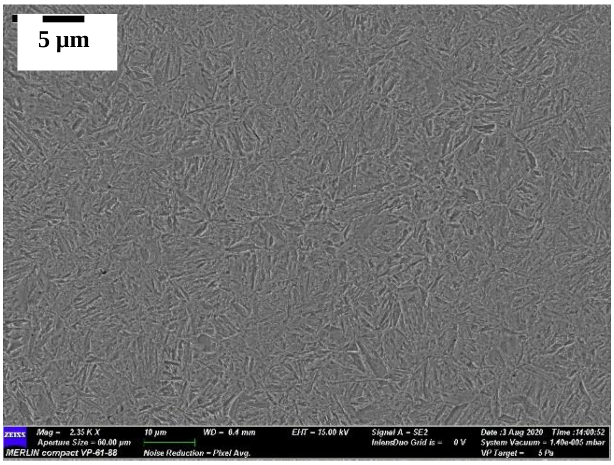

(d)

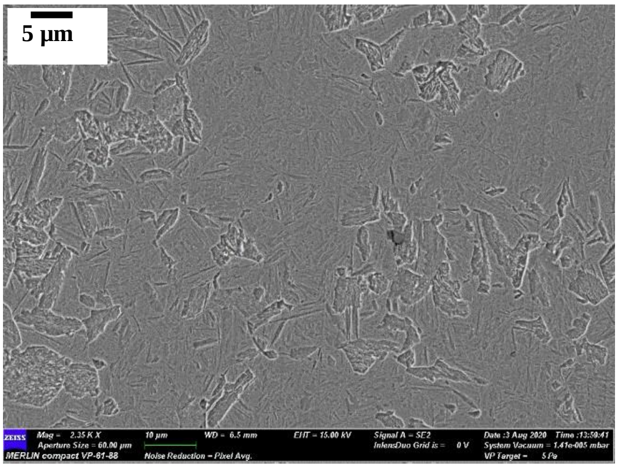

(e)

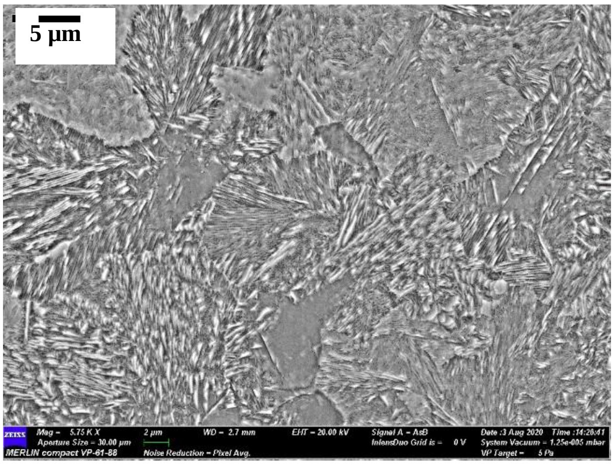

(f)

Figure A. 3 52CrMoV4 SEM images of the microstructure cooled at (a) 100 °C/s, (b) 30 °C/s, (c) 20 °C/s, (d) 10 °C/s, (e) 1 °C/s, and (f) 0.1 °C/s.

Appendix B: Strain hardening exponent graphs

Graphs that were used to determine strain hardening exponent for the three materials at various tempering temperatures and soaking times are covered in this section.

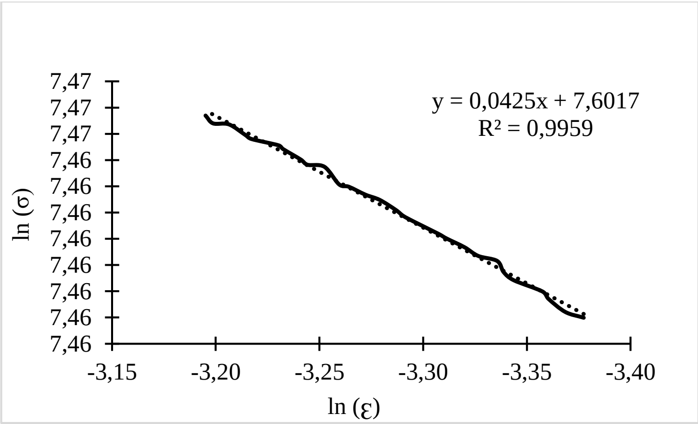

(a)

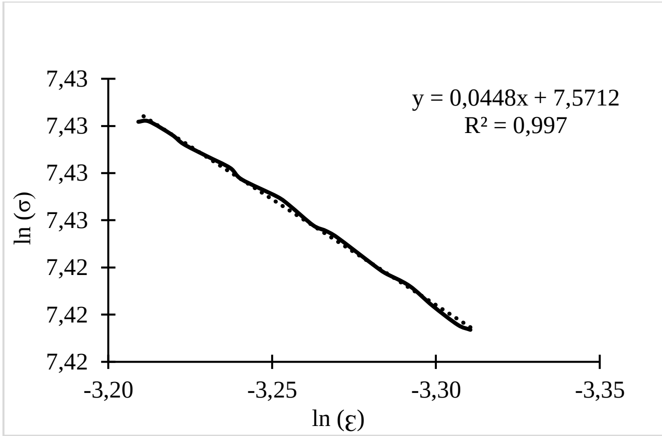

(b)

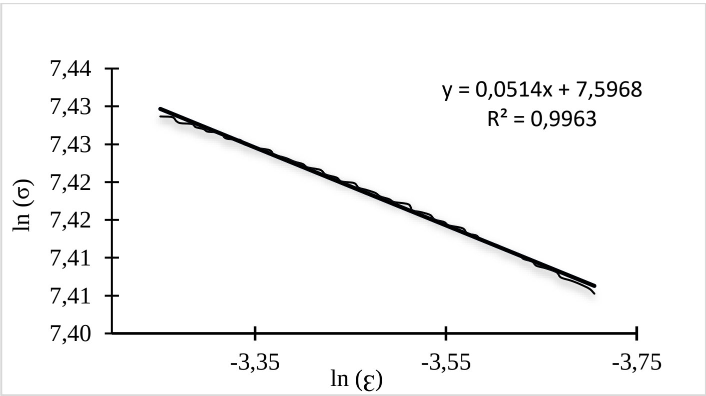

(c)

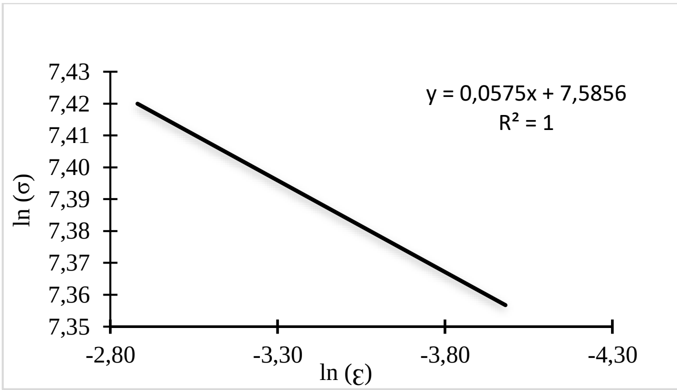

(d)

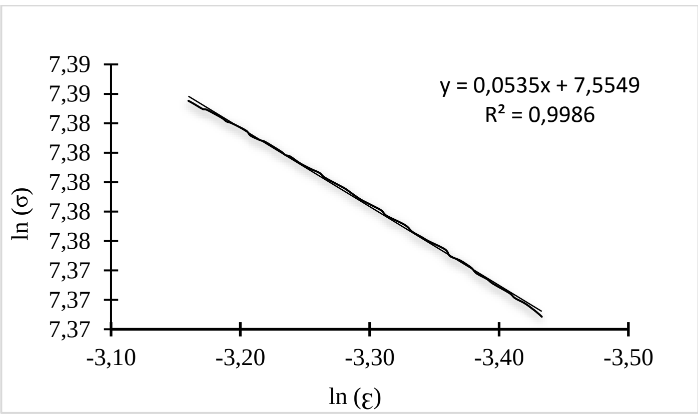

(d)

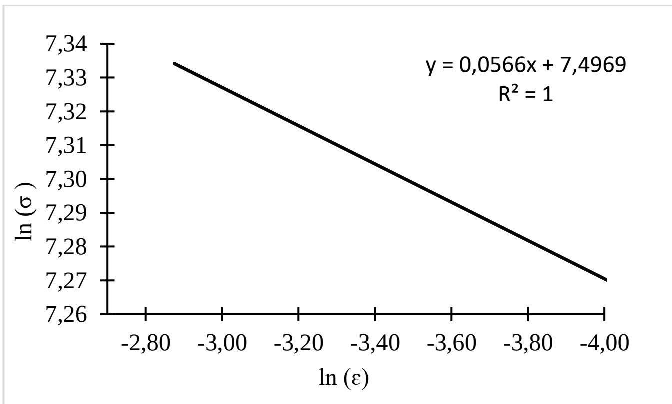

(f)

Figure B. 1 Steel grade 55Cr3 strain hardening exponent (a) 410°C for 2h, (b) 410°C for 3h, (c) 450°C for 2h, (d) 450°C for 3h, (e) 470°C for 2h, and (f) 470°C for 3h.

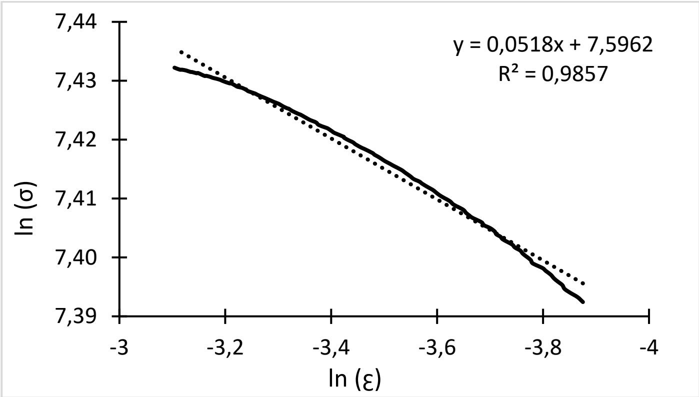

(a)

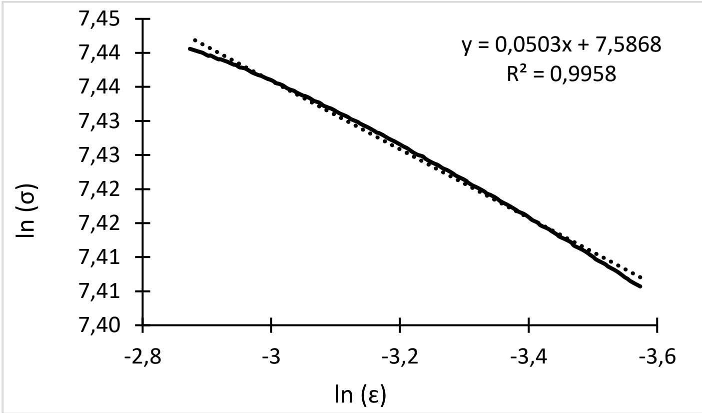

(b)

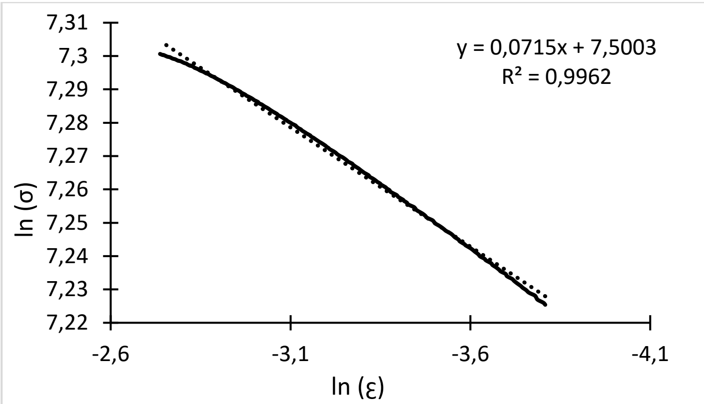

(c)

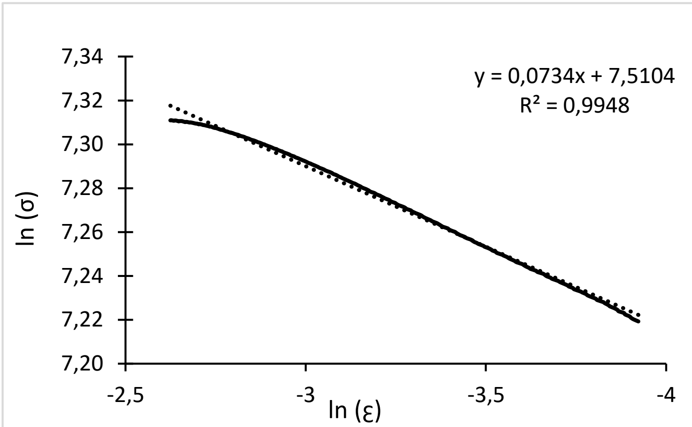

(d)

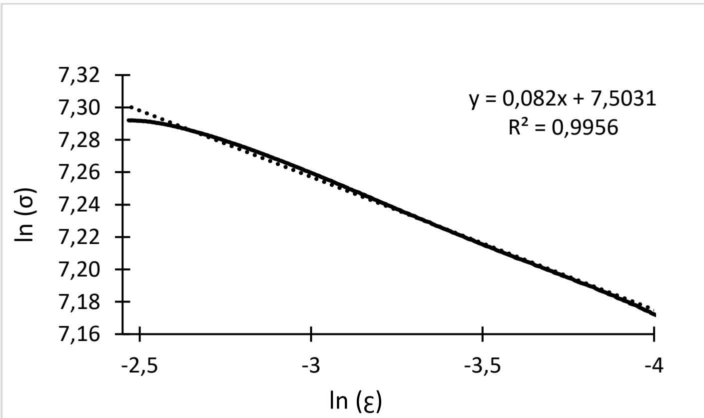

(e)

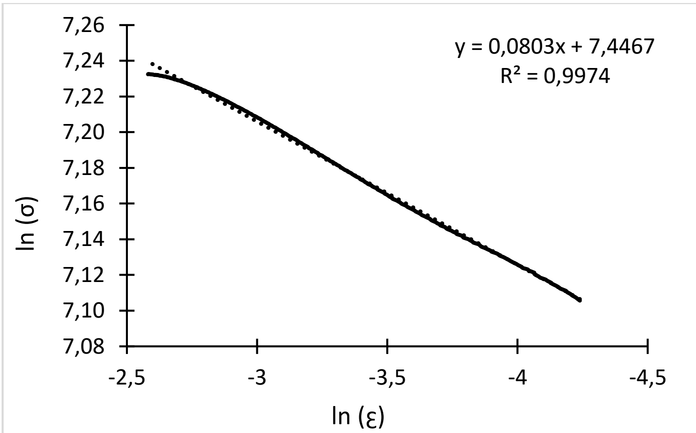

(f)

Figure B. 2 Steel grade 54SiCr6 strain hardening exponent (a) 410°C for 2h, (b) 410°C for 3h, (c) 450°C for 2h, (d) 450°C for 3h, (e) 470°C for 2h, and (f) 470°C for 3h.

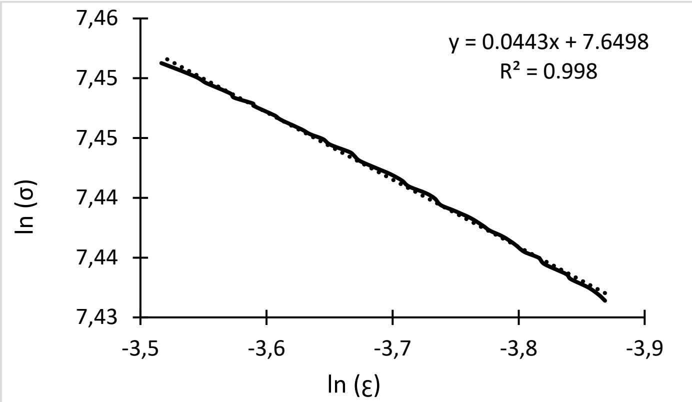

(a)

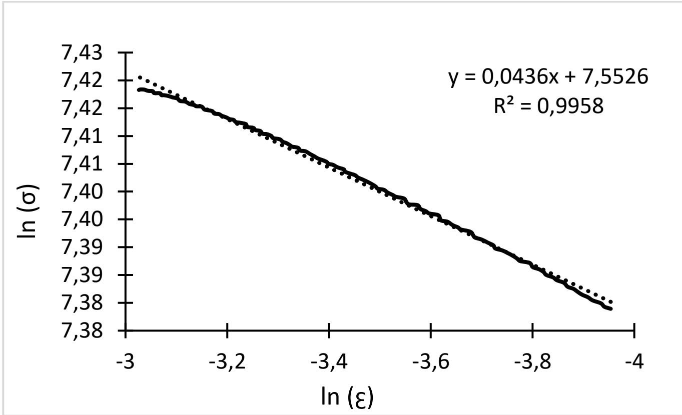

(b)

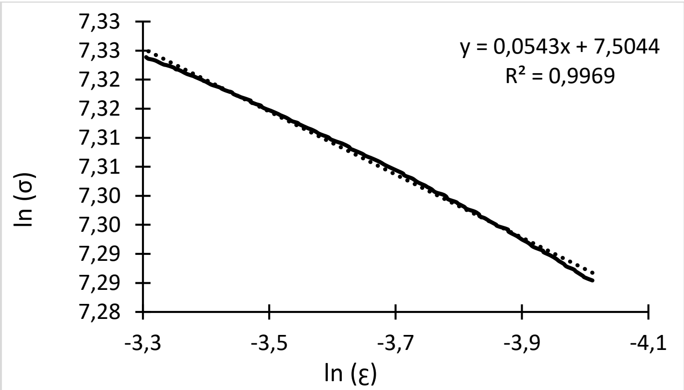

(c)

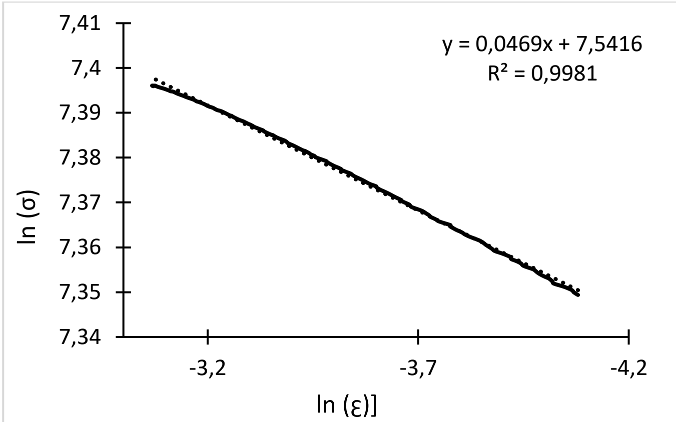

(d)

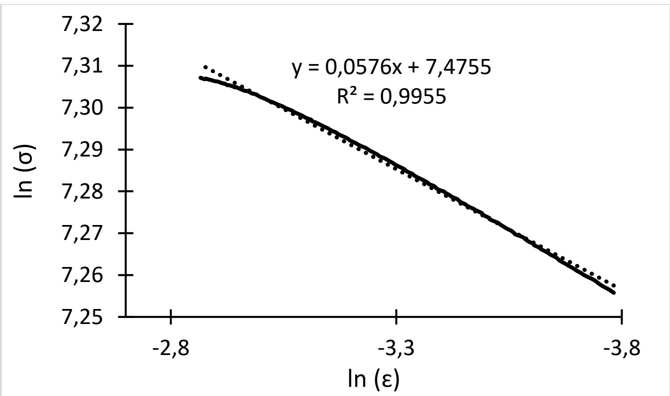

(e)

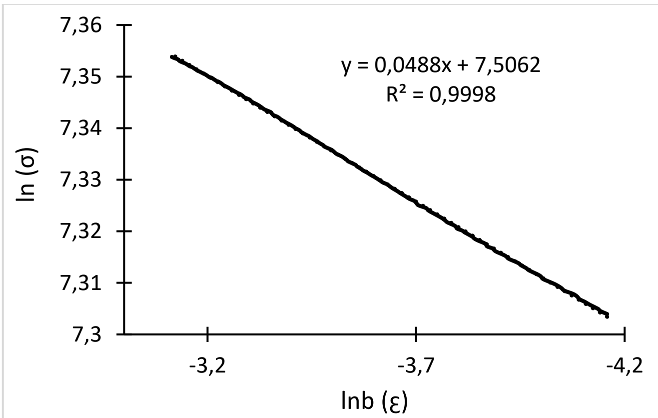

(f)

Figure B. 3 Steel grade 52CrMoV4 strain hardening exponent (a) 410°C for 2h, (b) 410°C for 3h, (c) 450°C for 2h, (d) 450°C for 3h, (e) 470°C for 2h, and (f) 470°C for 3h.

Appendix C: Tensile deformation behaviour graphs

The graphs below validate the yields strength and strength coefficient (K). This section is important in helping us understanding the deformation behaviour of the steels that underwent various heat treatments.

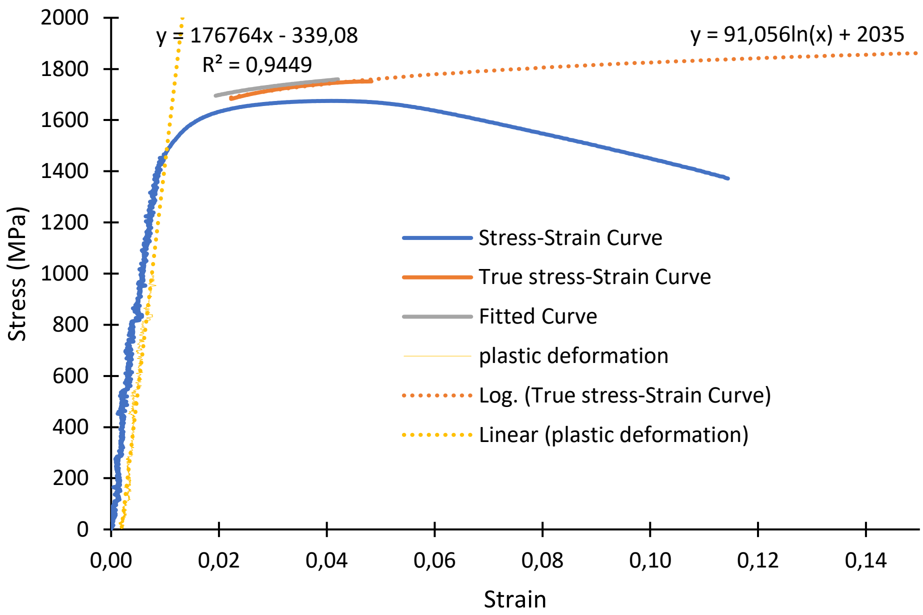

Figure C. 1 Flow stress curves for 55Cr3 tempered at 410°C for two hours.

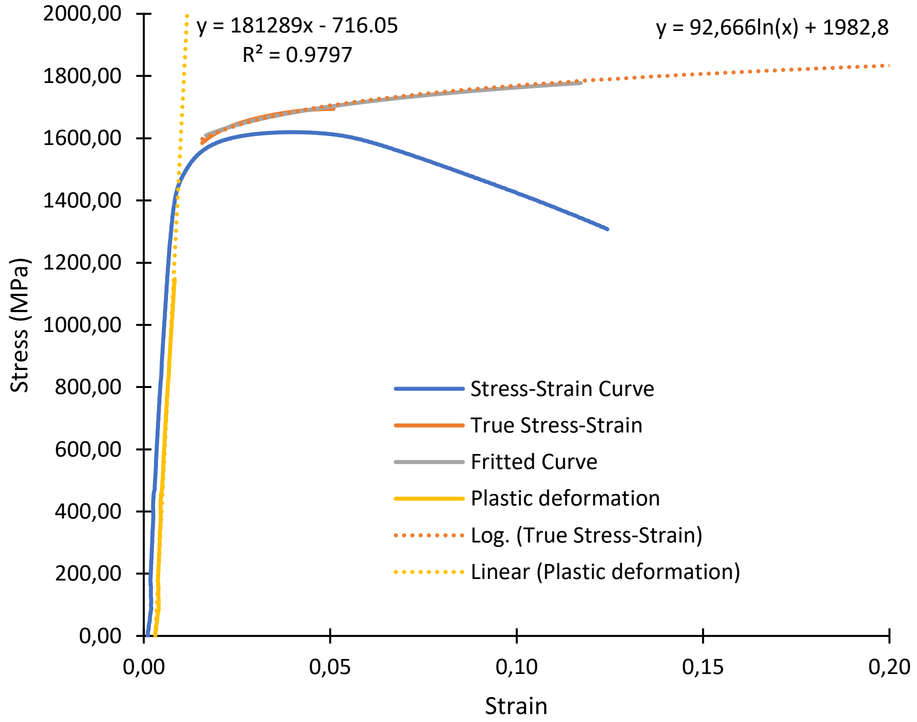

Figure C. 2 Flow stress curves for 55Cr3 tempered at 410°C for three hours.

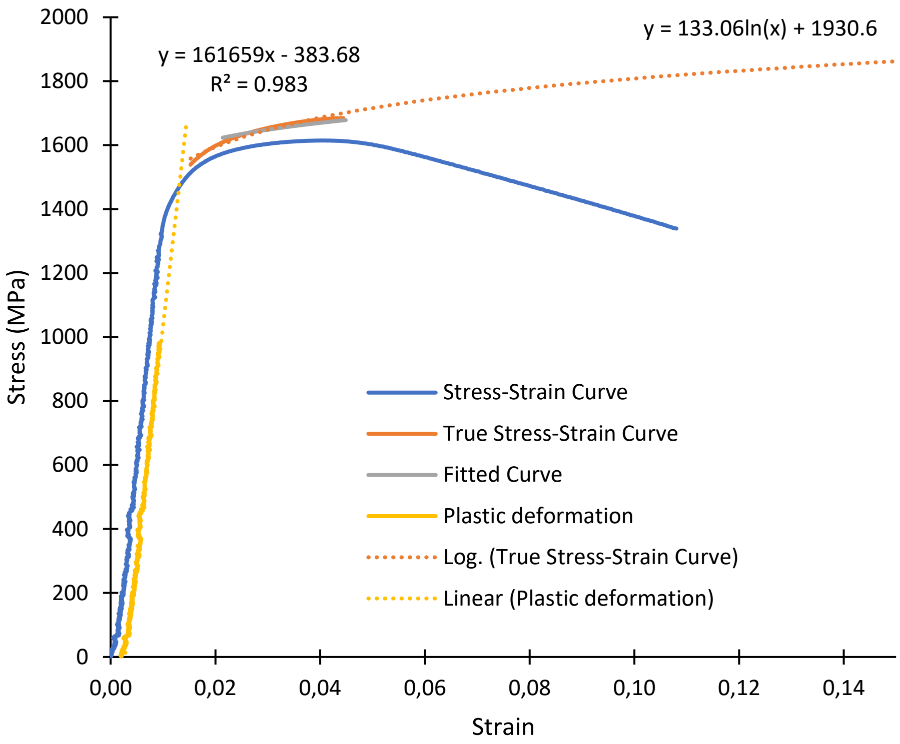

Figure C. 3 Flow stress curves for 55Cr3 tempered at 450°C for two hours.

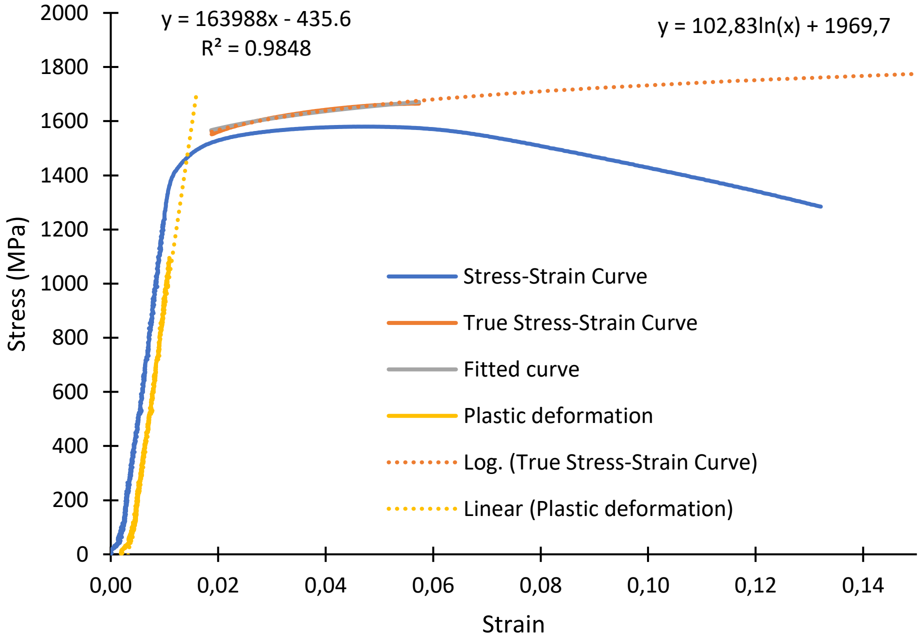

Figure C. 4 Flow stress curves for 55Cr3 tempered at 450°C for three hours.

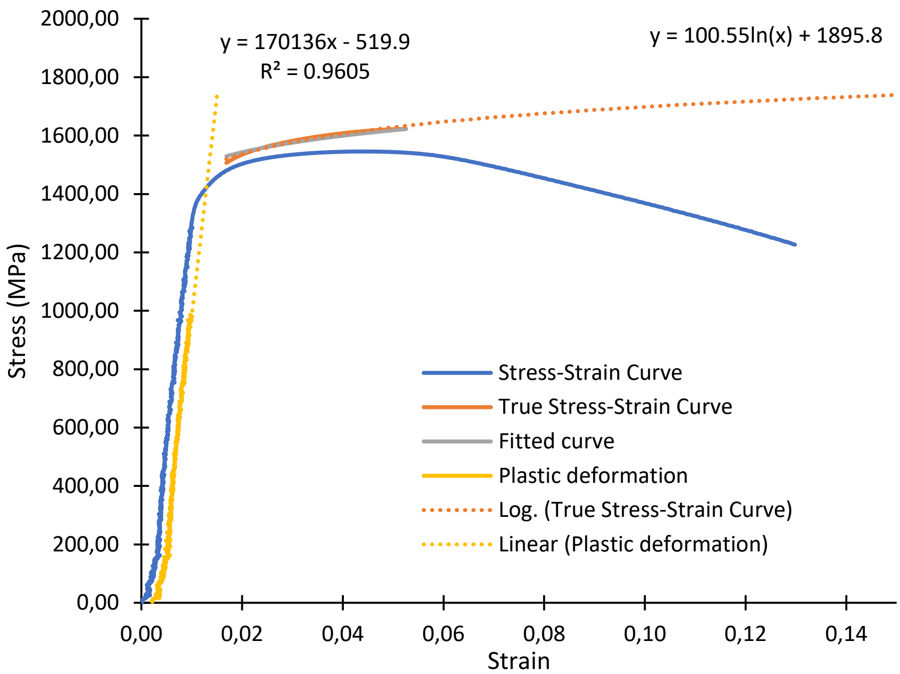

Figure C. 5 Flow stress curves for 55Cr3 tempered at 470°C for two hours.

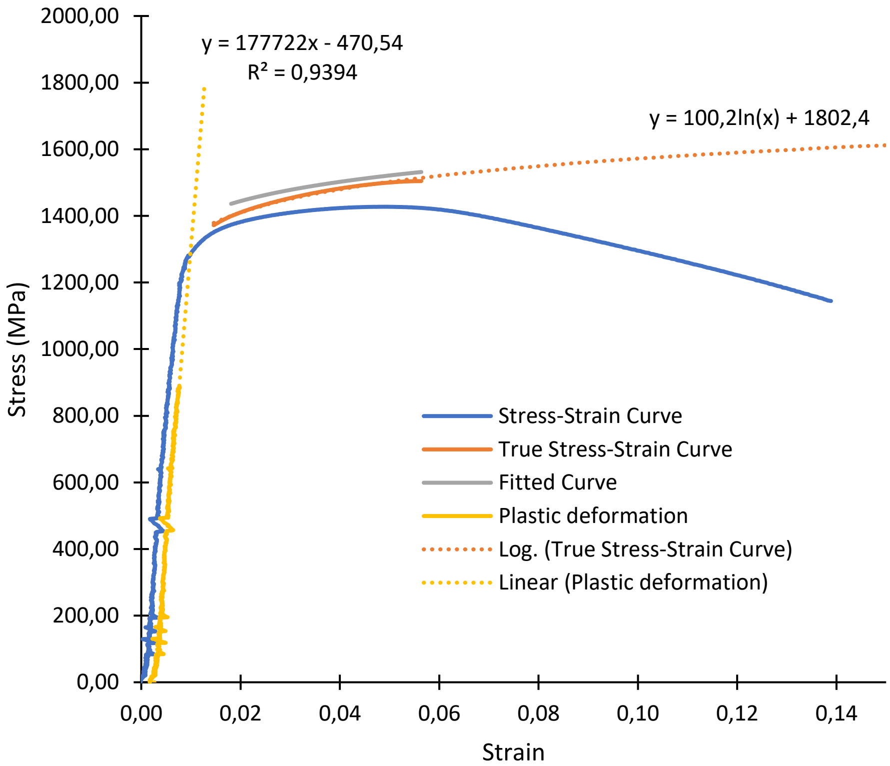

Figure C. 6 Flow stress curves for 55Cr3 tempered at 470°C for three hours.

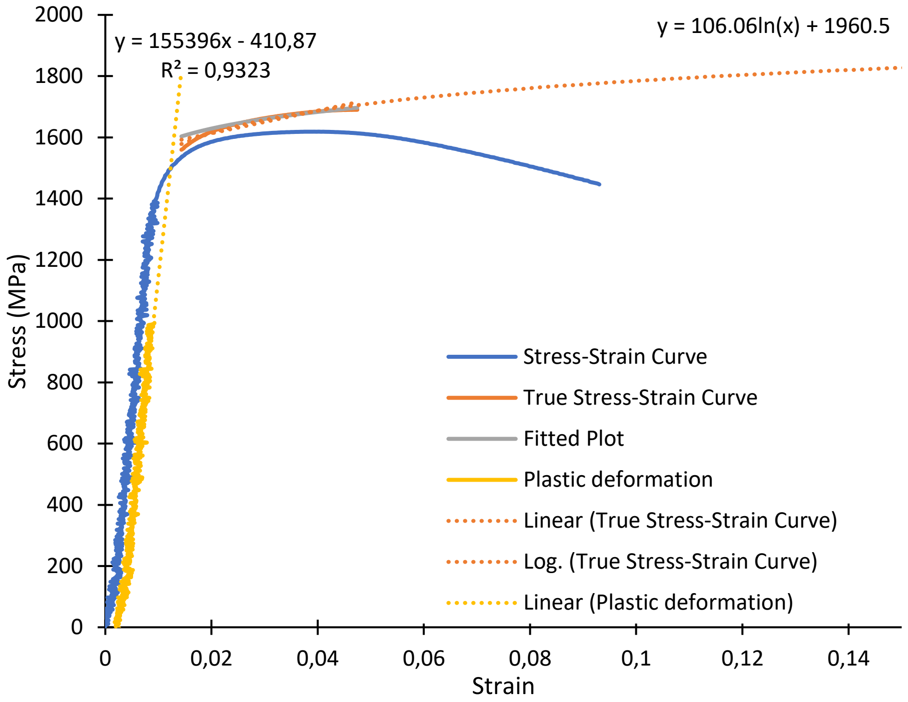

Figure C. 7 Flow stress curves for 54SiCr6 tempered at 410°C for two hours.

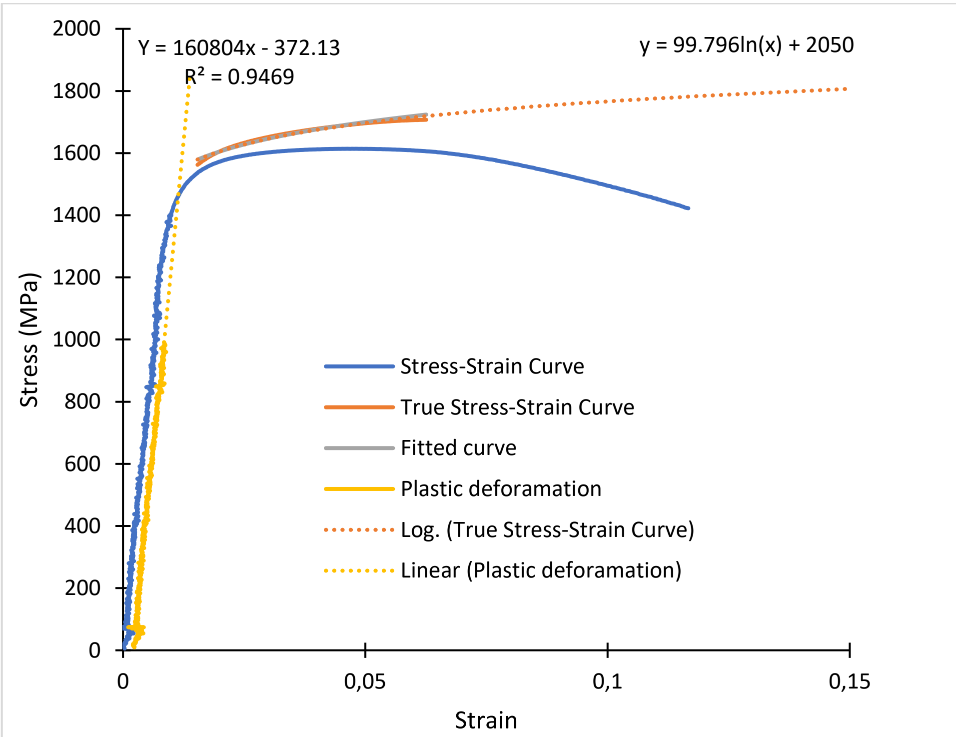

Figure C. 8 Flow stress curves for 54SiCr6 tempered at 410°C for three hours.

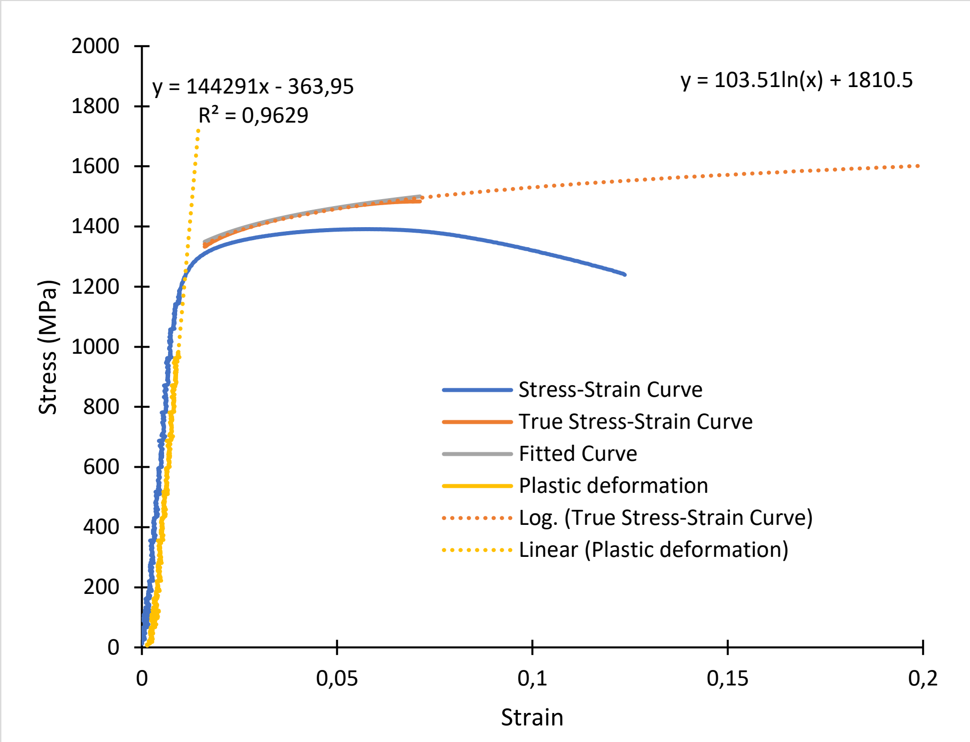

Figure C. 9 Flow stress curves for 54SiCr6 tempered at 450°C for two hours.

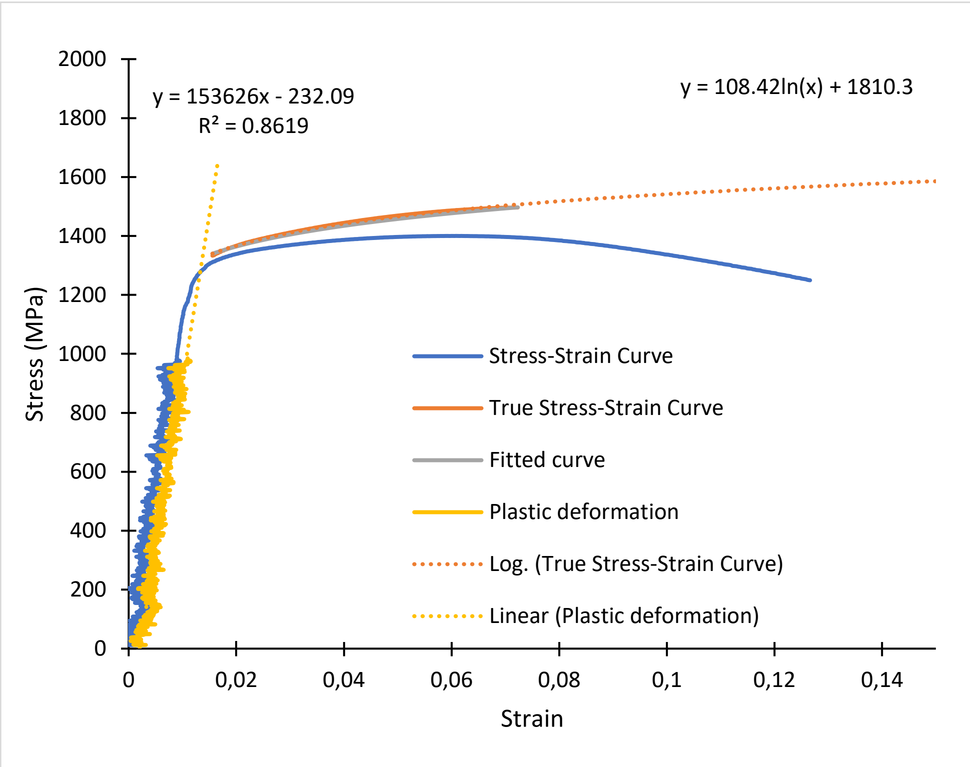

Figure C. 10 Flow stress curves for 54SiCr6 tempered at 450°C for three hours.

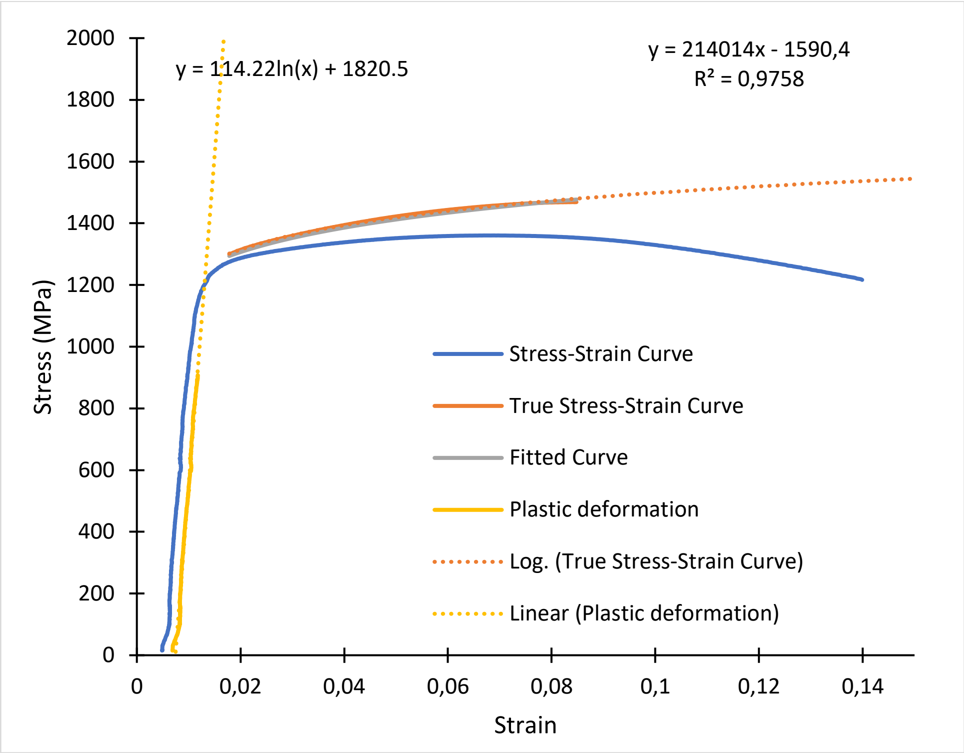

Figure C. 11 Flow stress curves for 55SiCr6 tempered at 470°C for two hours.

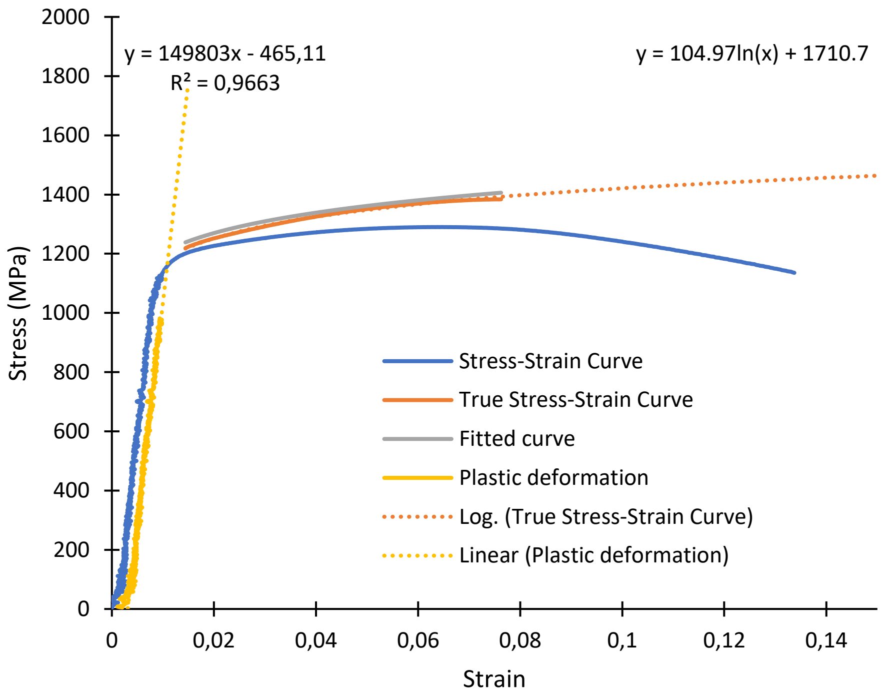

Figure C. 12 Flow stress curves for 54SiCr6 tempered at 470°C for three hours

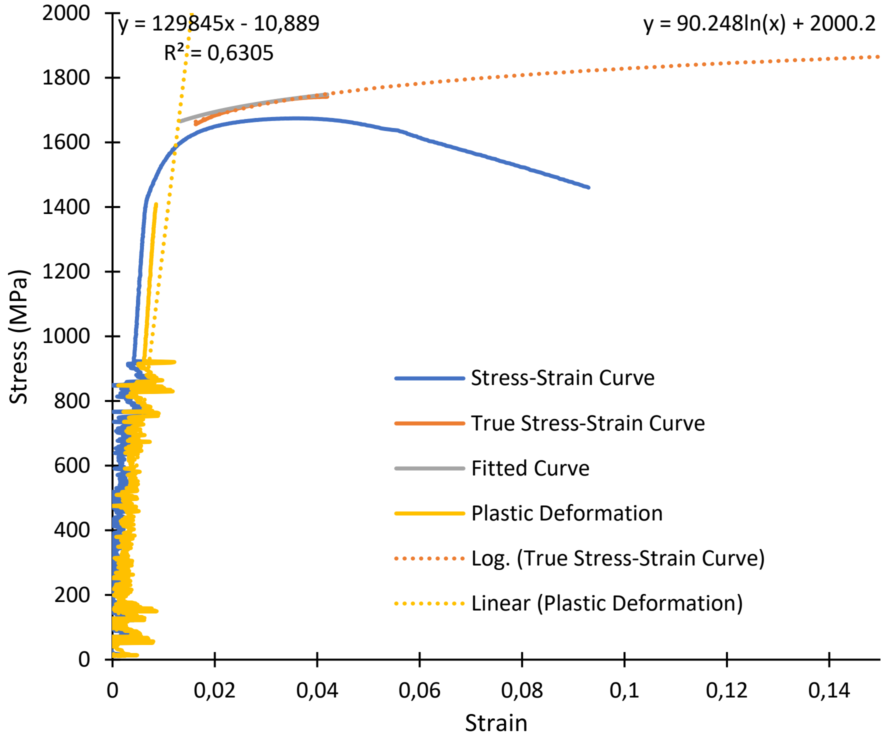

Figure C. 13 Flow stress curves for 52CrMoV4 tempered at 410°C for two hours.

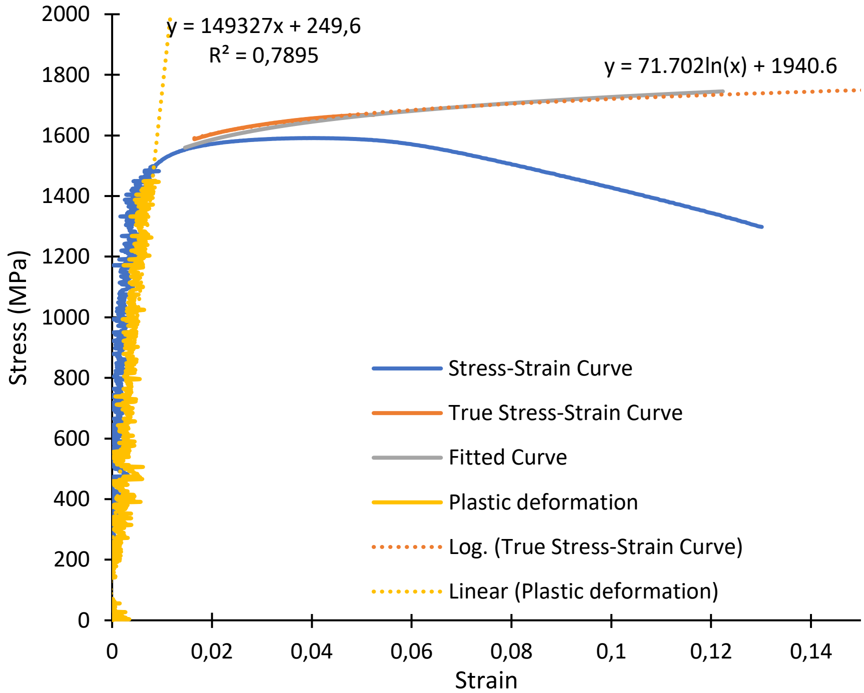

Figure C. 14 Flow stress curves for 52CrMoV4 tempered at 410°C for three hours.

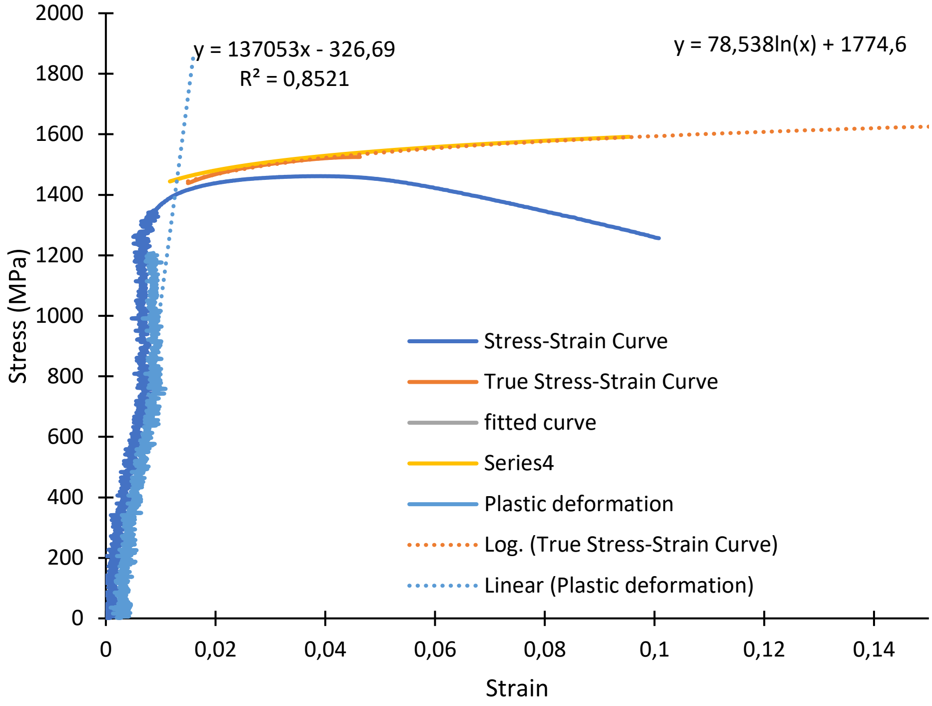

Figure C. 15 Flow stress curves for 52CrMoV4 tempered at 450°C for two hours.

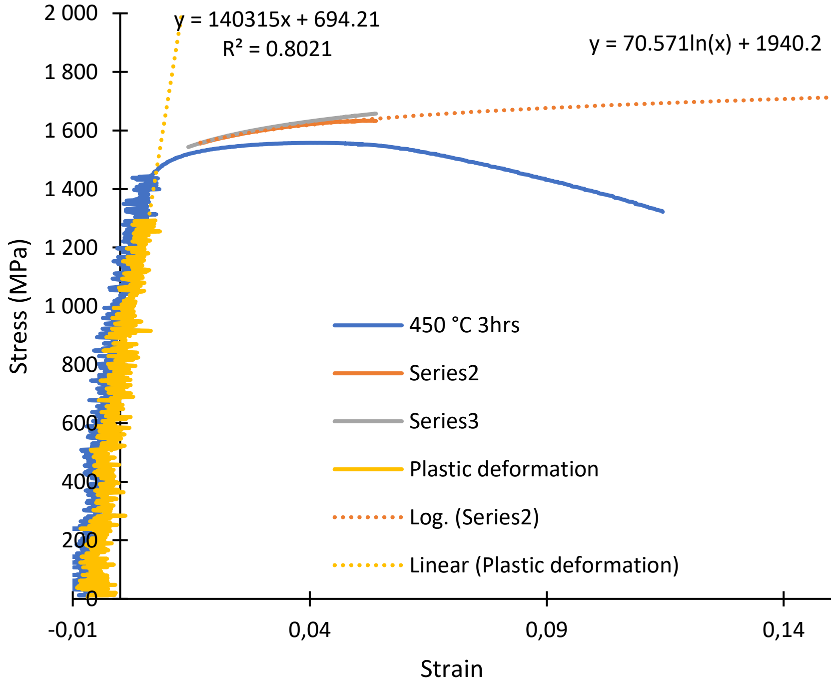

Figure C. 16 Flow stress curves for 52CrMoV4 tempered at 450°C for three hours.

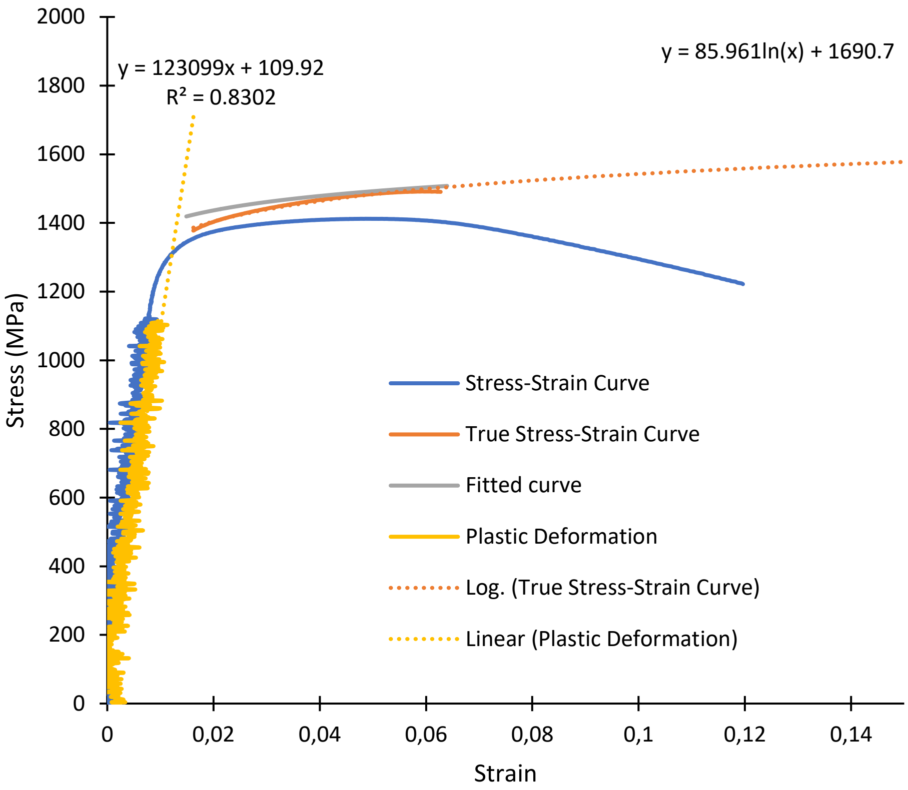

Figure C. 17 Flow stress curves for 52CrMoV4 tempered at 470°C for two hours.

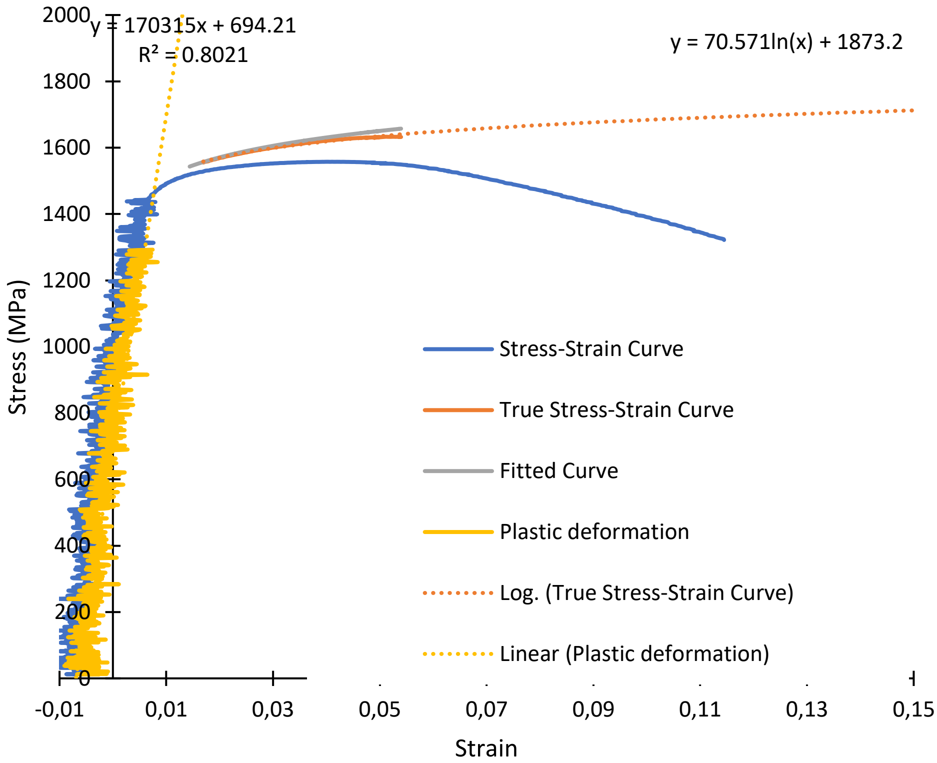

Figure C. 18 Flow stress curves for 52CrMoV4 tempered at 470°C for three hours.